A COMPLETE ANALYSIS FOR REINFORCED CONCRETE SLABS AND SHELLS

A thesis presented for the degree of Ph.D. in Civil Engineering in the University of Canterbury, Christchurch, New Zealand,

by

John C. Bell

1970

E R R A T A

Pages 137 and 140. The cracks spanning the corner at point 2 should be on the top surface, as in Fig. 6.24 on page 157.

Page 149, line 1. Delete "(these curves are both normalised to 1)".

Page 177, line 11. Delete "(both of these curves have been normalised to 1)".

Page 186. The empty spaces in the top surface crack pattern should contain single dark lines, as in Fig. 7.7 on page 184.

ABSTRACT

A complete analysis for reinforced concrete slabs and shells, which analyses a structure for successive loads, is formulated.

For each load a simulated structure is formed from anisotropic (or isotropic) finite elements whose stiffnesses are degraded if they are not compatible with the current stress system. The material constants for the anisotropic finite elements are determined by an analogy with the degradation of the load-moment-curvature relationships of an equivalent beam cross-section.

The method of analysis gives results which compare favourably with existing results of two rectangular slabs, an L-shaped slab, and a cylindrical shell roof model. The comparisons include crack patterns, load-displacement curves, and displacement profiles. The theoretical crack patterns include the direction and area of cracking. They are similar to the experimental crack patterns, and they follow the directions indicated by the yield-line theory, though the theoretical yield regions have substantial width. The theory predicts stiffer behaviour for some points on the structures and more flexible behaviour for the other points.

ACKNOWLEDGMENTS

Grateful acknowledgment is made to the following:

Professor H.J. Hopkins, the Head of the Civil Engineering Department, under whose overall guidance this study was made.

Dr. D.G. Elms, supervisor for this study, for his interest, guidance, and assistance both in the research, and in the writing, of this thesis.

Dr. A.J. Carr, for his helpful comments and advice on finite elements.

The staff of the Computer Centre, for punching cards and executing programs.

Mrs. M. Sewell and Mrs. D. Ball for typing the manuscript.

My wife, Robyn, for her constant help and encouragement.

The University Grants Committee, for financial assistance in the form of a Post-Graduate Scholarship.

TABLE OF CONTENTS

LIST OF FIGURES

LIST OF TABLES

LIST OF SYMBOLS

A list of the commonly used symbols and their general meaning follows.

1) Scolars

a	Global dimensions of a triangle.
a_{sb}	Area of reinforcement per unit width in the bottom of a reinforced concrete section.
a_{sm}	Area of reinforcement per unit width in the middle of a reinforced concrete section.
a_{st}	Area of reinforcement per unit width in the top of a reinforced concrete section.
b	Global dimension of a triangle.
c	Coefficient.
d	Differential symbol. Crack width.
e	Exponential symbol.
f	General function.
f_c	Concrete stress.
f'_c	Cylinder strength of concrete.
f_t	Tensile strength of concrete.
h	Thickness. Height of triangle.
ℓ	Length.
ℓ_b	Bond length.
ℓ_c	Length of cracked region.
m	Minimum of a variational expression. Moment/unit length.
n	Normal to boundary.

p	Neutral axis depth.
q	Loading function. Coefficient.
r	Coordinate in the polar coordinate system.
s	Triangle side direction.
t	Thickness.
u	x displacement component.
v	y displacement component.
w	z displacement component. Coordinate function.
x	General displacement component. (dx = displacement element.) Local coordinate system and coordinate.
y,z	Local coordinate system and coordinates.
A	Area of two-dimensional finite elements. (dA = area element.) Coefficient.
C1,C2,CC,TC	Concrete force.
CS,TS	Reinforcement force.
D	Plate flexural rigidity.
E	Modulus of elasticity.
F	General function.
G	Shear modulus.
H	Coefficient.
I	Integral. Moment of inertia.
J	Polar moment of inertia.
L	Length.
M	Bending moment.

N	Force.
P	Potential energy of the applied or nodal forces. Force. Point.
P*	Complementary potential energy of the applied forces.
T	Force. Bond stress. Torque.
U	Strain energy of deformation.
U*	Complementary strain energy of deformation.
V	Total potential energy. Volume. (dV = volume element.)
V*	Total complementary potential energy.
W	Work.
X, Y, Z	Global coordinate system and coordinates.
α	Angle. Coefficient.
β	Coefficient.
γ	Total shear strain. Angles that the triangle sides make with the x axis.
δ	Variation symbol.
ε	Strain components.
$\varepsilon_{bs}, \varepsilon_{ts}$	Reinforcement strain.
ε_c	Concrete strain.
ε_o	Concrete strain corresponding to the maximum concrete stress.
ε_{su}	Reinforcement ultimate strain.
ε_t	Maximum concrete tensile strain.
ε_u	Maximum concrete compressive strain.

ε_y Reinforcement yield strain.

ζ Natural coordinates.

θ Angle.

κ Strain hardening function. Coefficient of orthotropy.

λ Coefficient of proportionality in the flow rate of plasticity. Coefficient.

μ Coefficient.

ν Poisson's ratio.

ρ Curvature.

σ, τ Stress components.

σ_{su} Reinforcement ultimate stress.

σ_y Reinforcement yield stress.

ϕ, ψ Interpolation function. General function.

ω Average rotation.

Σ_o Reinforcement surface area.

2) Vectors and Matrices

$\{\}$ Column vector.

$[]$ Matrix.

f Vector of known values of the function F .

k Element stiffness matrix in terms of the nodal displacements.

q Nodal displacement vector (for the whole structure).

r Nodal displacement vector (for an element).

u, v, w	Submatrices of r including specific (x, y, z) components.
A	Transformation matrix.
B	Strain-nodal displacement matrix.
C	General stress-strain matrix.
D	Nodal stress-nodal strain matrix. Diagonal matrix.
E	Connective matrix.
G	Constraint matrix.
I	Identity matrix.
K	Stiffness matrix in terms of nodal displacements (for the whole structure).
L	Upper triangular matrix with diagonal terms unity.
M	Moment vector.
N	Stiffness matrix in terms of nodal strains.
O	Null vector.
Q	Weighting matrix resulting from strain energy integration over an element. Nodal force vector (for the whole structure).
R	Nodal force vector (for an element).
S	Stress matrix.
T	Transformation matrix.
U, V	Submatrices of the strain-nodal displacement matrix, B.
α	Diagonal matrix of coefficients.
ε	Infinitesimal strain vector.
ζ	Natural coordinate vector.

ϕ , ψ	Interpolation vector.
χ	Nodal curvature vector.
σ , τ	Stress vector.

INTRODUCTION AND SCOPE OF RESEARCH

Present day analyses of reinforced concrete slabs and shells rely predominantly upon elastic analyses and, to a more limited extent, upon yield-line or limit analyses[1,2,3,4]. An elastic analysis is advantageous becuase it is relatively simple and also, both stresses and displacements can be obtained from it. A yield-line analysis provides both an ultimate load and a collapse mechanism for the structure. However, it has the severe disadvantage that it does not give any indication of the displacements near the ultimate load.

The present emphasis on ultimate strength analyses indicates the interest for a greater knowledge of a structure's behaviour after cracking has commenced. However, our knowledge of the behaviour of a structure is almost unknown from the load at which cracking commences until the ultimate load is reached. Additional information that would be useful includes,

a) load-displacement relationships for points on the structure,

b) crack patterns at different loads,

c) regions of high stress intensity - including their magnitude and effective area, and

d) the variation in the structural behaviour at different loads - especially near the working load.

Hence, there is a need for a complete analysis (implying an analysis giving structural information for any load from zero to ultimate rather than an analytical utopia) for reinforced concrete slabs and shells. Some work has already been done in this field: for reinforced concrete Bhaumik and Hanley[5], Riera and Billington[6], and McNiece and Kemp[7] have made contributions. The present report endeavours to add to these contributions by presenting a method for a complete analysis for reinforced concrete slabs and shells which can take into account most of the actual changes that a reinforced concrete section undergoes as it cracks and as the reinforcement yields.

Objectives of this Research: The objectives of this research are,

a) to extend an elastic finite element analysis[8,9] so that non-linear and inelastic effects for both plate bending and shell problems can be included,

b) to compare two different methods of incorporating inelastic or non-linear effects, namely,

i) the use of finite elements which are either totally uncracked or totally cracked, and

ii) the development of a finite element which can be partially uncracked, and

c) to compare these methods of analysis with existing experimental results.

Scope of the Thesis: This thesis has been divided into three parts which describe,

a) the finite element method of analysis,

b) a complete analysis for reinforced concrete slabs and shells, and

c) a comparison between this method of analysis and some existing experimental results.

The first part of the thesis describes the history of the finite element method of analysis from its origins by Hrennikoff[10], Argyris[11], and Turner, Clough, Martin and Topp[12] to its present day status. Finite elements formed by the displacement model are described in detail because these elements have been used in the analyses described in this thesis. The basic steps of the finite element method of analysis are also described and then a chapter is devoted to the errors that are associated with the method and where possible, examples of these errors are given.

The second part of this thesis commences with a review of some of the previous work that has been done in the field of inelastic analysis which is of interest to this work. This is followed by a description of a complete analysis for reinforced concrete slabs and shells, both in a summarised form and also in detail. Two methods of forming partially cracked elements for both plate bending and plane stress finite elements are described together with two examples comparing their behaviour with elements that are either totally

cracked or totally uncracked.

Some structures that had been tested experimentally were analysed and their results have been compared in the third part of this thesis. Four structures were analysed, a rectangular and an L-shaped slab which were tested by Islam[13], another rectangular slab which was tested by Sharpe[14], and a cylindrical shell roof model which was tested by Hedgren[15]. At the end of each analysis the principal results and conclusions are stated. Also, at the end of the report general conclusions are stated together with suggestions for further research within this field.

PART I: THE FINITE ELEMENT METHOD

C H A P T E R 1

THE DEVELOPMENT OF THE FINITE ELEMENT METHOD

1.1 Review of Previous Work

The finite element method of analysing complex structures originated from the works of Hrennikoff[10], Argyris[11] and Turner, Clough, Martin and Topp[12]. Basically, the finite element method idealizes a structure as an assemblage of interconnected discrete elements, whose properties are known, thus forming a structural model which can be analysed using basic matrix algebra.

Hrennikoff (1941), by idealizing a two dimensional structure as a framework of bar elements, employed this method to analyse plane stress and plate bending problems. However, because of the laborious amount of hand computation involved, the framework method did not receive much attention until the early 1950's when this onerous task was eliminated with the introduction of digital computers.

The foundations of the finite element method were established in 1954 when Argyris described two methods of analysing complex structures depending on whether the displacements or the forces are the unknowns (the displacement method and the force method respectively); also, he concisely summarised the energy methods which are the basis of all element stiffness derivations.

Turner, Clough, Martin and Topp further developed the displacement method (which they called the "direct stiffness" method) by arranging the analysis in a matrix form suitable for automatic computation. They derived the in-plane stiffness of plate elements and extended the earlier work of Levy[39] who had proposed analysing aircraft structures as an assemblage of beam and torque box elements.

Improved elements have since been developed for the analysis of plane stress problems[16, 17, 18, 19]. For example, in the displacement model of finite element analysis, initial elements had a constant strain field throughout each element whereas subsequent elements possessed a linearly varying or a quadratically varying strain field thus enabling a more accurate representation of the true strain field to be obtained.

The early triangular plate bending elements did not give reliable or consistent results[20] (refer Section 3.2) and this resulted in a new and more concentrated study of the assumptions and conditions underlying the finite element method, and in particular, the displacement model of finite element analysis. Fraeijs de Veubeke[21], Felippa[19], Tong and Pian[22,23], and Oliveira[24] were among those who studied the bases of the finite element method and enumerated the conditions that finite elements must fulfil if monotonic convergence to the correct solution is require. Due to this increased understanding plate bending elements of greater

sophistication and accuracy have been developed which eliminate the difficulties that were formerly encountered[25, 26,27,28,29,30].

Shells of revelution (i.e. axisymmetric shells) have been analysed using conical elements[31,32,33], and more recently with a doubly curved element[34]. For non-axisymmetric shells planar triangular elements have normally been used although recently some curved elements have also been derived[35,36,37]. The derivation of non-planar elements, however, becomes increasingly complex due to the difficulty of including all the rigid body movements, of maintaining interelements compatibility, and of keeping the number of degrees of freedom of the element within reasonable limits.

The present trend in element derivations is towards the development of improved elements that will depict the structural topology as closely as possible and also maintain interelement compatibility. At the same time the use of the finite element method is expanding and includes the elastic and dynamic analyses of many structures including buildings and building components (e.g. slabs, roofs, beams etc.), arch and gravity dams, embankments and openings in rock structures, and flow nets.

1.2 Classification of Finite Elements

Following Fraeijs de Veubeke's method[21] we classify finite elements depending on whether they:

1) satisfy compatibility but not equilibrium (displacement model),

2) satisfy equilibrium but not compatibility (equilibrium model), and

3) violate both compatibility and equilibrium.

In this classification the derivations of finite elements belonging to group 1) or to group 2) are termed "pure" derivations because bounds on the unknown displacements or forces can be postulated. No bounds however can be postulated for those derivations belonging to group 3), the "impure" derivations.

Displacement (or Compatibility) Model: The displacement model is based upon assumed displacement fields over each element which provide a continuous displacement field over the complete structure. This method utilizes the principle of minimum total potential energy which seeks to minimize the total potential energy of a structure that has been deformed from its equilibrium position by small compatible displacements (i.e. compatibility is maintained)[11,38]. For example, consider a body which is deformed by a compatible displacement system $\{\delta r\}$ which induces a strain system $\{\delta \varepsilon\}$ (Fig. 1.1 illustrates this for a one dimensional case), then

$$V = U - P \tag{1.1}$$

where V is the total potential energy, U is the strain energy of deformation, and P is the potential energy of the

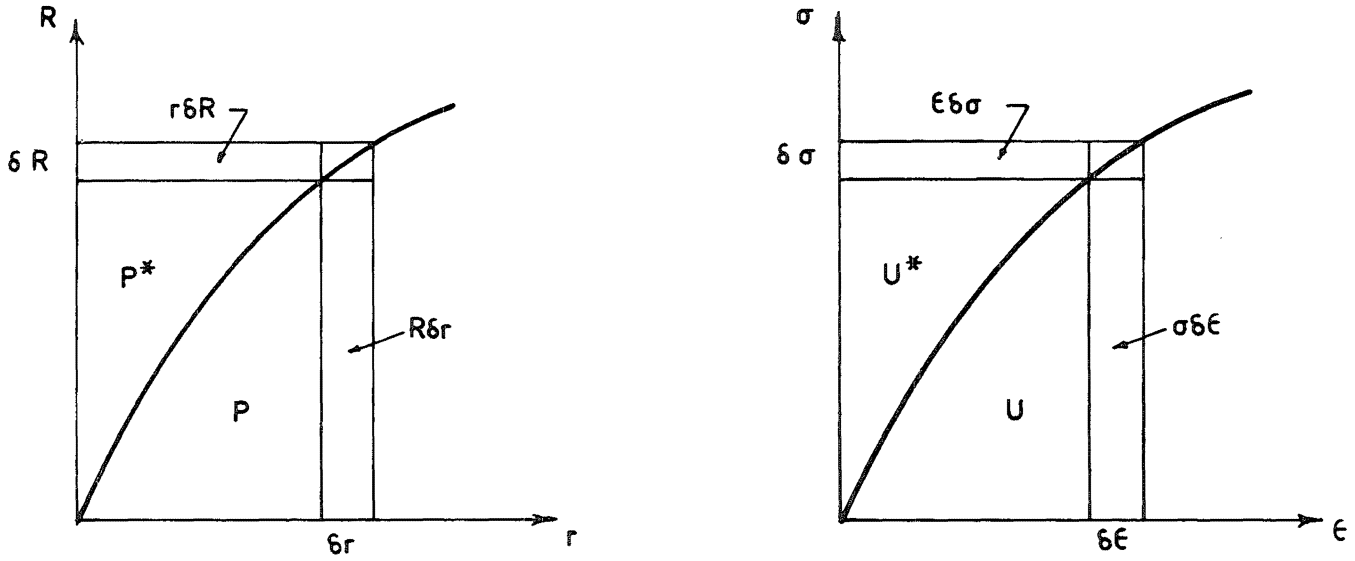

Fig. 1.1. Force-Displacement and Stress-Strain Relationships

applied forces. Minimizing the total energy we obtain

$$\delta V = \delta U - \delta P$$

$$= \int_V \{\sigma\}^T \{\delta\varepsilon\} dV - \int_W \{R\}^T \{\delta r\} dV = 0 \qquad (1.2)$$

Equilibrium Model: The equilibrium model is based upon assumed stress fields within each element which maintain equilibrium over the complete structure. This method utilizes the principle of minimum complementary energy which seeks to minimize the total complementary potential energy of a structure that has been stressed from its compatible position by small self-equilibrating stresses (i.e. equilibrium is maintained)[11,38]. For example, consider a body which is stressed by a self-equilibrating force system $\{\delta R\}$ which induces a stress system $\{\delta\sigma\}$ (Fig. 1.1), then

$$V^* = U^* - P^* \qquad (1.3)$$

where V^* is the total complementary potential energy, U^* is the complementary strain energy of deformation, and P^* is the complementary potential energy of the applied forces. Minimizing the total complementary energy we obtain

$$\delta V^* = \delta U^* - \delta P^*$$

$$= \int_V \{\varepsilon\}^T \{\delta\sigma\} dV - \int_V \{r\}^T \{\delta R\} dV = 0 \qquad (1.4)$$

Other Methods: Three examples of element derivations, which do not follow the "pure" derivation of the two preceding

methods, are given below:

a) In the displacement model some plate bending element derivations deviate from the "pure" derivations becuase they do not maintain compatibility between elements and hence the displacement field over the complete structure will not be continuous[16].

b) Another method was developed by Pian[17] who formed a plane stress element from assumed stress fields, thus maintaining equilibrium, and at the same time interelement compatibility was ensured by constraining the appropriate boundary displacement variation. This method has also been used by Severn and Taylor[25] and Krahwla and Pahems[40] for plate bending elements.

c) Herrman[41] introduced a "mixed" method in which the unknowns include both displacements and stresses.

The finite element derivations used in this thesis are based upon the displacement model, which at the present is the commonest and best understood model. For this reason only the displacement model will be studied from hereon.

To determine the minimum of the total potential energy the displacement model employs the Rayleigh-Ritz method. A short description of this method is given below because, through it, we can obtain a greater understanding of both the basis of the displacement model, and also the inherent errors in the displacement model.

1.3 The Rayleigh-Ritz Method

The Rayleigh-Ritz method is a technique for generating a minimizing sequence with which we can find the minimum m of a variational expression. In general the minimizing sequence will also provide a good approximation to the function that actually solves the problem.

If we take a variational expression $I(\phi)$ (for example, the strain energy of deformation for a beam is $I(\phi) = \frac{1}{2}\int_0^L EI\left(\frac{d^2\phi}{dx^2}\right)dx$) we can construct a minimizing sequence, $\phi_1, \phi_2, \phi_3, \cdots \phi_n$ such that

$$\phi_r = c_1 w_1 + c_2 w_2 + \cdots + c_r w_r \tag{1.5}$$

where the terms $w_1, w_2, \cdots, w_r$ are called the coordinate functions and are known, but where the coefficients c_i are unknown. (For example, the first three terms of a minimizing sequence with which the above example could be solved are,

$$\phi_1 = a_1 \sin\frac{\pi x}{L},$$

$$\phi_2 = a_2 \sin\frac{\pi x}{L} + a_2 \sin\frac{2\pi x}{L},$$

$$\phi_3 = a_1 \sin\frac{\pi x}{L} + a_2 \sin\frac{2\pi x}{L} + a_3 \sin\frac{3\pi x}{L}.)$$

Each successive term of the minimizing sequence is substituted into the variational expression $I(\phi)$ which then becomes a function of the unknown scalars c_i, i.e.

$$I(\phi_r) = F(c_1, c_2, \cdots, c_r) \tag{1.6}$$

and, minimizing this equation implies that

$$\frac{\partial F}{\partial c_i} = 0 \qquad i = 1, 2, \cdots r. \tag{1.7}$$

Expression (1.7) leads to a system of r linear equations for the parameters c_i which can then be solved: thus, the minimizing sequence ϕ_r, r = 1,2, n can be determined.

To ensure that the minimums, determined from each successive term of the minimizing sequence, converge monotonically to the true minimum m the coordinate functions must comply with the following two conditions[42]:

1) for any n, the coordinate functions $w_1, w_2, \cdots, w_n$ must be linearly independent, and

2) the coordinate functions should form a "complete" system of functions. This means that any function ψ, and its relevant derivatives, may be approximated to any degree of accuracy by a linear combination of coordinate functions and of their corresponding derivatives.

If these conditions are met then each successive term of the minimizing sequence will improve the accuracy of the solution. Thus,

$$I(\phi_1) \geq I(\phi_2) \geq \cdots \text{ tending to } m \tag{1.8}$$

and $I(\phi_r)$ will be an upper bound to m.

The Rayleigh-Ritz method has two disadvantages; firstly it is often very difficult to select suitable coordinate functions - a serious matter as both the degree of approximation and the amount of calculations involved in obtaining the answer depend upon the choice of these functions. Secondly, the method does not contain a principle for estimating the accuracy of a solution (this cannot be judged by studying successive terms of the minimizing sequence because their convergence is dependent upon the coordinate functions).

1.4 The Displacement Model

The derivation of a plate bending element stiffness matrix, formed by the displacement model, is given below. (The formation of the plane stress element follows the same approach but the moment-curvature relationship is replaced by the stress-strain relationship.)

Firstly, the displacement at any point is related to the nodal displacements,

$$w = \{\phi\}^T\{r\} \qquad (1.9)$$

where w is the displacement at any point, $\{\phi\}$ is called the interpolation (or shape) vector, and $\{r\}$ is the nodal displacement vector.

Defining the positive curvature states as

$$\chi_{xx} = -\frac{\partial^2 w}{\partial x^2},$$

$$\chi_{yy} = -\frac{\partial^2 w}{\partial y^2}, \quad \text{and} \tag{1.10}$$

$$\chi_{xy} = -\frac{\partial^2 w}{\partial x \partial y}$$

we can determine the curvatures at the nodal points by appropriately differentiating equation (1.9) and finding the values at the nodal points. Hence, we obtain

$$\{\chi\} = [B]\{r\} \tag{1.11}$$

where

$$\{\chi\} = \begin{Bmatrix} \chi_1 \\ \chi_2 \\ \chi_3 \end{Bmatrix}$$

and, for node 1,

$$\{\chi_1\} = \begin{Bmatrix} \chi_{xx} \\ \chi_{yy} \\ \chi_{xy} \end{Bmatrix}_1,$$

similarly for nodes 2 and 3.

We know the variation of the curvatures over the element and therefore we can relate the curvatures at any point to the nodal curvatures by means of another interpolation vector $\{\psi\}$, i.e.

$$\{\tilde{\chi}\} = \{\psi\}^T\{\chi\} \tag{1.12}$$

where the tilde on the curvature vector denotes the value at any point.

The moments at any point are related to the curvatures at the same point by the constitutive law,

$$\{\tilde{M}\} = [C]\{\tilde{\chi}\} \tag{1.13}$$

and for an isotropic material,

$$\begin{Bmatrix} \tilde{M}_{xx} \\ \tilde{M}_{yy} \\ \tilde{M}_{xy} \end{Bmatrix} = \frac{Et^3}{12(1-\nu^2)} \begin{bmatrix} 1 & \nu & \cdot \\ \nu & 1 & \cdot \\ \cdot & \cdot & \frac{1-\nu}{2} \end{bmatrix} \begin{Bmatrix} \tilde{\chi}_{xx} \\ \tilde{\chi}_{yy} \\ \tilde{\chi}_{xy} \end{Bmatrix} . \tag{1.14}$$

The strain energy in bending is

$$U = \tfrac{1}{2}\int_A \tilde{M}^T \tilde{\chi} dA$$

$$= \tfrac{1}{2}\{\chi\}^T \left(\int_A \{\psi\}[C]\{\psi\}^T dA\right)\{\chi\} \tag{1.15}$$

and incorporating Eq. (1.11) we obtain

$$U = \tfrac{1}{2}\{r\}^T[k]\{r\} \tag{1.16}$$

where

$$[k] = [B]^T \left(\int_A \{\psi\}[C]\{\psi\}^T dA\right)[B]$$

is called the element stiffness matrix.

The potential energy of the nodal forces is

$$P = \{R\}^T\{r\} \tag{1.17}$$

where $\{R\}$ is the force vector comprising both body and surface forces "lumped" at the nodal points, and $\{r\}$ is the nodal displacement vector.

The total potential energy V is thus

$$V = U - P$$

$$= \tfrac{1}{2}\{r\}^T[k]\{r\} - \{R\}^T\{r\}, \qquad (1.18)$$

and the principle of minimum total potential energy sets the first variation of the total energy to zero, and thus we obtain the basic force-displacement equation,

$$\{R\} = [k]\{r\}. \qquad (1.19)$$

We see that the displacement method utilizes a Rayleigh-Ritz analysis within each element. Recapitulating the basic steps of the Rayleigh-Ritz method, and including the displacement method counterparts in brackets, se see that the variational expression (total potential energy) is minimized by a minimizing sequence (the displacement shape) formed by a linear combination of coordinate functions (interpolation vector coefficients) and unknown scalars (the nodal displacements). When the variational expression (total potential energy) is minimized the unknown scalars (nodal displacements) can be determined if the boundary conditions of the problem are known.

The conditions that the Rayleigh-Ritz method impose upon the coordinate functions also apply to the coefficients of the interpolation vector. From a physical viewpoint we can postulate two further conditions[28],

1) the displacement function must allow the presence of the rigid body modes, and

2) the displacement function must be able to express constant strain conditions (for a plate bending element this implies constant curvature).

These conditions are necessary because a normal displacement distribution will include some rigid body modes, and also, when an element becomes smaller, its strain distribution becomes constant. A comparison with the conditions imposed upon the coordinate functions in the Rayleigh-Ritz method (Section 1.3) shows that these two physical conditions are analogous to the condition that the coordinate functions would form a "complete" system, i.e. they should be capable of approximating any function including those that produce rigid body modes or constant strain conditions.

If the Rayleigh-Ritz conditions are fulfilled then the best stiffness matrix, for a given load system, will be the one giving the greatest strain energy[21]. (This is most easily proved for the case where the forces acting on a body increase from zero to their final value. Clapeyron's Theorem for a linear stress-strain relationship states that the strain energy of deformation of such a body is equal to half the potential energy of the applied loads. Hence the total potential energy $V = -U$ and when the total potential energy is a minimum the strain energy will be a maximum.) Hence, for a given load system the strain energy of an element will be a lower bound and the element stiffness matrix derived

by the displacement model will be stiffer than the true stiffness matrix.

1.5 Kinematically Equivalent Nodal Forces

In representing a complex structure as a series of elements connected only at their nodes we assume that the structural loading, including both surface and body forces, can be represented by equivalent generalised forces acting at the nodal points. There are two methods of determining these generalised forces,

1) according to static equivalence, and

2) according to the virtual work theorem.

The first method of taking static equivalence, generally based upon the area surrounding a node, will be exact in the limiting case when the element size is very small. Melosh[43], however, found that this method was not very satisfactory because the solution does not improve monotonically as the network is refined.

The second method is more accurate because it is consistent with minimizing the total potential energy of a structure. Consider a set of virtual displacements such that,

$$[r] = \sum_i \{r_{virtual}\}_i = [I]. \tag{1.20}$$

Substituting into Eq. (1.9) we have

$$w_{virtual} = \{\phi\}^T[r] = \{\phi\}^T. \tag{1.21}$$

If the structural loading, including body, surface, and edge forces, is $q(\zeta_1,\zeta_2,\zeta_3)$ then the work done by this structural loading in moving through the virtaul displacement $w_{virtual}$ is

$$W_D = {}_V\int w^T q(\zeta_1,\zeta_2,\zeta_3)\,dV$$

$$= {}_V\int \{\phi\}^T q(\zeta_1,\zeta_2,\zeta_3)\,dV. \qquad (1.22)$$

The work done by the nodal forces $\{Q\}$ is

$$W_N = [r]^T\{Q\} = \{Q\}. \qquad (1.23)$$

We desire these two separate systems to yield equivalent work and therefore, equating Eqs (1.22) and (1.23), we obtain the nodal loads as

$$\{Q\} = {}_V\int \{\phi\}^T q(\zeta_1,\zeta_2,\zeta_3)\,dV$$

C H A P T E R 2

THE FINITE ELEMENT ANALYSIS OF STRUCTURES

Having looked at the development of the finite element method, and in particular, the displacement model of deriving stiffness matrices, we will now examine the overall analysis of a complex structure using the displacement method. As this has been well documented elsewhere[44] only a brief summary will be given. Basically the analysis is very simple and logical: however, various difficulties are encountered and these will be described within this chapter and in Chapter 3.

Referring to Eq. (2.1), we wish to form the nodal force vector {Q} and the complete stiffness matrix [K] and then solve for the unknown nodal displacements {q}.

$$\{Q\} = [K]\{q\} \qquad (2.1)$$

The analysis consists of four steps:

(a) the structure is idealized as an assemblage of elements,

(b) the complete stiffness matrix for the structure is formed from the element stiffness matrices,

(c) for a given loading system the resultant displacements are calculated, and

(d) the nodal stresses are determined from the nodal displacements.

2.1 Structural Idealization

The finite element method is a simulation technique in which a structural model is developed and analysed, normally within a computer. The method, however, simulates an idealized structure and we assume that the results are closely related to the original structure.

All civil engineering structures are idealized to some extent; e.g. a partially restrained joint may be assumed to act as a "pin"; ignoring the effect of axial shortening in columns assumes an infinite compressive modulus within the column; etc.. These basic idealizations are also incorporated in the finite element method. Hrennikoff, as mentioned in Section 1.1, idealized two dimensional structures as an assemblage of bars, i.e. he idealized the elements to form more elementary components which were, before computers became available, easier to analyse than the original elements. However, this additional idealization is not used very often because it is normally not necessary and only incurrs additional problems of obtaining compatible behaviour between the element and its idealized counterpart.

Another structural idealization is introduced when analysing shells. Because no element can conform to all the possible shapes of a shell surface, a geometrical idealization is introduced whereby the shell surface is replaced by an assemblage of elements which are normally planar although some curved elements are now being used.

2.2 Formation of the Complete Stiffness Matrix and the Solution of the Resulting Matrix Equation

The structural idealization forms an element mesh over the structure thus defining the shape of each element. The next step is to determine the element stiffness matrices; normally by using one of the methods described in Section 1.2. The derivations of the element stiffness matrices used within this thesis were developed and tested by Felippa [8,19] and Carr [9] and a summary of there derivations can be found in Appendix A.

In the analysis of shells each element stiffness matrix is derived in a local coordinate system (e.g. axes x-y-z in Fig. 2.1) and must be transformed to a common, global coordinate system (e.g. axes x_0-y_0-z_0 in Fig. 2.1) before it is added into the complete stiffness matrix. The behaviour of the element can be described using either the local or the global coordinate system;

$$\{R_\ell\} = [k_\ell]\{r_\ell\} \qquad (2.2)$$

or $$\{R_g\} = [k_g]\{r_g\}$$

where the subscripts "ℓ" and "g" denote the local and the global coordinate systems respectively. If the transformation matrix of direction cosines relating the local coordinate system to the global coordinate system is [A], i.e.

$$\{r_\ell\} = [A]\{r_g\}, \qquad (2.3)$$

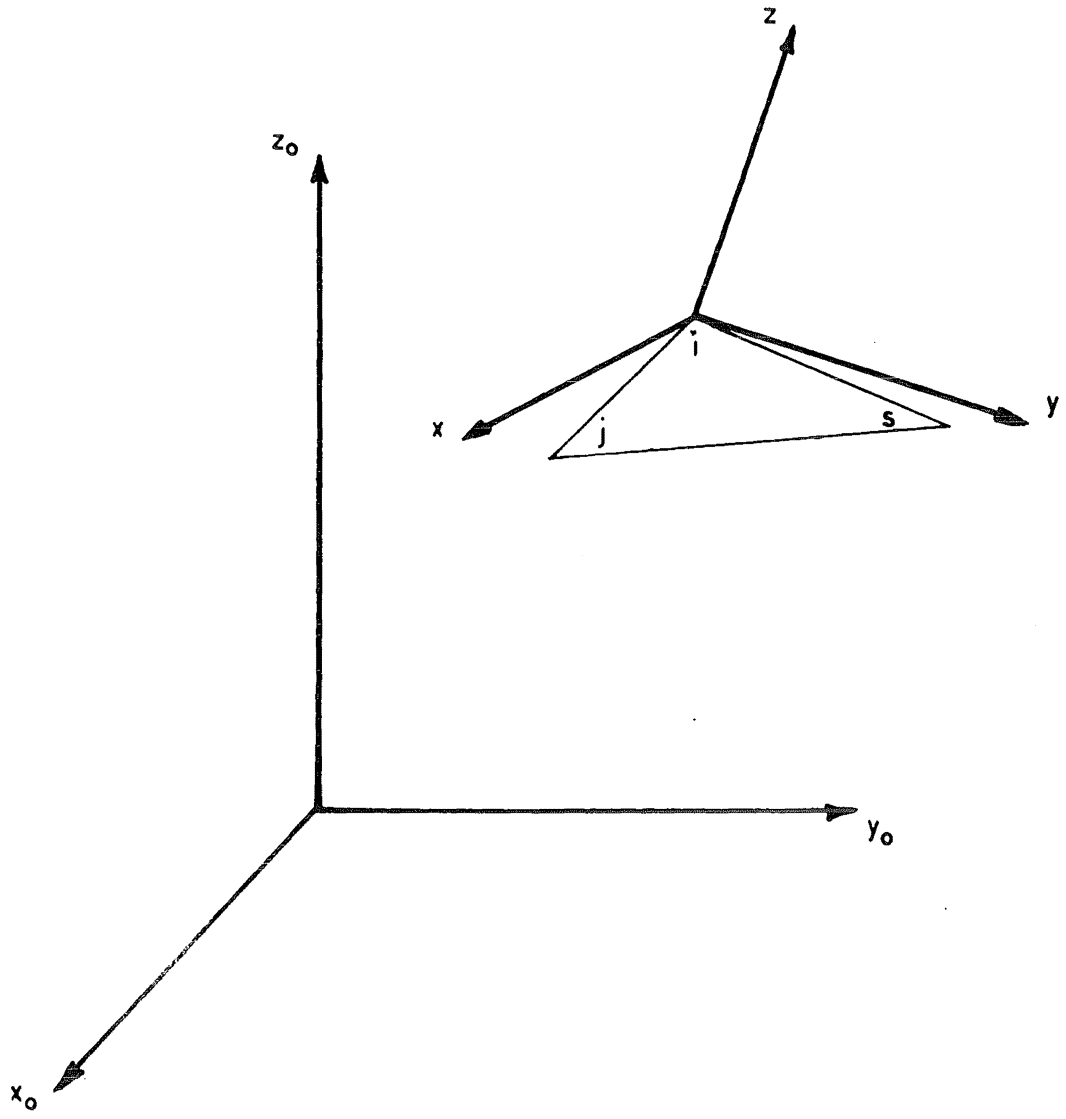

Fig. 2.1. Local and Global Coordinate Systems

then the element stiffness matrix in the global coordinate system is

$$[k_g] = [A]^T[k_\ell][A]. \tag{2.4}$$

Each element stiffness matrix is added into the appropriate position of the complete stiffness matrix, e.g. for triangle i-j-s in Fig. 2.1 we have

$$\begin{Bmatrix} R_i \\ R_j \\ R_s \end{Bmatrix} = \begin{bmatrix} k_{ii} & k_{ij} & k_{is} \\ k_{ji} & k_{jj} & k_{js} \\ k_{si} & k_{sj} & k_{ss} \end{bmatrix} \begin{Bmatrix} r_i \\ r_j \\ r_s \end{Bmatrix} \tag{2.5}$$

where each k_{pq} is a nodal submatrix of stiffness coefficients.

The appropriate positions in the complete stiffness matrix would be

$$\begin{array}{ccccccccccc}
 & | & | & & & & & & | & & \\
 & | & | & & & & & & | & & \\
- & - & k_{ii} & k_{ij} & - & - & - & - & - & k_{is} & - & - \\
- & - & k_{ji} & k_{jj} & - & - & - & - & - & k_{js} & - & - \\
 & | & | & & & & & & | & & \\
 & | & | & & & & & & | & & \\
- & - & k_{si} & k_{sj} & - & - & - & - & - & k_{ss} & - & - \\
 & | & | & & & & & & | & & \\
 & | & | & & & & & & | & &
\end{array} \tag{2.6}$$

Having formed the complete stiffness matrix the support conditions are represented by deleting the appropriate rows and columns in the complete stiffness matrix and this

prevents the simulated structure from deforming as a rigid body. The unknown nodal displacements can then be solved directly by rearranging Eq. (2.2) so that

$$\{q\} = [K^{-1}]\{Q\}. \tag{2.7}$$

In general, however, the stiffness matrix is not inverted as it is heavily banded and sparsely filled so either an iterative solution is employed or the stiffness matrix is reduced, allowing the displacements to be found by a back substitution process (e.g. Gauss or Jordan Method). The method of solution used within this thesis is a slight modification of Cholesky's method[45], i.e.

$$\{Q\} = [L^T][D][L]\{q\} \tag{2.8}$$

where [L] is an upper triangular matrix with the diagonal terms unity, and [D] is a diagonal matrix. The unknown displacements {q} can be determined after a forward substitution on Eq.(2.9), to find the intermediate vector {y}, followed by a back substitution on Eq. (2.10),

$$\{Q\} = [L^T][D]\{y\} \tag{2.9}$$

$$\{y\} = [L]\{q\}. \tag{2.10}$$

2.3 Interpretation of the Results

In the Rayleigh-Ritz method the convergence of the derivatives of the minimizing sequence is never as rapid as the convergence of the minimizing sequence. Hence the stresses (moments for the plate bending elements) will not

be as accurate as the displacements. This is to be expected for, taking a plate bending element with a cubic transverse displacement variation, the moment variation over the element is only linear and therefore the moments will not be capable of representing the true moment variation very accurately. Furthermore, the values of the stress resultants will vary depending upon which method is used to determine them.

Nodal stresses are determined for each element from the nodal displacements and element stress matrices are normally derived during the formation of the element stiffness matrices, e.g. the nodal moments {M} are related to the nodal curvatures {χ},

$$\{M\} = [D]\{\chi\} \qquad (2.11)$$

where [D] is a (21x21) diagonal matrix comprising the constitutive matrix [C] (refer Eq. (1.13)), i.e.

$$[D] = \text{diag.}[C\ C\ C\ C\ C\ C\ C].$$

Incorporating Eq. (1.13)

$$\{\chi\} = [B]\{r\},$$

we can form a stress matrix [S], such that

$$\{M\} = [S]\{r\} \qquad (2.12)$$

where $[S] = [D][B]$.

Because the element stresses are related to all the element displacements the nodal stresses will in general vary depending on which element is used to obtain the result.

To circumvent this problem an averaging process is normally used to give an average value at each node, consequently this method is most accurate for interior nodes because on the boundaries of the structure the averaging process is taken over fewer elements.

Other methods of determining stresses are given by Navaratna[46]. However, the aforementioned method is the commonest.

C H A P T E R 3

ERRORS ASSOCIATED WITH THE FINITE ELEMENT METHOD

3.1 Structural Idealization Errors

It is very difficult to determine the error of idealizing a shell structure as an assemblage of planar or curved elements. One method is to repeat the analysis using a more geometrically correct element, but, as most analyses employ the best available finite element and as there are very few tested curved elements, this method is not very practical. The other possibility is to reduce the angular discontinuities by repeating the analysis using a smaller mesh. From the convergence of the solution an idea of the effect of the idealization errors can be obtained. However, this method also has practical difficulties when the size of the computer prohibits further subdivision of the mesh.

The accuracy of the solution is also dependent upon the shape of the elements which are determined by the mesh that is used. Tapered elements do not depict structural deformations very accurately and the best triangular finite elements are formed from equilateral triangles. The error that is incurred when using tapered elements occurs in the formation of the element stiffness matrix but, because of its geometric dependence, it is a structural idealization error and not an error in the formation of the element

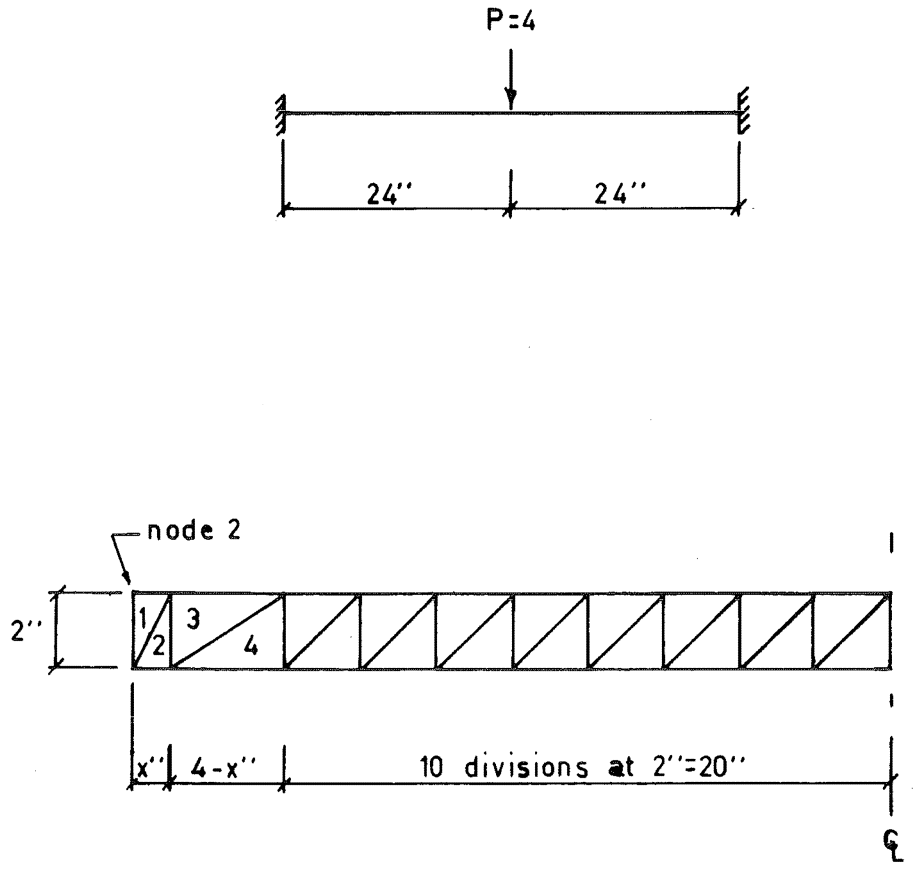

Fig. 3.1. Fixed Beam to Test the Mesh Shape

stiffness matrix. As an example of this error consider the fixed beam shown in Fig. 3.1. The variation of the moment at node 2, which occurred when the aspect ratio of elements 1, 2, 3 and 4 was varied, is shown in Table 3.1.

Aspect Ratio x : 2	M_2	% Error
1 : 1	-11.36	0
1 : 2	-11.80	3.9
1 : 4	-12.23	7.7
1 : 8	-12.73	12.1
1 :16	-13.29	17.0

Table 3.1 Variation of Moment with Aspect Ratio

Another type of idealization error will occur when large geometrical or stress discontinuities are encountered (e.g. when an extremely stiff element is attached to a very flexible element) thus causing the complete stiffness matrix to become ill-conditioned. In the previous example the stiffnessand stress matrices for the tapered elements were incorrectly proportioned whereas, in this example, the element stiffness and stress matrices are correct and the simulated structure could, theoretically, be solved. However, due to the limitation of a computer's precision,

rounding or truncation errors occur which can seriously affect the accuracy of the solution. Although this form of error occurs because of computer limitations it is dependent upon the mesh idealization which, to some extent, determines the magnitude of the stiffness coefficients. As an example of this error consider the simply supported beam shown in Fig. 3.2. All the elements have a modulus of elasticity of 5×10^{6} except for elements 23 and 24 whose modulus of elasticity varies from 5×10^{6} to 5×10^{-3}. As the ratio of the two moduli vary errors will build up, firstly in the determination of the nodal moments and then in the nodal displacements (refer Fig. 3.3).

3.2 Errors in the Formation of Finite Elements

Apart from the idealization errors that were discussed above, errors can occur in the formation of the element stiffness matrices. These errors are normally due to violation of the principles of the Rayleigh-Ritz method and can occur in two ways; firstly by violating the conditions imposed upon the coordinate functions, and secondly, by violating the element boundary conditions.

An example of the conditions imposed upon the coordinate functions being violated occurred with the early derivations of triangular plate bending elements which had a cubic displacement function over each element. The complete cubic equation has ten coefficients,

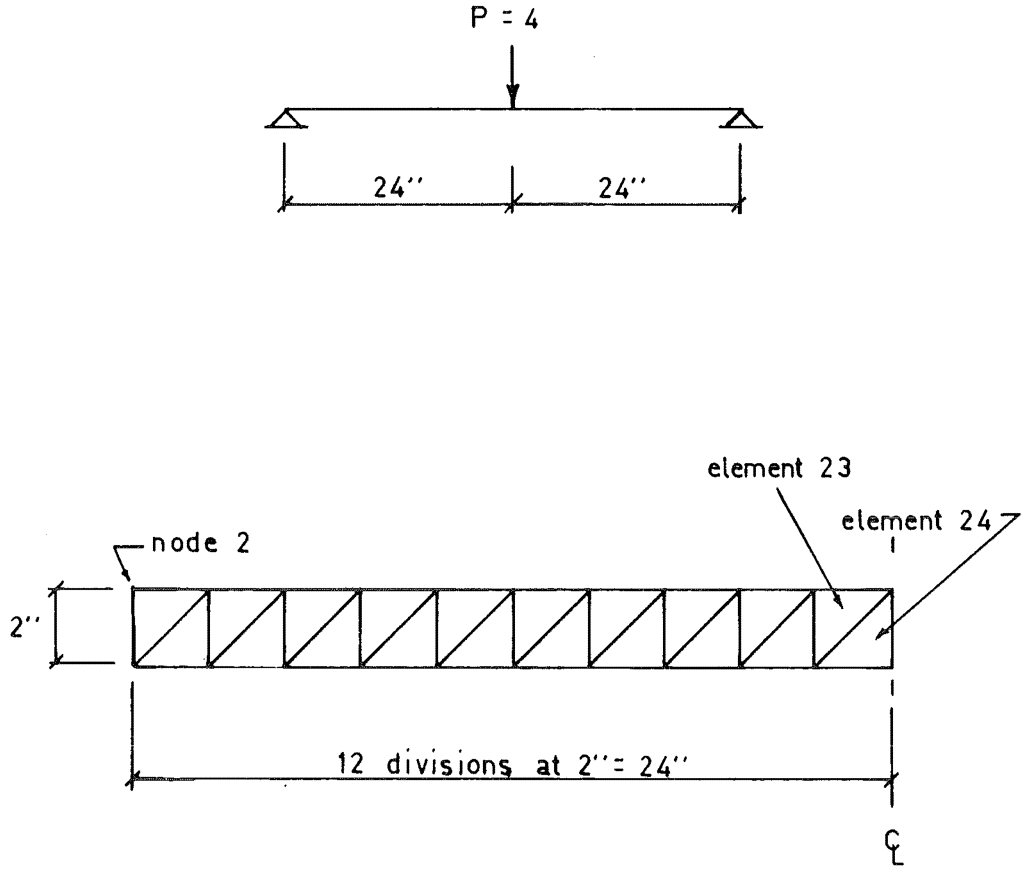

Fig. 3.2. Simply Supported Beam to Test Element Stiffness Variations

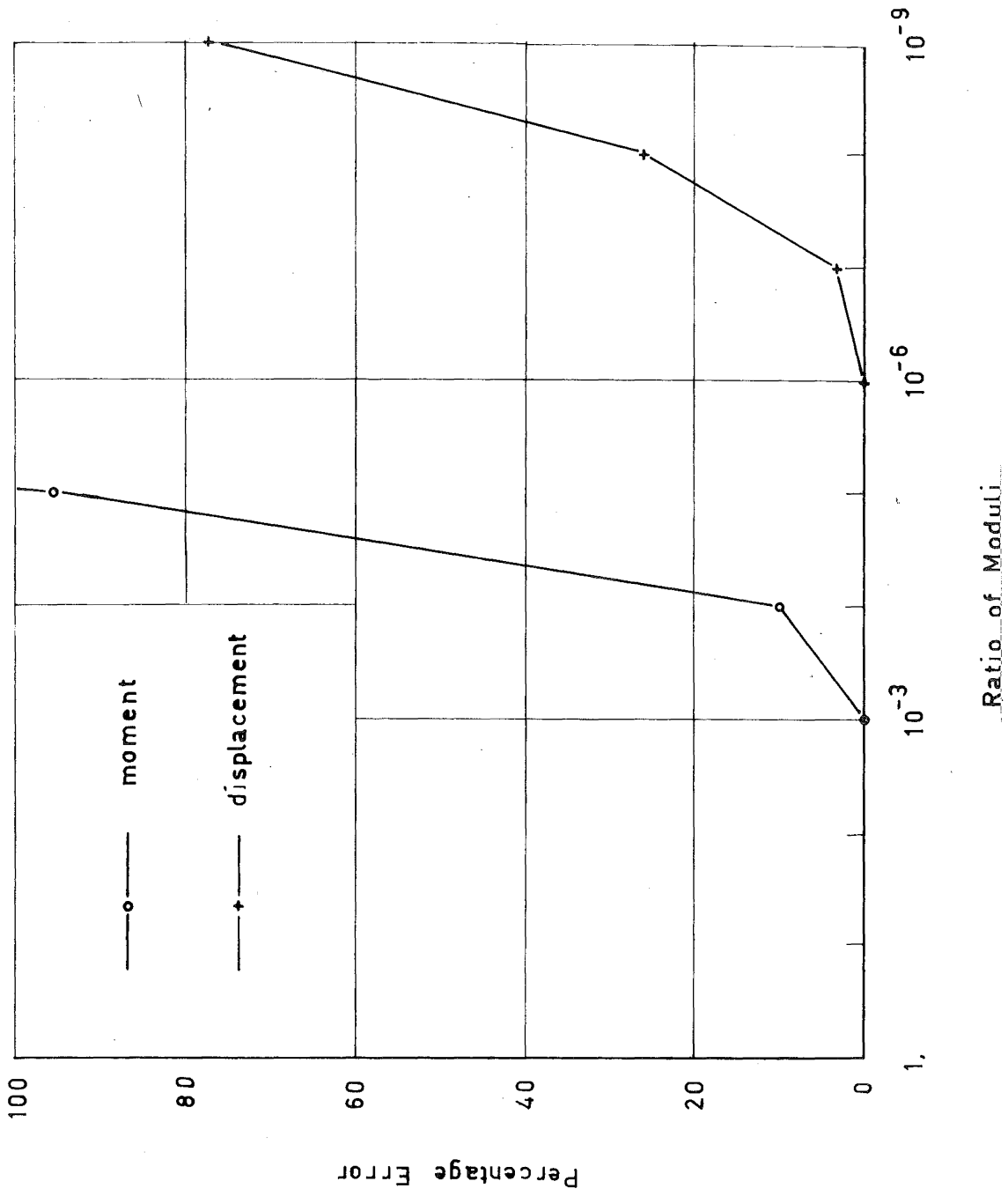

Fig. 3.3. Errors Caused by Geometrical Discontinuities

$$w = a_1 + a_2x + a_3y + a_4x^2 + a_5xy + a_6y^2 + a_7x^3 + a_8x^2y + a_9xy^2 + a_{10}y^3 \quad (3.1)$$

but the simplest triangular element has only nine degrees of freedom, therefore, to make w a function of nine coefficients either one term of the displacement function was omitted, or two terms were combined with the same scalar[20]. This restriction means that the displacement function is not a "complete" system, thus violating the second condition applying to the coordinate functions (Section 1.3), and this results in the structure becoming stiffer.

The boundary conditions for any finite element are imposed by adjoining elements, i.e. displacement boundary conditions, and, at the boundaries of the complete structure, by the structural boundary conditions. Errors will occur if an element does not conform to its boundary conditions because interelement compatibility will be lost (this is equivalent to imposing incorrect boundary conditions on each Rayleigh-Ritz solution). To restore compatibility we must apply self-equilibrating forces acting between the nodal points. Thus the potential energy of the nodal forces will be unchanged but the strain energy of each finite element will be increased and therefore the structure will become more flexible.

We can now summarise the possible bounds for the displacement method; we saw in Section 1.4 that the displacement method yields an element that is stiffer than it should be and therefore, for a given load, the displacements will be a lower bound. If the displacement function is not a "complete" system then the element will become even stiffer and the displacements will remain a lower bound. If the element boundary conditions are violated however, the element will become more flexible and no bounds can be postulated for the displacements.

3.3 Computer Limitations

The type of computer can affect a solution in three ways;

a) by restricting the possible mesh size of the idealized structure,

b) by the time of computation - an important factor to any person having to pay for their computer time, and

c) by the precision of its arithmetic unit.

The problem of analysing very large structures can sometimes be overcome by dividing the structure into substructures[49]. Each substructure is analysed independently assuming that all the common boundaries with the adjacent substructures are fixed. The forces at these common boundaries are determined and then these boundaries are released simultaneously and new boundary displacements are determined.

This procedure is repeated until a stable situation arises.

The time of solution becomes an important factor with small core computers because the computer employs most of its time transferring data to and from the core (this can easily double or treble the time of a job).

Because a computer operates with a fixed word length, serious errors can occur due to a loss of precision as illustrated by the example in Section 3.1. A further example of this problem of ill-conditioning occurred for the fixed beam shown in Fig. 3.1. Table 3.2 gives the moment at node 2 for varying values of the modulus of elasticity and with different word length precisions within the program. (Single precision corresponds to 7.2 decimal figures and double precision to 16 decimal figures.)

E	Single Precision	Partial Double Precision	Double Precision
1	-11.14	-11.82	-11.36048
10	- 8.91	-11.71	-11.36048
5.10^6	-19.04	-12.32	-11.36048

Table 3.2 Variation of Moment with Different Precisions

PART II: A COMPLETE ANALYSIS OF TWO-DIMENSIONAL STRUCTURES

C H A P T E R 4

A COMPLETE ANALYSIS

4.1 Review of Previous Work

The incorporation of plasticity has evolved along two paths; the classical approach of limit analysis which was developed for metals, and the fracture approach of yield-line analysis which is used predominantly for reinforced concrete.

The classical approach originated about 1864 when Tresca[50] stated that yielding of a metal would occur when the maximum shearing stress attained a critical value. A further yield criterion was postulated mathematically by von Mises[51] in 1913 and shown by Hencky[52] to imply that yielding will occur when the elastic strain energy of distortion reaches a critical value. Incremental stress-strain relationships can be determined from the yield criterion and a flow law which relates the plastic strain increment at a point to the stress at that point. The flow law is normally dependent upon the yield criterion that is used. Many structures have been analysed using these theories and Hodge[53] gives a summary of their progress.

The fracture approach or yield-line theory has been developed specifically for reinforced concrete. Johansen[3] in 1948 extended the earlier work of Bach[1] and Ingerslev[2] and

formulated the yield-line method of analysis which is still being used. The analysis is a limit design method, i.e. elastic/perfectly-plastic behaviour is assumed, and is used for analysing concrete structures in which the steel reinforcement yields before the ultimate strength of the structure is reached. Yielding is restricted to yield lines,and thus at the ultimate load the structure is divided into a number of segments which form a collapse mechanism. A review of the yield-line theory for reinforced concrete is given by Hognestad[4].

The applications of these methods have normally been concerned with the limit analysis of a structure and, until very recently little attention has been paid to the behaviour of structures in the region after the onset of inelasticity and before failure. This neglect was due to the voluminous quantity of numerical calculations which arise in a complete inelastic analysis. However, digital computers have now removed this problem. A complete inelastic analysis is very useful in ascertaining the general behaviour of a structure, including load-deflection curves, crack propagation, and regions of high stress.

In 1966 Pope[54] analysed elasto-plastic plane stress problems using a "step by step" analysis, i.e. the structure is solved for each load increment or step. Within each load increment the structure was assumed to behave elastically, and at the end of the load increment the newly yielded regions

were accounted for by changing their constitutive equations. Marcal and King[55] improved this method by using a partially elastic and partially plastic element for those elements that are elastic at the beginning of the load increment and plastic at the end of the increment. They calculated a mean value for the stiffness coefficients of a partially elastic and partially plastic element, i.e.

$$(k_{ij})_{ep} = m(k_{ij})_e + (1-m)(k_{ij})_p \qquad (4.1)$$

where $(k_{ij})_{ep}$ is the mean stiffness coefficient, $(k_{ij})_e$ is the elastic stiffness coefficient, $(k_{ij})_p$ is the plastic stiffness coefficient, and m is a scalar such that $0 \leqslant m \leqslant 1$. This method has also been extended by Marcal and Pilgrim[56] to analyse axisymmetric shells.

A general formulation of this method, given by Zienkiewicz, Valliapan and King[57], is described below. For an infinitesimal increment of stress the corresponding strain increment is divided into its elastic and plastic components,

$$\delta\{\varepsilon\} = \delta\{\varepsilon\}_e + \delta\{\varepsilon\}_p. \qquad (4.2)$$

The elastic increment of strain is related directly to the stress increment by the elastic constitutive relationship

$$\delta\{\varepsilon\}_e = [C^{-1}]\delta\{\sigma\}. \qquad (4.3)$$

Yielding will occur when the stresses $\{\sigma\}$ satisfy a yield criterion

$$F(\sigma) = \kappa \tag{4.4}$$

where F is a yield function and κ is a strain hardening function. Eq. (4.4) may also be written as

$$\frac{\partial F}{\partial \sigma_1}\delta\sigma_1 + \frac{\partial F}{\partial \sigma_2}\delta\sigma_2 + \cdots + \frac{\partial F}{\partial \kappa}\delta\kappa = 0$$

i.e.

$$\left\{\frac{\partial F}{\partial \{\sigma\}}\right\}^T \delta\{\sigma\} + A\lambda = 0 \tag{4.5}$$

where

$$A = \frac{1}{\lambda}\frac{\partial F}{\partial \kappa}\delta\kappa.$$

The plastic increment of strain is related to the yield function by the flow law

$$\delta\{\varepsilon\}_p = \lambda\frac{\partial F}{\partial \{\sigma\}} \tag{4.6}$$

where λ is a positive constant.

Hence, combining Eqs (4.3) and (4.6) we obtain

$$\delta\{\varepsilon\} = [C^{-1}]\delta\{\sigma\} + \frac{\delta F}{\delta\{\sigma\}}\lambda$$

and incorporating Eq. (4.5)

$$\left\{\begin{array}{c} \delta\varepsilon_1 \\ \delta\varepsilon_2 \\ \vdots \\ \hline 0 \end{array}\right\} = \left[\begin{array}{ccc|c} & [C^{-1}] & & \frac{\partial F}{\partial \sigma_1} \\ & & & \frac{\partial F}{\partial \sigma_2} \\ & & & \vdots \\ \hline \frac{\partial F}{\partial \sigma_1} & \frac{\partial F}{\partial \sigma_2} & \cdots & A \end{array}\right] \left\{\begin{array}{c} \delta\sigma_1 \\ \delta\sigma_2 \\ \vdots \\ \hline \lambda \end{array}\right\} \tag{4.7}$$

From Eq. (4.7) an elasto-plastic constitutive relationship can be obtained, i.e.

$$\delta\{\sigma\} = [C]^*_{ep}\delta\{\varepsilon\} \tag{4.8}$$

where

$$[C]^*_{ep} = [C] - [C]\left\{\frac{\partial F}{\partial\{\sigma\}}\right\}\left\{\frac{\partial F}{\partial\{\sigma\}}\right\}^T[C]\left[A + \left\{\frac{\partial F}{\partial\{\sigma\}}\right\}^T[C]\left\{\frac{\partial F}{\partial\{\sigma\}}\right\}\right]^{-1}$$

If von Mises yield criterion is used then Eq. (4.7) gives the Prandtl-Reuss stress-strain-increment equations which is the formulation used by Pope, Marcal and King, and Marcal and Pilgrim.

Brotchie[58,59] (1961) examined the inelastic behaviour of thin plates which obey the Tresca criterion for yielding. By applying appropriate boundary conditions to the elastic and plastic areas and then solving by expanding into series involving Bessel's functions, Brotchie considered yielding along lines and, for axisymmetric structures, yielding of an area.

Bhaumik and Hanley[5] (1967) formulated the problem in two parts; firstly the equilibrium equation for a plate element, which is independent of the material property,

$$\frac{\partial^2 M_x}{\partial x^2} + 2\frac{\partial^2 M_{xy}}{\partial x \partial y} + \frac{\partial^2 M_y}{\partial y^2} = -q \tag{4.9}$$

where M_x is the bending moment in the x direction, M_y is the bending moment in the y direction, M_{xy} is the twisting moment in the x-y plane, and q is the load intensity.

Secondly, in the elastic region the moment-displacement relationship is

$$M_x = -D\left(\frac{\partial^2 w}{\partial x^2} + \nu \frac{\partial^2 w}{\partial y^2}\right)$$

$$M_y = -D\left(\nu \frac{\partial^2 w}{\partial x^2} + \frac{\partial^2 w}{\partial y^2}\right) \qquad (4.10)$$

$$M_{xy} = -D\,(1-\nu)\,\frac{\partial^2 w}{\partial x \partial y}$$

where D is the flexural rigidity of the plate, ν is Poisson's ratio, and w is the transverse displacement.

Considering Johansen's square yield criterion the following conditions exist at a yield line, i.e. in the inelastic region,

$$|M_n| = M_p$$

$$|M_t| \leq M_p \qquad (4.11)$$

$$M_{nt} = 0$$

where M_n is the moment across the yield line, M_t is the moment along the yield line, M_{nt} is the twisting moment, and M_p is the plastic moment capacity of the section. Therefore, the moment at any point can be defined by Eqs (4.10) or Eqs (4.11).

Bhaumik and Hanley solved these equations by converting them into finite difference form. As well as studying Johansen's yield criterion they studied the yield criteria

of Tresca and von Mises (each of which will alter the form of Eq. (4.11)).

Riera and Billington[6] (1968) assumed a plane stress yield curve $F(\sigma_1,\sigma_2) = 0$, where σ_1 and σ_2 are principal stresses, and this defines a yield curve $f(\varepsilon_1,\varepsilon_2) = 0$ where ε_1 and ε_2 are the principal strains. They expressed the constitutive equations for concrete as a function of the principal stresses σ_1 and σ_2 (which defines two principal strains, ε_1 and ε_2), i.e.

$$\sigma_1 = \sigma_{1f}(1 - e^{-\frac{r}{r_o}})$$
$$\sigma_2 = \sigma_{2f}(1 - e^{-\frac{r}{r_o}}) \qquad (4.12)$$

where r is a strain measured from the origin of the yield curve $f(\varepsilon_1,\varepsilon_2) = 0$ to the point $(\varepsilon_1,\varepsilon_2)$, r_o is a strain having the same slope as r and it is measured from the origin of the yield curve $f(\varepsilon_1,\varepsilon_2) = 0$ to its point of intersection with this curve, and σ_{1f} and σ_{2f} are the yield stresses in the principal stress directions. Riera and Billington assumed an elliptical yield criterion for reinforced concrete as shown in Fig. 4.1, and they solved the differential shell equations by numerical integration.

McNiece and Kemp[7] analysed reinforced concrete slabs using the finite element method and assuming elastic/perfectly-plastic behaviour of the concrete, i.e. a square-yield criterion. They retained the same structural stiffness

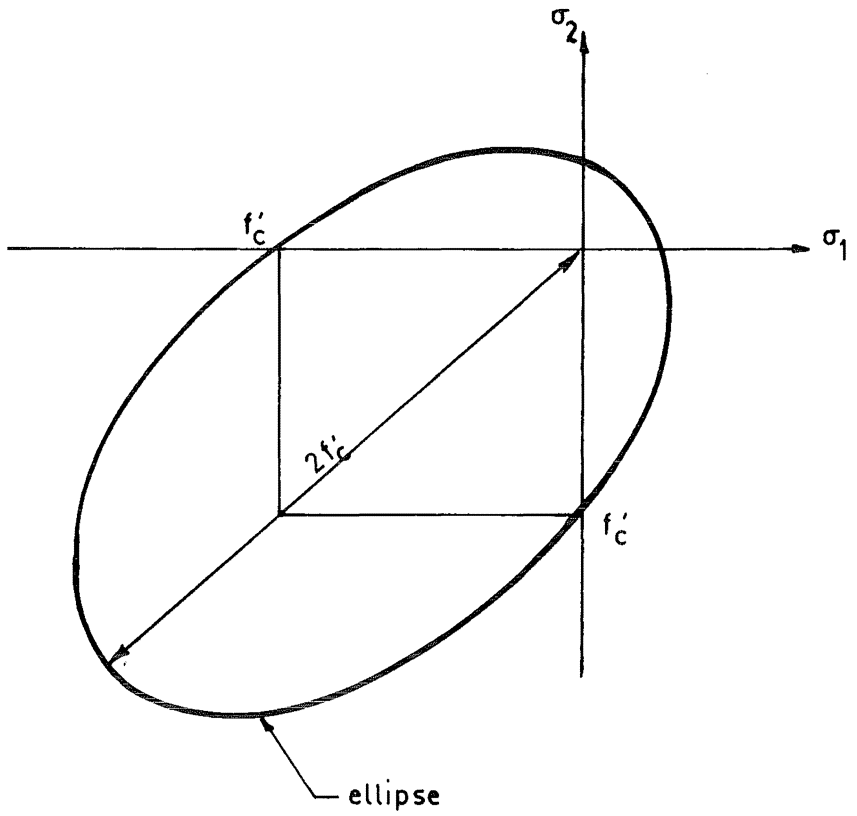

Fig. 4.1. Yield Criterion used by Riera and Billington

matrix throughout the analysis and incorporated the inelastic effects by applying plastic rotations at the appropriate nodes. These plastic rotations were determined by introducing additional equations which enforced the moment at the inelastic nodes to remain at the yield moment.

4.2 Complete Analysis for Reinforced Concrete Slabs and Shells

In most step by step analyses the constitutive equations are modified at the end of each load increment to account for the points that have yielded. Thus the analysis is based upon two premises;

a) a yield criterion, and

b) a method of modifying the constitutive equations for non-linear and/or inelastic effects.

The most suitable yield criterion for a reinforced concrete section in flexure is Johansen's square-yield criterion (Fig. 4.2) which postulates that when one or both of the principal moments reaches the plastic moment M_p then the plane associated with that principal moment will become plastic, i.e. elastic/perfectly-plastic behaviour is assumed. The plastic moment is generally taken as the yield moment. Reinforced concrete, however, does not behave in an elastic/perfectly-plastic fashion. Referring to the moment-curvature curve of an under-reinforced concrete section shown in Fig. 4.3, we can distinguish four principal phases:

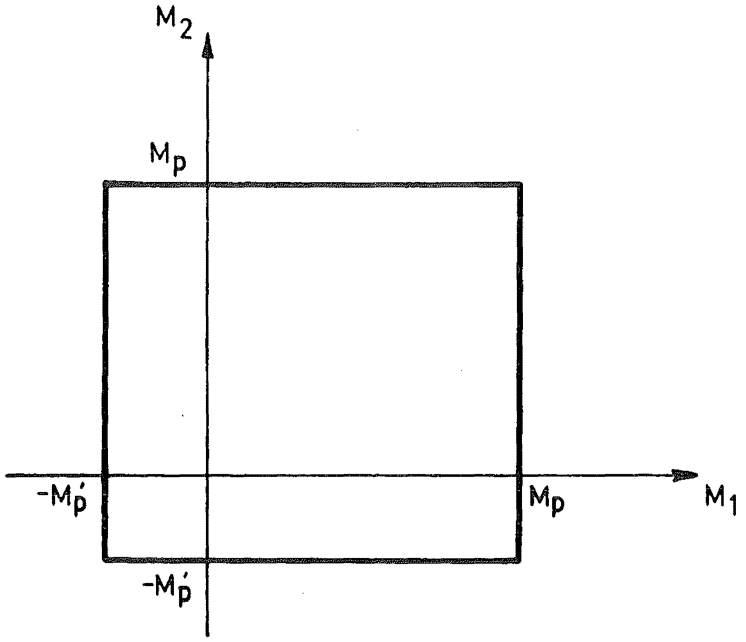

Fig. 4.2. Johansen Square-Yield Criterion

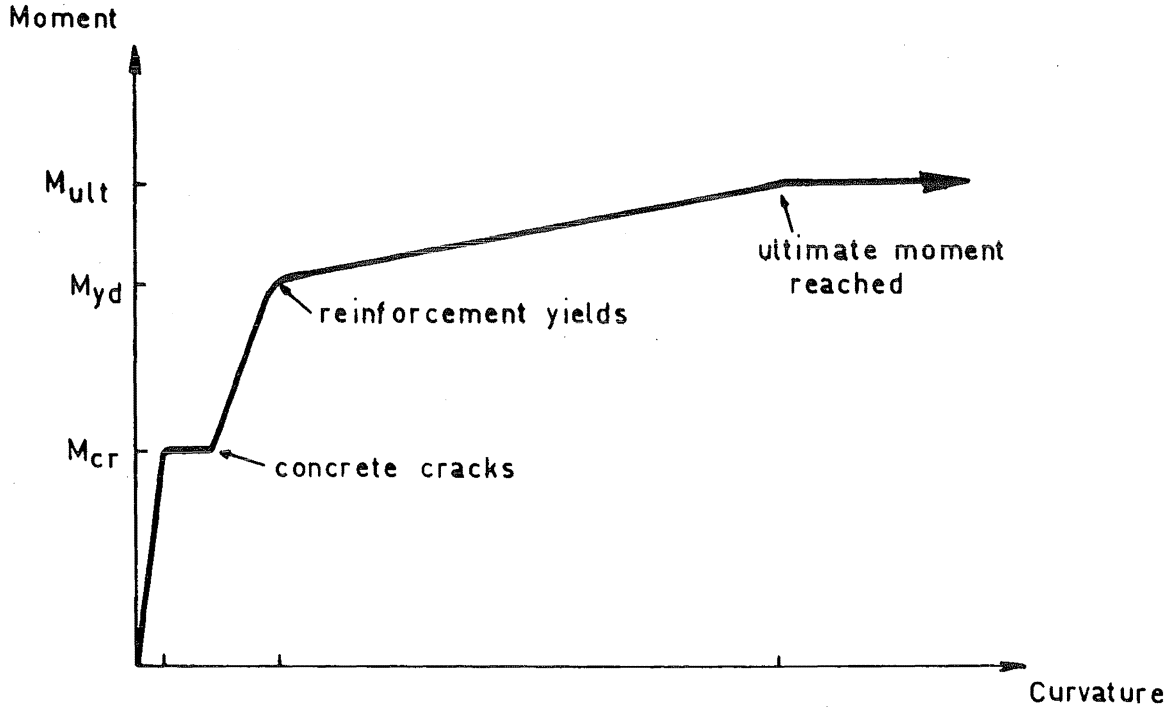

Fig. 4.3. Moment-Curvature Curve for an Under-Reinforced Concrete Section

a) before cracking, $M < M_{cr}$,

b) after cracking but before the steel has yielded, $M_{cr} \leq M < M_{yd}$,

c) after the steel has yielded but before the ultimate moment is reached, $M_{yd} \leq M < M_{ult}$, and

d) when the ultimate moment is reached, $M = M_{ult}$.

(The extent of this fourth phase is variable, and in the case of a simply supported beam will not exist at all. However, for those structures that undergo redistribution of stresses the structure will not fail when one section fails but only when a collapse mechanism is formed.)

It was decided to represent these phases in a diagram called a section property diagram (refer Fig. 4.4). This particular diagram assumes that there is no interaction between the principal planes and therefore the moment-curvature relationship of a slab section will be identical to the moment-curvature relationship of a beam which possesses an equivalent section. If the moment-curvature relationship is multi-linear (refer Fig. 4.5) then a multi-linear section property diagram could be constructed. Furthermore, the components of the section property diagram need not be square, i.e. interaction between the principal moments could be accounted for, and also additional variables could be introduced and a multi-dimensional section property diagram could be constructed. For example, a third axis of time, to incorporate the effects of creep, would form a three-dimensional

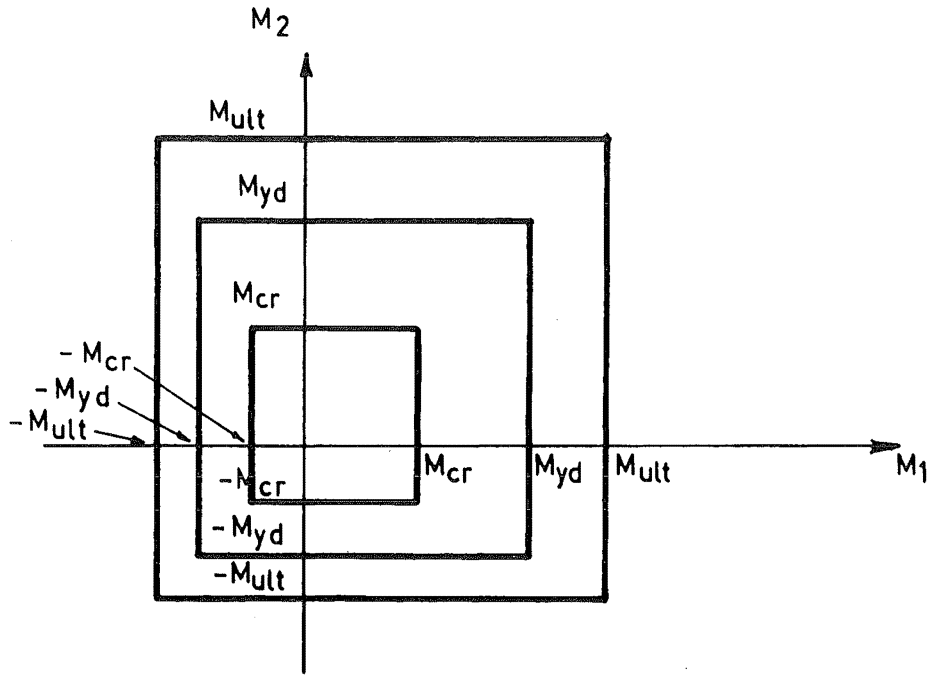

Fig. 4.4. Section Property Diagram

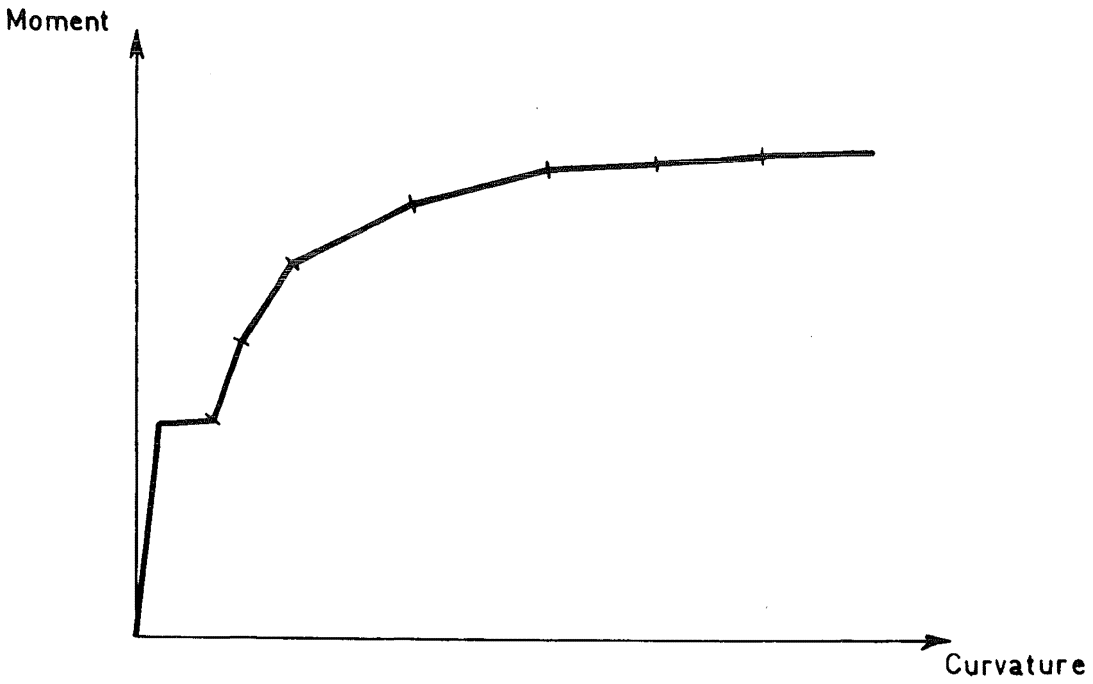

Fig. 4.5. Multi-Linear Moment-Curvature Curve

diagram. Finally, there is no compulsion to retain the same basic shape for each component in the diagram. Thus, the section property diagram shown in Fig. 4.4 represents the simplest possible case.

Two advantages of the diagram are; that a physical picture of the properties of a section can be obtained, and by defining this diagram mathematically the conditions at any point on a structure can be readily determined.

The method of solution involves a step-by-step building up process. At the end of each load increment the load-deflection characteristics of the nodal points are related to the moment-curvature relationship of the section, and thus the extent of the non-linear or inelastic effects can be determined. Using this information the stiffness of any partially or fully cracked finite elements is determined and a new structural stiffness matrix can be formed. Within each load increment moment redistribution can be taken into account using the "initial stress" method[57] (refer Section 4.6).

The adoption of the section property diagram shown in Fig. 4.4 assumes that there is no interaction between planes that are perpendicular to each other. Due to this assumption two objections can arise. Firstly, when the angle between the principal planes and the reinforcement is not zero it has been postulated[60] that the yield moment will increase, and secondly, Poisson's ratio for reinforced concrete is not

zero and hence some interaction will occur. These two objections are covered in the following two sections.

4.3 Distortion of the Reinforcement Across Cracks

For a slab reinforced along the x and y axes (Fig. 4.6) the normal method of determining the yield moment across a fracture line, which is inclined at an angle α to the x axis, is to assume that the fracture line is stepped, and further, that the principal moments are in the x and y directions. Hence

$$m_n = m_x \sin^2\alpha + m_y \cos^2\alpha \qquad (4.13)$$

where m_n is the yield moment across the fracture line, m_x is the yield moment along the x axis, and m_y is the yield moment along the y axis. Although the assumption that the principal moments will always be in the x and y directions is incorrect it leads to conservative results and is normally used.

Wood[60], however, stated that whenever the angle α was greater than zero the moment across a fracture line would be greater than the yield moment proposed by Johansen's Square-Yield criterion due to distortion (also known as "kinking") of the reinforcement across the crack. If the reinforcement is distorted completely so that it is perpendicular to the fracture line then the yield moment across the fracture line is

$$m_n = m_x \sin\alpha + m_y \cos\alpha \qquad (4.14)$$

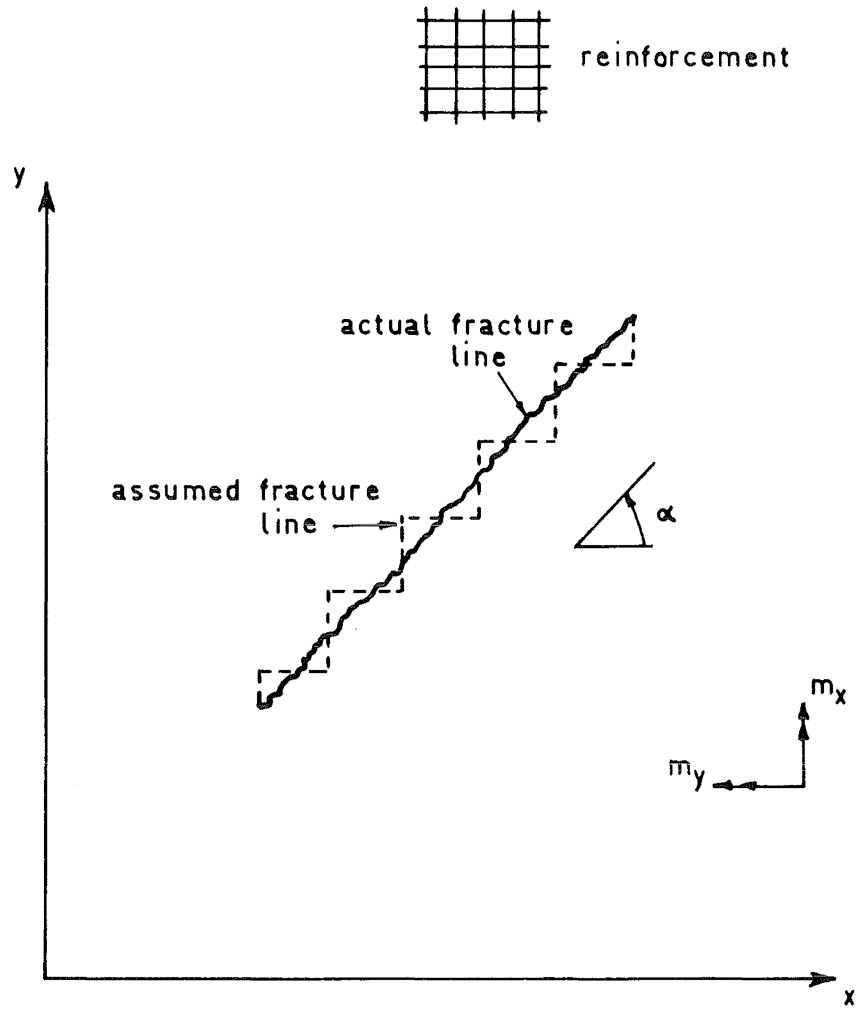

Fig. 4.6. General Fracture Line

For the case of equal reinforcing in the x and y directions and an angle α of 45^{o} the yield moment across the fracture line, assuming full distortion of the reinforcement, would theoretically be 41% higher than that proposed by Johansen's Square-yield criterion.

In experimental tests both Wood[60] and Kwiecinski[61] noted an increase of approximately 17% in the aforementioned example thus showing that a partial distortion of the reinforcement occurred.

In other series of tests, however, Moreley[62], and Prince and Kemp[63] found no such enhancement in the moment and they believe that extraneous factors caused the increase that both Wood and Kwiecinski observed.

Because the controversy is not finalised provision was made to accept either no distortion or partial distortion of the reinforcement. When partial distortion is assumed the yield moment across a fracture line is calculated according to the formula proposed by Kwiecinski[64], namely,

$$m_n = \{\cos\alpha\sqrt{1 - A^2\sin^2\alpha} + \kappa \sin\alpha\sqrt{1 - \frac{A^2}{\kappa^2}\cos^2\alpha}\}m \quad (4.15)$$

where m is the yield moment at $\alpha = 0^{o}$, κ is the coefficient of orthotropy $= \frac{m_n}{m}$ $(\alpha = 90^{o})$,

$$A = \sqrt{2 - \frac{1}{4\mu^2}(2\mu^2 - \kappa^2 + 1)^2},$$

and μ is the ratio $\frac{m_n}{m}$ $(\alpha = 45^{o})$ such that

$$\tfrac{1}{2}(\sqrt{2-\kappa^2} + \kappa) \leq \mu \leq \frac{1+\kappa}{\sqrt{2}}$$

An example comparing the effect of either including or excluding the distortion of the reinforcement is described in Section 7.2.

4.4 Anisotropic Finite Elements

The section property diagram shown in Fig. 4.4 assumes that there is no interaction between stresses acting in two perpendicular directions. However, this assumption is only exact when Poisson's ratio for the reinforced concrete is zero. For uncracked concrete Poisson's ratio varies within the approximate limits of 0.14 and 0.20 and Poisson's ratio for steel is approximately 0.33. (For the analyses in Part III of this thesis Poisson's ratio for uncracked reinforced concrete was assumed to be 0.167.) With the onset of cracking, however, Poisson's ratio for the reinforced concrete will decrease; for example, consider an uncracked element which is subjected to a stress system of $\sigma_x = \tau_{xy} = 0$, and $\sigma_y = 1$. The strain in the x direction will be $\varepsilon_x = -\nu_{yx}/E_x$. If this same element is cracked in the y direction and subjected to the same stress system then the strain in the x direction will remain constant. Therefore, because E_x decreases upon cracking, the ratio ν_{yx} will decrease by the same ratio. (A similar argument proves that ν_{xy} will not change its value.) Hence, the interaction of moments will be reduced as the

elements crack and the reinforcement yields.

Anisotropy may arise from either differing quantities of reinforcement in different directions or due to directional inelastic behaviour (e.g. yielding across a fracture line). The latter form of anisotropy affects the structural behaviour far more than the former which has not been taken into account in the analyses within this thesis. To form anisotropic finite elements the constitutive relationship

$$\{\sigma\} = [C]\{\varepsilon\} \tag{4.16}$$

is altered. The simplest form of anisotropic element is what Hearmon[65] has called a "specially orthotropic" element (refer Fig. 4.7a), i.e. the principal directions of orthotropy coincide with the directions of the axes. For this case

$$[C] = \frac{1}{1-\nu_{xy}\nu_{yx}} \begin{bmatrix} E_x & \nu_{yx}E_y & \cdot \\ \nu_{xy}E_x & E_y & \cdot \\ \cdot & \cdot & G(1-\nu_{xy}\nu_{yx}) \end{bmatrix} \tag{4.17}$$

When the principal directions of orthotropy do not coincide with the directions of the axes we have a "generally orthotropic" element whose constitutive relationship can be determined by transforming the constitutive relationship of the specially orthotropic element, i.e. if θ is the angle between the principal directions of orthotropy and the directions of the axes then

$$[\bar{C}] = [T]^T[C][T] \tag{4.18}$$

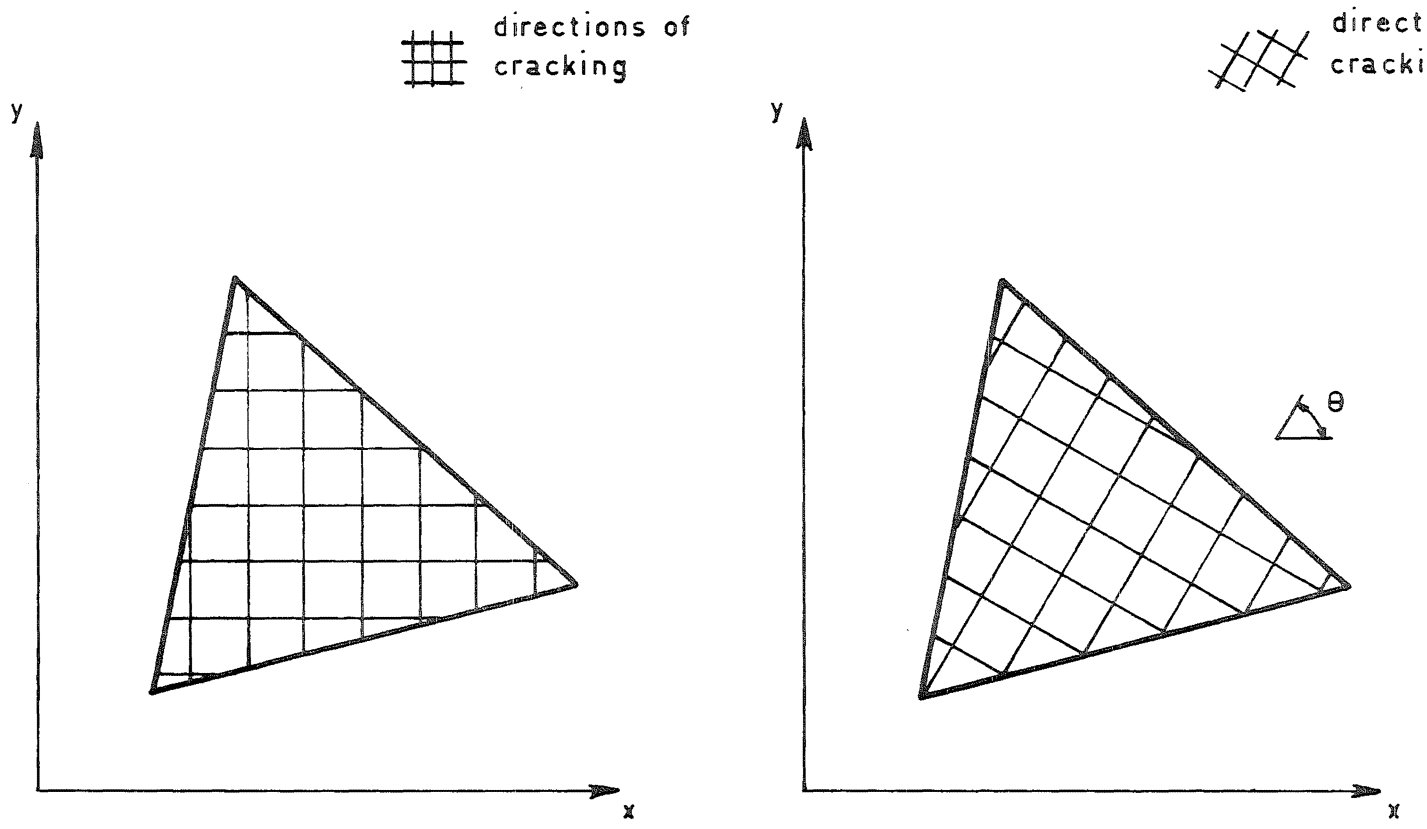

Fig. 4.7. A Specially Orthotropic and a Generally Orthotropic Finite Element

where $[\bar{C}]$ is the matrix of material constants for the generally orthotropic element, [C] is the matrix of material constants for the specially orthotropic element (Eq. 4.17), and

$$[T] = \begin{bmatrix} \cos^2\theta & \sin^2\theta & -\cos\theta\sin\theta \\ \sin^2\theta & \cos^2\theta & \cos\theta\sin\theta \\ 2\cos\theta\sin\theta & -2\cos\theta\sin\theta & \cos^2\theta-\sin^2\theta \end{bmatrix}.$$

In the constitutive relationship there are five constants, E_1, E_2, ν_{12}, ν_{21} and G. However, due to symmetry

$$\nu_{12}E_1 = \nu_{21}E_2 \tag{4.19}$$

so that only four of the constants are independent. Because of the difficulty in determining the shear modulus G it was decided to introduce an approximation and make its value dependent upon the other four constants. This dependence may be obtained as follows. Consider an orthotropic finite element subjected to shear strain only and such that the angle θ, between axes 1-2 and x-y, is 45°. Substituting into Eq. (4.18) we obtain

$$\tau_{xy} = \tfrac{1}{4}\,\frac{E_1(1-\nu_{12}) + E_2(1-\nu_{21})}{1-\nu_{12}\,\nu_{21}}\,\gamma_{xy}. \tag{4.20}$$

Also, for the same element, when the angle θ is zero

$$\tau_{xy} = G\gamma_{xy}. \tag{4.21}$$

The approximation consists of equating Eqs (4.20) and (4.21) from which

$$G = \frac{E_1(1-\nu_{12}) + E_2(1-\nu_{21})}{4(1-\nu_{12}\nu_{21})} . \qquad (4.22)$$

Because the shear modulus is independent of the constants E_1, ν_{12}, ν_{21} and E_2 we cannot state very much about the accuracy of this expression except that:

a) Eq. (4.22) will be correct for an isotropic element,

b) Eq. (4.22) will be correct when the angle θ is 45^o, and

c) Zienkiewicz[66] makes a similar approximation by putting $1/G = 1/E_1 + 1/E_2$ and he did not find any detrimental side effects.

After an element is cracked in one direction the stresses will redistribute and, if the element becomes doubly cracked, the angle between the two sets of cracks may not be 90^o. This anisotropic element is shown in Fig. 4.8.

If the first set of cracks occurred in the y direction then, referring to Eq. (4.17), E_x would be replaced by αE_x and ν_{xy} would be replaced by $\alpha\nu_{xy}$ where the coefficient α is the reduction factor. Taking Poisson's ratio for reinforced concrete as 1/6 and a reduction factor of .2, then the modified Poisson's ratio in any direction will approximately be 1/30 and because this value is so small it is assumed to be zero for all doubly cracked elements. This means that we ignore the interaction of perpendicular stresses.

The doubly cracked anisotropic element may be replaced by a lattice comprised of two sets of bars which lie in

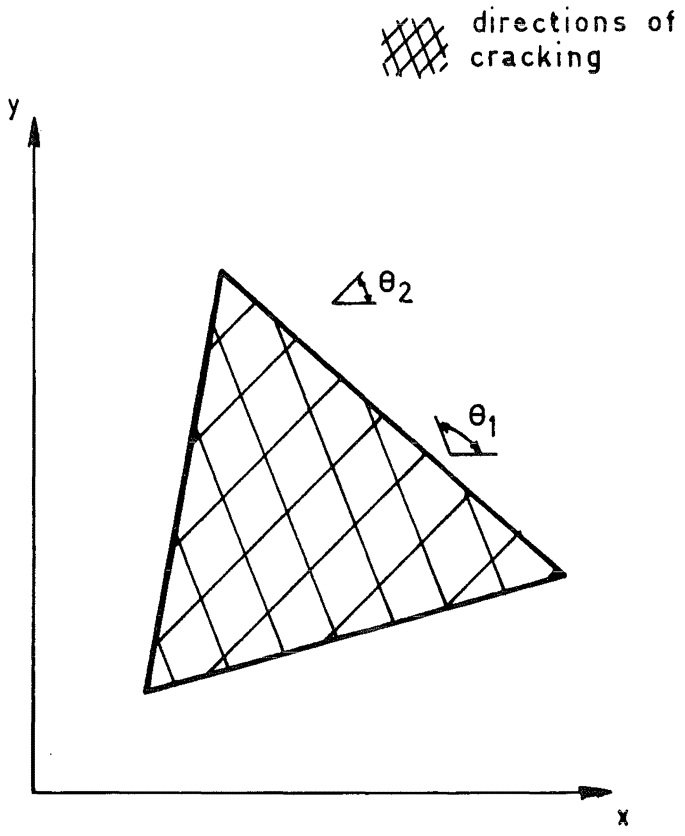

Fig. 4.8. An Anisotropic Finite Element

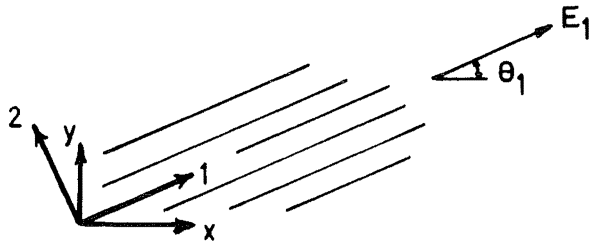

Fig. 4.9. Elements of a Lattice in Direction 1

the directions of the cracks. From Eq. (4.22), the shear modulus of the lattice is taken as $G = (E_1+E_2)/4$, i.e. we can assume that each set of bars absorbs a shear stress in proportion to its modulus of elasticity, and hence we can consider the lattice components separately. Fig. 4.9 illustrates the portion of the lattice lying in a direction θ_1 to the x axis and having a modulus of elasticity of E_1. The constitutive matrix for such a lattice will be

$$\begin{Bmatrix} \sigma_1 \\ \sigma_2 \\ \tau_{12} \end{Bmatrix} = \begin{bmatrix} E_1 & & \\ & 0 & \\ & & E_1/4 \end{bmatrix} \begin{Bmatrix} \varepsilon_1 \\ \varepsilon_2 \\ \gamma_{12} \end{Bmatrix} \qquad (4.23)$$

Eq. (4.23) can be transformed to the x-y coordinate system using Eq. (4.18) and putting $\nu_{12} = \nu_{21} = 0$. The same procedure is repeated for the other part of the lattice and the constitutive matrix is taken as the sum of the constitutive matrices of the two parts.

Computationally the procedure of forming anisotropic elements can be divided into three groups depending on whether the element is initially uncracked, cracked in one direction, or cracked in two directions. (It is assumed that an element cannot be cracked in more than two directions.) This procedure is given below for a slab and, including bracketed phrases, for a shell.

The aim of the analysis of an initially uncracked element is:

a) to determine the principal moments (and the principal forces) and the angle that they make with the x axis, and

b) to check the principal moments (and the principal forces) with a load-moment-curvature relationship and hence determine the flexural rigidities in the directions of the principal moments (and the principal forces).

The analysis of an element that is already cracked in one direction is more complex. The aim is:

a) to determine the principal moments (and the principal forces) and the angles that they make with the x axis,

b) to take the principal moment (and the principal force) which has the largest absolute value and ckeck that the angle that it makes with the existing set of cracks is greater than a prescribed angle - this comparison is necessary to prevent two sets of cracks being formed which are almost parallel, in which case, any reduction of stiffness is assumed to occur at the existing set of cracks. If the angle is greater than the prescribed angle then the flexural rigidity corresponding to this principal moment (or principle force) is determined.

c) If the angle is less than the prescribed angle then the flexural rigidity corresponding to the other principal moment (and principal force) is determined.

d) To determine the moment (and force) acting at the

angle of the existing set of cracks and if necessary to alter the flexural rigidity in this direction.

This procedure is not exact if a new set of cracks is formed and the stiffness of the existing set of cracks is altered because, when one of the stiffnesses is altered, the moment variation within the element is affected; but this is not taken into account when calculating the other stiffness. If the element is too stiff, however, it would be reduced in the following cycle and therefore the final result will always be conservative.

The analysis of an element that is doubly cracked is simply,

a) to determine the moment (and force) across each set of cracks and hence determine the flexural rigidity for each crack angle.

For all the analyses the elements always undergo a degrading stiffness, and therefore, even if the moment at a section is reduced by redistribution, the stiffness of that section will never increase.

Summarising this section and the previous section we can state that distortion of the reinforcement may affect the square-yield criterion, and in the worst possible situation the stress given by the square-yield criterion would be 87% of the actual stress. Poisson's ratio will also alter the square-yield criterion but mainly in deter-

mining the cracking stresses because, after cracking, Poisson's ratio is substantially reduced. Acknowledging these facts the section-property diagram shown in Fig. 4.4 is still retained because it means that the properties of a slab or shell section can be described by the properties of an equivalent beam - a considerable simplification of the problem and one that loses very little accuracy.

4.5 Load-Moment-Curvature Relationships for Reinforced Concrete Sections

The accuracy of the inelastic analysis will be dependent upon the accuracy with which a representative load-moment-curvature curve for a section can be depicted. (For a slab section it would be possible to determine the moment-curvature relationship by an experimental test on a beam having an equivalent section, though a theoretical method would be more general and quicker to use.)

Consider part of a cracked beam which is within a constant moment region; Fig. 4.10 shows the approximate variation of:

a) the steel stress,

b) the concrete tensile stress

c) the bond stress, and

d) the curvature.

The variations are only approximately known because the bond stress variation is dependent upon many factors including the

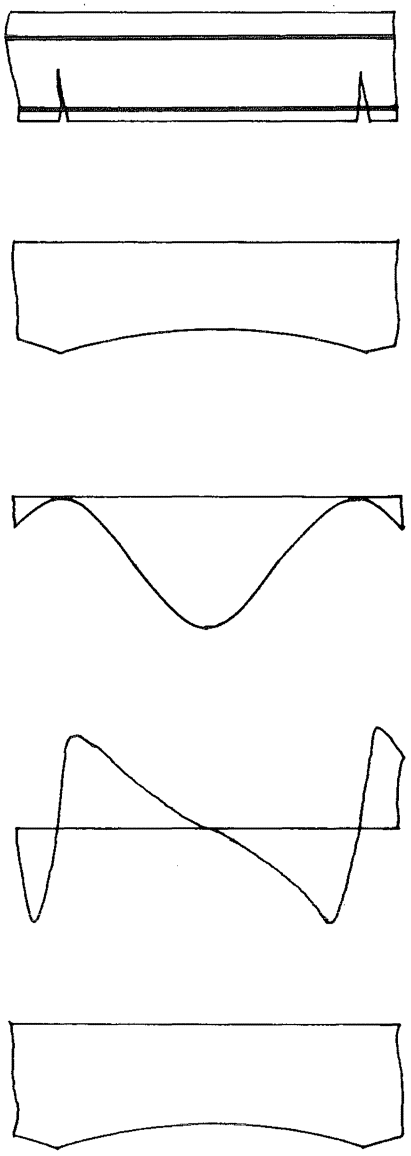

Fig. 4.10. Cracked Concrete Segment in a Constant Moment Region

size and surface properties of the reinforcement, the quality of the concrete, and the loading distribution: for these reasons the bond stress variation cannot be specified exactly.

Theoretical load-moment-curvature relationships, however, have been developed by Pfrang, Siess and Sozen[67] and Ferry-Borges and Oliveira[68], but they assumed that the concrete tensile strength is zero: thus their formulations are applicable to cracked sections only. Priestley[69] went a step further and determined an "average" curvature for a cracked prestressed concrete beam segment by assuming a triangular bond stress distribution between cracked sections. Following this method a computer program was written to determine the load-moment-curvature characteristics of a reinforced concrete beam section, and in addition, the method was extended so that the effect on the load-moment-curvature relationship of varying,

a) the bond stress distribution,

b) the section where the curvature was calculated, and

c) the method of determining an equivalent curvature

for a cracked segment, could be studied.

Three different bond stress variations were investigated, triangular, rectangular and sinusoidal (refer Fig. 4.11). These distributions correspond to those predicted by Wastlund, Brice and Saliger respectively[70]. Within each cracked

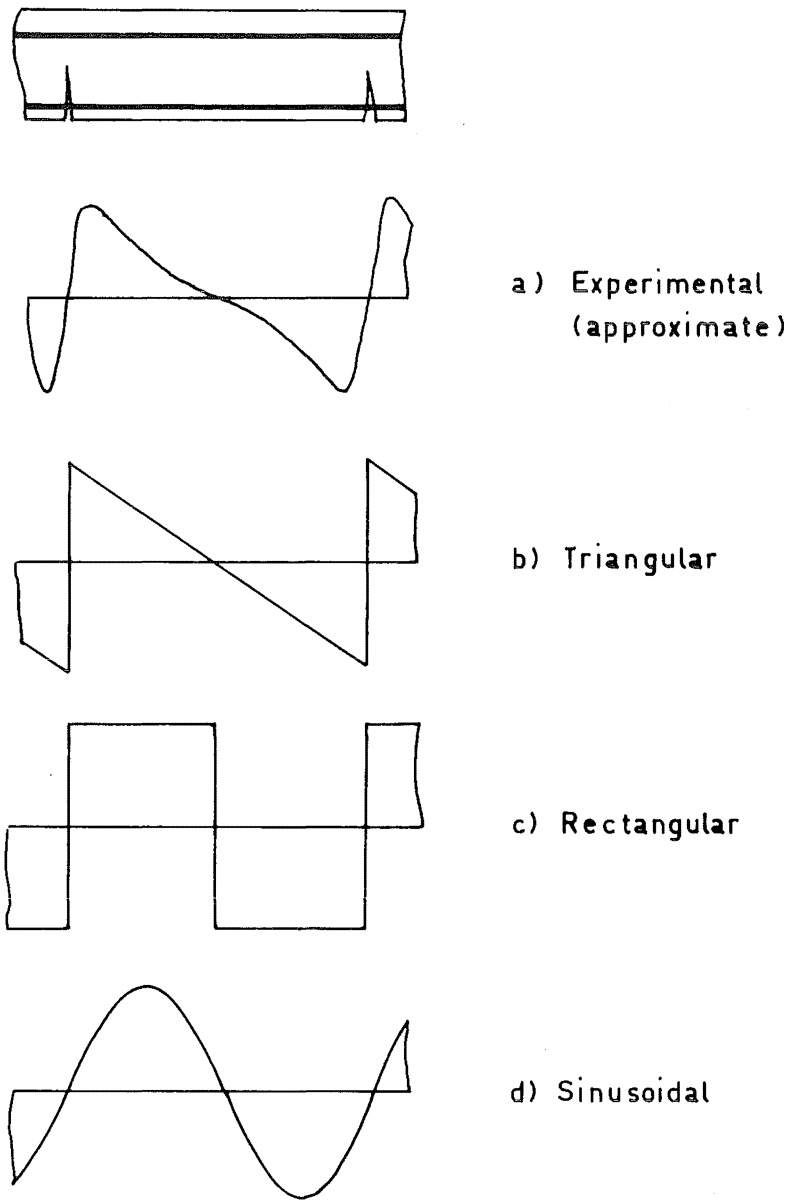

Fig. 4.11. Bond Stress Distribution in a Constant Moment Region

segment the curvature was calculated at six equally spaced sections ranging from the section at a crack to the section midway between the crack and an adjacent crack.

Fig. 4.12 shows a segment of a cracked beam such that the segment contains only one crack and its boundaries are the midsections of the adjacent cracks. The load-moment-curvature characteristics of this segment are determined by assuming that it is within a constant moment region. This is an acceptable approximation because the length of the segment will in general be less than two times the section thickness and hence, for a slab or a shell, the error in assuming that the internal moment is constant will normally be small; furthermore, the moment due to the applied load will be much smaller than the internal moment and therefore it can also be neglected.

Priestly took an average curvature which gives equivalent rotations at sections 1 and 2 (this shall be called an equivalent-rotation curvature), so that

$$\rho_r = .1\rho_1 + .2\rho_2 + .2\rho_3 + .2\rho_4 + .2\rho_5 + .1\rho_6 \qquad (4.24)$$

where ρ_r is the equivalent-rotation curvature and ρ_1, ρ_2, ρ_3, ρ_4, ρ_5 and ρ_6 are the curvatures at the sections progressing away from the cracked section, i.e. ρ_1 is the curvature at the cracked section and ρ_6 is the curvature at the midsection.

If, however, we require an equivalent displacement at section 3 then the average curvature (which shall be called

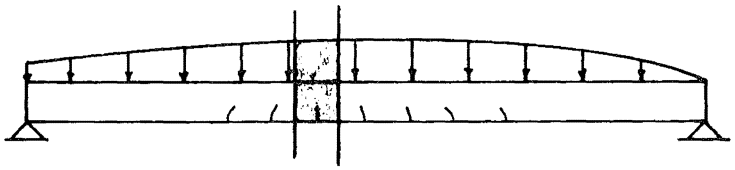

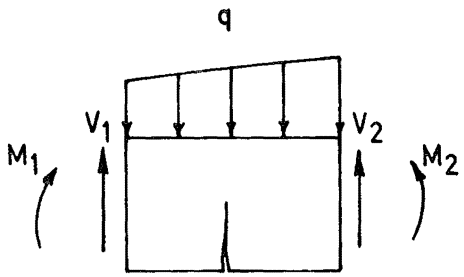

equals

Fig. 4.12. Cracked Segment of a Beam

an equivalent-displacement curvature) is

$$\rho_d = .19\rho_1 + .32\rho_2 + .24\rho_3 + .16\rho_4 + .08\rho_5 + .01\rho_6 \quad (4.25)$$

where ρ_d is the equivalent-displacement curvature.

As we move away from the cracked section the curvatures always decrease, i.e.

$$\rho_1 > \rho_2 > \rho_3 > \rho_4 > \rho_5 > \rho_6$$

and therefore

$$\rho_d > \rho_r. \quad (4.26)$$

Hence, if an equivalent-rotation curvature is used the displacement at section 3 will be underestimated; but if an equivalent-displacement curvature is used the rotations at sections 1 and 2 will be overestimated. Because accurate displacements are more important to engineers than accurate rotations, and because the displacement method normally gives a lower bound to the displacements (Section 3.2), the equivalent-displacement curvature will generally be used. (An example in Section 6.2 illustrates the effect of using an equivalent-rotation curvature compared with an equivalent-displacement curvature.)

The concrete tensile force, which varies from zero at a crack to a maximum value midway between two cracks, was assumed to have a triangular stress distribution at all sections. The maximum tensile stress that the concrete can take before it cracks is best determined from the modulus of

rupture. Unfortunately values for the modulus of rupture vary considerably and are dependent upon many factors including the quality of the concrete, its water/cement ratio, the type and shape of the aggregrate, the method of curing, and the rate and method of loading. Also,the modulus of rupture test takes a specimen which is free from shrinkage stresses; but in a reinforced concrete section shrinkage stresses will be concentrated near the reinforcement so that weaker sections will be formed.

Neville[71] records three formulae relating the modulus of rupture to the concrete compressive strength. The first is that assumed by the Comité Europeen du Beton,

$$f_t = 9.5 \sqrt{f'_c} \text{ lb./sq.in.} \qquad (4.27)$$

where f_t is modulus of rupture.

The second is from tests done at the University of Illinois[72] and is,

$$f_t = \frac{3,000}{4 + \frac{12,000}{f'_c}} \text{ lb./sq.in.} \qquad (4.28)$$

Also, from Walker and Bloem[73] the modulus of rupture, if the concrete compressive strength is greater than 2,000 lb./sq.in., is

$$f_t = 0.97f'_c + 180 \text{ lb./sq.in.} \qquad (4.29)$$

Tests done by Ramakrishnan, Ananthanarayana, and Gopal[74] for concrete compressive strengths between 2,500 and

5,000 lb./sq.in., indicate that

$$f_t = .10f'_c + 130 \text{ lb./sq.in.} \qquad (4.30)$$

Fig. 4.13 shows the values of the modulus of rupture calculated by these four formulae for a selected range of compressive strengths.

The variation in the value of the modulus of rupture will be even greater than that shown in Fig. 4.13 because each formula defines an "average" value; for example, Ramakrishnan's values of the modulus of rupture vary by approximately ± 100 lb./sq.in.

Further details of this method, including the stress-strain relationships that were assumed for the reinforcement and for the concrete, and the analysis of the possible sections, are given in Appendix B.

For the reinforced concrete beam section shown in Fig. 4.14, moment curvature curves (normalised to 1) were drawn (Fig. 4.15) assuming a rectangular bond stress distribution and taking:

a) the curvature at a cracked section,

b) the equivalent-rotation curvature, and

c) the equivalent-displacement curvature.

The principal differences in the curves can be explained by studying the curvatures at sections away from the cracked section. Fig. 4.16a shows the curvature variation (normalised to 1) from the above example when the applied moment is 0.6

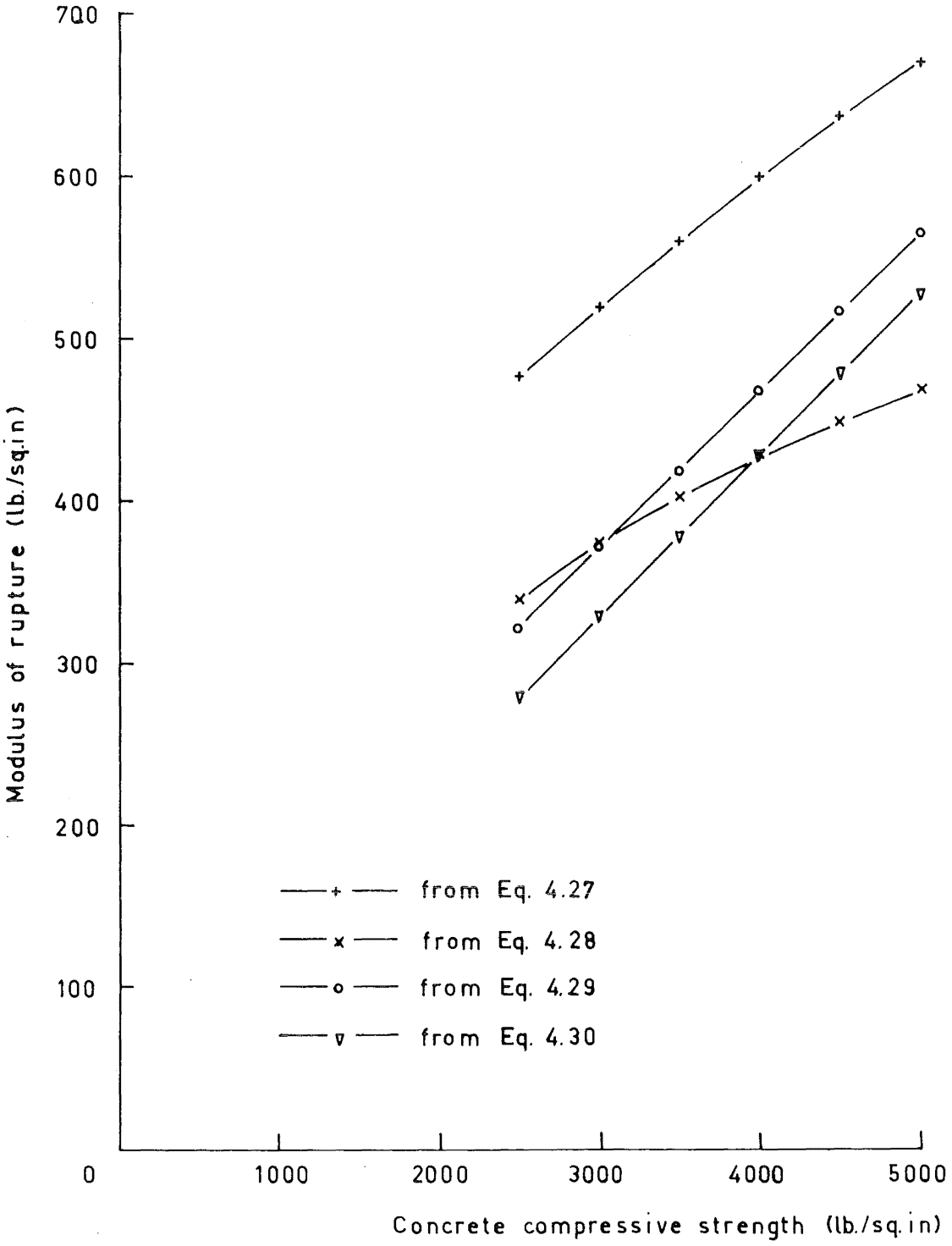

Fig. 4.13. Variation of the Modulus of Rupture with the Concrete Compressive Strength

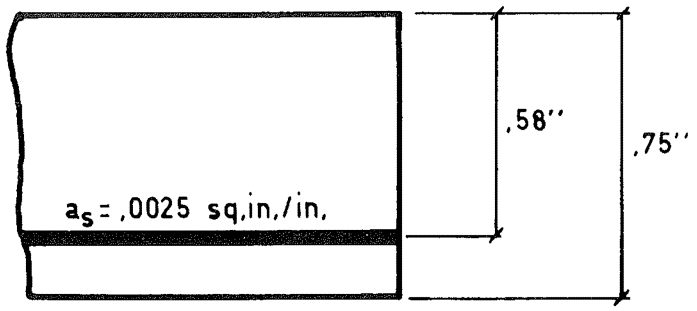

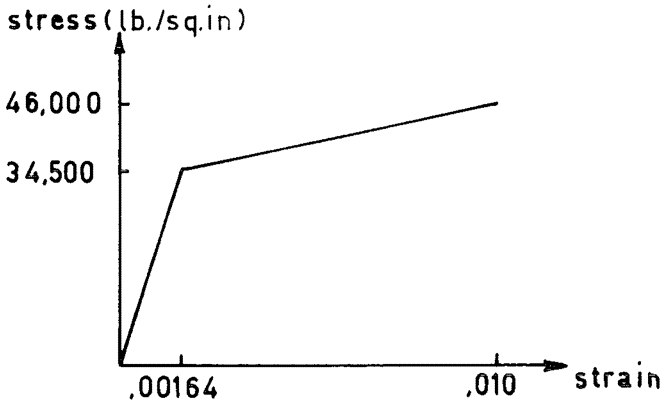

Reinforcement Stress-Strain Relationship

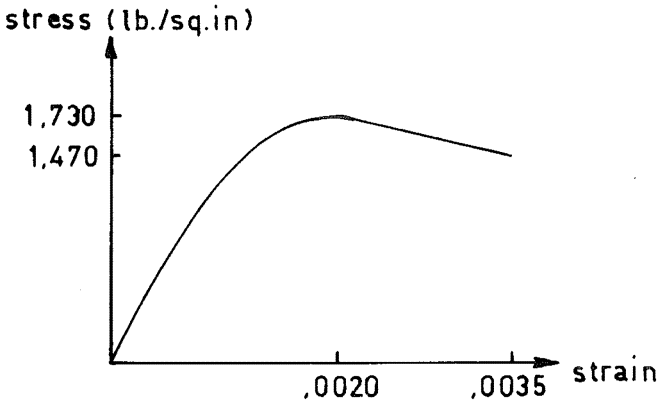

Concrete Stress-Strain Relationship

Fig. 4.14. Reinforced Concrete Beam Section

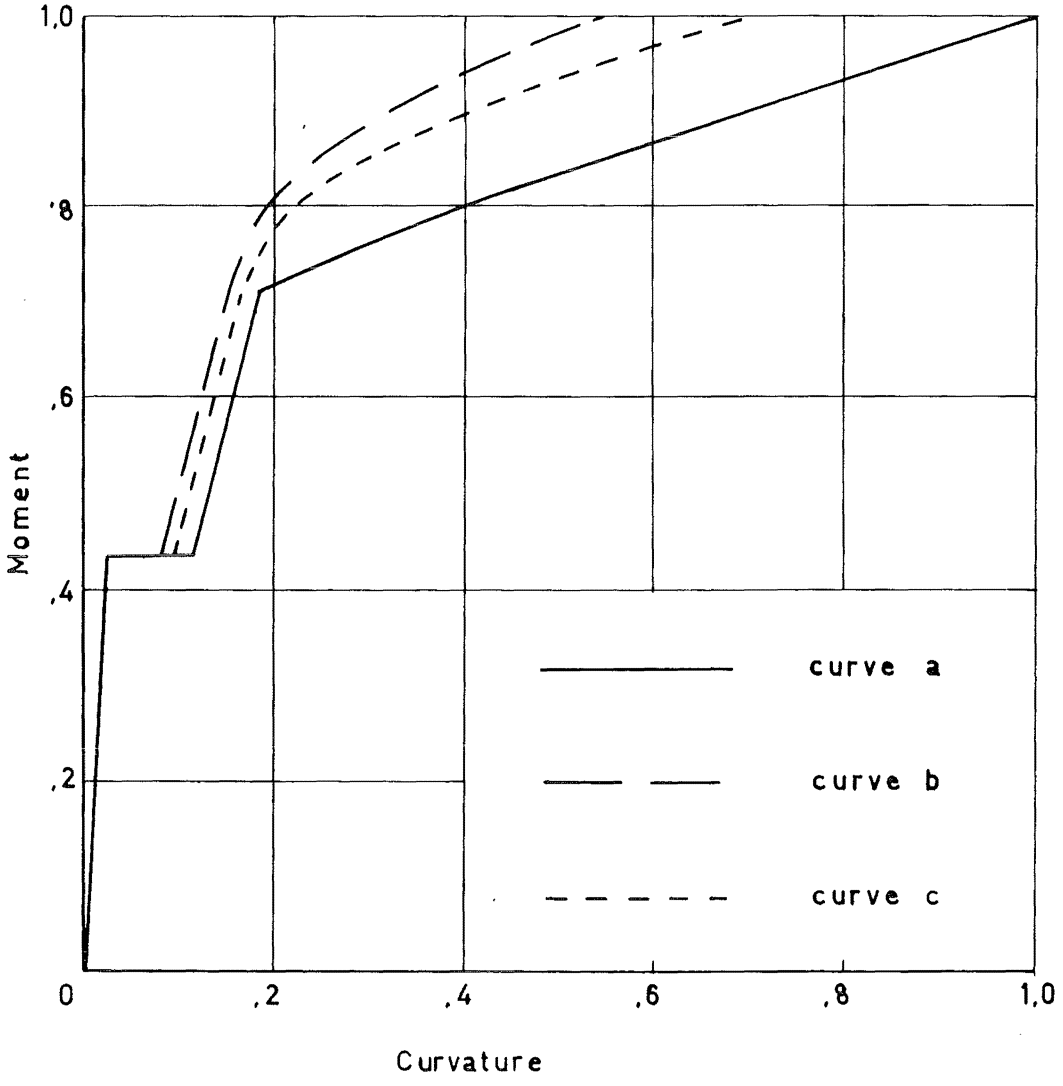

Fig. 4.15. Moment-Curvature Curves

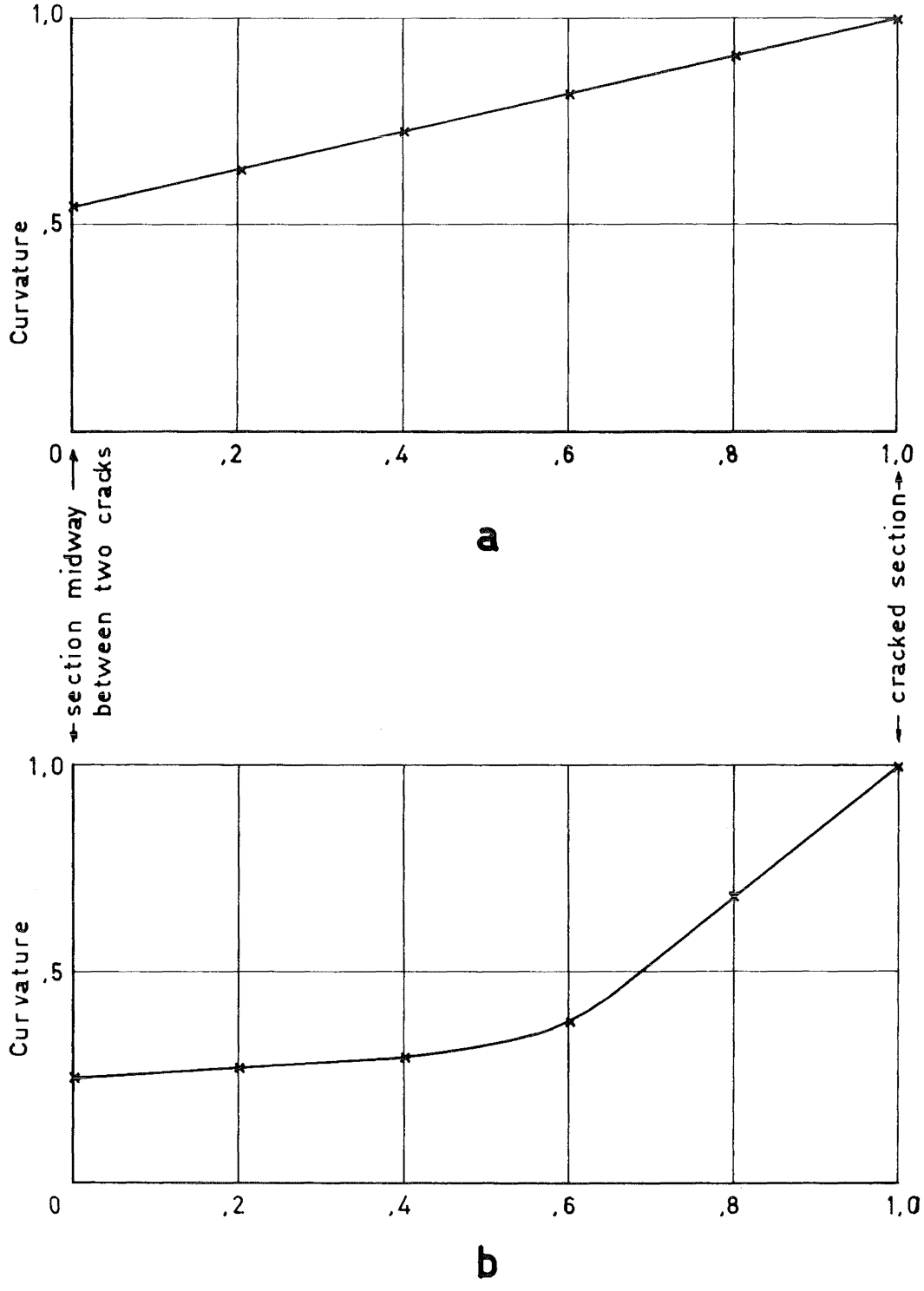

Fig. 4.16. Curvature Variation in a Cracked Segment

of the ultimate moment (i.e. the section has cracked but the steel has not yielded) and Fig. 4.16b shows the curvature variation (normalised to 1) when the applied moment is 0.9 of the ultimate moment (i.e. the steel has yielded). The different behaviour of the three curves in Fig. 4.15 can be explained by the method of determining their curvatures; the curvature at a cracked section is always the greatest and the equivalent-displacement curvature given in Eq. (4.25) will be larger than the equivalent-rotation curvature given in Eq. (4.24) because Eq. (4.25) comprises larger proportions of the curvature near the cracked section than does Eq. (4.24). Hence, curve (b) is stiffer than curve (c) which in turn is stiffer than curve (a).

Assuming an equivalent-displacement curvature, moment-curvature curves (normalised to 1) are shown in Fig. 4.17 taking:

a) a triangular bond stress distribution,

b) a rectangular bond stress distribution (i.e. curve (c) of Fig. 4.15, and

c) a sinusoidal bond stress distribution.

Again the variation of the curves can be explained by the method of determining their curvatures. The triangular bond stress distribution will decrease the steel force (and hence the curvature) at sections near a crack more quickly than the rectangular bond stress distribution, and the rectangular bond stress distribution will decrease the

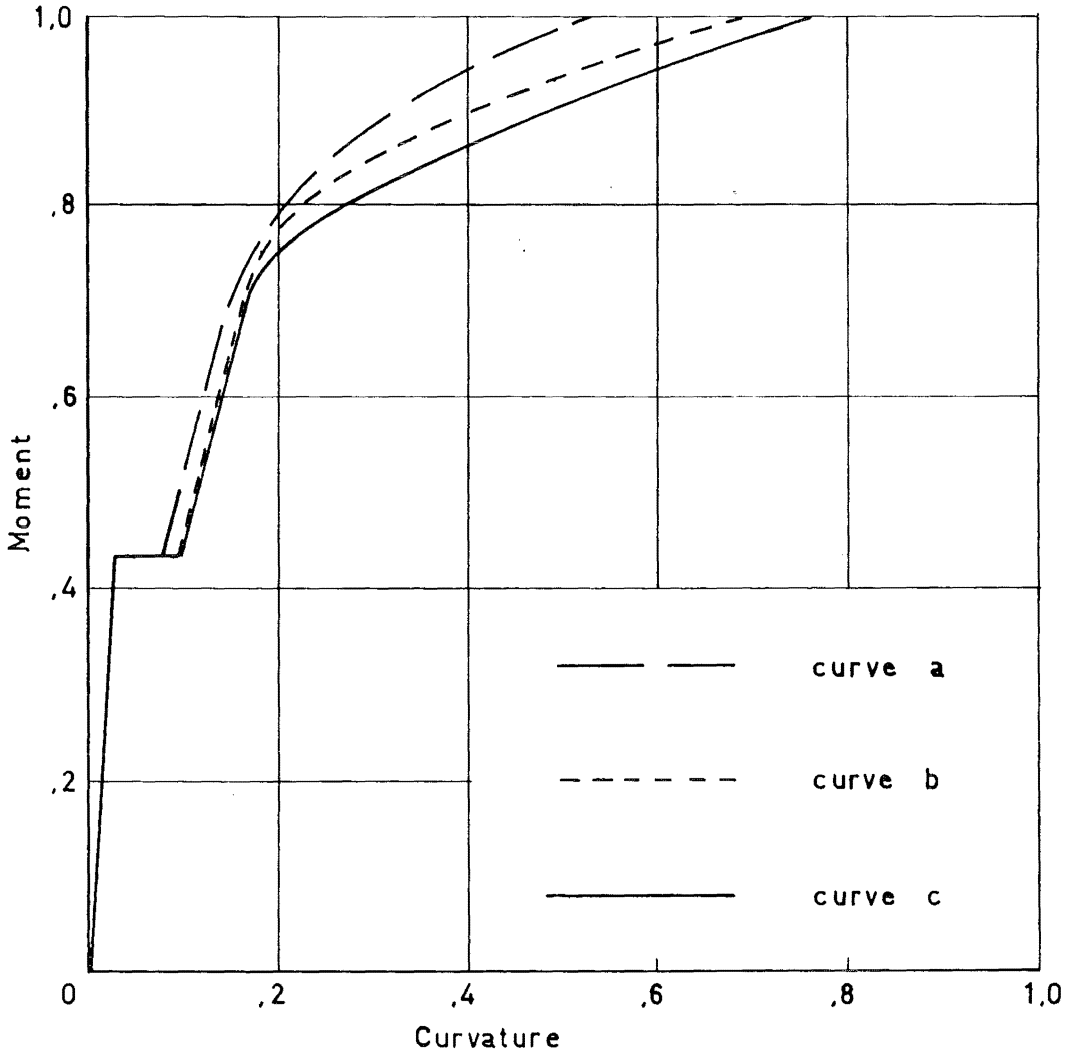

Fig. 4.17. Moment - Curvature Curves

curvature more quickly than the sinusoidal bond stress distribution. Hence, curve (a) is stiffer than curve (b) which in turn is stiffer than curve (c).

Any bond slip will alter the bond stress variation and will decrease the effective stiffness of the cracked segment. Some bond slip will always exist at a crack but its extent is difficult to determine, and among other factors, will depend upon the moment variation over the cracked segment. It has been assumed that each cracked segment is within a constant moment region but it is worthwhile considering what moment variation would be necessary to cause bond failure. If the difference in steel force at two adjacent cracks is ΔT then

$$\Delta T = \Sigma_0 \, s \, T_{av} \qquad (4.31)$$

where Σ_0 is the surface area of the reinforcement, s is the distance between the two cracks, and T_{av} is the average bond stress. For the example cited above, if we assume an average bond stress of 250 lb./sq.in. (which equals the ultimate average bond stress for non-deformed bars specified in the ACI Building Code[75]) and that the minimum distance between two cracks is equal to the section thickness, $\frac{3}{4}$ inch, then $T = 46.9$ lb. This corresponds to a moment variation of approximately 25 lb.in. over a distance of $\frac{3}{4}$ inch which is unlikely to occur in the slab shown in Fig. 4.14. Furthermore, the value of 250 lb./sq.in. for the average bond stress of

could be conservative; Mains[76] measured the average bond stress of undeformed bars and found that it varied from 240 lb./sq.in. to 415 lb./sq.in. If deformed bars were used the chance of bond failure occurring would be considerably less due to their higher average bond stress of 335 lb./sq.in. to 890 lb./sq.in.

Assuming an equivalent-displacement curvature and a rectangular bond stress, moment-curvature curves (normalised to 1) were drawn in Fig. 4.18 taking the cracking moment as:

a) 17.1 lb.in./in. width (this corresponds to a maximum concrete tensile stress of f_t = 166 lb./sq.in.),

b) 27.4 lb.in./in. width (i.e. curve (c) of Fig. 4.15). This corresponds to a maximum tensile stress of f_t = 266 lb./sq.in.), and

c) 37.6 lb.in./in. width (this corresponds to a maximum concrete tensile stress of f_t = 366 lb./sq.in.)

It is seen that the stiffnesses of the curves vary quite considerably. In the above example the true cracking moment was 27.4 lb.in./in. width (refer Section 6.1) but the cracking moments 17.1 and 37.6 lb.in./in. width were tried because they represent two extreme values that could occur.

To summarise this section, we have shown that moment-curvature curves can be developed for slabs or shells whilst including many variables. At the same time there is an obvious deficiency in experimental knowledge on the bond stress variation and also a reliable determination of the

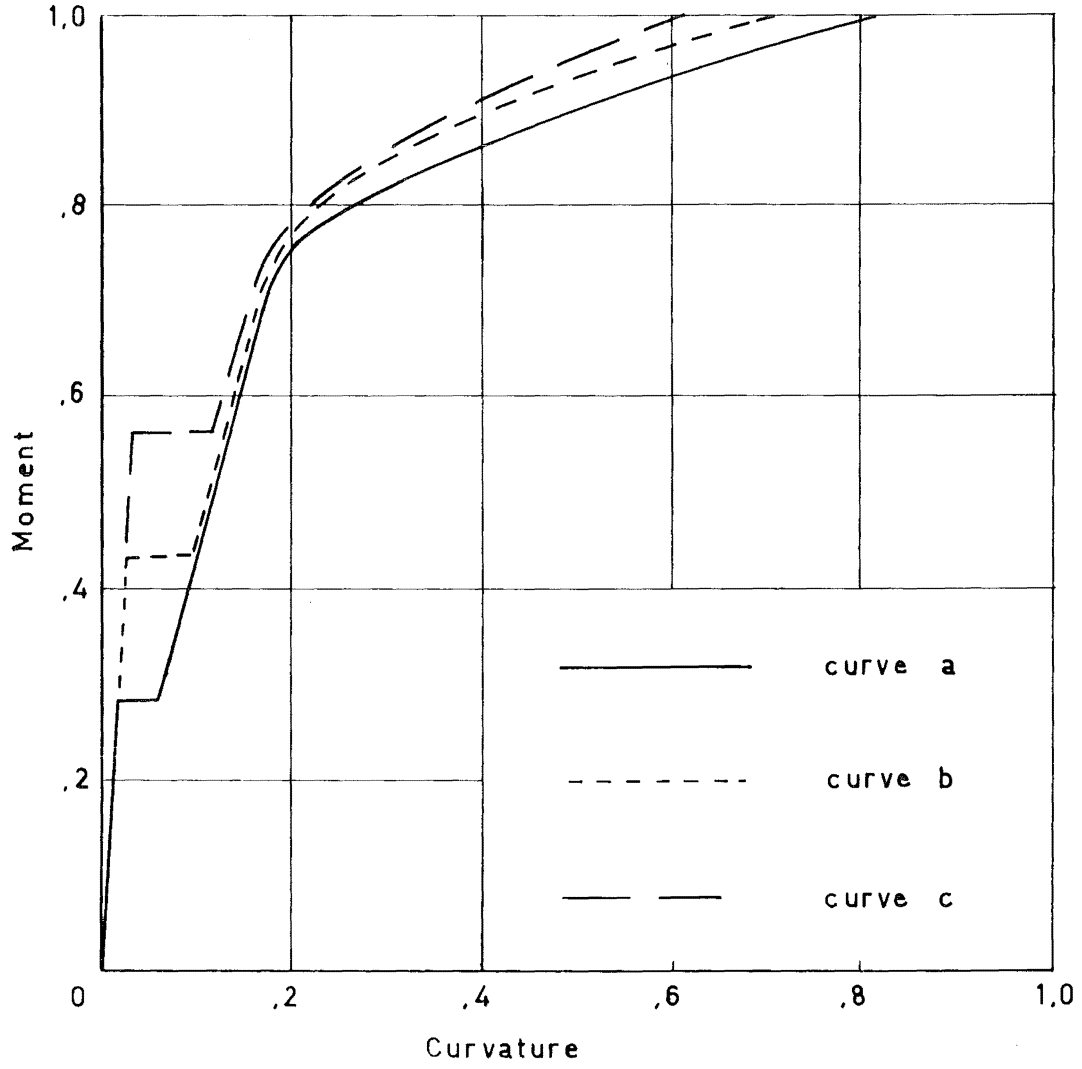

Fig. 4.18. Moment-Curvature Curves

maximum tensile stress that a reinforced concrete section can take when subjected to bending stresses.

The effect of using these different moment-curvature relationships is shown in an example in Section 6.2.

4.6 Method of Solution

Early methods of solving inelastic structures used either the step by step method or the method of successive approximations. Nowadays, however, many analyses utilize both these methods.

In the step by step method the behaviour of an inelastic structure is approximated to the behaviour of a series of elastic structures each subjected to a load increment $\{\Delta R\}$ and whose stiffness is determined from the stress state at the end of the previous load increment, i.e.

$$\{\Delta R_n\} = [K_n]\{\Delta r_n\} \qquad (4.32)$$

where, for the n^{th} load increment, $\{\Delta R_n\}$ is the load increment vector, $[K_n]$ is the complete stiffness matrix, and $\{\Delta r_n\}$ is the displacement increment vector. The total displacements are

$$\{r_n\} = \{r_{n-1}\} + \{\Delta r_n\} \qquad (4.33)$$

where $\{r_n\}$ is the displacement vector at the end of the n^{th} load increment, and $\{r_{n-1}\}$ is the displacement vector at the end of the n-1 load increment.

A typical load-displacement relationship for any point,

using the step by step method, is shown in Fig. 4.19. This figure illustrates a disadvantage of the step by step method; because the stiffness matrix for each load increment is determined from the stress state at the end of the previous load increment, the simulated structure becomes increasingly stiffer compared with its prototype. This error can be overcome by using the "partial stiffness" concept of Marcal and King[55] whereby elements that are elastic at the beginning of a load increment and plastic at the end of the increment are given a "partial stiffness" which is less than the elastic stiffness but greater than the plastic stiffness. The analysis is repeated using these "partial stiffnesses" until a stable situation arises. Thus the solution utilizes both a step by step method and a form of successive approximations.

A major disadvantage of most inelastic analyses is that, for each load increment, the structure must be completely analysed and this can become very time consuming for a complete analysis. There are two exceptions to this; for problems where an inelastic element stiffness matrix is proportional to its elastic stiffness matrix we can retain the elastic stiffness matrix and account for the inelasticity by increasing the element loading system, i.e. for an inelastic element

$$\{R\} = [k']\{r\} \tag{4.34}$$

where $[k']$ is an inelastic element stiffness matrix and

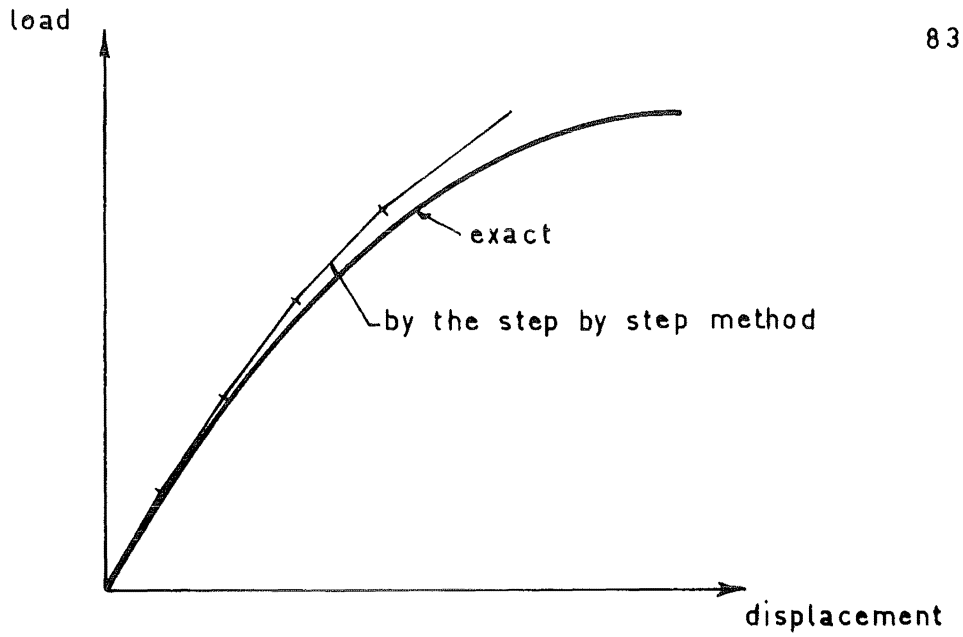

Fig. 4.19. Load-Displacement Relationship using the Step by Step Method

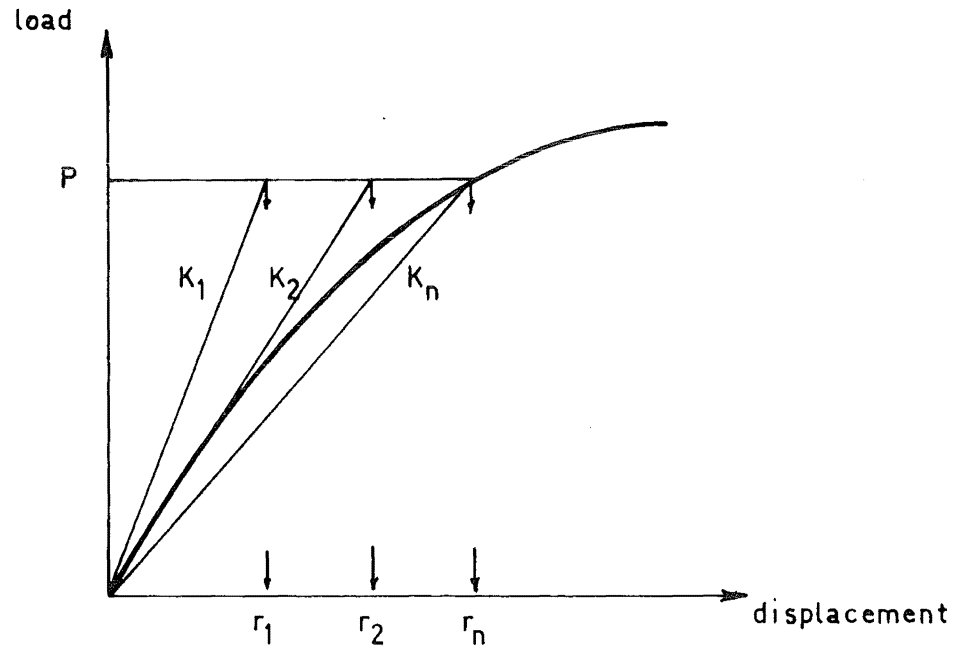

Fig. 4.20. Load-Displacement Relationship using the Method of Successive Approximations

$[k'] = [\alpha][k]$ where $[k]$ is the elastic element stiffness matrix, and $[\alpha]$ is a diagonal matrix. We can form the same displacement system by

$$[\alpha^{-1}]\{R\} = [k]\{r\} \tag{4.35}$$

and therefore the inelastic history of a structure can be followed by re-forming the applied load at each step. Unfortunately not many materials behave in this manner and therefore the method is rather limited.

Another method of reducing the time of analysis is to use an iterative solution; but as the inelastic effects propagate the stiffness matrix becomes increasingly ill-conditioned and an iterative solution is not always very efficient. This is especially so for plate bending problems which are never as well-conditioned as plane stress problems.

The method of successive approximations is best if only one load case is required. The equilibrium position of a structure is determined by successively solving the equation

$$\{Q\} = [K_{n-1}]\{q_n\} \tag{4.36}$$

where $\{Q\}$ is the force vector, $[K_{n-1}]$ is the complete stiffness calculated from cycle n-1, and $\{q_n\}$ is the displacement vector at cycle n. Having obtained the displacements the stress system can be determined and hence, if the inelastic region has altered, the complete stiffness matrix can be suitably changed. Fig. 4.20 illustrates a typical load-displacement relationship, for any point, using the method of

successive approximations. Wilson[77] notes that, in general, there is no guarantee that this method will converge to the true solution. For a progressively degrading force-displacement relationship, however, the displacement at any point will always be a lower bound and will therefore converge monotonically to the true displacement.

Originally it was decided to base the method of analysis upon the method of successive approximations but to include the ability to increment the load system at the operator's request. For any given loading system the stress redistribution is accounted for using the "initial-stress" method described by Zienkiewicz, Valliapan and King[57].

The program execution can be summarised below.

a) the loading system is either read into the computer or determined from an existing load system (i.e. if the load is being incremented). For the applied load, and assuming elastic behaviour throughout the increment, both the displacement system and the principal stress system are determined.

b) If any inelastic regions have propagated within this load increment the structural stiffness matrix is appropriately altered. This new structural model is held in the existing displacement system with the aid of 'restraining forces' acting at the nodal points.

c) Forces that are equal in magnitude and opposite in direction to the 'restraining forces' are applied at the nodal points and new displacement and stress systems are determined.

d) If the inelastic effects have propagated steps (b) and (c) are repeated. When the structural model is stable the program either terminates or a new load increment is applied depending on the will of the operator.

The program's method of analysis effectively reanalyses the structure at each cycle and the operator has no opportunity to alter any of the results. For example, in the middle of the analysis the operator may wish to change the mesh layout so that a region of high stress can be accounted for. Many occasions occurred when such changes were desirable and these are stated in the analyses contained in Part III of this thesis. For this reason the above method of analysis was discarded and a different method used. The second program execution is summarised below.

a) The loading system is read into the computer and, assuming elastic behaviour, both the displacement system and the principal stress system are determined.

b) The conditions of anisotropy of each element are determined, i.e. two moduli of elasticity, the angles that they make with the x-axis, and one value of Poisson's ratio (refer Section 4.4 for the element analysis). These values are punched onto cards and serve as part of the program data for the next cycle.

c) Steps (a) and (b) are repeated until the inelastic region is stable.

This method is quite simple insofar as it utilizes a normal elastic analysis and one additional phase is included to determine the element conditions.

No matter which method of analysis is used there are two possible methods of representing the inelastic regions:

a) to form a mesh at each step so that all the elements are either totally elastic or totally inelastic, and

b) to retain the same mesh throughout the analysis and to develop a finite element containing both elastic and inelastic regions.

If the first method is used then the finite elements are formed as anisotropic elements (refer Section 4.4). The development and limitations of finite elements which contain both elastic and inelastic regions (which we shall subsequently call elastic/inelastic finite elements) are studied in the following chapter.

C H A P T E R 5

ELASTIC/INELASTIC FINITE ELEMENTS

It would be advantageous to have a finite element that is capable of containing both elastic and inelastic regions because this would remove the necessity of having to use a mesh which contained wholly elastic or wholly inelastic finite elements; a difficult task which necessitates the use of a large number of small elements within the zones of cracking and yielding. Hence, the use of elastic/inelastic elements would enable a uniform mesh to be used, larger structures to be analysed (because we would not need to have small elements in the regions where high stresses were expected), and operator interaction would be reduced to a minimum (because we would not have to adjust the cracking boundary to ensure that elements were either cracked or uncracked).

A cubic displacement plate bending element will have a linear variation of moment over its area, and a quadratic-strain plane-stress element will have a linear variation of axial force (per unit width); therefore, considering the case of one portion of the element being elastic, and the other portion inelastic, a line can be drawn from two sides of the element separating these regions (Fig. 5.1). Alternatively, the element may be totally inelastic and the stiffness of any section will be dependent upon the moment at the section.

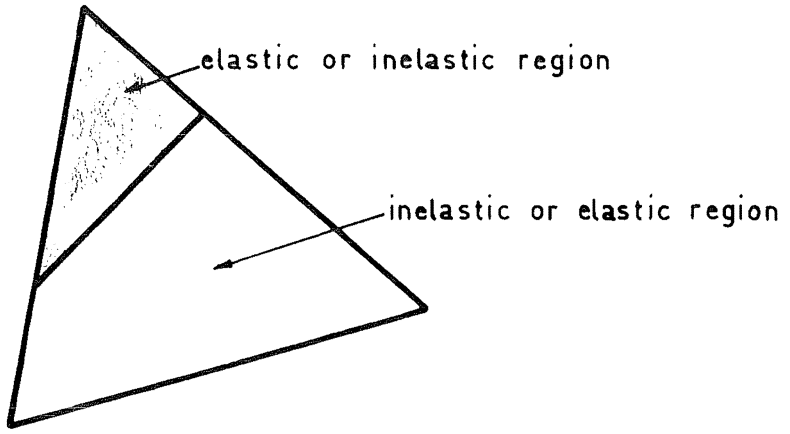

Fig. 5.1. Elastic/Inelastic Finite Element

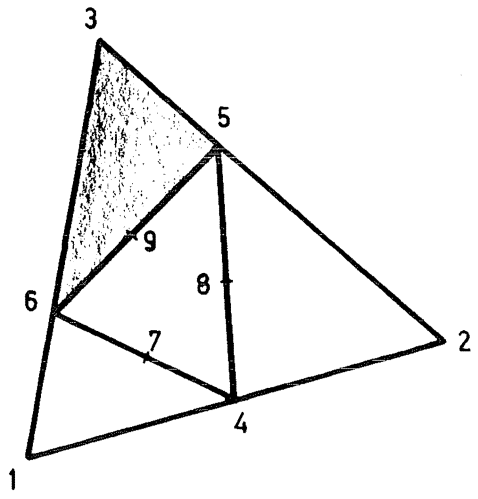

Fig. 5.2. Triangular Finite Element Divided into Four Subelements

Both of these possibilities lead to a finite element comprising elastic and/or inelastic regions. The following sections consider the formation of such elements and their merits and demerits.

5.1 Elastic/Inelastic Plate Bending Finite Element Formed by a Beam Analogy

Consider a triangular element 1-2-3 which contains both an elastic and an inelastic region. If the points of intersection of the line that separates the two regions and the element sides are taken as nodal points (say, points 5 and 6 in Fig. 5.2) and on the remaining side a nodal point is placed at the midside, then the element can be divided into four subelements as shown in Fig. 5.2.

The stiffness of each subelement can be determined (refer Section 4.4) and we can write the basic stiffness equation for the whole element as

$$\begin{Bmatrix} R_c \\ R_s \\ R_i \end{Bmatrix} = \begin{bmatrix} k_{cc} & k_{cs} & k_{ci} \\ k_{sc} & k_{ss} & k_{si} \\ k_{ic} & k_{is} & k_{ii} \end{bmatrix} \begin{Bmatrix} r_c \\ r_s \\ r_i \end{Bmatrix} \qquad (5.1)$$

where the terms of this matrix equation represent submatrices whose sizes are determined by their subscripts, i.e.

the subscript "c" refers to the corner nodes 1, 2 and 3,

the subscript "s" refers to the side nodes 4, 5 and 6, and

the subscript "i" refers to the interior nodes 7, 8 and 9.

(The corner and side nodes have one translational and two rotational degrees of freedom but the interior nodes have only one rotational degree of freedom.)

The strain energy of the element is

$$U = \tfrac{1}{2}\begin{Bmatrix} r_c \\ r_s \\ r_i \end{Bmatrix}^T \begin{bmatrix} k_{cc} & k_{cs} & k_{ci} \\ k_{sc} & k_{ss} & k_{si} \\ k_{ic} & k_{is} & k_{ii} \end{bmatrix} \begin{Bmatrix} r_c \\ r_s \\ r_i \end{Bmatrix} . \tag{5.2}$$

A connective matrix [E] was constructed so that the displacements of the side nodes 4, 5, and 6 could be related to the displacements of the corner nodes 1, 2, and 3, i.e.

$$\{r_s\} = [E]\{r_c\} \tag{5.3}$$

and substituting into Eq. (5.2) we obtain

$$U = \tfrac{1}{2}\begin{Bmatrix} r_c \\ r_i \end{Bmatrix}^T [\bar{k}] \begin{Bmatrix} r_c \\ r_i \end{Bmatrix} \tag{5.4}$$

where

$$[\bar{k}] = \left[\begin{array}{c|c} k_{cc} + k_{cs}E + E^T k_{sc} + E^T k_{ss}E & k_{ci} + E^T k_{si} \\ \hline k_{ic} + k_{is}E & k_{ii} \end{array}\right] .$$

The basic element stiffness equation is now

$$\begin{Bmatrix} R_c \\ R_i \end{Bmatrix} = [\bar{k}] \begin{Bmatrix} r_c \\ r_i \end{Bmatrix} \tag{5.5}$$

and this can be further reduced by condensing out the interior nodes. Thus

$$\{R_c\} = [k]\{r_c\} \tag{5.6}$$

where

$$[k] = [k_{cc} + k_{cs}E + E^T k_{sc} + E^T k_{ss}E - (k_{ci} + E^T k_{si})k_{ii}^{-1}(k_{ic} + k_{is}E)]$$

and the stiffness matrix [k] relates the forces at the corner nodes to the displacements at the corner nodes.

From a computational viewpoint it is best to take each subelement in turn and eliminate the side nodes. Hence the stiffness matrix $[\bar{k}]$ of Eq. (5.4) is formed as the sum of the contributions from each subelement. Finally, the condensation process can easily be performed by an inverse symmetric Gaussian elimination upon the bottom three rows.

Before constructing the connective matrix we note that, for the plate bending element described in Appendix A, the displacement of any point p on side i-j and distance s from node i (Fig. 5.3a) is

$$\begin{aligned} w_p &= w_i(1-3x^2+2x^3) + w_j(3x^2-2x^3) \\ &\quad + \ell\theta_{ni}(-x+2x^2-x^3) + \ell\theta_{nj}(x^2-x^3), \\ \theta_{sp} &= \left(\frac{\partial w}{\partial n}\right)_p \\ &= \theta_{si}(1-x) + \theta_{sj}(x), \end{aligned} \tag{5.7}$$

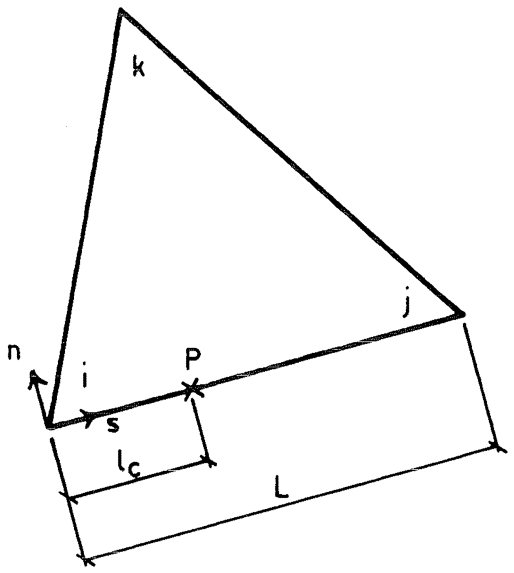

a

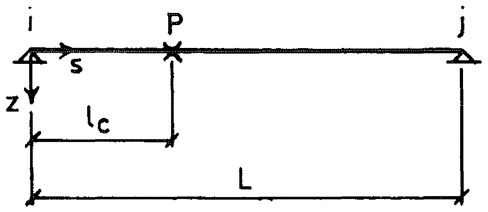

b

Fig. 5.3. Finite Element and an Equivalent Beam for Side i-j

$$\theta_{np} = \left(-\frac{\partial w}{\partial s}\right)_p$$

$$= \frac{6}{\ell}(w_1 - w_2)(x - x^2) + \theta_{ni}(1 - 4x + 3x^2) + \theta_{nj}(-2x + 3x^2),$$

where ℓ is the length of side i-j, and $x = s/\ell$, and these equations are identical to those for a beam whose length is the same as the element side i-j (Fig. 5.3b).

For an elastic/inelastic finite element either one or three subtriangles will be inelastic. Within the inelastic region, although the stiffness will vary as the moment varies, it is assumed that each subtriangle will have a constant stiffness which is determined by averaging the stiffnesses at the subtriangle nodes. The error incurred due to this approximation will be small because, in general, an elastic/inelastic element will not contain yielded regions, and the variation in stiffness within cracked regions is not very large. Yielded regions will normally occur in a totally inelastic element and in this case there are two possible methods of determining the side nodes. The first is to form the subelements by taking the additional nodal points at the midsides, while alternatively the yielded region can be separated from the cracked region and subtriangles formed in a similar manner to the partially elastic and partially inelastic case described above. In either case the stiffnesses of the subelements are taken to be constant. Hence, we require the connective matrix to relate the displacement of a side node p to the

displacements of the corner nodes i and j given that the stiffness of the element from i to p is E_1 and the stiffness from p to j is E_2. This problem can be solved using the moment-area method on the equivalent beam, such that the length of the beam equals the length of the side i-j, and the stiffness of the beam from i to p is E_1 and the stiffness from p to j is E_2. Thus, the displacements of each side node can be related within an intermediate coordinate system n-s-z to the displacements of the corner nodes, and after these have been transformed to the common coordinate system x-y-z, the connective matrix [E] of Eq. (5.3) can be formed. (A fuller description of this method is given in Appendix C.)

The construction of this elastic/inelastic finite element illustrates an inherent error of the displacement model which can be increased when the element is partially inelastic; namely that the displacement of the node p on side i-j, given in Eqs (5.7), is independent of the position of the third corner node k. (From consideration of symmetry the best finite elements will be formed by equilateral triangles - refer Section 3.1.) This error can be accentuated when cracking occurs because:

a) the displacement of node p is independent of the position of both the third corner node and the other side nodes,

b) the subtriangles will sometimes contain large differences in their flexural rigidities, and

c) inelastic regions occur randomly and therefore extremely tapered elements can be formed.

Nothing can be done about the first two errors because compatibility of edge displacements necessitates that side nodes are dependent only upon the corner nodes that are on the same side. The third possible error, however, can be guarded against by imposing limits upon the position of the side nodes, and thus preventing very tapered elements from being formed.

One advantage of this method is that if an elastic element is formed then, because of the additional interior degrees of freedom, the stiffness matrix will be more accurate than the normal element stiffness matrix. If, however, we had constrained these interior degrees of freedom by relating their displacements to those of the corner nodes then the stiffness matrices would be identical. This advantage will remain with an elastic/inelastic element but it may be negated by the disadvantages mentioned above.

A simple comparison of this elastic/inelastic element and an equivalent four-element structure was studied. The sub-elements of the elastic/inelastic element form the elements of the four-element structure and hence the effect of constraining the side displacements of the elastic/inelastic element can be observed. The element configuration is shown in Fig. 5.4 together with the coordinates of the fixed nodes. The flexural rigidity of triangle 3-6-5 was one tenth the

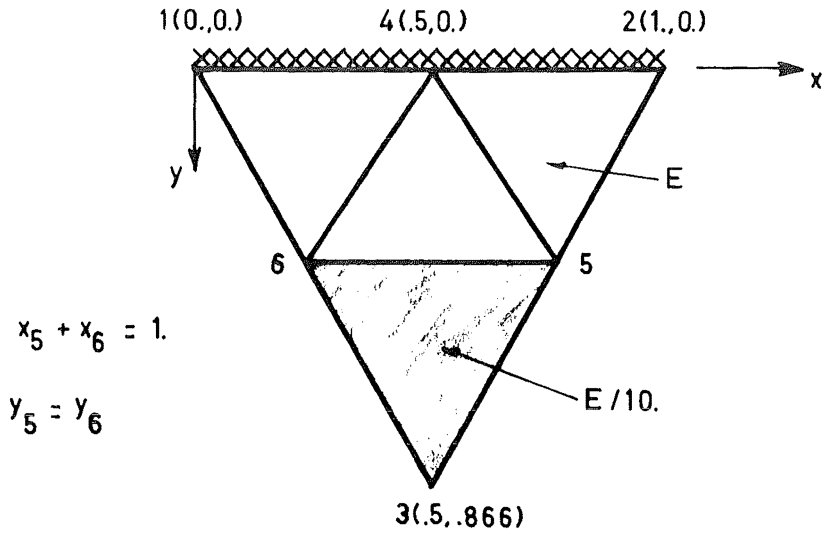

Fig. 5.4. Elastic / Inelastic Finite Element and an Equivalent Four Element Structure

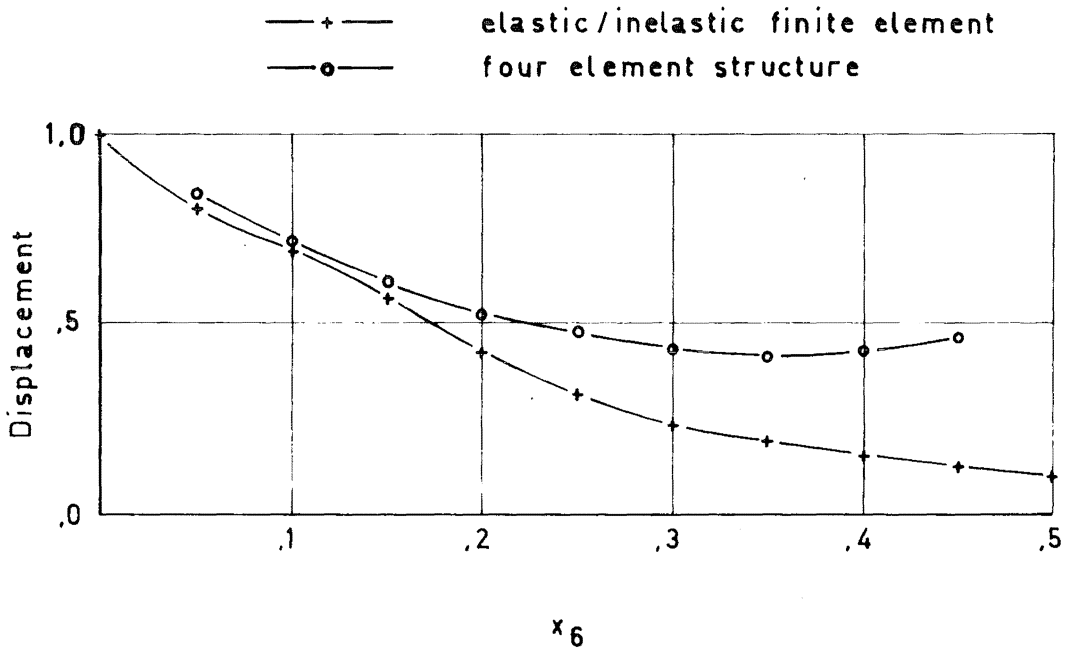

Fig. 5.5. Displacement Profile of Node 3

flexural rigidity of the other triangles, and it is assumed that the side 1-2 is fixed and that node 3 may displace but not rotate. The displacement of node 3 is shown in Fig. 5.5 for different positions of the line 5-6 (which moves parallel to the fixed edge 1-2).

For the four element structure the limiting values, as x_6 tends to either 0 or 0.5, are not very accurate because the structure contains some very tapered elements at these values. The elastic/inelastic element appears to have quite a smooth curve and all the points lie within the values of a totally cracked and a totally uncracked element.

Another example was studied; it consisted of a simply supported beam containing a uniformly distributed load which caused the middle portion of the beam to crack. This beam was analysed, firstly by making the crack boundary coincide with an element boundary and hence having totally cracked or totally uncracked elements, and secondly, when the crack boundary did not coincide with the element boundaries elastic/inelastic elements were used. The displacements (normalised to 1) from this analysis are shown in Fig. 5.6 and we see that the elastic/inelastic analysis produces a slightly stiffer structure but the results are quite acceptable.

Further examples using this elastic/inelastic element are given in Section 7.3.

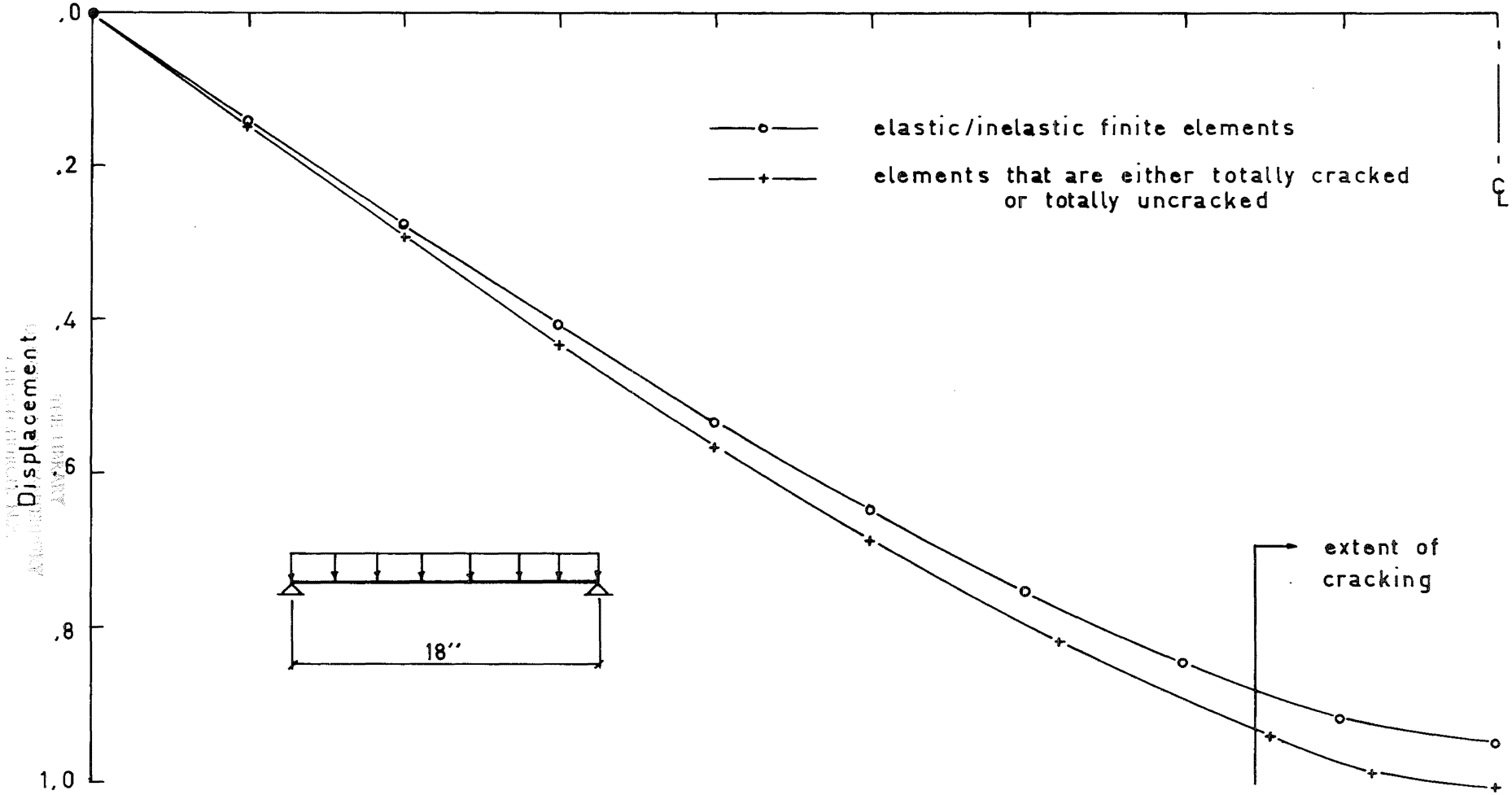

Fig. 5.6. Displacement Profiles of a Cracked Beam

5.2 Elastic/Inelastic Plate Bending Finite Element Formed by "Integrating by Parts".

The elastic/inelastic finite element formed by a beam analogy contained the defect that tapered elements could occur and thus distort the resulting stiffness matrix. To overcome this problem a new element was formed by "integrating by parts"; in effect the strain energy of the plate bending finite element, given in Eq. (1.15), is summed over the elastic/inelastic element, i.e.

$$U = \tfrac{1}{2} \int_A \tilde{M}^T \tilde{\chi} dA$$

$$= \tfrac{1}{2} \int_{A_1} \tilde{M}^T \tilde{\chi} dA + \tfrac{1}{2} \int_{A_2} \tilde{M}^T \tilde{\chi} dA + \cdots + \tfrac{1}{2} \int_{A_n} \tilde{M}^T \tilde{\chi} dA \quad (5.8)$$

where $A_1, A_2, \cdots, A_n$ are distinct areas within the element and $A_1 + A_2 + \cdots + A_n = A$ is the area of the whole element. The evaluation of Eq. (5.8) yields

$$U = \tfrac{1}{2}\{\chi\}^T ([N_1] + [N_2] + \cdots + [N_n])\{\chi\} \quad (5.9)$$

where $\{\chi\}$ is the nodal curvature vector, and $[N] = [N_1] + [N_2] + \cdots + [N_n]$ is the nodal curvature stiffness matrix. Each element of the nodal curvature stiffness matrix can be expressed as

$$[N_i] = \int_{A_i} [\psi]\,[C_i]\,[\psi]^T \, dA_i$$

and if the constitutive matrix is constant within the subarea A_i it can be taken outside the integral because the

matrix $[\psi]$ comprises diagonal submatrices of the same order as $[C_i]$, i.e.

$$[N_i] = [D_i] \int_{A_i} [\psi][\psi]^T \, dA \qquad (5.10)$$

where $[D_i]$ contains a diagonal of submatrices of $[C_i]$.

Because the plate bending finite element used within this thesis is formed from three subelements (refer Appendix A) the integrations must be performed over each subelement. Furthermore, because of the difficulty of integrating in triangular coordinates over a partial area, a numerical integration was used. Appendix D contains details of how the plate bending finite element was divided and also how the numerical integration was performed.

As it stands, however, this new finite element will be too stiff because, even though the variation in material property can be incorporated, the curvature distribution over the structure is constrained to a linear variation (i.e. the displacement distribution is cubic). For elements that are almost totally elastic, however, the error will be small. To determine the extent of the error the examples described in Section 5.1 were repeated using this elastic/inelastic element. The results of the four-element structure example are shown in Fig. 5.7 and we can see immediately that the elastic/inelastic element is very stiff and does not accurately depict an element containing both elastic and inelastic regions. The displacement is only represented

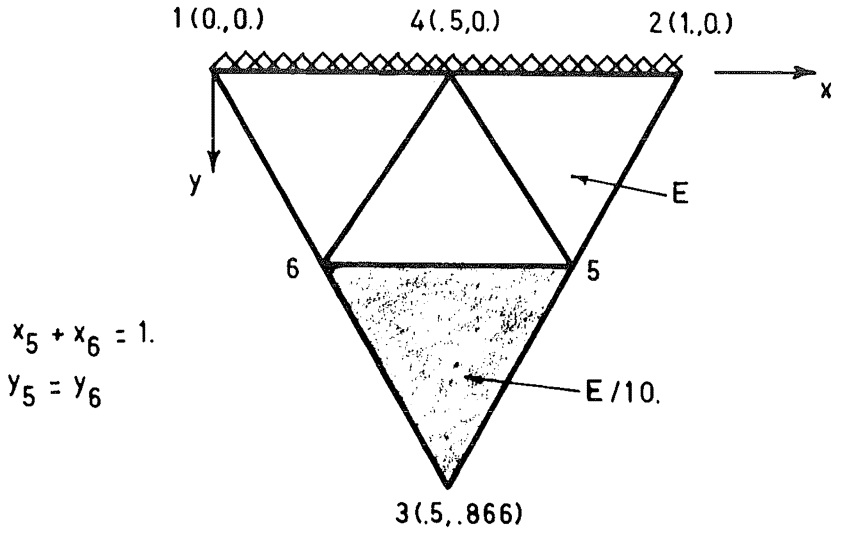

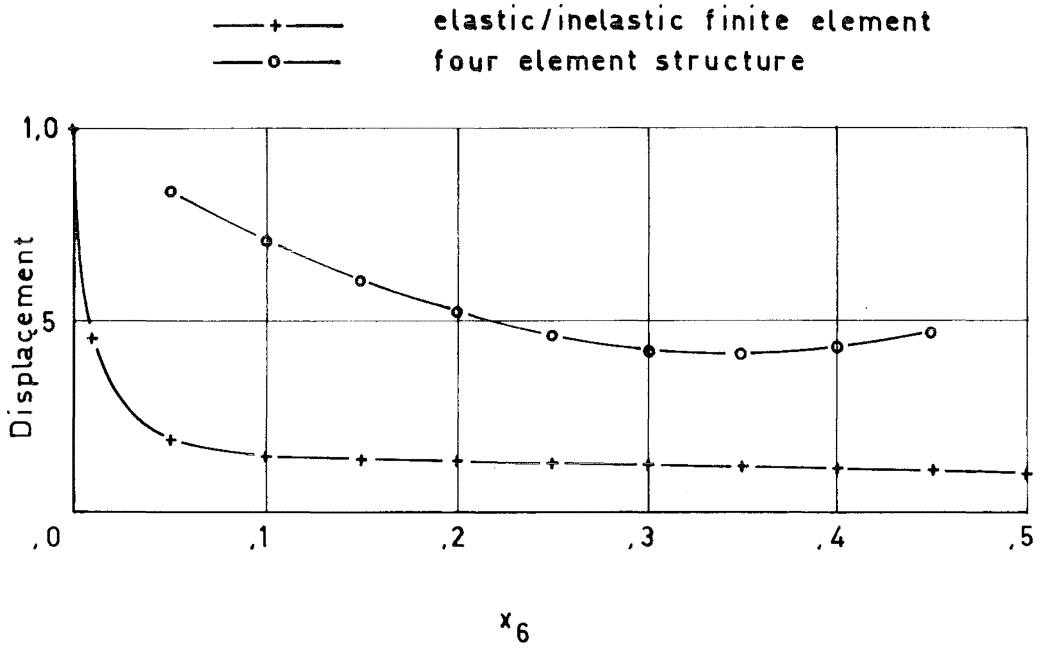

Fig. 5.7. Displacement Profile of Node 3

accurately close to the two limits and in between these limits the stiffness variation is small. The results of the beam example are shown in Fig. 5.8 and again the displacement profile for the elastic/inelastic element is very stiff.

An investigation of the elastic/inelastic element stiffness matrix showed that, upon cracking, the stiffness coefficients on the diagonal had been reduced but a few of the stiffness coefficients off the diagonal were increased (in the above examples the coefficients depicting twisting of the element had increased). The only method of improving this element would be to construct a non-linear interpolation vector and reconstruct the element stiffness matrix according to the method described in Appendix A - an extremely formidable task.

A further example of this elastic/inelastic element is given in Section 7.3.

5.3 Elastic/Inelastic Plane Stress Finite Elements

In Section 7.3 analyses using the elastic/inelastic plate bending elements described in Sections 5.1 and 5.2 indicated that these elements, in their present form, did not give as accurate results as analyses which used elements that were either totally cracked or totally uncracked. For this reason no elastic/inelastic plane stress elements were formed. However, the theoretical development of such elements according to the methods described in the previous

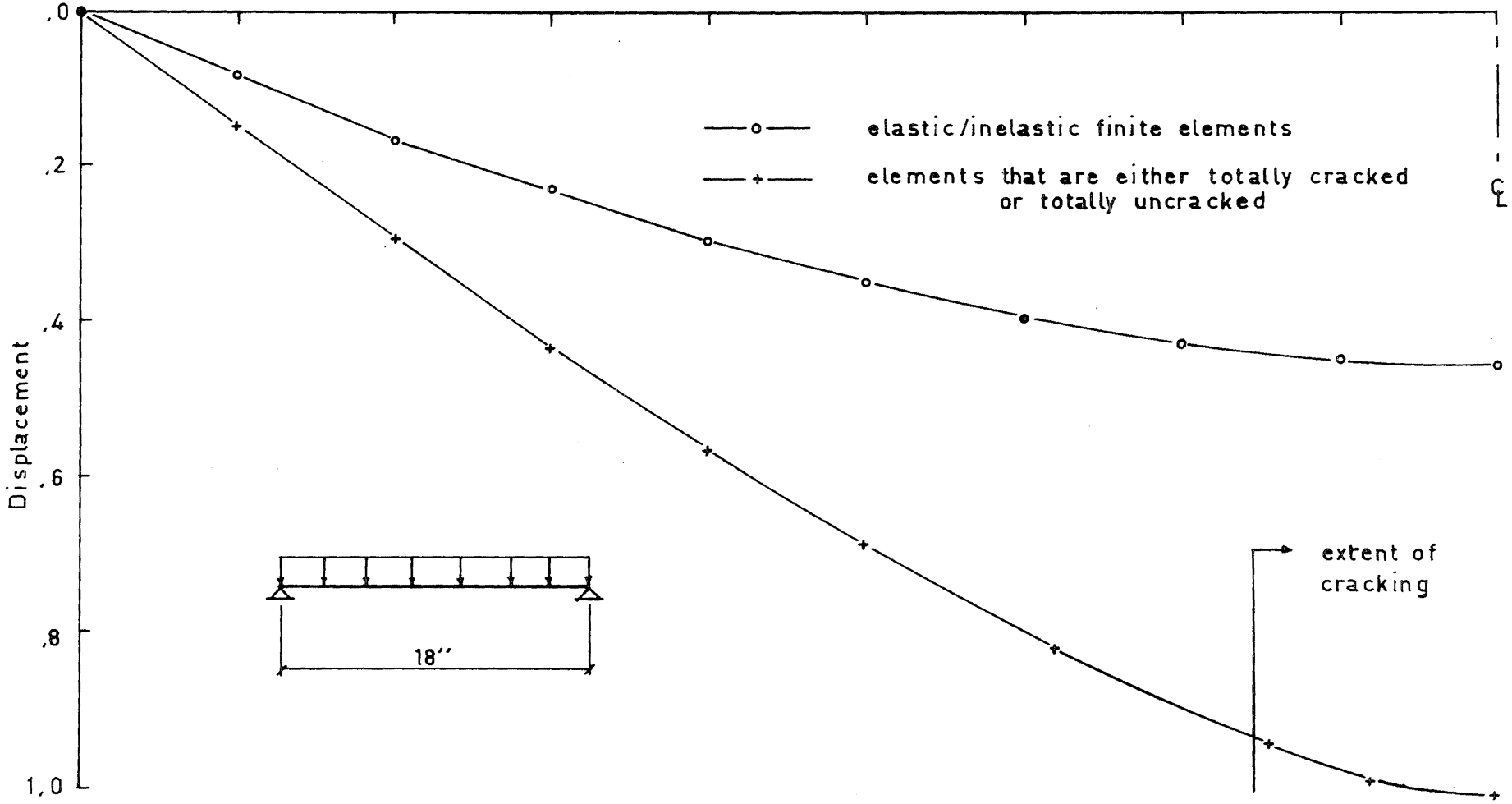

Fig. 5.8. Displacement Profiles of a Cracked Beam

two sections is not complex and will be briefly discussed below.

Because the axial force variation within each element is linear an elastic/inelastic plane stress finite element that is formed by a beam analogy will have the subelement layout as shown in Fig. 5.9. The development of the elastic/inelastic element is identical to that in Section 5.1 except that some of the subscripts have a different meaning. The basic stiffness matrix for the whole element is

$$\begin{Bmatrix} R_c \\ R_s \\ R_i \end{Bmatrix} = \begin{bmatrix} k_{cc} & k_{cs} & k_{ci} \\ k_{sc} & k_{ss} & k_{si} \\ k_{ic} & k_{is} & k_{ii} \end{bmatrix} \begin{Bmatrix} r_c \\ r_s \\ r_i \end{Bmatrix} \qquad (5.9)$$

where the elements of this matrix equation represent submatrices whose size is determined by their subscripts, i.e.

the subscript "c" refers to the corner nodes 1, 2, and 3,

the subscript "s" refers to the side nodes 4, 5, and 6, and

the subscript "i" refers to the subelement centroidal nodes 7, 8, 9, and 10.

(The corner and side nodes have one translational degree of freedom and two degrees of freedom from the x and y derivatives of the translation. The centroidal nodes, however, have only one translational degree of freedom.)

The strain energy of the element is

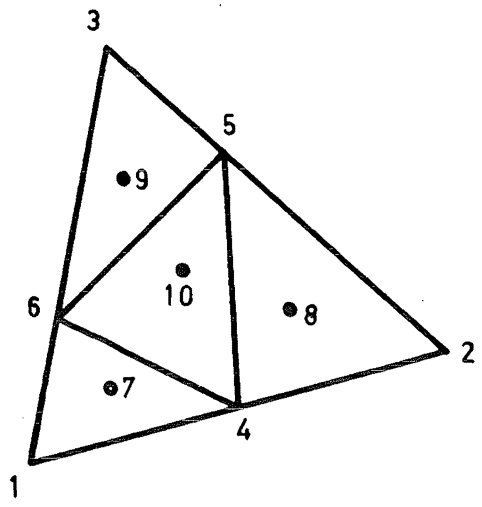

Fig. 5.9. Triangular Plane Stress Finite Element Divided into Four Subelements

$$U = \tfrac{1}{2} \begin{Bmatrix} r_c \\ r_s \\ r_i \end{Bmatrix}^T \begin{bmatrix} k_{cc} & k_{cs} & k_{ci} \\ k_{sc} & k_{ss} & k_{si} \\ k_{ic} & k_{is} & k_{ii} \end{bmatrix} \begin{Bmatrix} r_c \\ r_s \\ r_i \end{Bmatrix} . \qquad (5.10)$$

A connective matrix [E] could be constructed so that the displacements of the side nodes 4, 5, and 6 would be related to the displacements of the corner nodes 1, 2, and 3, i.e.

$$\{r_s\} = [E] \{r_c\} \qquad (5.11)$$

and substituting into Eq. (5.10) we obtain

$$U = \tfrac{1}{2} \begin{Bmatrix} r_c \\ r_i \end{Bmatrix}^T [\bar{k}] \begin{Bmatrix} r_c \\ r_i \end{Bmatrix} \qquad (5.12)$$

where

$$\bar{k} = \left[\begin{array}{c|c} k_{cc} + k_{cs}E + E^T k_{sc} + E^T k_{ss} E & k_{ci} + E^T k_{si} \\ \hline k_{ic} + k_{is}E & k_{ii} \end{array}\right]$$

The basic element stiffness equation is now

$$\begin{Bmatrix} R_c \\ R_i \end{Bmatrix} = [\bar{k}] \begin{Bmatrix} r_c \\ r_i \end{Bmatrix} \qquad (5.13)$$

and this can be further reduced by condensing out the centroidal nodes. Thus

$$\{R_c\} = [k] \{r_c\} \qquad (5.14)$$

where

$$[k] = [k_{cc} + k_{cs}E + E^T k_{sc} + E^T k_{ss} E - (k_{ci} + E^T k_{si})\, k_{ii}^{-1}\, (k_{ic} + k_{is}E)]\,.$$

Because the in-plane displacements have a cubic variation and its derivatives have a quadratic variation the simplest connective matrix will utilise a similar connective matrix to that used for the plate bending element (derived in Appendix C). The physical analogy for this relationship is still a beam with a transverse displacement as used in Section 5.1.

An elastic/inelastic plane stress finite element formed by "integrating by parts" follows a similar pattern to that of the plate bending element formed in Section 5.2. The strain energy of a plane stress element is summed over the elastic/inelastic finite element, i.e.

$$U = \tfrac{1}{2}h \int_A \tilde{\sigma}^T \tilde{\varepsilon}\, dA \qquad (5.15)$$

$$= \tfrac{1}{2}h \int_{A_1} \tilde{\sigma}^T \tilde{\varepsilon}\, dA_1 + \tfrac{1}{2}h \int_{A_2} \tilde{\sigma}^T \tilde{\varepsilon}\, dA_2 + \cdots + \tfrac{1}{2}h \int_{A_n} \tilde{\sigma}^T \tilde{\varepsilon}\, dA_n$$

where $\tilde{\sigma}$ is the stress at any point, $\tilde{\varepsilon}$ is the strain at any point and A_1, A_2, $\cdots$ A_n are distinct areas within the finite element such that $A_1 + A_2 + \cdots + A_n = A$, the area of the element.

The evaluation of Eq. (5.15) yields

$$U = \tfrac{1}{2}\{\varepsilon\}^T ([N_1] + [N_2] + \cdots + [N_n])\{\varepsilon\} \qquad (5.16)$$

where $\{\varepsilon\}$ is the nodal strain vector and

$[N] = [N_1] + [N_2] + \cdots + [N_n]$ is the nodal strain stiffness

matrix; and

$$[N_i] = \int_{A_i} [\psi]\ [C]_i [\psi]^T\ dA_i \qquad (5.17)$$

where $[\psi]$ is a quadratic interpolation matrix and $[C]_i$ the constitutive matrix. Hence the stiffness matrix can be formed by summing the stiffness components in each subarea of the element.

This elastic/inelastic finite element would suffer a similar disadvantage to that of its plate bending counterpart because the strain distribution over the element is constrained to a quadratic variation and this will stiffen the element.

PART III: A COMPARISON OF THE THEORY WITH EXISTING EXPERIMENTAL RESULTS

C H A P T E R 6

RECTANGULAR AND L-SHAPED SLABS TESTED BY ISLAM

This chapter describes the analysis and comparison of two reinforced concrete slabs which were tested by Islam[13] at Manchester College of Science in 1964. Islam was making a comparative study of two upper bound methods of analysing yield-line patterns in isotropically reinforced concrete slabs, i.e. the virtual work method and the equilibrium method.

The first section of this chapter describes Islam's two slabs, which were rectangular and L-shaped. It also describes both the properties of the slabs that were given, and the properties that had to be assumed. The free end of the rectangular slab behaves like a simply supported beam and the second section of this chapter commences with some analyses of this beam comparing the effect on the load-deflection curve of varying the moment-curvature relationship which defines the beam behaviour. All the analyses in this chapter employ elements that are either totally cracked or totally uncracked. This is followed by an analysis of the rectangular slab, for two load cases, using a moment-curvature relationship that takes an equivalent-displacement curvature and a rectangular bond stress distribution.

The L-shaped slab is analysed in the third section also using a moment-curvature relationship that takes an equivalent-displacement curvature and a rectangular bond stress distribution. At the end of the chapter there is a summary of the principal results and conclusions which arose from these analyses.

6.1 Slab Information

The rectangular slab was considered first. Fig. 6.1 shows the slab dimensions and its support conditions (the single hatching represents simple support conditions and the remaining boundaries are free). Islam measured the transverse displacement at the points A, B, and C.

Two rectangular slabs were tested and they had identical properties except for the concrete cube strengths which were 1980 lb./sq.in. and 2090 lb./sq.in. The material properties that Islam gave were:

Reinforcement - ½ in. square welded wire mesh S.W.G. 19 (annealed)

Yield stress of the reinforcement = 34,520 lb./sq.in.

Total depth of the slab = 0.75 in.

Effective depth to the reinforcement = 0.54 in.

Concrete cube strength = 1,980 lb./sq.in. (for slab B.3), and 2090 lb./sq.in. (for slab B.4).

Furthermore, in his Appendix E Islam showed a representative load-deflection curve of the reinforcement for each

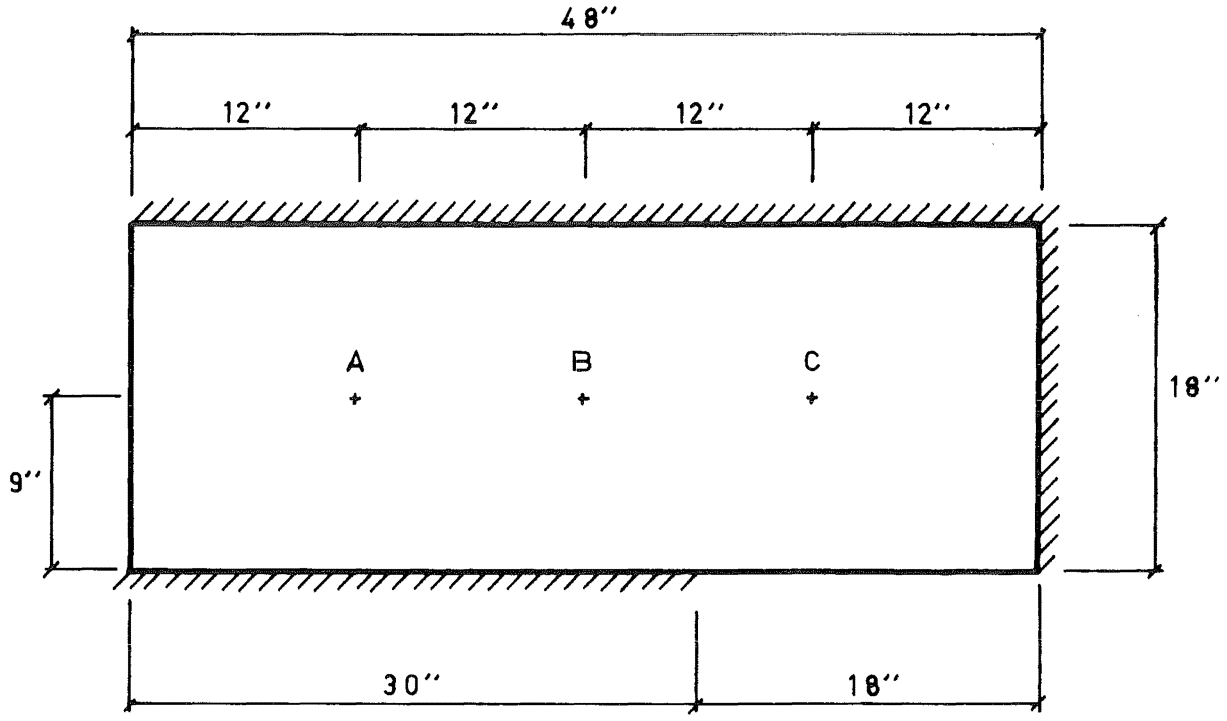

Fig. 6.1. Islam's Rectangular Slab

test. The ultimate force of the reinforcement which was used in slabs B.3 and B.4 was approximately 58.0 lbs (refer to Fig. 6.2) which corresponds to an ultimate stress of 46,000 lb./sq.in. Unfortunately the unit of extension that was used has not been recorded.

To obtain the moment-curvature curves for this slab additional information was required. For the reinforcement two of the following variables were required; the two moduli (the stress-strain curve was very close to being bilinear) and also the yield and ultimate strains. Islam annealed a roll of the reinforcement in a furnace at 860^{o}C for a period of three hours and then it was withdrawn from the furnace and allowed to cool in the atmosphere. Two such rolls were annealed, one of which was used for slabs B.3 and B.4. The yield and ultimate forces for the unannealed and the two annealed rolls are listed in Table 6.1 so as to illustrate the variation in the two annealed samples.

	Yield Force (lbs)	Ultimate Force (lbs)
Not Annealed	76.7	83.0
Annealed Roll 1	55.0	76.0
Annealed Roll 2	43.5	58.0

Table 6.1 Reinforcement Properties

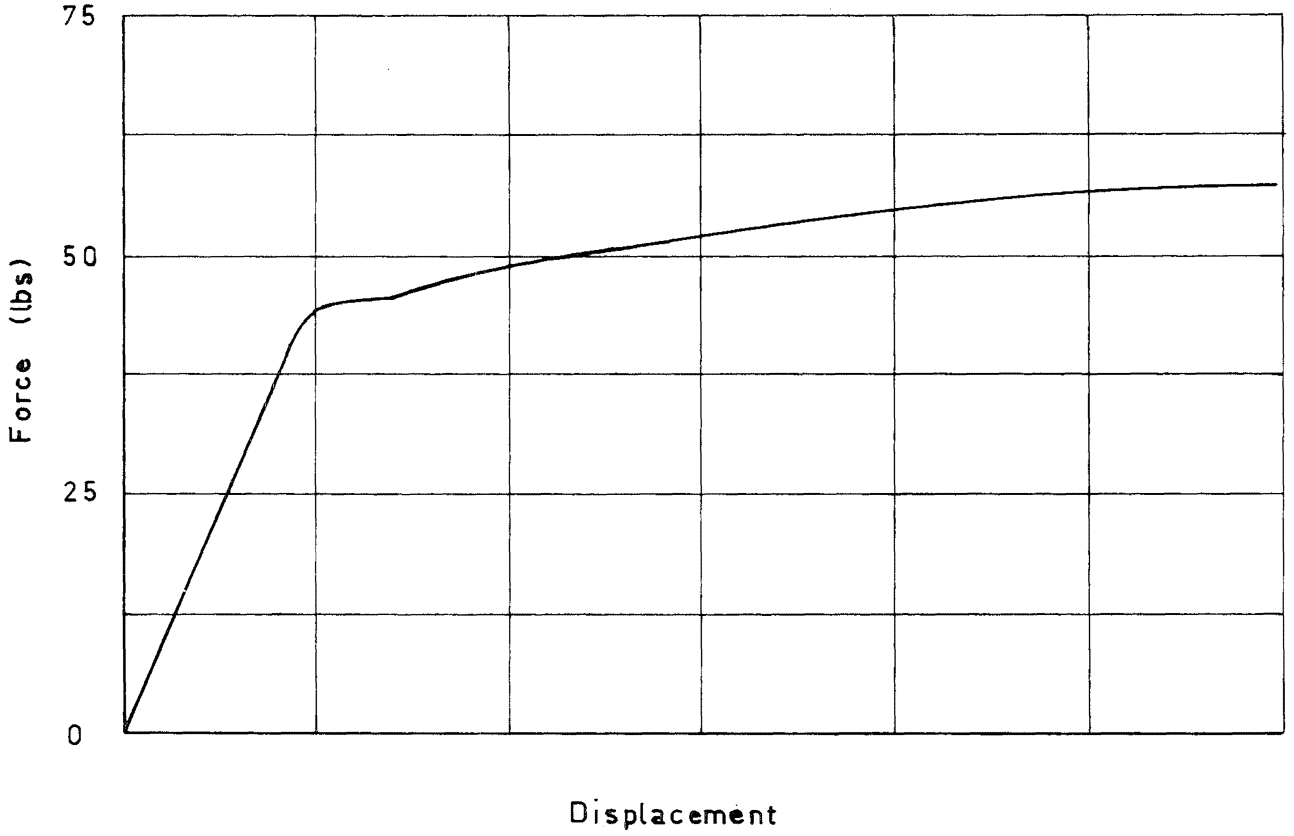

Fig. 6.2. Force-Displacement Relationship for the Reinforcement

It was assumed that the unannealed reinforcement had a modulus of elasticity of 29.0×10^6 lb./sq.in. and hence the modulus of elasticity of the annealed reinforcement is defined as 21.0×10^6 lb./sq.in. and the effective modulus of elasticity after yielding is 1.37×10^6 lb./sq.in.

The crushing stress of the concrete was taken as 0.85 times the average cube strength for the two tests, and hence $f'_c = 1{,}730$ lb./sq.in.

For the concrete stress-strain curve, the strain corresponding to the maximum concrete stress was taken as .002 and the ultimate strain was taken as .0035.

The values of the modulus of elasticity for the mortar was determined by comparing balues found by Magura[78] and assuming that the modulus of elasticity is proportional to the square root of the concrete crushing stress (as for reinforced concrete[75]). Islam used a sand-cement ratio of 3.0 and a water-cement ratio of 0.65. Magura used two different sand gradations and some of his results that are closest to Islam's mix proportions are listed in Table 6.2 together with the modulus of elasticity that would be obtained if the crushing stress was 1730 lb./sq.in. From the results of this table the modulus of elasticity for Islam's rectangular slab was assumed to be 1.5×10^6 lb./sq.in.

Mix No.	Water/cement (wt ratio)	Sand/cement (wt ratio)	f_c' lb./in.^{2}	$E_c \times 10^6$ lb./in.^{2}	$E_c \times 10^6$ if $f_c' = 1730$ lb./in.^{2}
3	.575	2.75	5,270	2.50	1.43
4	.769	3.98	3,250	2.12	1.55
5	1.000	5.25	2,160	1.86	1.67
9	.667	4.08	4,060	2.47	1.61

Table 6.2 Properties of Mortar from Magura

The free end of the rectangular slab deforms like a simply supported beam and therefore, for a given loading on the slab, the moment at the centre of the free edge is approximately known. From the load-deflection curves given by Islam cracking occurred at a total load of 580 lb which corresponds to a moment at the centre of the free edge of 27.4 lb.in./in. Applying this moment to an uncracked section indicated that the ultimate tensile strain was .000178 which corresponds to a maximum tensile stress of 15.4% f_c'.

The L-shaped slab is shown in Fig. 6.3; again the hatching represents a simple support condition and the remaining boundaries are free. Islam measured the transverse displacements at the points A, B, and C.

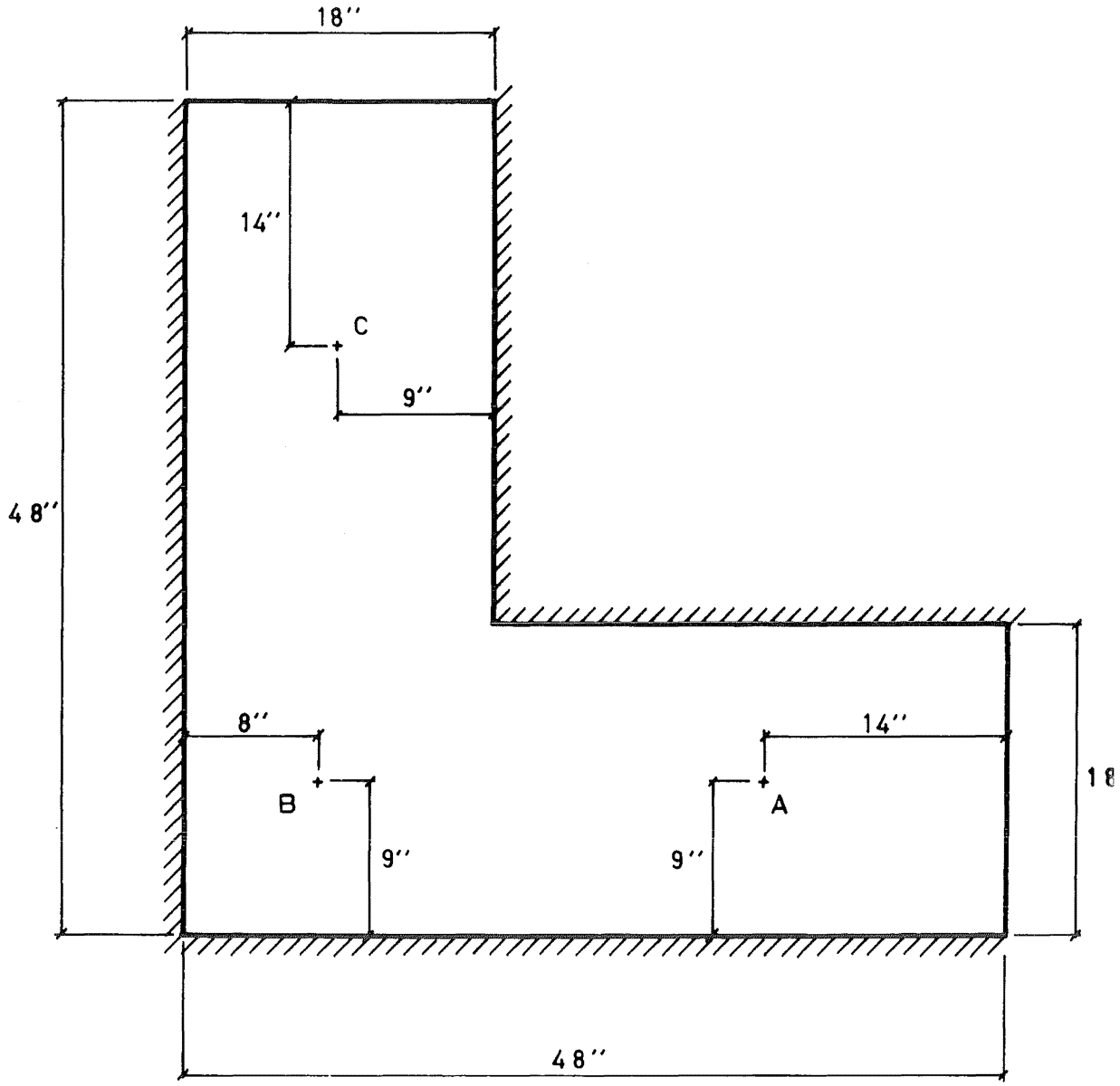

Fig. 6.3. Islam's L-Shaped Slab

The slab properties given by Islam were:

Reinforcement	= ½ in. square welded wire mesh S.W.G.19 (not annealed)
Yield stress of the reinforcement	= 60,850 lb./sq.in.
Total depth of the slab	= .75 in.
Effective depth to the reinforcement	= .58 in.
Concrete cube strength	= 3,660 lb./sq.in.

From the load-deflection curve for the reinforcement (reproduced in Fig. 6.4) the ultimate force of the reinforcement was 83.1 lbs which corresponds to an ultimate stress of 66,500 lb./sq.in. Assuming that the modulus of elasticity for the mesh was 29.0×10^6 lb./sq.in. the ultimate strain, taken from the load-deflection curve, was .00433, and therefore the effective modulus of elasticity after yielding was 2.2×10^6 lb./sq.in.

The crushing stress of the concrete was taken as 0.85 times the cube strength which corresponds to f'_c = 3,110 lb./sq.in. For the concrete stress-strain curve, the strain corresponding to the maximum concrete stress was taken as .002 and the ultimate strain was .0035. The mortar was the same mixture as that for the rectangular slab described above, and from Table 6.2 the modulus of elasticity of mortar corresponding to a crushing strength of 3,110 lb./sq.in. is approximately 2.0×10^6 lb./sq.in.

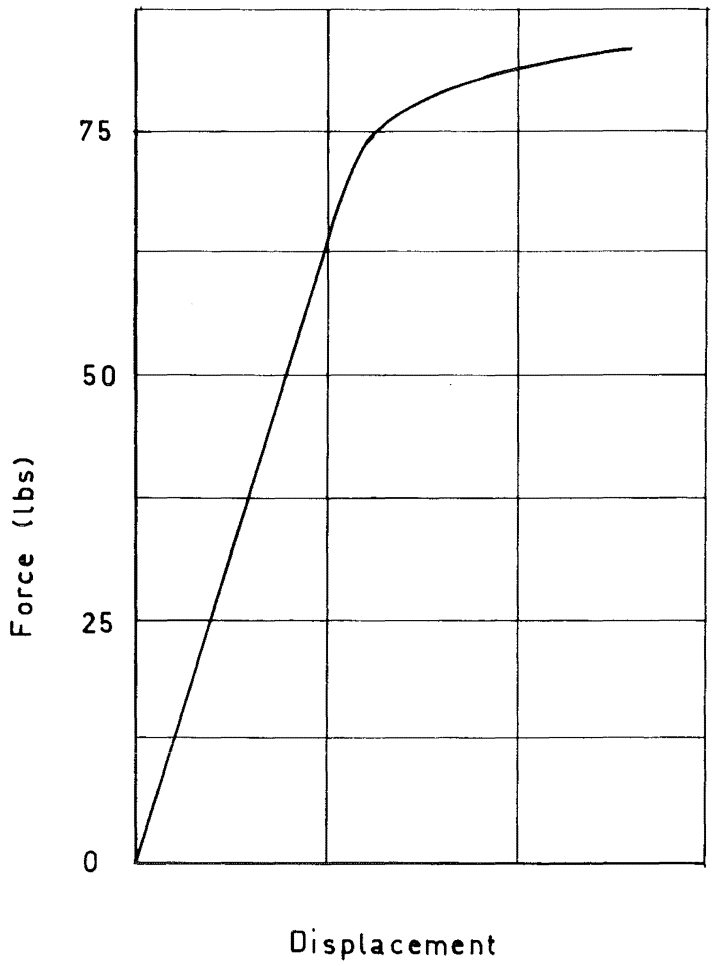

Fig. 6.4. Force-Displacement Relationship for the Reinforcement

From the load-deflection curves given by Islam, cracking occurred at a total load of 2,700 lb and, taking a simply supported strip at either of the free ends, this load corresponds to a cracking moment of 77.8 lb.in./in. Applying this moment to an uncracked section indicated that the ultimate tensile strain was .000353 which corresponds to a maximum tensile stress of 22.8 % f'_c.

6.2 Analysis of Islam's Rectangular Slab Including a Variation of the Governing Moment-Curvature Relationships

The first analyses were of a unit width simply supported beam whose properties correspond to a unit-width section taken from the free end of Islam's rectangular slab (Fig. 6.1). The dimensions and the element mesh for this simply supported beam are shown in Fig. 6.5.

The aim of these analyses was to compare the resulting load-deflection curves of the midspan section when different moment-curvature relationships were taken.

The theoretical regions of cracking and yielding are similar in all these analyses. Fig. 6.6 shows the theoretical regions of cracking and yielding for the moment-curvature relationship that assumes an equivalent-displacement curvature and a rectangular bond stress distribution. This diagram shows the region which is theoretically predicted to crack and yield, and near the ultimate load, the yielded region

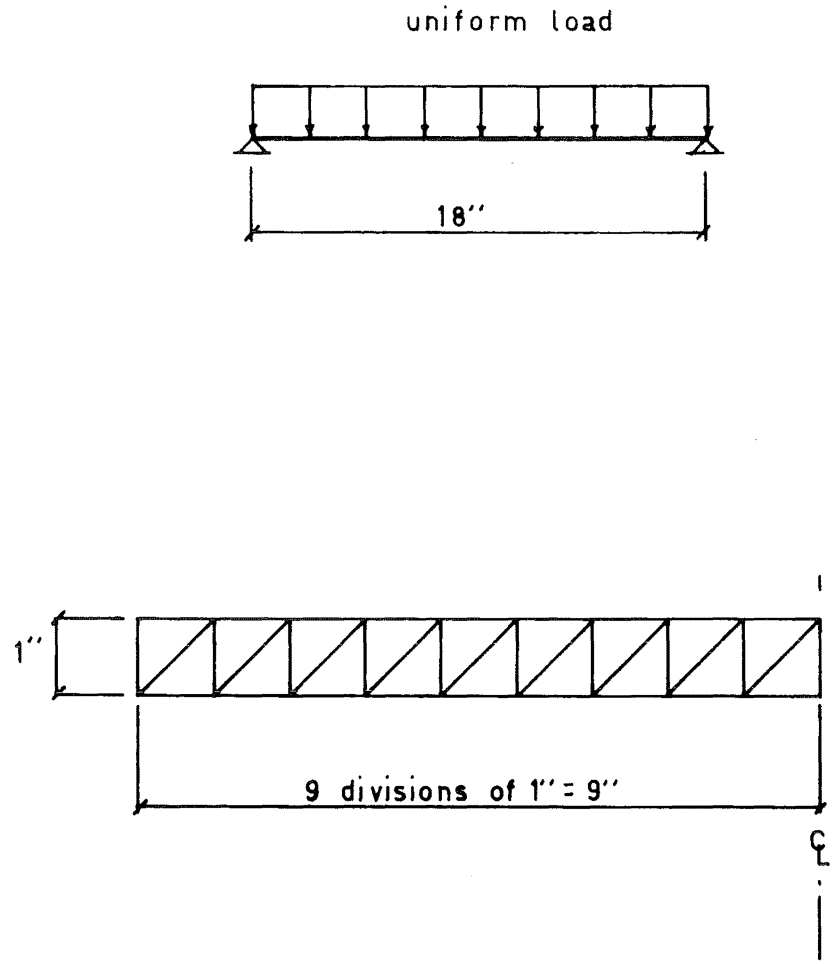

Fig. 6.5. Dimensions and Mesh for the Simply Supported Beam

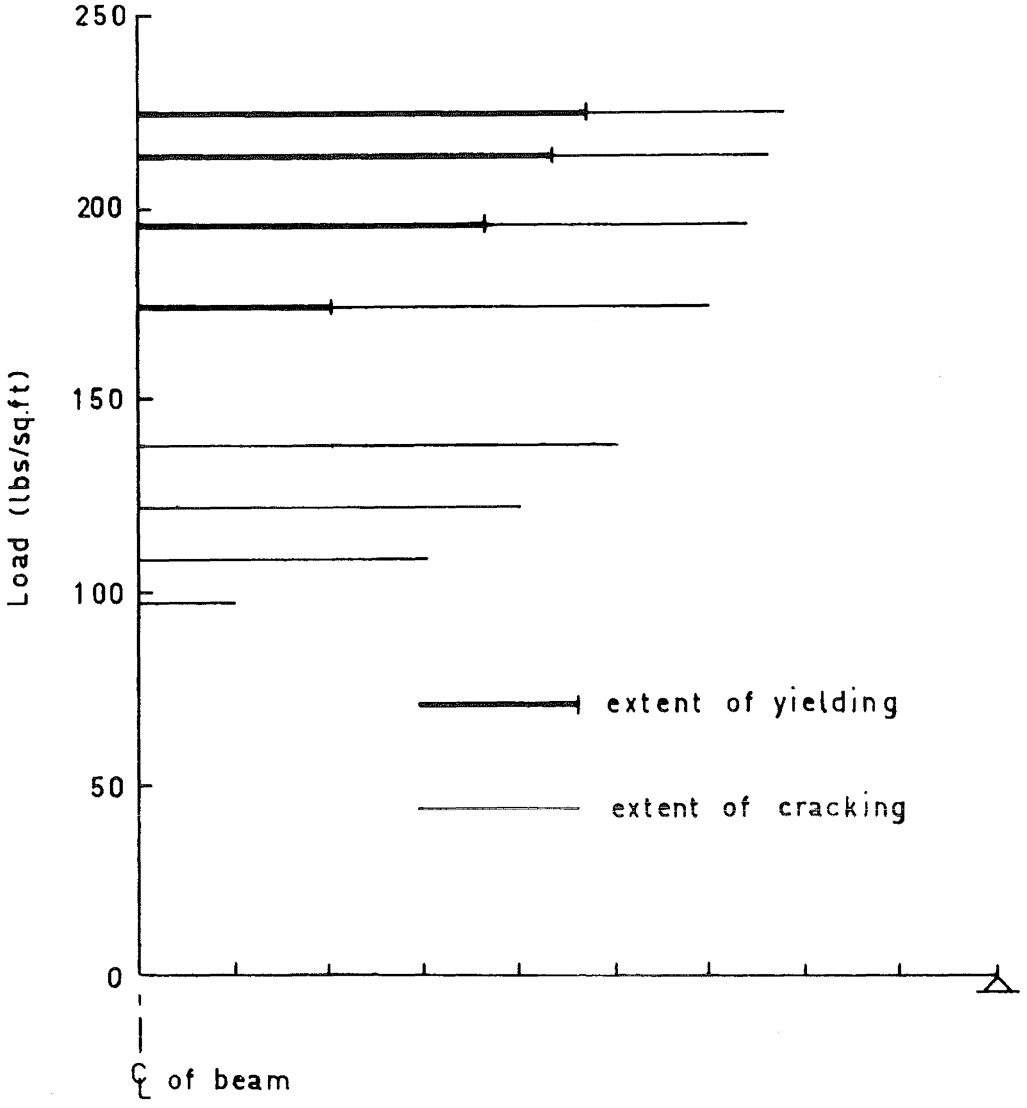

Fig. 6.6. Theoretical Regions of Cracking and Yielding for the Beam

is quite extensive and it is greater than that shown at the free end in the experimental slabs (refer Fig. 6.7).

Fig. 6.8 shows the load-deflection curves for the mid-span section taking the moment-curvature relationships shown in Fig. 4.15. These relationships were formed by assuming a rectangular bond stress distribution and taking:

a) the curvature at a cracked section,

b) the equivalent-rotation curvature, and

c) the equivalent-displacement curvature.

Also, shown in dotted lines, are the two experimental load-deflection curves taken at the point A (refer Fig. 6.1). The load-deflection relationship will not be a continuous curve and, because its variation is unknown, all points have been joined by straight lines.

In the elastic, uncracked state the theoretical model is stiffer than the experimental model by a factor of 4.2. This implies that either the experimental slabs were partially cracked at the time of testing, i.e. due to shrinkage stresses or through handling, or else the value of the modulus of elasticity assumed in the theory is too high. The former hypothesis appears to be a more dominant factor because the experimental curves do not appear to have a significant step at cracking; instead there is a gradual transition from the uncracked to the cracked state. The theoretical cracked stiffness, however, corresponds reasonably well with the stiffer experimental curve (Islam's slab B.3). If it is

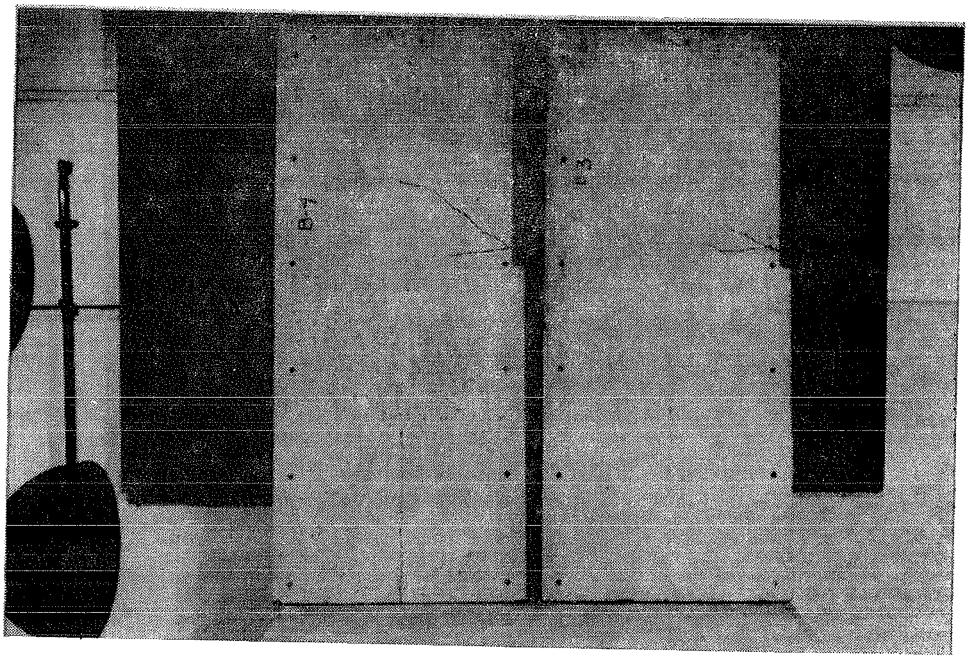

Top surface

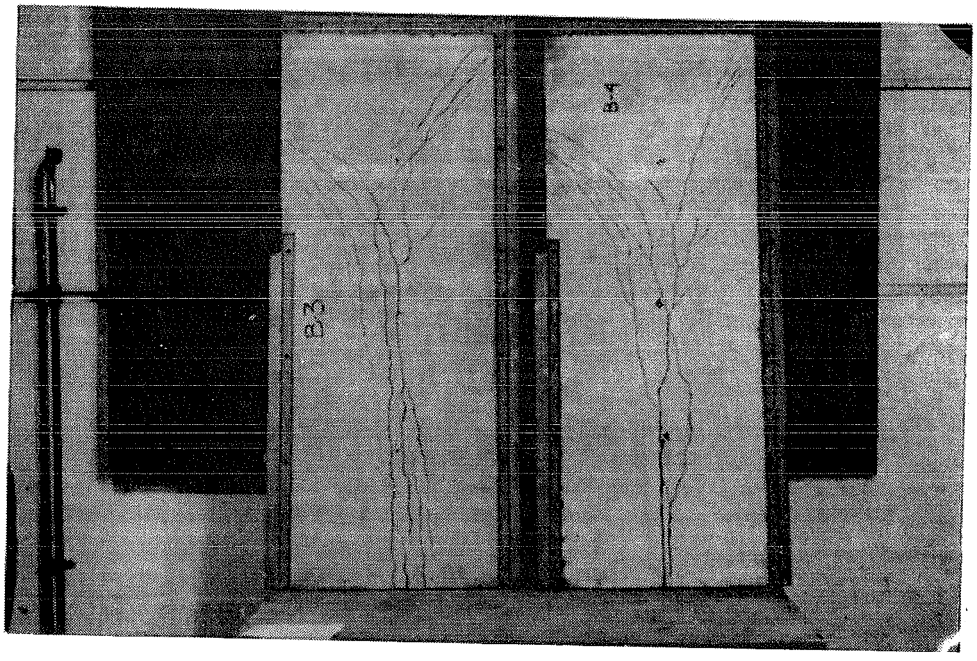

Bottom surface

Fig. 6.7. Experimental Crack Patterns

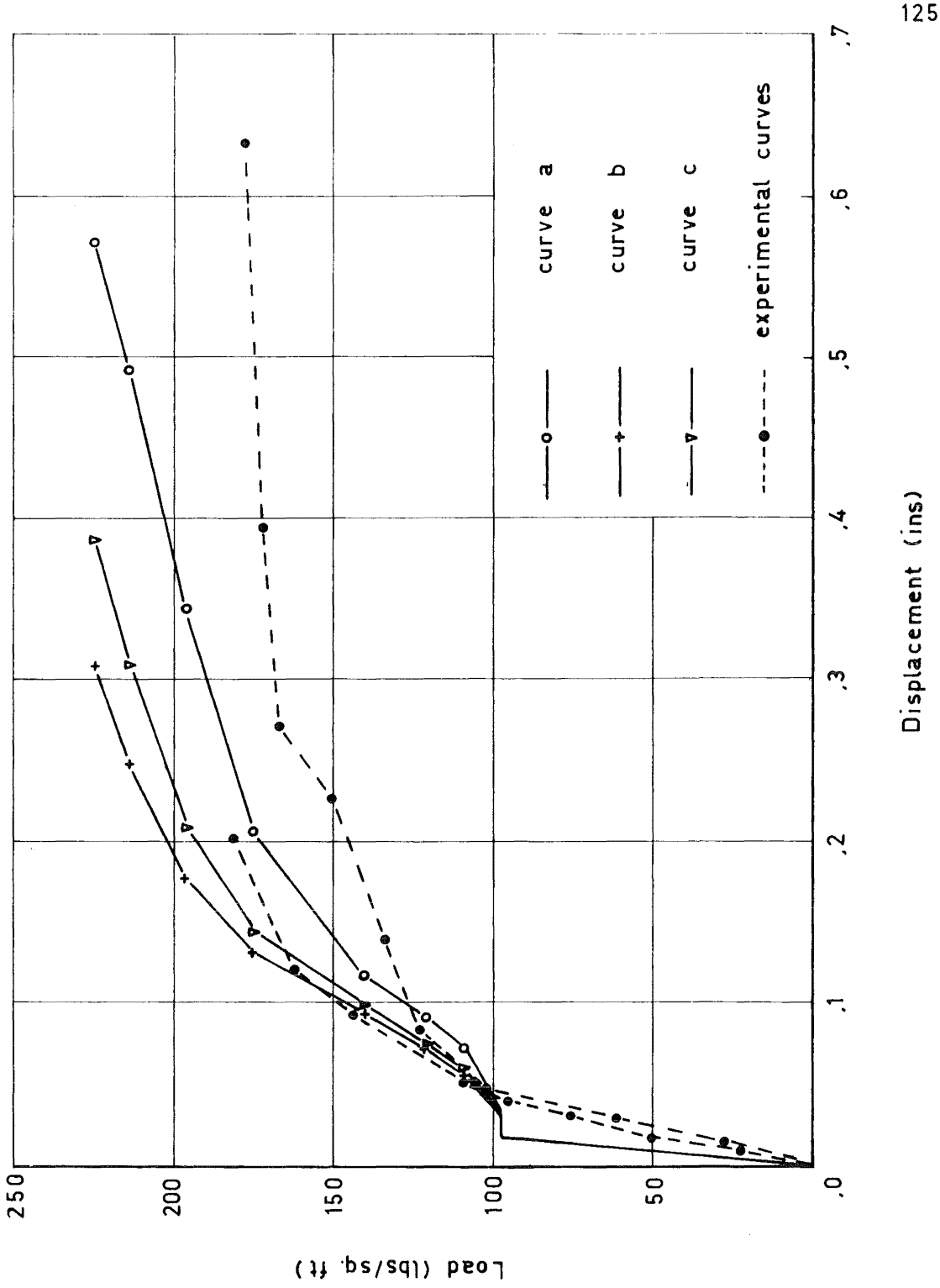

Fig. 6.8. Load-Displacement Curves for the Beam

assumed that the slab is initially uncracked then a theoretical modulus of elasticity of 0.36 x 10^6 lb./sq.in. must be used to obtain the experimental displacements. However, this value is much smaller than we would expect from a laboratory prepared mortar. After the reinforcement has yielded a large discrepancy occurs because the theoretical curves postulate a much greater strength capacity for the slab than is indicated by the experimental curves.

The two experimental load-deflection curves are similar until the cracking load is reached, and from here on the curves diverge although the ultimate loads are almost identical. The large variation in the two curves would be due to variation in the material properties. Possibly the steel was not consistently annealed, or the mortar at the midspan section could have spalled or been weak. Islam, unfortunately, does not comment upon this discrepancy. However, he photographed the final crack patterns (these have been reproduced in Fig.6.7) and we see that the yield region passing through the point A is narrower in the slab B.4 than in the Slab B.3. If the mortar was weaker in slab B.3 then we would expect a large number of longitudinal cracks to form. Also, it is possible that slight spalling of the mortar occurred above the central cracks in slab B.3. This would reduce the stiffness of the central section; the reinforcement would be further strained and would yield sooner than expected.

The relative stiffnesses of the theoretical curves follow the relative stiffnesses of their moment-curvature curves, i.e. the more flexible the moment-curvature relationship the more flexible is the load-displacement curve. After cracking or yielding of the reinforcement there is a large increase in deflection as the centre sections crack or yield. The degradation of the stiffness does not increase at this rate, however, because the midspan displacement is more sensitive to a decrease in stiffness at the midspan than to a similar decrease in stiffness between the midspan and the support.

Fig. 6.9 shows load-deflection curves for the midspan section taking the moment-curvature relationships shown in Fig. 4.17. These relationships were formed assuming an equivalent-displacement curvature and taking:

a) a triangular bond stress distribution,

b) a rectangular bond stress distribution, and

c) a sinusoidal bond stress distribution.

The two experimental load-deflection curves for the point A have been included as a reference.

The comments made about Fig. 6.6 apply equally to this example. The theoretical curves in Fig. 6.9 do not vary much, especially when it is remembered that time effects and spalling of the concrete become very critical near the ultimate load thus causing the theoretical displacements near the ultimate load to be an approximate guide. The relative

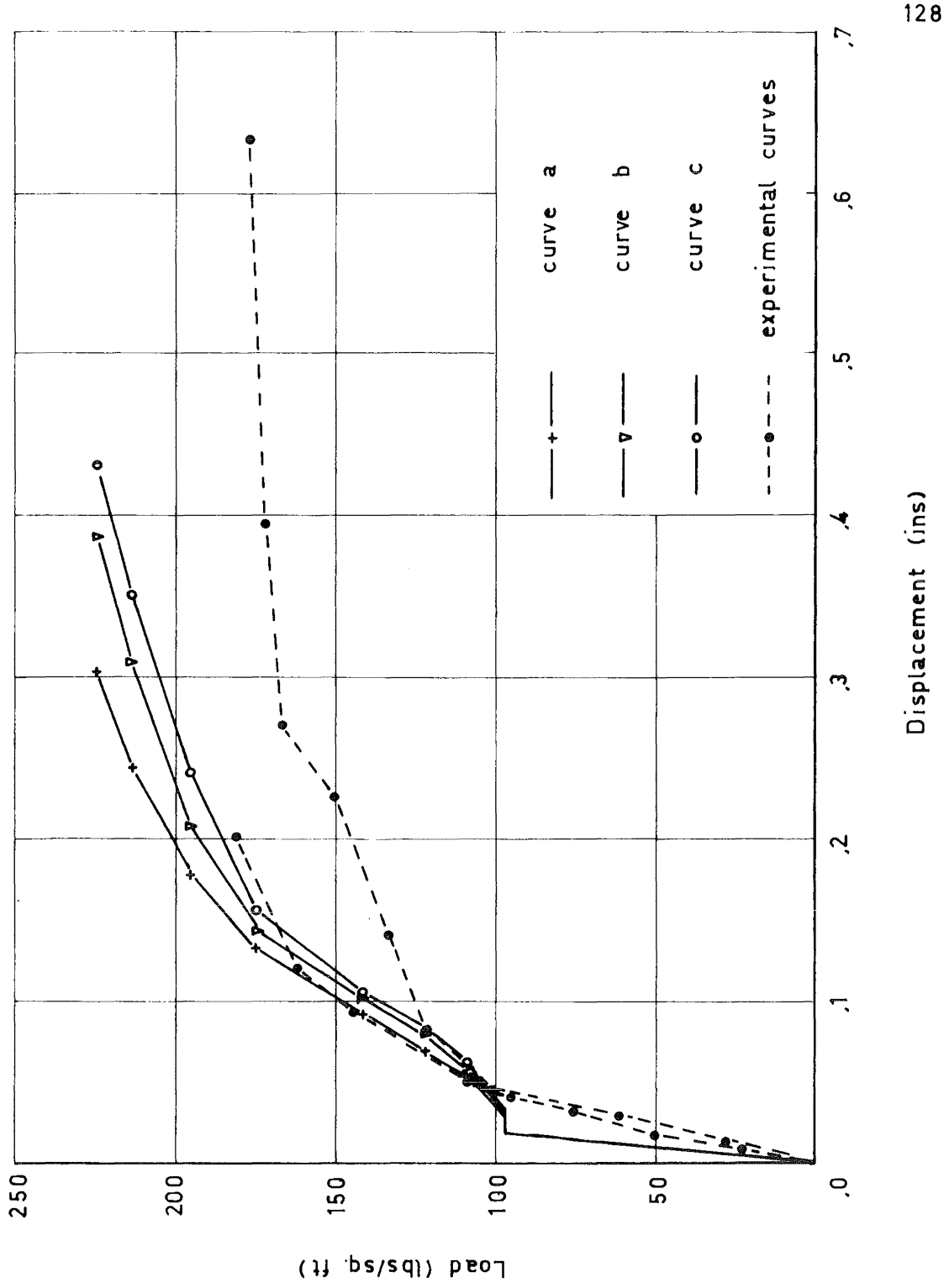

Fig. 6.9. Load-Displacement Curves for the Beam

stiffness of the theoretical curves again follow those of their moment-curvature relationships.

Fig. 6.10 shows load-deflection curves for the midspan section taking the moment-curvature relationships shown in Fig. 4.18 which were formed assuming an equivalent-displacement curvature and a rectangular bond stress and taking the cracking moment as:

a) 17.1 lb.in./in.,

b) 27.4 lb.in./in. (which is the value taken in the previous examples), and

c) 37.6 lb.in./in.

Again the two experimental load-deflection curves for the point A have been included as a reference.

It is seen that the variation of the cracking moment has a significant effect on the load-deflection relationship, especially within the cracking to yielding region. As explained in Section 4.5 the cracking moment of 27.4 lb.in./in. corresponds to the apparent cracking moment of this slab and the cracking moments of 17.1 lb.in./in. and 37.6 lb.in./in. represent two extreme values that could occur.

Because the material properties produce an ultimate moment capacity of the section which is too high the stress-strain curve of the reinforcement was altered to produce an ultimate moment capacity of 51.0 lb.in./in. which approximately corresponds to the ultimate moment capacity of the experimental slabs. The only modification made was to change

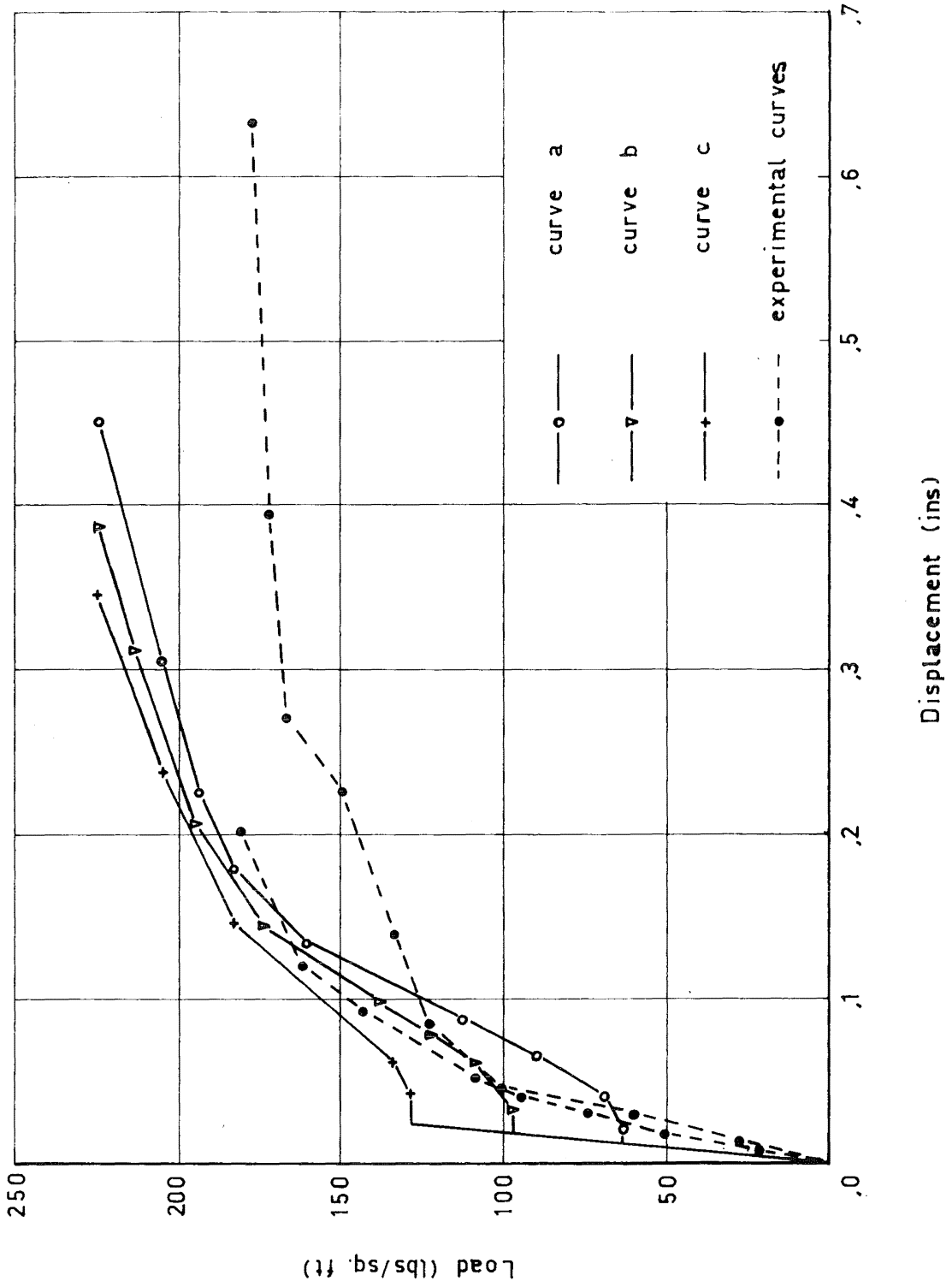

Fig. 6.10. Load - Displacement Curves for the Beam

the yielded modulus of elasticity of the reinforcement to .30 x 10^6 lb./sq.in. (the remaining properties are the same as in Section 6.1). Fig. 6.11 shows the resulting load-deflection curves for the midspan section assuming a rectangular bond stress distribution and taking:

a) the curvature at a cracked section, and

b) the equivalent-displacement curvature.

The theoretical curves are identical to those in Fig. 6.6 up to the load at which the steel yields and therefore some of the comments made for those curves will also apply to these curves. Once cracking occurs the stiffness of the theoretical curve that takes the curvature at a cracked section decreases substantially, in fact, more than either of the two experimental curves. The stiffness of the theoretical curve which takes the equivalent-displacement curvature agrees quite well with the stiffer experimental curve except near the ultimate load where the experimental curve is more flexible. This is to be expected, however, because spalling of the concrete and time effects will make the experimental slabs more flexible.

Using the moment-curvature relationship shown in Fig. 4.15 Islam's rectangular slab was analysed for two load cases, i.e. a uniformly distributed load of 122 lb./sq.ft. and another of 167 lb./sq.ft. The principal purposes of these two analyses were: to compare the load-deflection curves

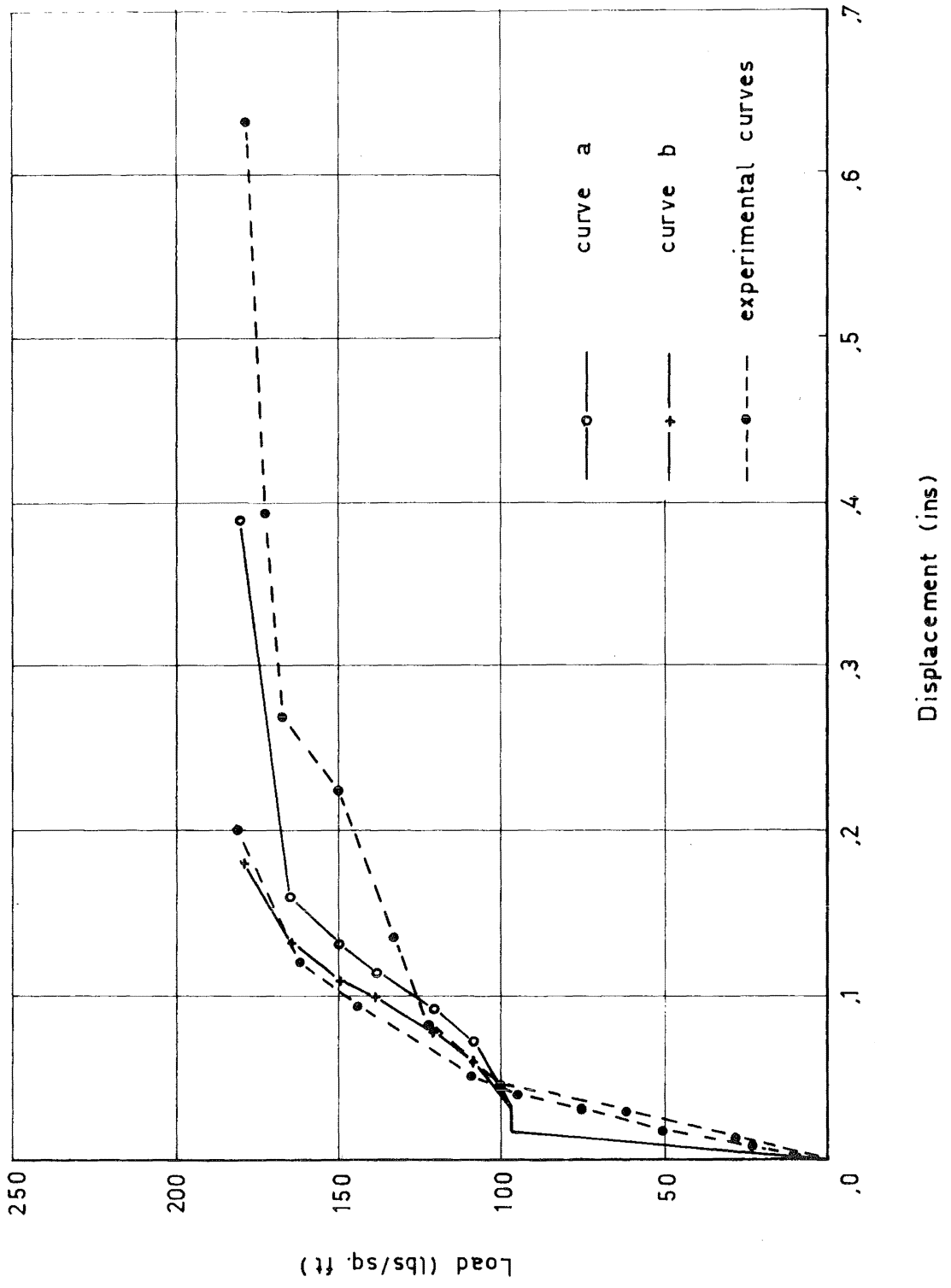

Fig. 6.11. Load-Displacement Curves for the Beam

with those of the simply supported beam (which can also be considered as a one-way slab), to determine the effect of the boundary conditions, and to study the cracked and yielded regions.

Fig. 6.12 shows the basic mesh that was used in these analyses together with the slab support conditions. The method of analysis used elements that were either totally cracked or totally uncracked and hence the form of the mesh was altered slightly for each load case. The mesh contains small elements in the regions where high stresses are expected so that any changes of stiffness will be recorded as accurately as possible. For this analysis the stiffness of each element was calculated manually at the end of each cycle which required quite a large amount of time and work for each analysis.

Several effects which arose in this analysis are characteristic of the method and these are discussed below. When the structure is cracked it is idealised as an elastic structure comprised of elements each of which has two constant flexural rigidities and occasionally, during redistribution of the moments, stress concentrations can occur. For example, midspan cracking was initiated at the end 1-3 (refer Fig. 6.12 for the nomenclature) and redistributed towards the end 2-5. If the redistribution was not complete then high stresses were obtained at those nodes which were about to become cracked. When determining the new element stiffnesses

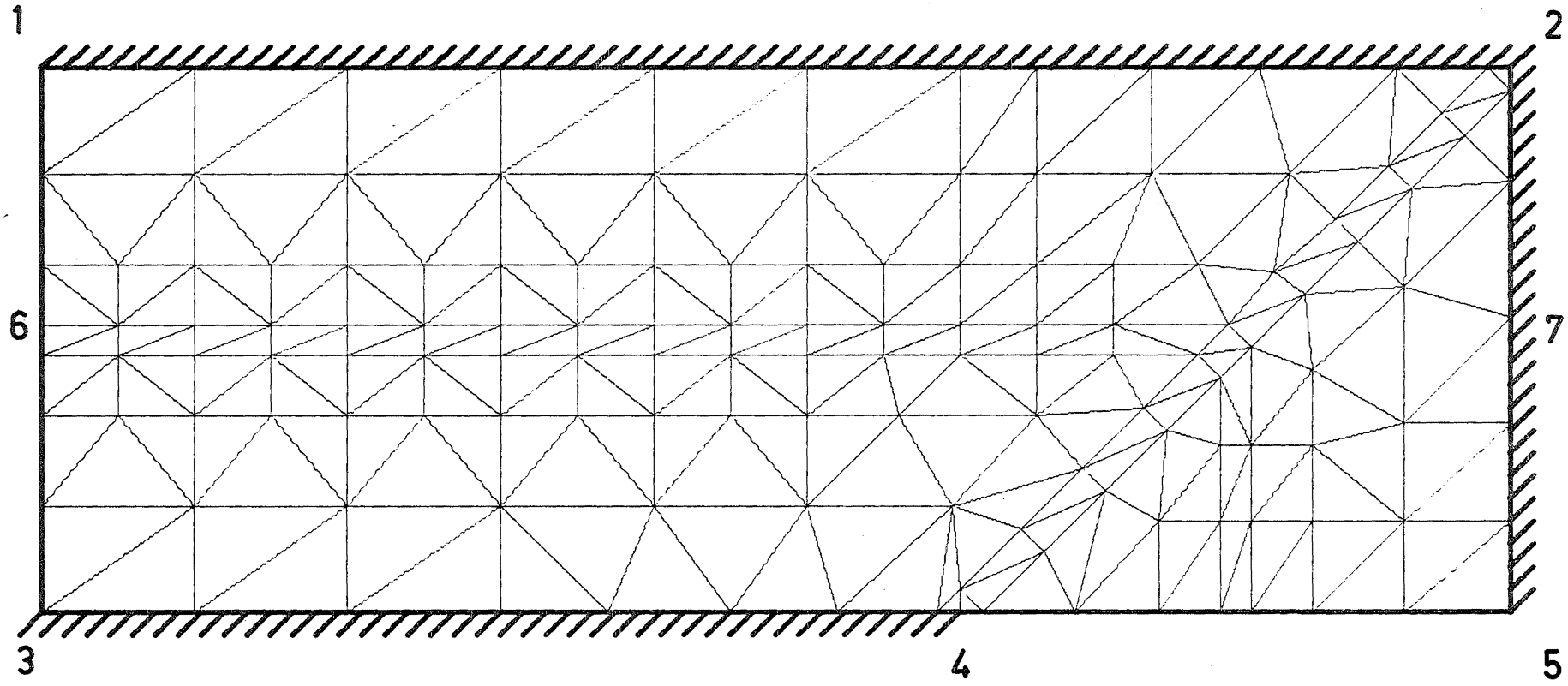

Fig. 6.12 Basic Finite Element Mesh for Islam's Rectangular Slab

this phenomenon was kept in mind and such elements were given a greater stiffness. If this stiffness was too large then it would be reduced in the next cycle and therefore this action is not detrimental to the final result.

Sometimes one node will have a very high stress but nodes a short distance away will have considerably lower stresses. In such circumstances it is difficult to reproduce a similar effect within the surrounding elements although, fortunately, such stresses normally have a local influence only. This phenomenon occurred at point 4 where, at the uniform load of 167 lb./sq.ft., the maximum moments at the four nodes nearest point 4 was -78.8, -45,6, -22.8, and -15.0 (all the units being lb.in./in.).

Another source of error occurs when the boundaries of a cracked element are altered to ensure that the element is totally cracked or that adjacent elements are totally uncracked. When a cracked element's boundaries are changed the new region is forced to become cracked in the same direction as the original element. However, the effect of this approximation will in general be small and again, if it is not conservative then the region of cracking will propagate in the next cycle.

The crack patterns will now be considered because they help to explain the changes in the deflection profiles (which will be considered next). After each analysis the condition of anisotropy of each element is known, i.e. the

the moduli of elasticity and the angles of cracking or yielding (if either exist) and these have been plotted using an IBM 1627 11 inch Calcomp graph plotter. If an element is cracked then lines are drawn within the element to show the direction of the cracks, i.e. the spacing of the lines does not represent the crack spacing. If, in a set of cracks, the reinforcement has yielded a darker and wider line is drawn and, if the element has failed, (i.e. the theoretical moment is greater than the theoretical ultimate moment for the section) then a double dark and wide line is drawn. Fig. 6.13 shows the regions of cracking at the loading of 122 lb./sq.ft. for both the bottom and the top surfaces. Near points 1 and 3 the slab acts like a one-way slab and the cracking on the bottom surface is parallel to the longitudinal sides. Near the opposite end, however, this crack band divides into two bands, one progressing towards the corner at point 2, and the other passing between points 4 and 5. Occasionally a stray set of cracks is seen. This is normally caused by high stresses at two nodes of an element indicating that the element is substantially cracked but adjacent elements are not. These elements reflect an inadequacy of the element mesh to accurately portray the moment variation and this can occur at different load cases and at different places within the mesh. However, the formation of extra nodes is not always possible due to limitations on the number of elements that the computer imposes; also, the temporary inclusion of additional nodes and

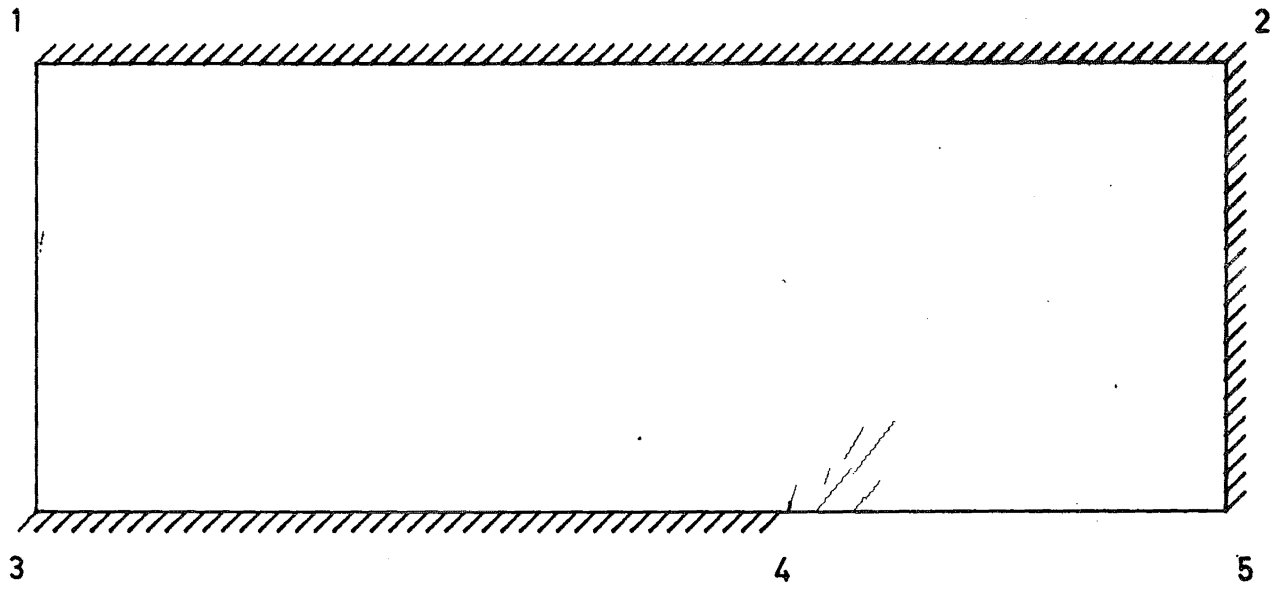

Top Surface

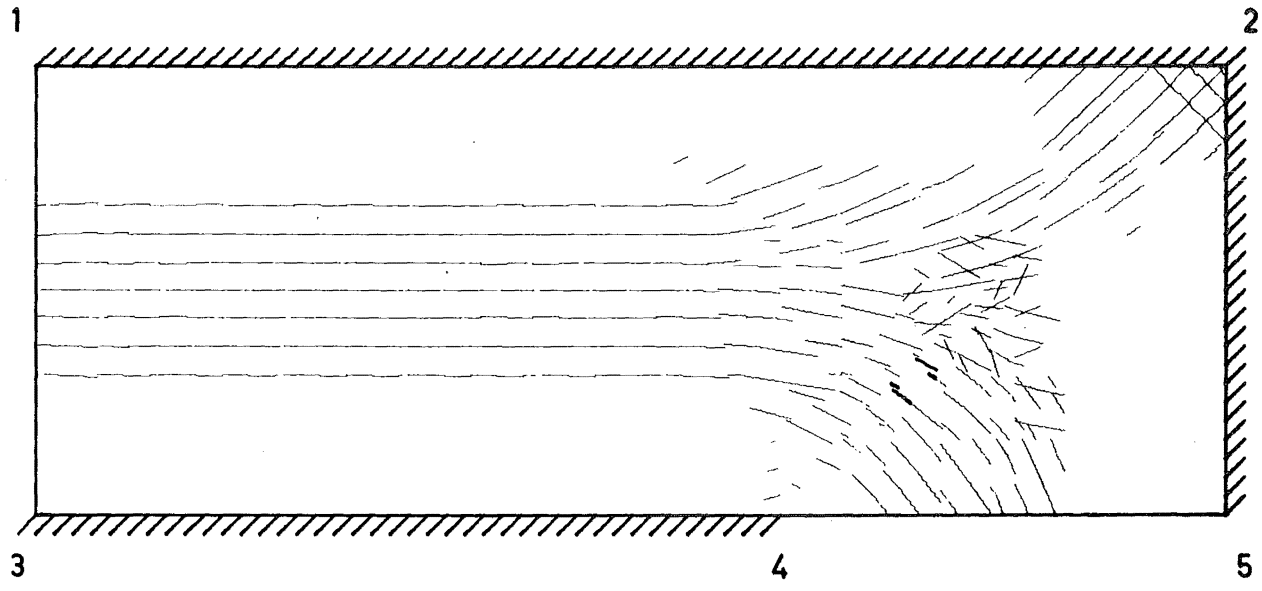

Bottom Surface

Fig. 6.13. Crack Patterns for Islam's Rectangular Slab - 122 lb./sq. ft

elements requires a lot of manual data manipulation. Often this discontinuous cracking is corrected as the loading increases and hence, if the stresses dictated this phenomenon, these elements were normally allowed to crack. (This task, however, would be simplified if a video-display unit and a light pen were available.)

Another discontinuity sometimes occurred when the elements became doubly cracked. If an element cracks in one direction then the principal stresses redistribute and the second angle that the element could crack at changes also. From the elements that have cracked in two directions it would appear that the second angle at which they crack is not always as accurately depicted as the first angle. (This is a similar occurrence to the phenomenon already mentioned of high stresses being observed when redistribution was not complete.) Most of the doubly cracked elements, however, have the semblance of following either the original crack direction or that of the divided regions.

Two portions of the slab have cracks across which the reinforcement has yielded, i.e. one region on the bottom surface and the other region on the top surface. On the bottom surface this yielded region appears to be at the point where the three cracked regions meet, i.e. the point about which the three cracked regions are "folding". For this reason we would not expect this yielded region to expand. On the top surface the element near point 4 has yielded due to

the very high hogging moment at, and close to, point 4.

The cracked and yielded regions of the slab, when the load was 167 lb./sq.ft., are shown in Fig. 6.14. Comparing this pattern with that of the previous load case (Fig. 6.13) we see that the band of cracking on the bottom surface has widened. The region that had yielded has not altered but a new region of yielded reinforcement has developed along the longitudinal direction and it is at this region that the failure mechanism initiates. Adjacent to the continuous line of yielding the elements have yielded randomly. The reason for this is that these elements have either just yielded or are just about to yield, and they have stiffnesses which are on either side of the yield stiffness, i.e. K^- and K^+ shown in Fig. 6.15. In practice we would expect a structure to redistribute its stresses so that the yielded regions would be continuous. However, the effect upon the theoretical displacements of having some element just yielded and others about to yield is minimal.

The experimental crack pattern, reproduced in Fig. 6.7, shows the cracks in which the reinforcement has a permanent set, i.e. the reinforcement has yielded. The theoretical crack pattern shown in Fig. 6.14, which occurred at approximately 92% of the experimental failure load, is similar to the experimental crack pattern although the yielded regions are not as extensive at this load.

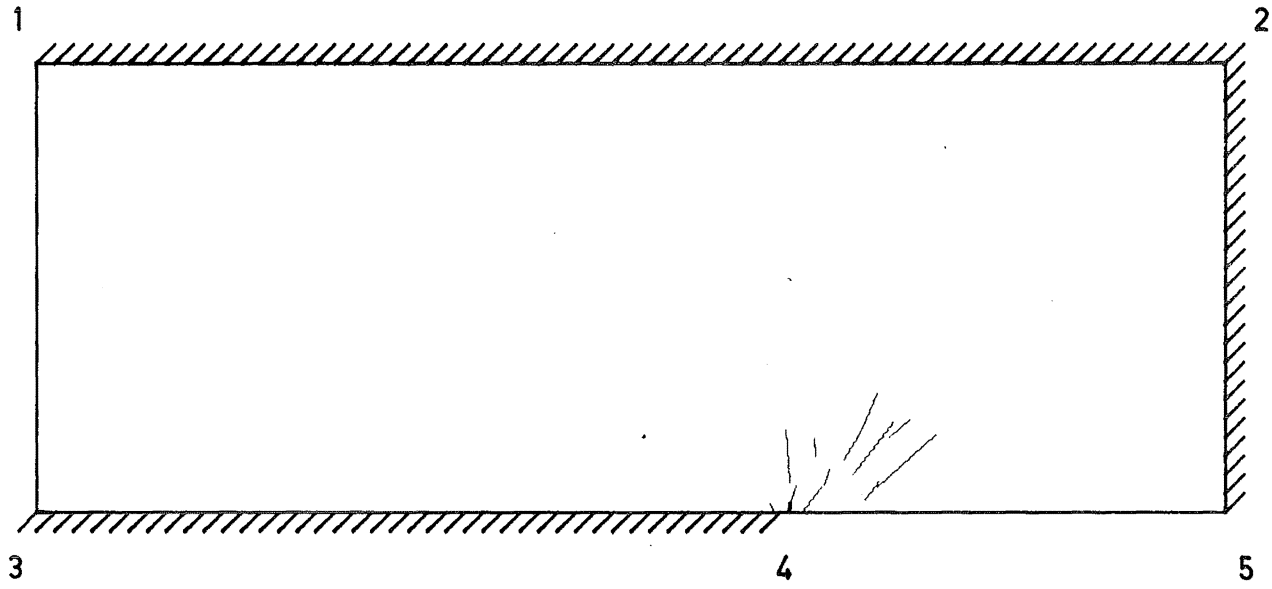

Top Surface

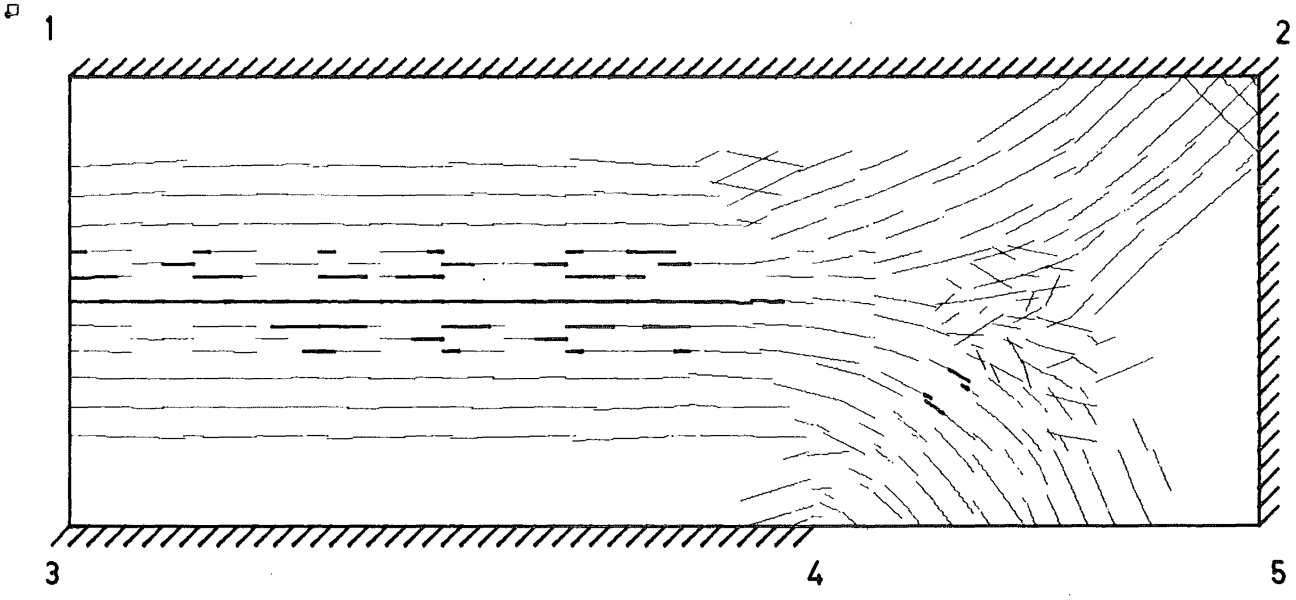

Bottom Surface

Fig. 6.14. Crack Patterns for Islam's Rectangular Slab - 167 lb./sq. ft

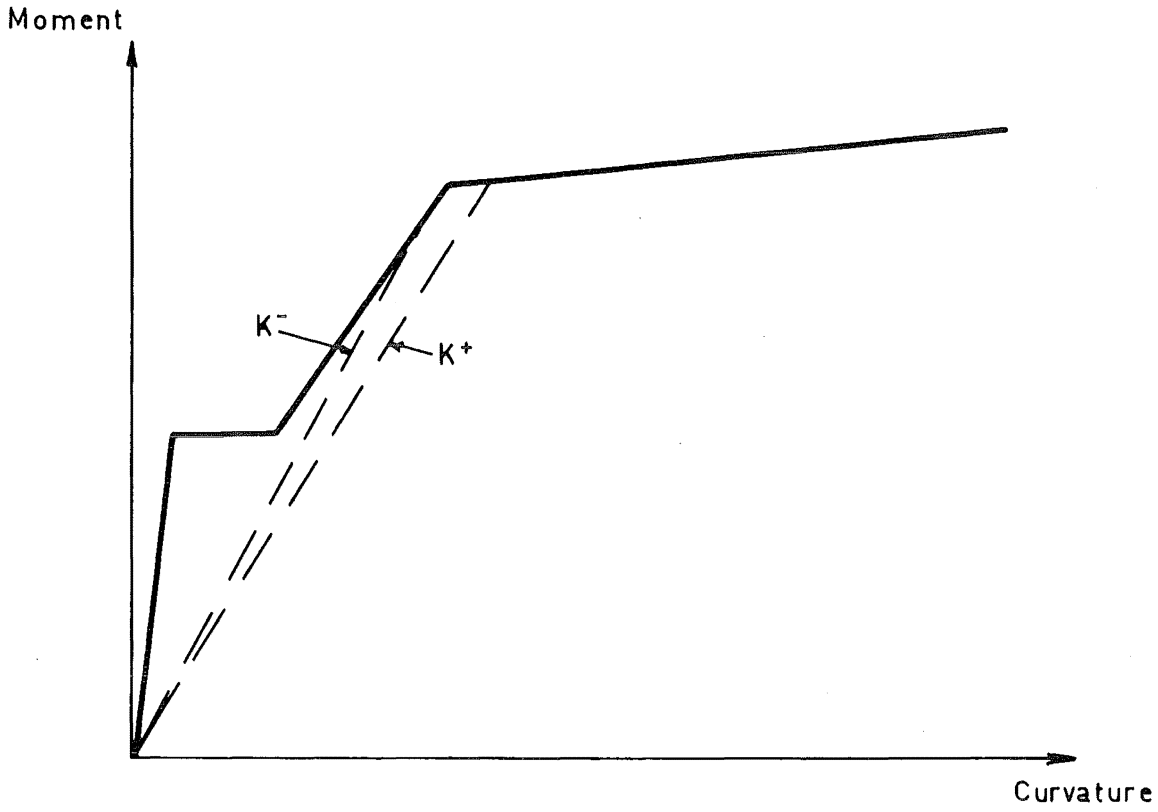

Fig. 6.15. Stiffnesses on either Side of the Yield Stiffness

The displacement profiles along the line 1-3 are shown in Figs 6.16a and 6.16b together with the displacement profiles of the simply supported beam for the load cases 122 lb./sq.ft and 167 lb./sq.ft respectively (because the curves are symmetrical only half of the profile is shown). The curves are very similar though the simply supported beam is slightly more flexible. There are two possible reasons for this; firstly, the effect of the boundary conditions in Islam's rectangular slab has stiffened this section, and secondly, the results of the simply supported beam, because it is comprised of more elements, would be more accurate and hence more flexible (refer Section 4.1).

The displacement profiles (normalised to 1) have also been compared for the uncracked state, for a load of 122 lb./sq.ft, and for a load of 167 lb./sq.ft. Fig. 6.17a shows such a comparison for the displacement profile along the line 1-3 (cracking was symmetrical along this line so that only half of the profile is shown). Because there is not a great difference in the profiles only the displacement profile at the load 122 lb./sq.ft is drawn. We see that the effect of cracking at the midspan section has caused the sides to deform as a rigid body. As the region of cracking broadens, i.e. at the load of 167 lb./sq.ft the length of the slab which deforms as a rigid body becomes smaller and the displacement profile moves back towards the uncracked displacement profile. This is due to a large portion of the slab

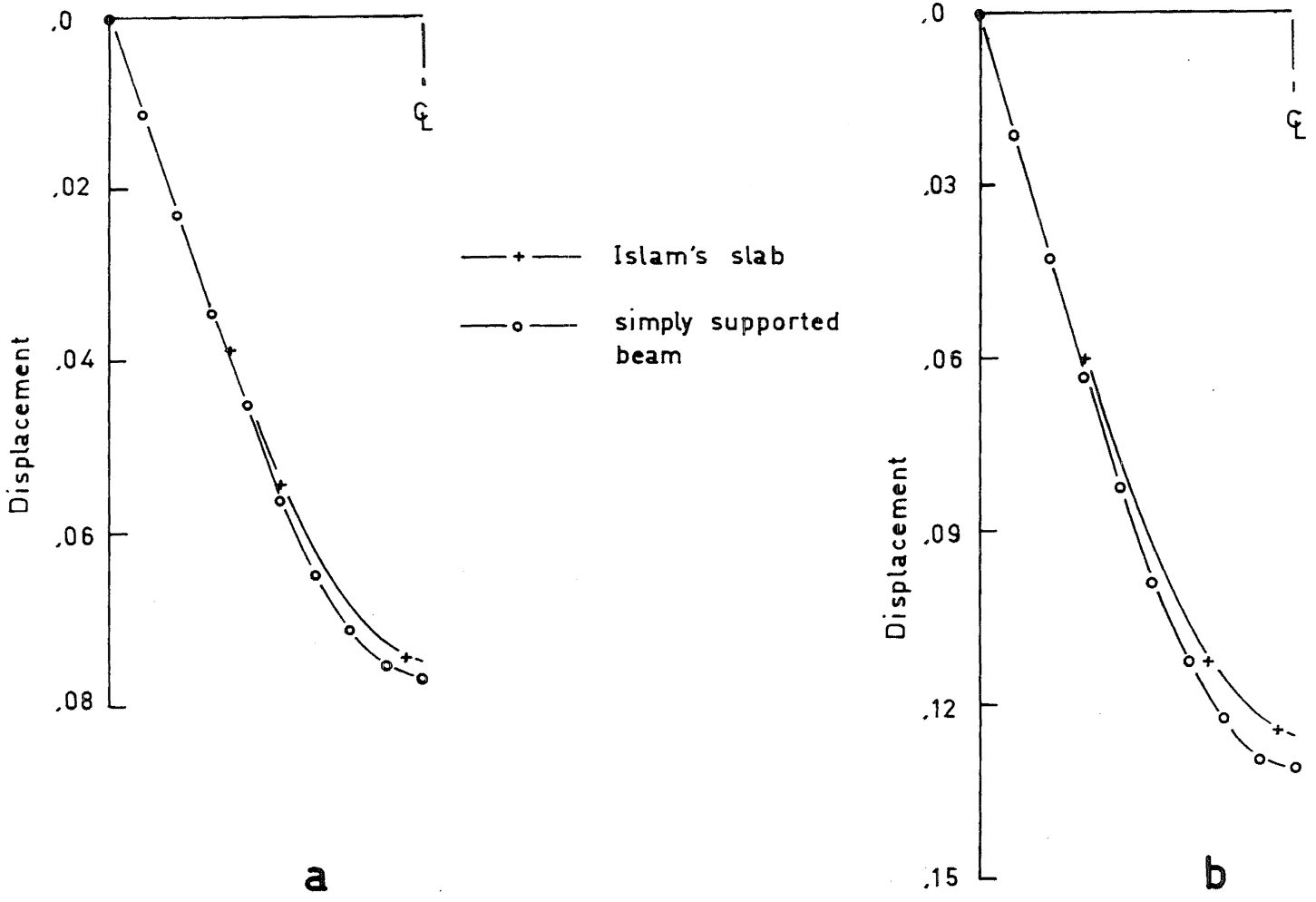

Fig. 6.16. Displacement Profiles for the Slab and Beam

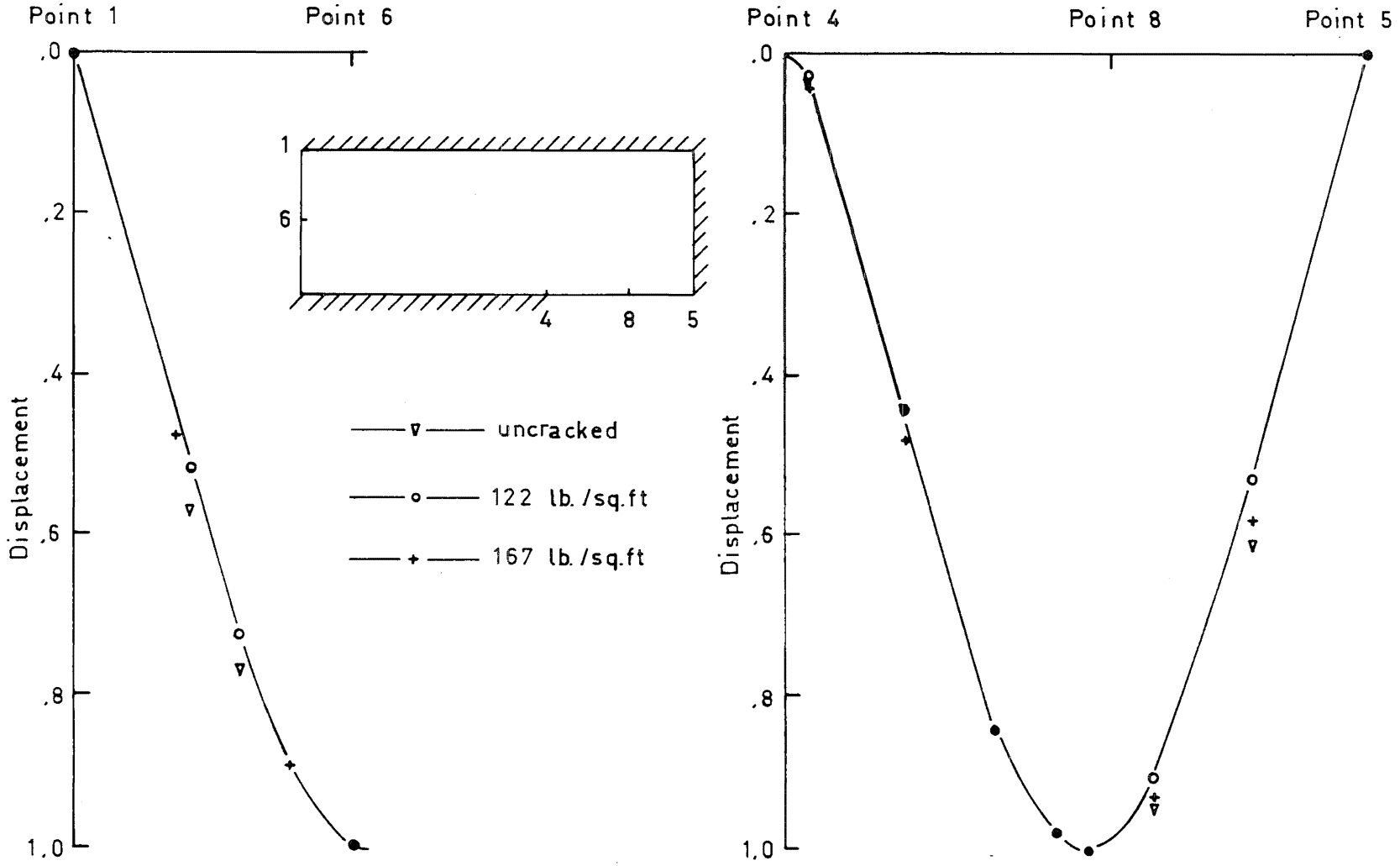

Fig. 6.17. Displacement Profiles Along Lines 1-6 and 4-5

being cracked and thus having an approximately constant stiffness.

Fig. 6.17b shows the deflection profile (normalised to 1) along the line 4-5 for the same load cases as above. (The maximum displacement on this line is approximately 50% of the maximum displacement on the line 1-3.) Again there is not a great difference in the profiles and only the deflection profile at the load 122 lb./sq.ft is drawn. For the portion 4-8 there is very little difference in the profiles. The reason for this can be seen by referring to the crack patterns for this region (Figs 6.13 and 6.14). At the load 122 lb./sq.ft the portion 4-8 is almost completely cracked and at the load 167 lb./sq.ft it is completely cracked. Hence, the stiffness along 4-8 is approximately constant for these three cases and therefore the deflection profiles do not vary much. Because the portion 8-5 is not totally cracked the displacement profile varies more. At the load 122 lb./sq.ft the uncracked portion of the slab near point 5 has deformed as a rigid body. When the load was 167 lb./sq.ft the region of cracking expanded and so a smaller portion of the slab deformed as a rigid body and the displacement profile moved towards the elastic profile.

The corresponding displacement profiles (again normalised to 1) along the line 6-7 are shown in Fig. 6.18. The displacement profile for the load 167 lb./sq.ft is very similar to the profile for the load 122 lb./sq.ft and hence it has not

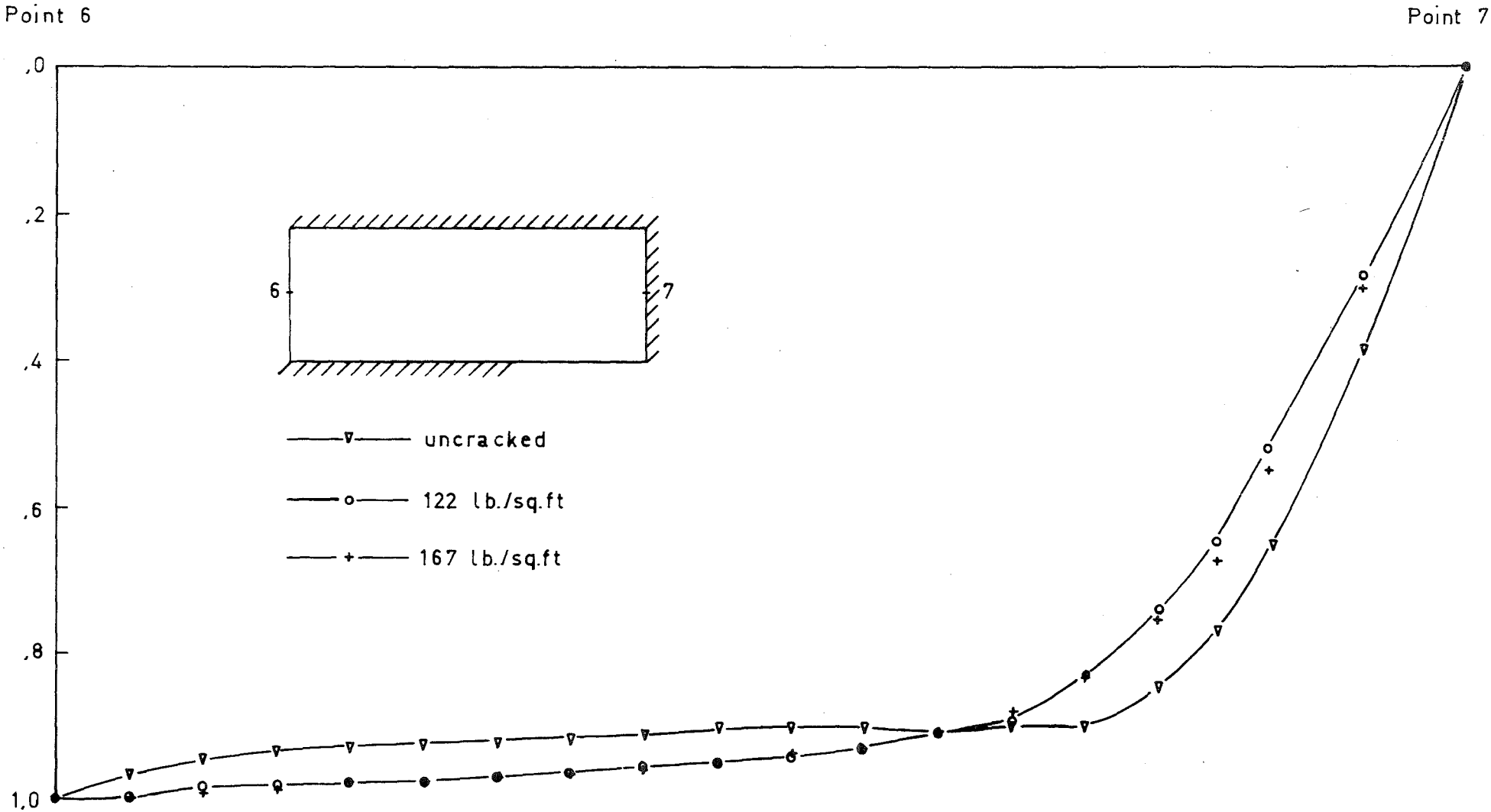

Fig. 6.18. Displacement Profile Along the Line 6-7

been drawn. The elastic displacement dropped quickly from point 6 and then levelled out. The large elastic displacement at point 6 would be due to the rotational freedom at the end 1-3. After the slab is cracked there is a folding action along most of the line 6-7 which tends to equalise the displacements along this line. Towards point 7 the effect of the support conditions between the points 2 and 5 is noticed. The cracked profile has a smoother transition than the uncracked profile due to rigid body movement near point 7 and also due to cracking at point 4. The only significant development when the load was 167 lb./sq.ft was the reduced portion of the slab that moved as a rigid body near point 7 (this is observed in the crack patterns by the expansion of the cracked region). Hence, both the crack patterns and the deflection profiles indicate a folding of the three sides that are simply supported. However, the folding is not about a line but rather about a significantly broad cracked region.

6.3 Analysis of Islam's L-Shaped Slab

Islam's L-shaped slab, shown in Fig. 6.3, was analysed assuming the material properties that were stated in Section 6.1. From these properties moment-curvature relationships were developed and Fig. 6.19 shows the moment-curvature curve taking an equivalent-displacement curvature and assuming a rectangular bond stress distribution, together with the moment-curvature curve taking the curvature at a cracked

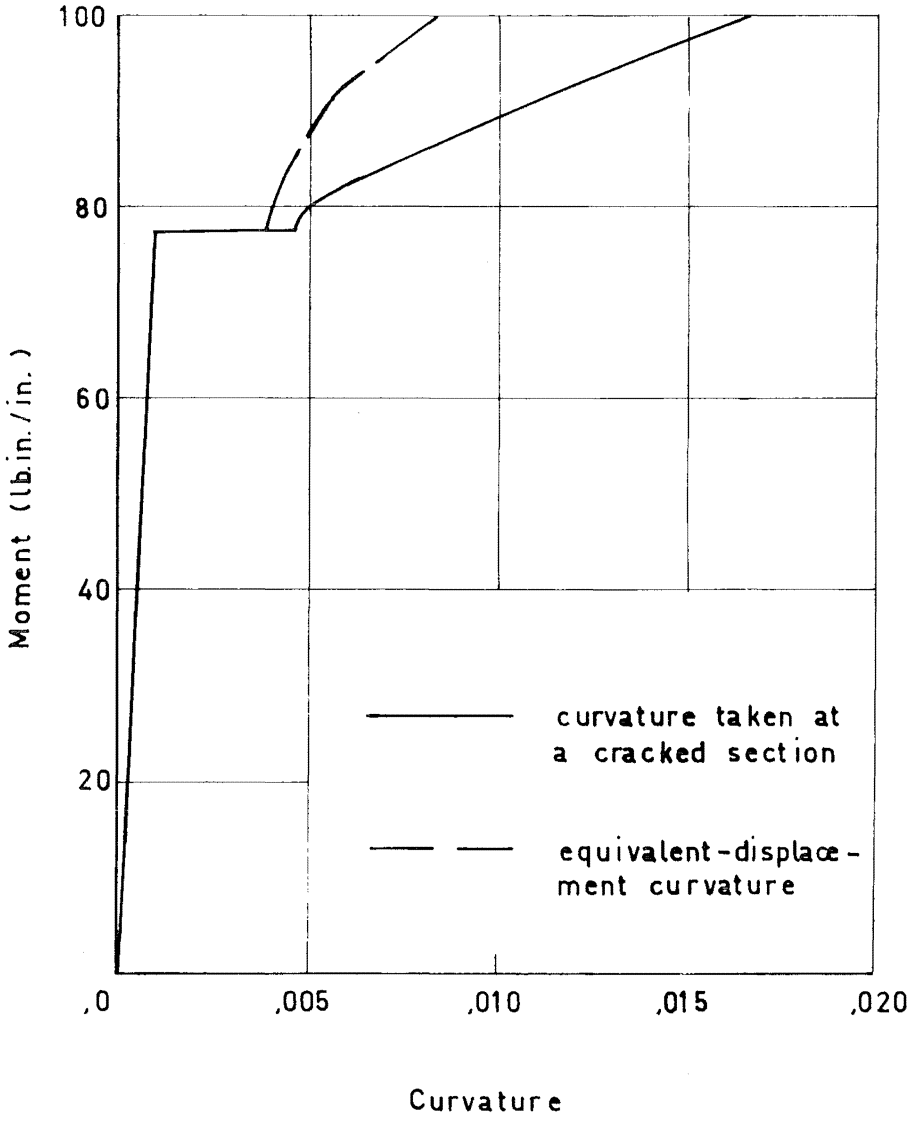

Fig. 6.19. Moment-Curvature Curves for Islam's L-Shaped Slab

section (these curves are both normalised to 1). The principal feature about these curves is the small difference between the cracking moment and the ultimate moment, i.e. 78.9 lb.in./in. and 89.6 lb.in./in. respectively. This is caused by the high cracking strength which this slab possesses together with the low ultimate strain of the reinforcement which is .00433 (compared with the value of .01 which was assumed for the other analyses).

The mesh used in this analysis is shown in Fig. 6.20. Because of symmetry we only need to consider one half of the structure and therefore the mesh that was used to analyse Islam's rectangular slab (Fig. 6.12) was modified for this analysis.

An automatic procedure was used to determine the stiffnesses at the end of each cycle (this replaced the manual method which was used when Islam's rectangular slab was analysed). For each element the moduli of elasticity and the angle of cracking (if any cracking was present) were determined by averaging both the nodal moments and the angle at each node that the principal moment makes with the x axis. The moment axis of the moment-curvature relationship shown in Fig. 6.19 was divided into 100 equal intervals and the stiffness at each of these intervals was predetermined. Hence, the moment-curvature curve was represented as a stepped relationship. (Thus other structures could be analysed simply by replacing this relationship and redefining the

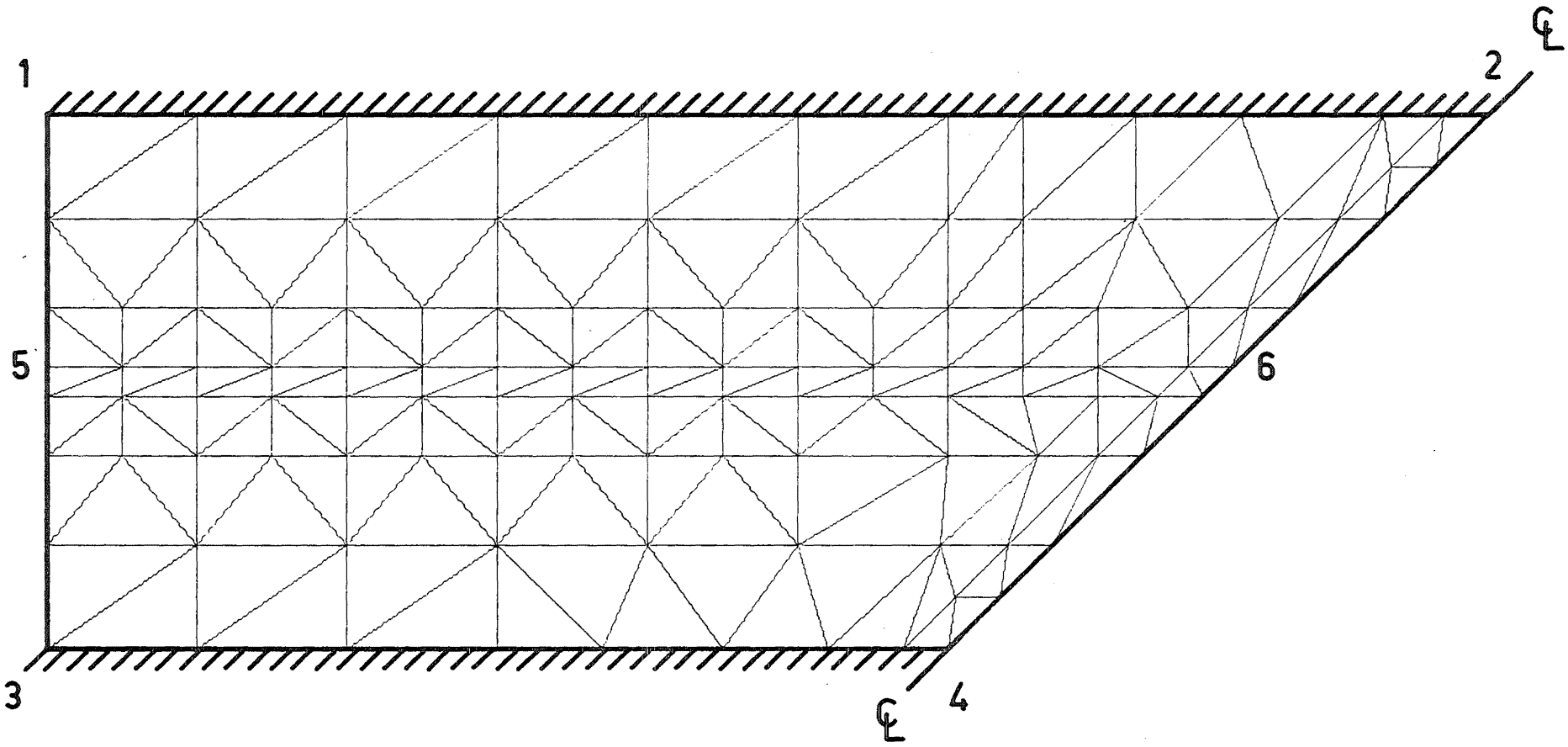

Fig. 6.20. Basic Finite Element Mesh for Islam's L-Shaped Slab

ultimate moment.) In terms of the section-property diagram which was discussed in Section 4.2, we can describe the slab properties by a multi-linear section property diagram comprised of one hundred closed squares similar to those shown in Fig. 4.4.

At the end of each analysis the resulting element stiffnesses were punched onto cards; these were used for the next cycle of the analysis and for plotting the crack patterns. Using this method the operator still retained control over the results because, if desired, he could alter the output. This is necessary if two nodes of an element are cracked but the third node is not cracked; the automatic averaging procedure may consider the element to be totally cracked whereas the operator may prefer to leave the element uncracked and change the element boundaries to coincide with the cracked region. This he can do by altering the appropriate cards. Another example occurred in this analysis for a few elements which had a high stress at one or two of their nodes and the automatic procedure considered the element to have failed (this was represented by giving the element a modulus of elasticity of 1.0 lb./sq.in.). If this was considered to be too severe the element could be given a cracked stiffness and if it was too stiff the element would crack further on the next cycle. This phenomenon did not occur very often and almost all of the elements were cracked automatically.

The method of automatic redistribution normally took more cycles to reach equilibrium than when the manual method was used. This is because, for those structures which have a large area behaving like a one-way slab, the redistribution in this area could be over-distributed for the first few cycles. However, this procedure would not be possible for many structures.

Crack patterns have been plotted for four load cases: 282 lb./sq.ft which is the cracking load and is 78.3% of the theoretical ultimate load, 308 lb./sq.ft which is 85.6% of the theoretical ultimate load, and 334 lb./sq.ft which is 92.7% of the theoretical ultimate load, and 360 lb./sq.ft which is just below the theoretical ultimate load. Fig. 6.21 shows the crack pattern at the cracking load 282 lb./sq.ft. Because there is very little difference between the cracking moment and the yielding moment (78.9 lb.in./in. and 79.8 lb.in./in. respectively) some of the elements have yielded already. There was a similar effect to that observed in the analysis of Islam's rectangular slab (Fig. 6.14) in which the longitudinal line of yielding on the bottom surface was not continuous. The same reason applies in this case; namely that the elements along this line have stiffnesses that are either just below or just above the yield stiffness. A short distance away from the line of symmetry the cracks have broadened. On the top surface a very high stress occurred at point 4 (refer Fig. 6.18 for the numbering) and

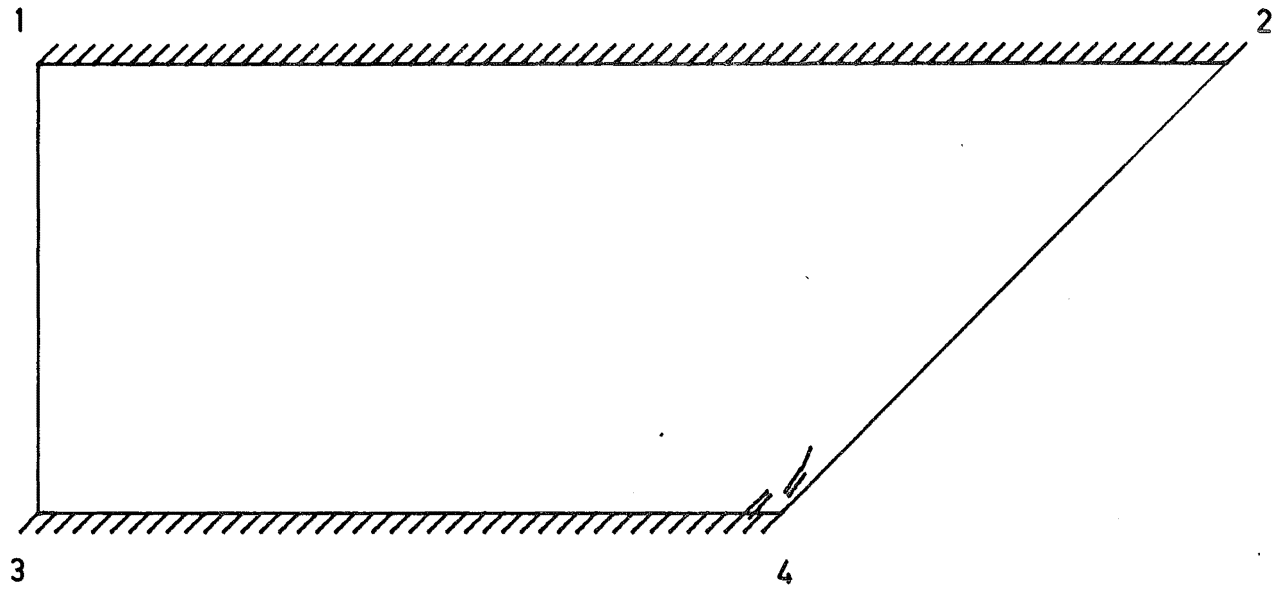

Top Surface

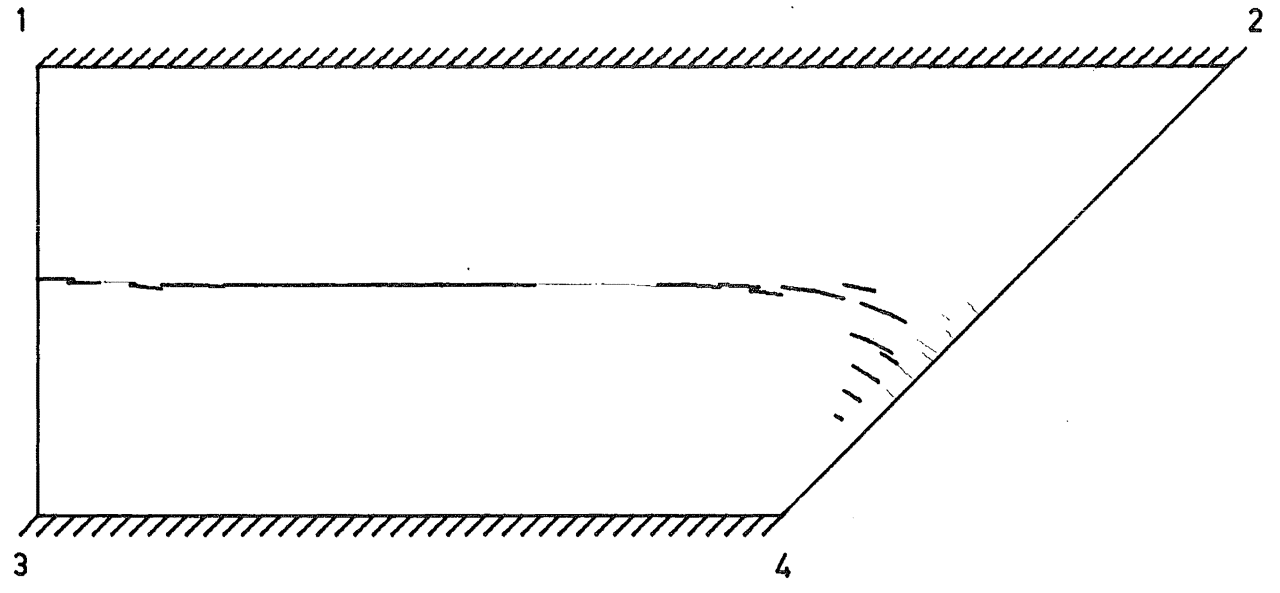

Bottom Surface

Fig. 6.21. Crack Patterns for Islam's L-Shaped Slab - 282 lb./sq.ft

two of the elements surrounding this point have failed. However, this high stress has not extended very far.

At the load 308 lb./sq.ft the cracked regions, shown in Fig. 6.22, broadened. On the bottom surface the cracking on the line 1-3 became non-symmetrical and had a bias towards point 1. Along the line of symmetry the stresses were not as high as at points inside this line. This is a result of the corner support condition at point 4. Cracking has propagated along the line of symmetry towards point 2 which has become doubly cracked as can be seen in the figure showing the top surface cracks. The top surface cracks at point 4 have propagated though the failure zone at this point has remained stationary.

Fig. 6.23 shows the cracked regions at the load 334 lb./sq.ft. Again the cracking has broadened and two new features have arisen. The central cracked zone on the bottom surface has started to propagate in a wide band towards point 2 and cracking on the bottom surface has progressed to a point on the boundary on the line 3-4. On the top surface a crack has formed near point 4 which approximately bisects the angle that lines 4-2 and 3-1 make.

Just below the theoretical ultimate load, at 360 lb./sq.ft the basic crack patterns (Fig. 6.24) have not changed very much apart from becoming broader. On the bottom surface the longitudinal cracked region divides into two paths, one region going towards point 2 and the other meeting a similar

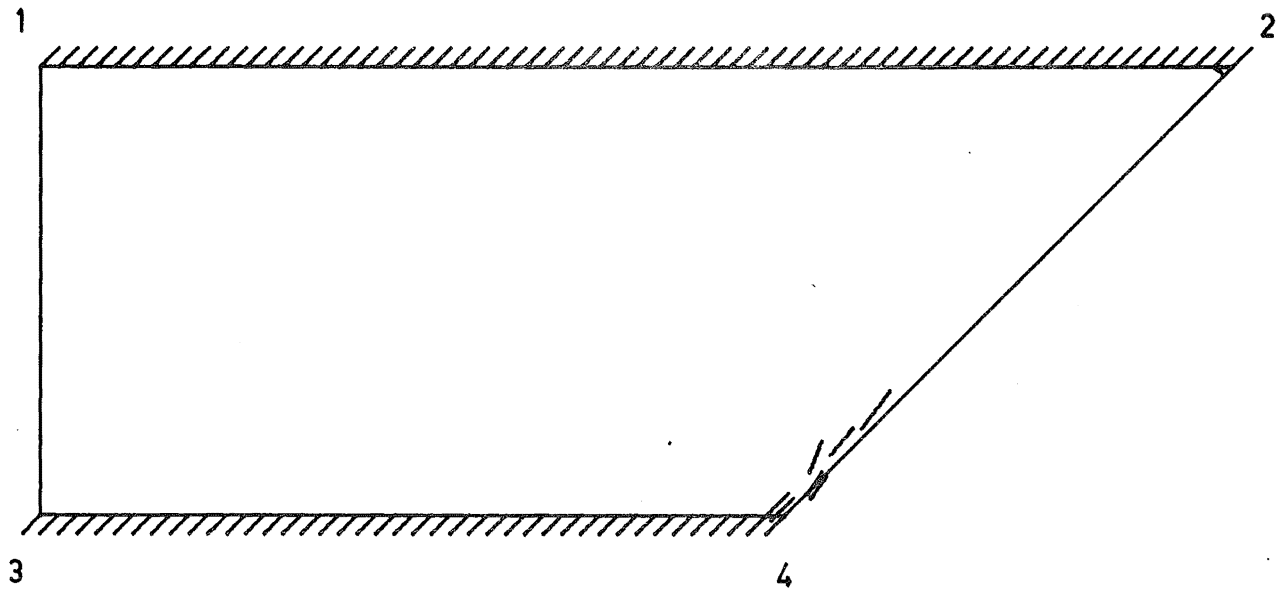

Top Surface

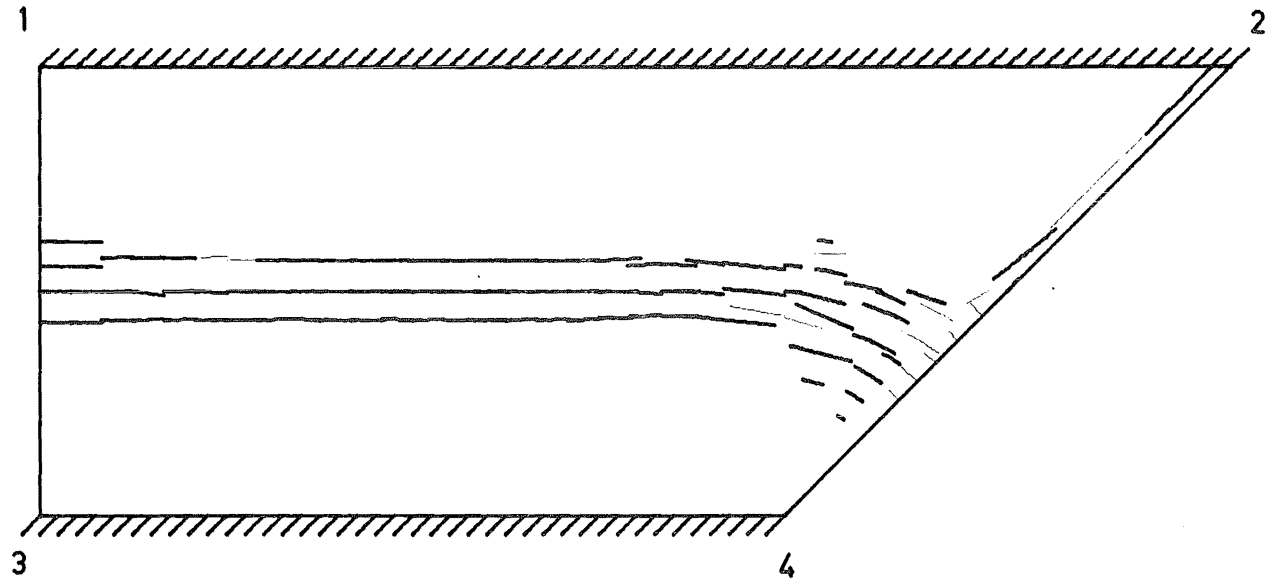

Bottom Surface

Fig. 6.22. Crack Patterns for Islam's L-Shaped Slab - 308 lb./sq. ft

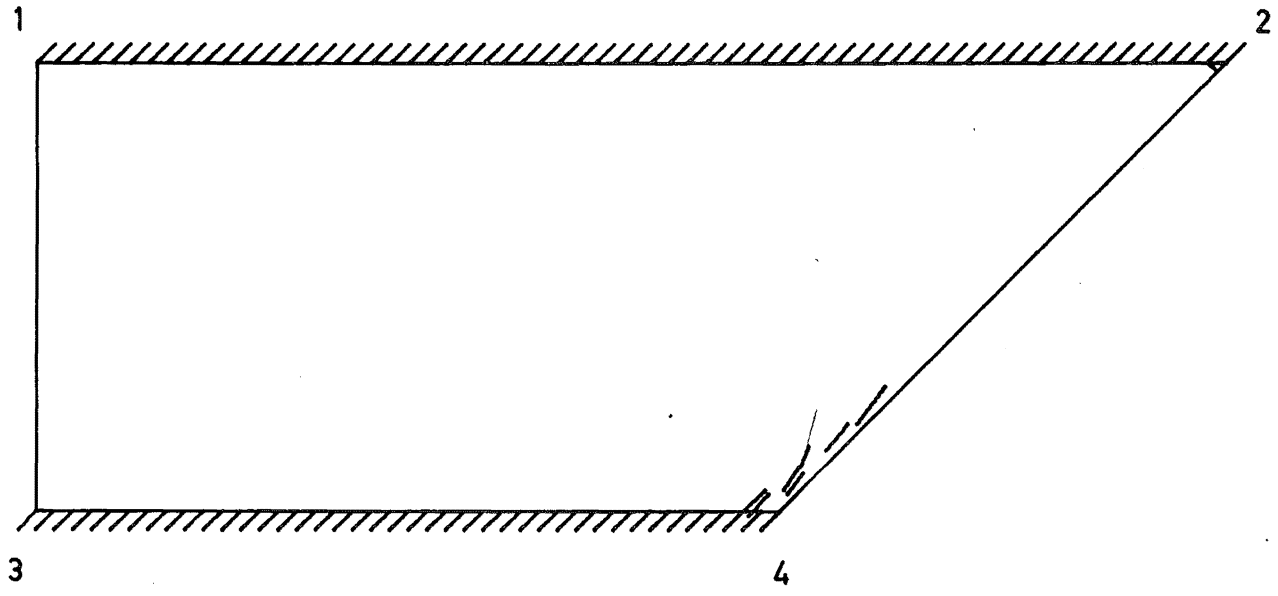

Top Surface

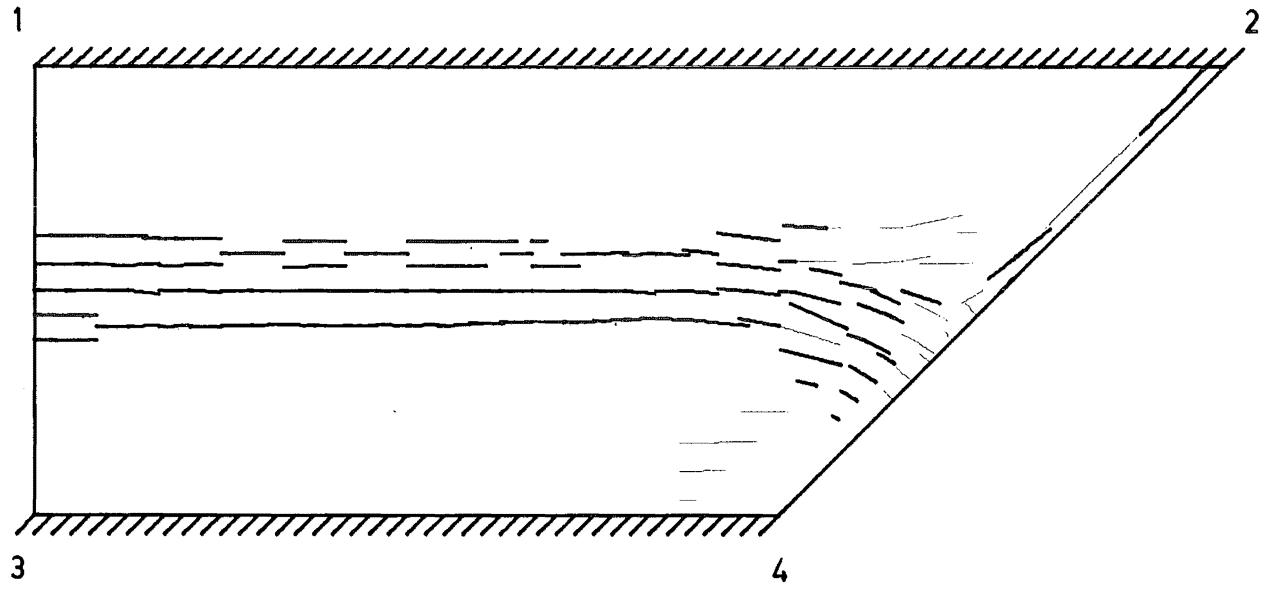

Bottom Surface

Fig. 6.23. Crack Patterns for Islam's L-Shaped Slab - 334 lb./sq. ft

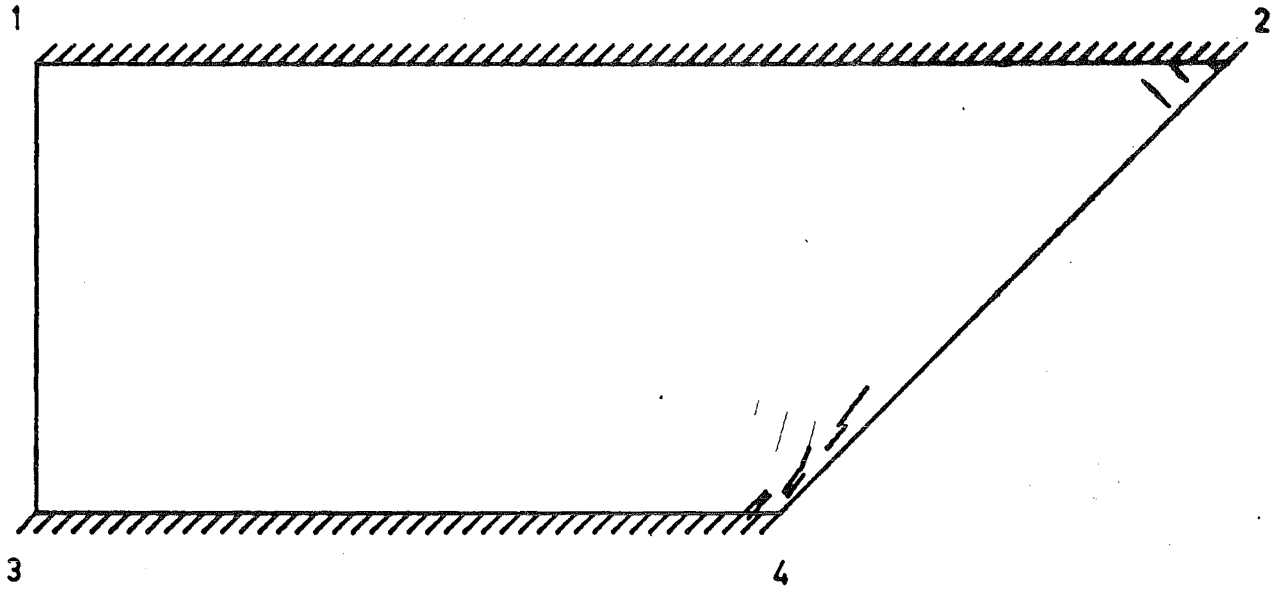

Top Surface

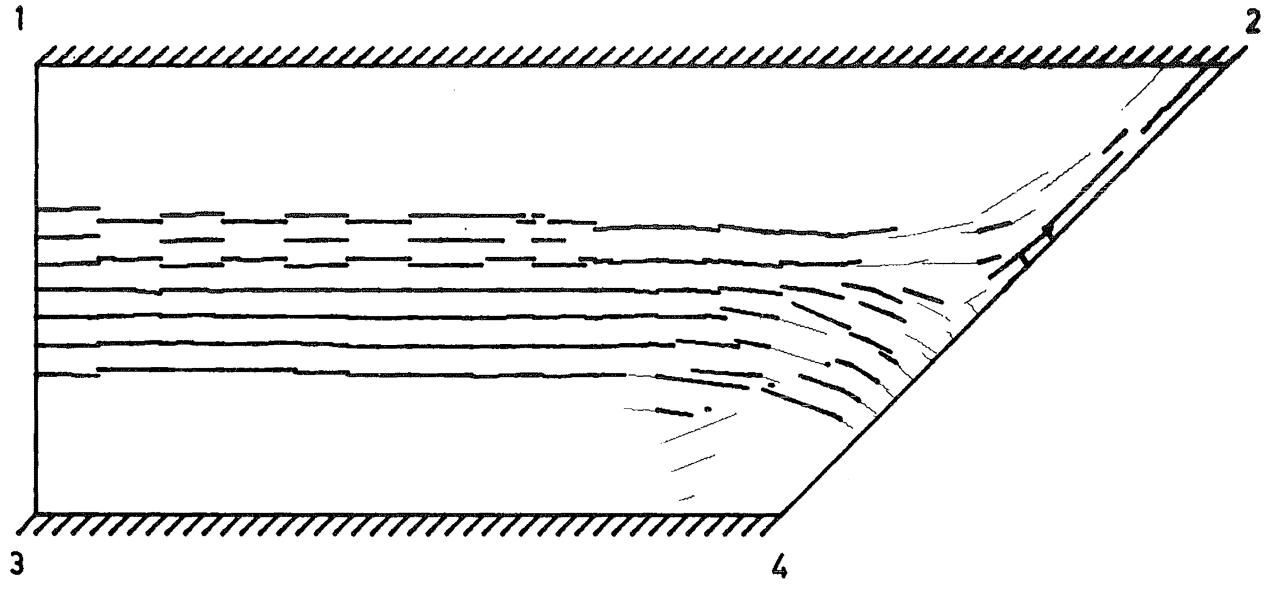

Bottom Surface

Fig. 6.24. Crack Patterns for Islam's L-Shaped Slab - 360 lb./sq. ft

region from the other half of the slab. There was also a tendency for a section near point 4 to fold away from the principal longitudinal portion along the line 3-4. This effect is a result of the high stress conditions and the cracking by point 4. Along the line of symmetry one element has been doubly cracked and this region is probably the point about which the longitudinal portion (along the line 1-2) has folded. On the top surface the cracking has increased at point 2 and also near point 4. The failure region near point 4 has not increased and the slab failure was by longitudinal folding (similar to Islam's rectangular slab, refer Section 6.2).

The final crack patterns were photographed by Islam and they have been reproduced in Fig. 6.25. The experimental cracks on the bottom surface vary considerably in width though there is a similarity between the experiment and the theory for the longitudinal cracks. However, the theory has predicted a narrower band of cracks progressing towards point 2. In the experimental slab there is a tendency (complete in one leg) for the longitudinal cracks to move towards the boundary near point 4 which also agrees with the theory. On the top surface the cracking near point 4 has not occurred along the line of symmetry but to either side of it. This again is the result of the support condition at point 4 imposing higher stresses to either side rather than along the line of symmetry. In the experimental slab there is no sign

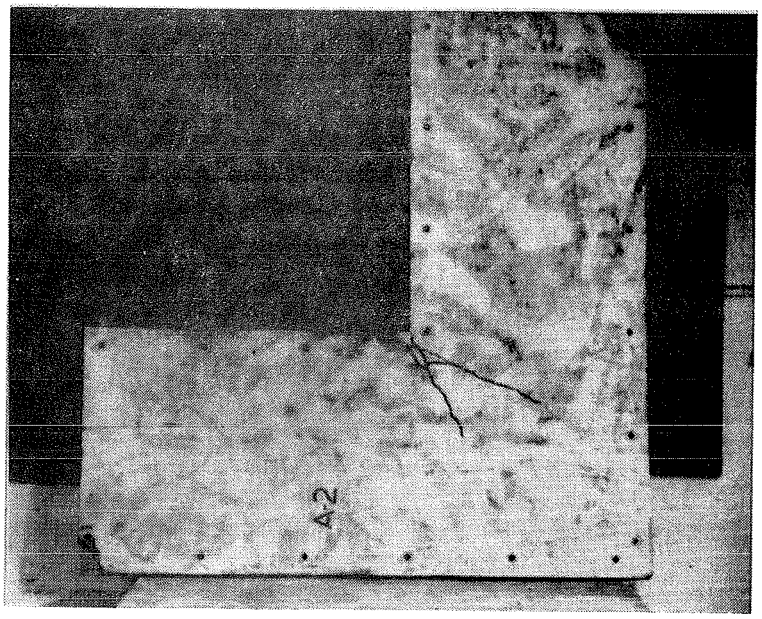

Top surface

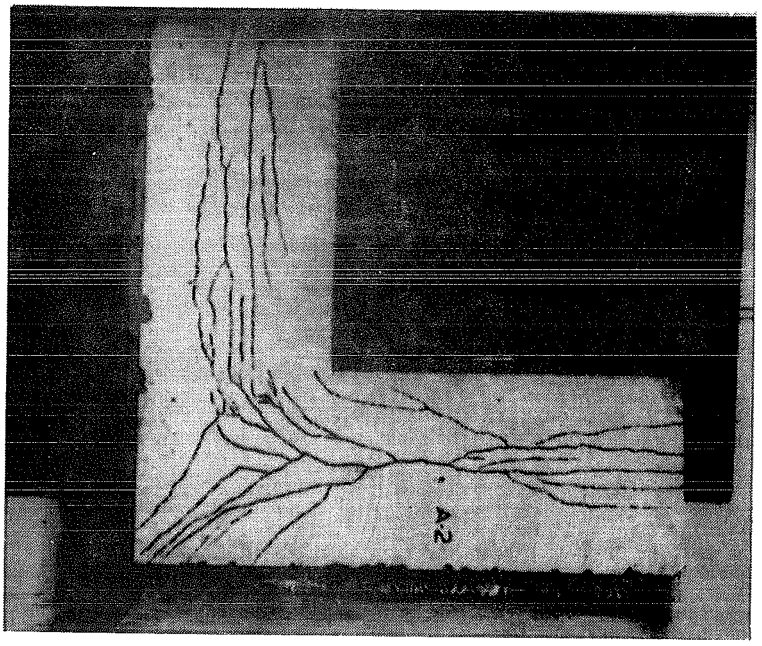

Bottom surface

Fig. 6.25. Experimental Crack Patterns

of the cracking which occurred in the theoretical crack patterns at the point 2. However, the reinforcement at these cracks may not have had a permanent set in which case they could not be seen in Fig. 6.25.

Fig. 6.26 shows the experimental and theoretical load-deflection curves for points A and C (refer Fig. 6.3 for the nomenclature) which theoretically, due to symmetry, behave identically. We will consider first the experimental curves; the more flexible curve was for point C, the other for point A. The displacement values are again joined by straight lines. Just prior to cracking the displacement at point C was almost four times as great as the displacement at point A. We would expect one of the legs of the slab to crack and yield before the other leg due to the natural variability of concrete but normally we would not expect to encounter such a large variation as is shown in Fig. 6.22. To obtain such a variation we could justifiably assume that the leg containing point C was already cracked at the time of, or soon after, the commencement of testing. When the cracking load was reached this initial cracking expanded and cracking commenced in the other leg containing point A. After the initial cracking it would appear that the reinforcement yielded at point C, but not at point A, and failure occurred in the leg containing point C. Approaching the failure load the displacement of point C is again almost four times the displacement of point A. From Islam's photographs of the final cracked

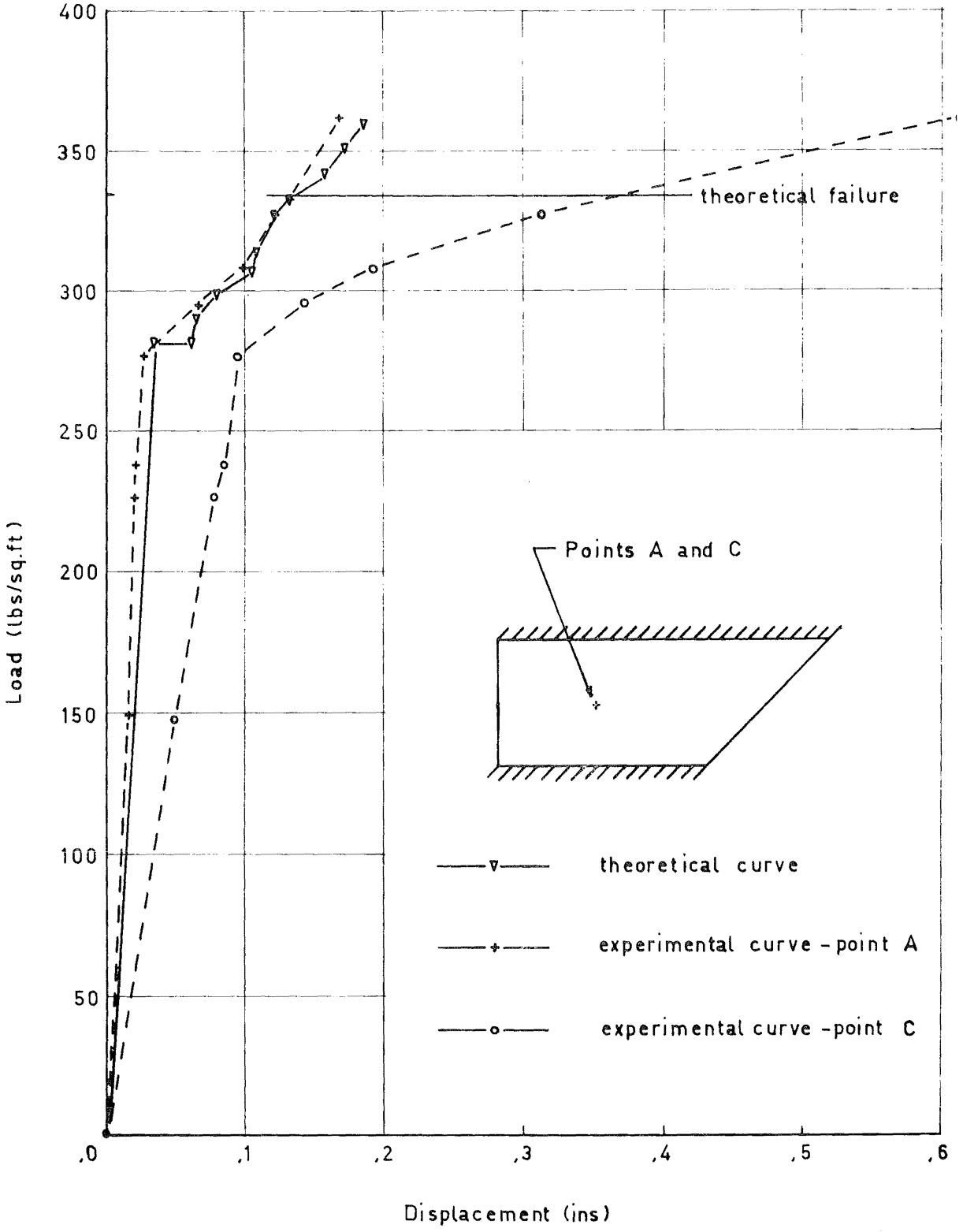

Fig. 6.26. Load - Displacement Curves for Points A and C

state of the slabs (Fig. 6.25) we see that the cracked and yielded regions are generally quite broad, the only exception being a small region on the bottom surface, near point A, where the central cracking merges into a single crack. It appears that the mortar properties may have caused excessive cracking at point C, and a deficit of cracking at point B (refer, also to Section 6.2). In another test on a similar mortar slab, again from Islam, the ratio of the displacement at the point C to the displacement at the point A was less than 2:1.

The theoretical curve is slightly more flexible than the curve for point A, the stiffer of the two experimental curves. At first cracking the theoretical curve almost doubled its uncracked deflection but with further increase of load there was very little increase in deflection and the curve returned, at a load of 290 lb./sq.ft, to a point close to the displacement curve for point A. At a loading of 334 lb./sq.ft the slab reached its ultimate moment capacity and theoretically failed. Because the ultimate strain of the reinforcement assumed in Section 6.1 was so low, i.e. .00433, the analysis was continued using the same section properties but assuming that the reinforcement did not fail at this strain. The experimental slab failed at a load of 362 lb./sq.ft and the theoretical maximum tensile strain of the reinforcement at this load was .00543 which is approximately 25% greater than the assumed maximum tensile strain.

The load-displacement curve of point B is shown in Fig. 6.27. We see that the first three displacement values are very small, i.e. .001", .004", and .011" and it is possible that some error may have occurred when reading them. The theoretical curve, apart from being much more flexible up to the cracking load, has undergone a larger displacement at the cracking load than the experimental curve. Similar to the curves in Fig. 6.26, however, the experimental and theoretical displacements are almost identical at a load of 300 lb./sq.ft. As the load increases the displacement in the experimental slab becomes larger than the theoretical displacement. This could be the result of two effects. The first effect is from the large displacements in the leg containing the point C; these displacements increase rapidly for loads greater than the cracking load and we would expect this effect to be carried into the other leg for a certain distance. The other effect arose in the theory and is from a very high stress which occurred near the centre of the line of symmetry (i.e. along line 2-4). The stresses at adjacent nodes were approximately 50% of this stress and therefore the effect of the high stress was nullified. However, in the experimental slab this stress may have initiated further cracking. (This would explain the greater region of cracking that was observed in the experimental slab along the line of symmetry.)

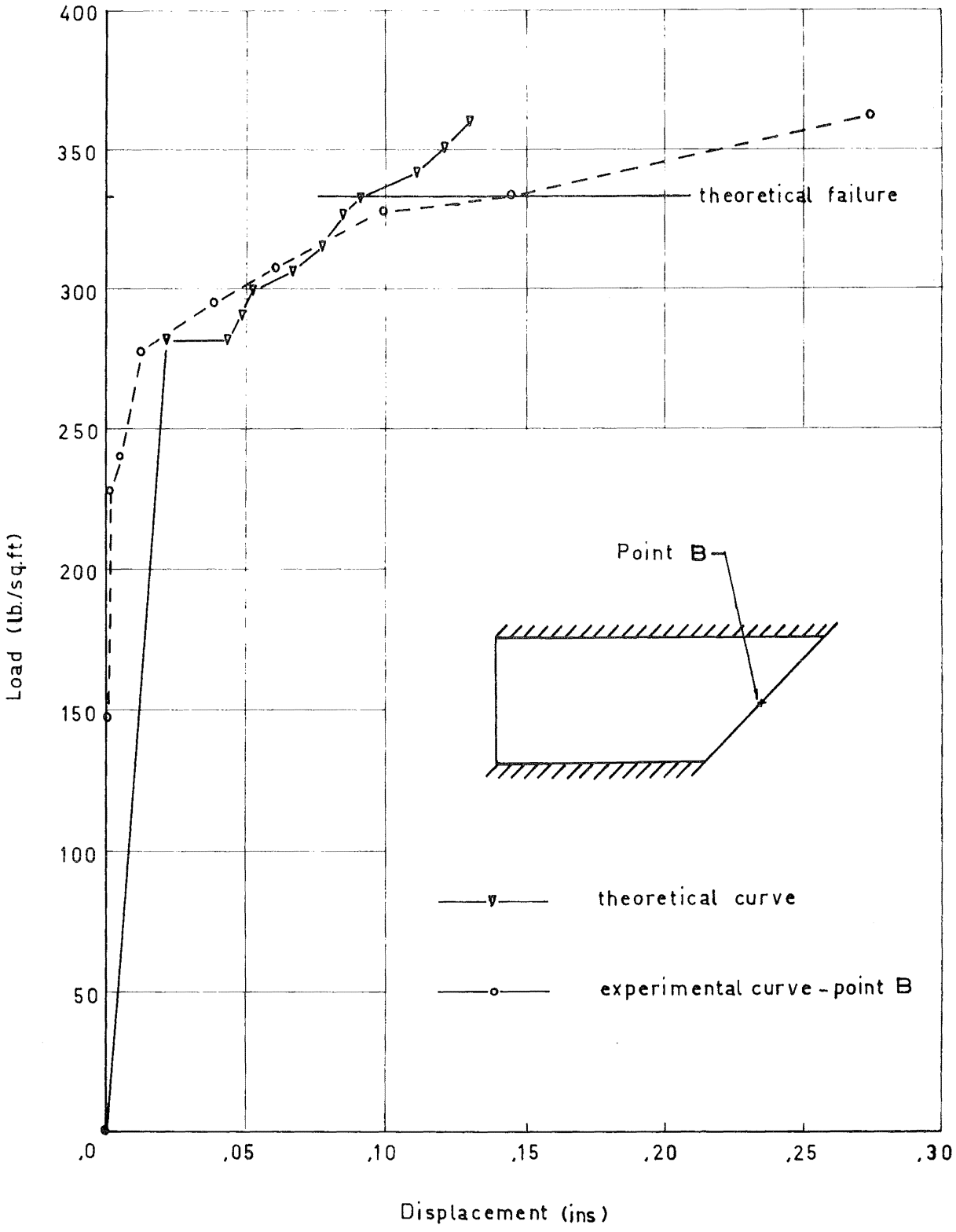

Fig. 6.27. Load - Displacement Curves for Point B

The displacement profile (normalised to 1) along line 1-3 is shown in Fig. 6.28: for the uncracked state, at a load of 282 lb./sq.ft, and at a load of 334 lb./sq.ft. The curves are very similar so only the curve for the load 282 lb./sq.ft has been drawn. In this slab cracking was not symmetrical on the line 1-3 although the displacements have not been significantly altered. Upon cracking the uncracked portions of the sides moved as a rigid body though this portion was reduced with further cracking.

Fig. 6.29 shows the displacement profiles (normalised to 1) for the line 2-4 for the above mentioned cases. Near point 2 the displacement is almost zero for all the cases but this is to be expected because it was only at the ultimate load that substantial cracking occurred at this region (refer Fig. 6.24). At point 4 the uncracked curve indicates a partial restraint but this is not seen after cracking. However, this was the point where the surrounding elements failed when cracking was initiated (refer Fig. 6.19) and hence the partial restraint was removed. This removal has had an additional effect on the cracked deflection profiles of moving the point of maximum displacement closer to point 4.

The displacement profiles along the line 5-6 are shown in Fig. 6.30 for these three cases. These profiles are quite different for the uncracked and cracked states. The uncracked profile decreases quickly from its maximum value at the point 5 and it reaches its minimum value before

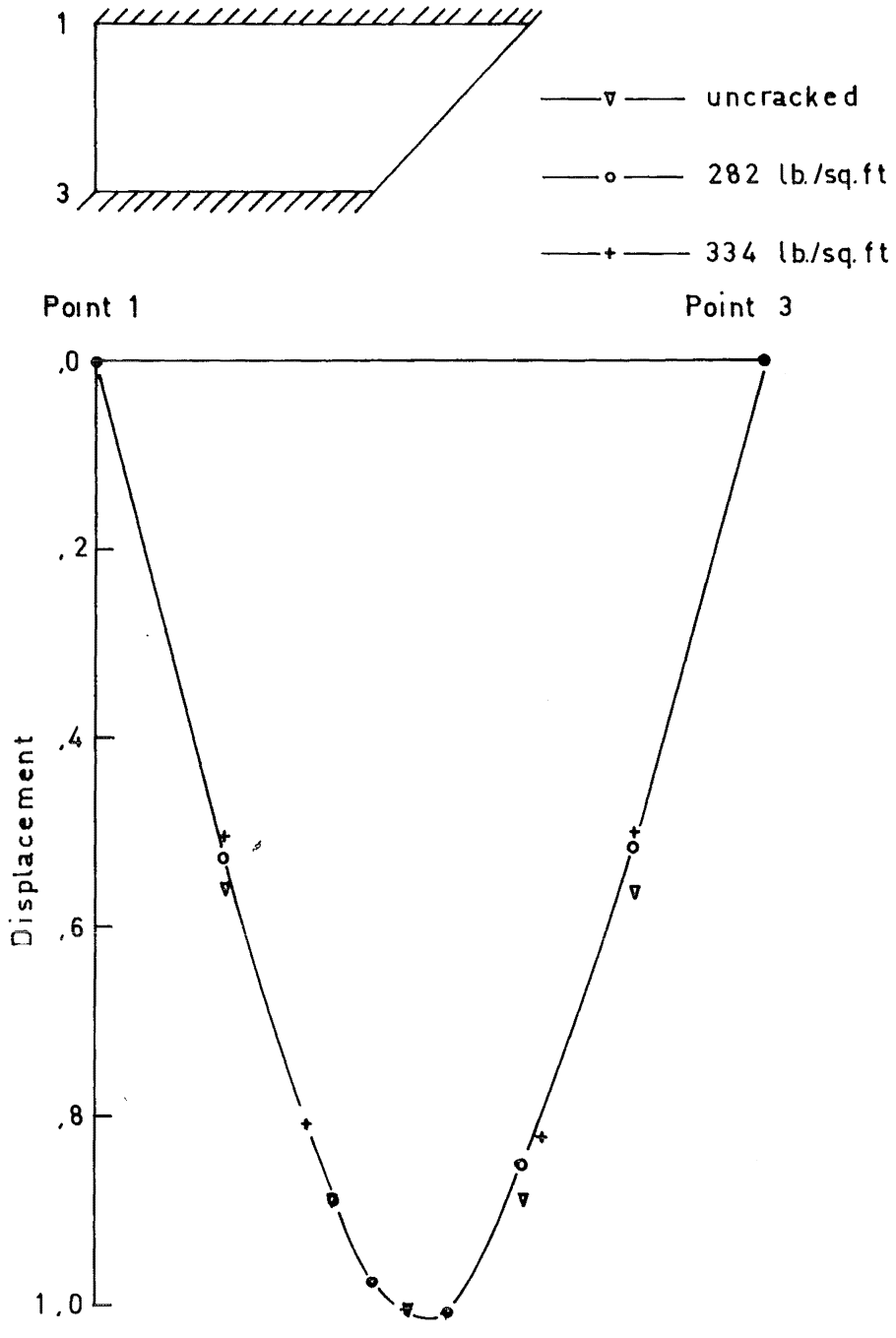

Fig. 6.28. Displacement Profiles Along the Line 1 - 3

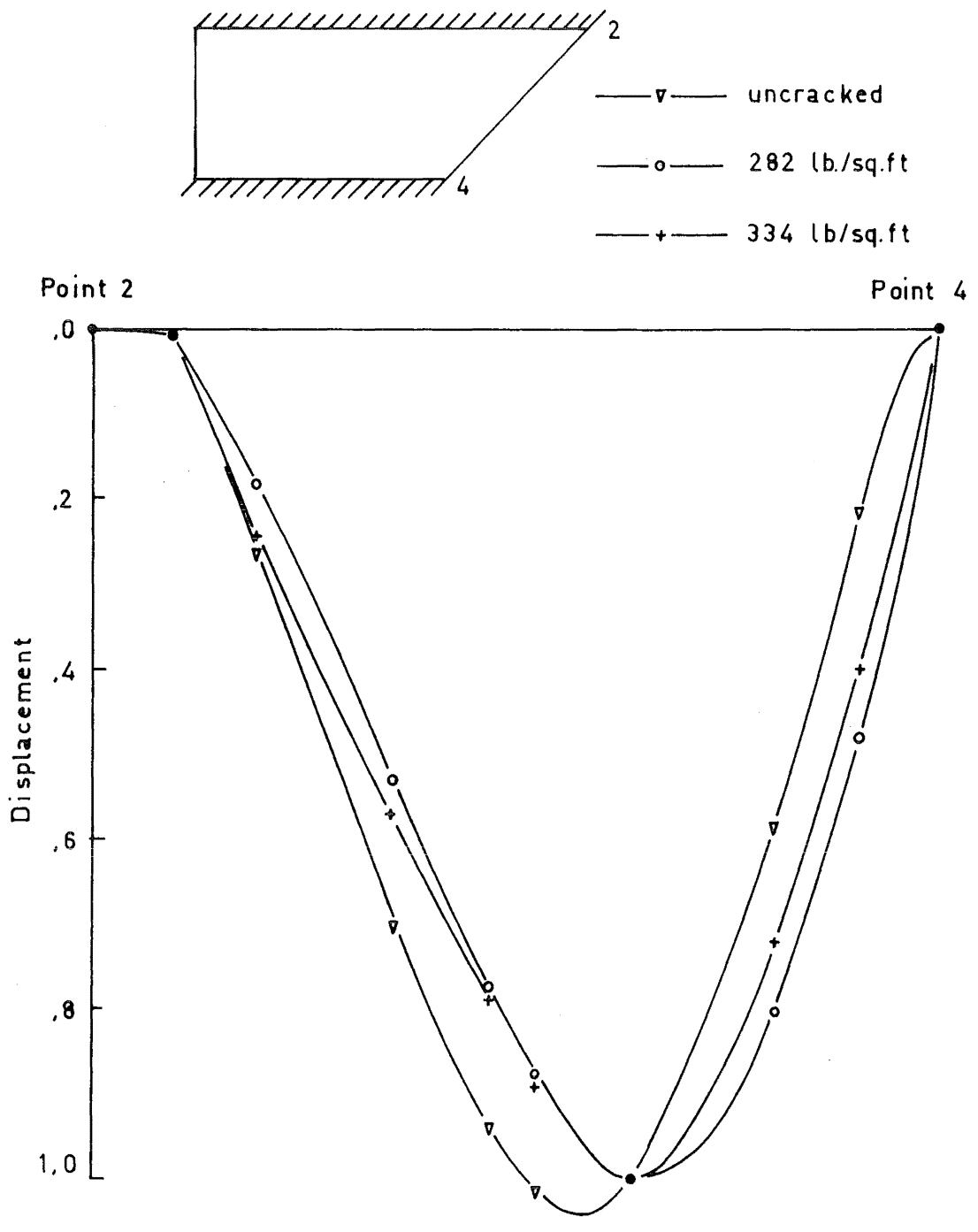

Fig. 6.29. Displacement Profiles Along the Line 2-4

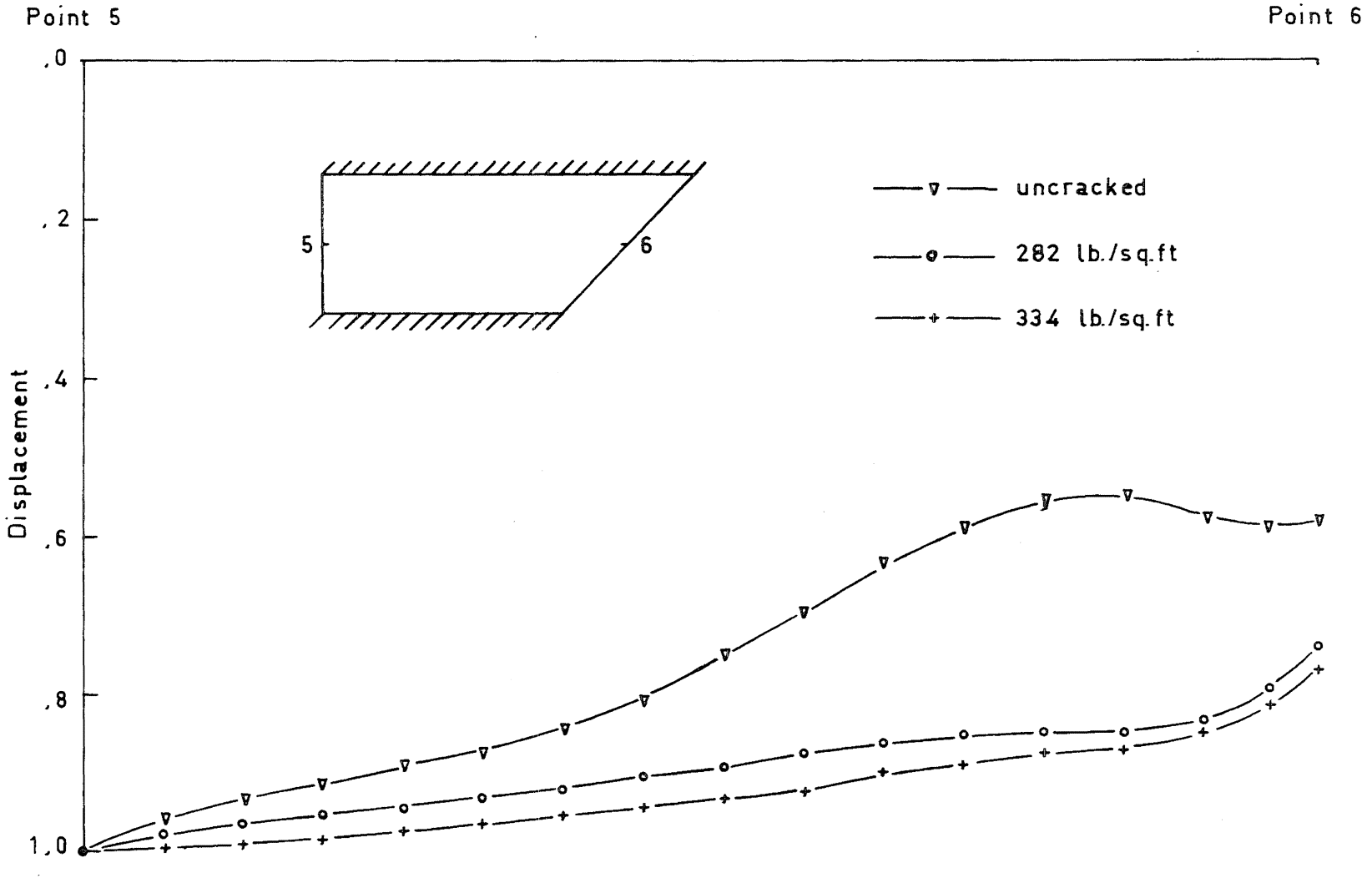

Fig. 6.30. Displacement Profiles Along the Line 5-6

reaching the point 6 (this is due to the effect of the corner support at point 4). When cracked we see the same phenomenon as was seen in Islam's rectangular slab (Section 6.2); namely a tendency for longitudinal folding which seeks to equalize the displacements along the line 5-6. However, due to the restraint imposed by the conditions of symmetry at line 2-4 this equality is not attained. The minimum displacement is now at point 6 because cracking has removed the effect of the support at point 4.

Summarising this series of tests the principal points are:

a) it was possible to obtain load-deflection curves for a variety of moment-curvature curves and hence the effect of assuming different material relationships could be observed,

b) the experimental slabs appeared to be influenced, to differing extents, by a slight spalling of the mortar in the compression region above the cracks. Thus, the cracked sections would be weakened even further and additional strains would be imposed upon the reinforcement. This would produce larger displacements than those predicted by the theory, and also the ultimate load would be reduced,

c) the theoretical analyses predicted a greater strength for the slab (approximately 27% greater) and smaller displacements,

d) the theoretical cracked and yielded regions were

normally wider than in the experimental slab,

e) the two experimental rectangular slabs were very dissimilar in their behaviour and the L-shaped slab did not behave symmetrically.

C H A P T E R 7

RECTANGULAR SLAB TESTED BY SHARPE

This chapter describes the analysis of a rectangular reinforced concrete slab which was tested by Sharpe[14] at the University of Melbourne in 1966. Sharpe was comparing the elastic yield-line method of design with lower bound methods.

The first section describes the slab and states the slab information that Sharpe gave and the slab information that had to be assumed. The second section contains an analysis of the slab using;

a) the moment-curvature relationship that takes an equivalent-displacement curvature and a rectangular bond stress distribution, and

b) the moment-curvature relationship that takes the curvature at a cracked section.

This is followed by a third analysis which assumes an enhancement in the slab strength due to partial distortion of the reinforcement (refer Section 4.3). The above analyses use elements that are either completely uncracked or completely cracked.

The third section describes two analyses of this slab which use the elastic/inelastic finite elements that were described in Sections 5.1 and 5.2. After this section there

is a summary of the principal results and conclusions which arose from this chapter.

7.1 Slab Information

The rectangular slab is shown in Fig. 7.1; the single hatching represents simple support conditions and the cross-hatching represents fixed support conditions. Sharpe measured the transverse displacement for this slab (which he labelled slab B.2) at the points A and B.

The material properties that Sharpe gave were:

Reinforcement (top and bottom)

in the long span $\frac{3"}{8}\,\emptyset$ at 9" centres,

and in the short span $\frac{3"}{8}\,\emptyset$ at 8" centres.

Yield stress of the reinforcement = 41,000 lb./sq.in.

Ultimate stress of the reinforcement = 67,000 lb./sq.in.

Total depth of the slab = 3.25 in.

Effective depth to the top reinforcement = .69 in.

Effective depth to the bottom reinforcement = 2.56 in.

Concrete cylinder strength = 5,450 lb./sq.in.

and the coefficient of variation was 11.5%, i.e.

626 lb./sq.in.

Additional information must be assumed to obtain the moment-curvature relationship. The modulus of elasticity of the reinforcement was assumed to be 30.0×10^6 lb./sq.in. which defines the yield strain as .00137 and, taking the ultimate reinforcement strain as .01, the effective modulus

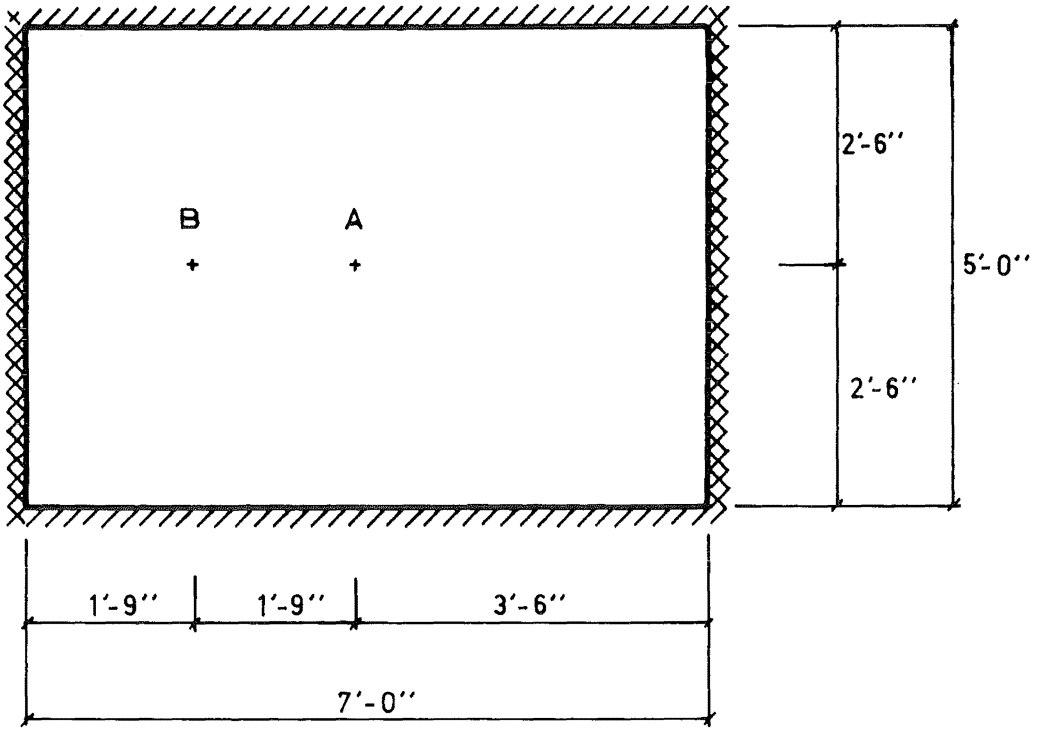

Fig. 7.1. Sharpe's Rectangular Slab

of elasticity after yielding was 3.0×10^6 lb./sq.in.

The modulus of elasticity for the concrete was calculated according to the formula given in the ACI Building Code[75], i.e.

$$E_c = w^{1.5}\ 33\ \sqrt{f'_c}$$

where E_c is the modulus of elasticity for the concrete, w is the weight of a cubic foot of concrete, and f'_c is the compressive strength of the concrete. From this formula the modulus of elasticity was calculated as 4.25×10^6 lb./sq.in. For the concrete stress-strain curve the strain corresponding to the maximum concrete stress was taken as .002 and the ultimate strain was .0035.

Sharpe notes that the cracking load was 480 lb./sq.ft, and from an elastic analysis of the slab the maximum moment at this load was 570 lb.in./in. which corresponds to a maximum concrete tensile stress of 290 lb./sq.in. which is $5.3\% f'_c$.

7.2 Analysis of Sharpe's Rectangular Slab Including a Comparison of the Effect of Allowing Partial Distortion of the Reinforcement

The analysis of Sharpe's rectangular slab utilised the mesh shown in Fig. 7.2 which has small elements where the yield region is expected to be and larger elements elsewhere. Because cracking was not as regular as for Islam's slabs this mesh was not altered to ensure that the elements were

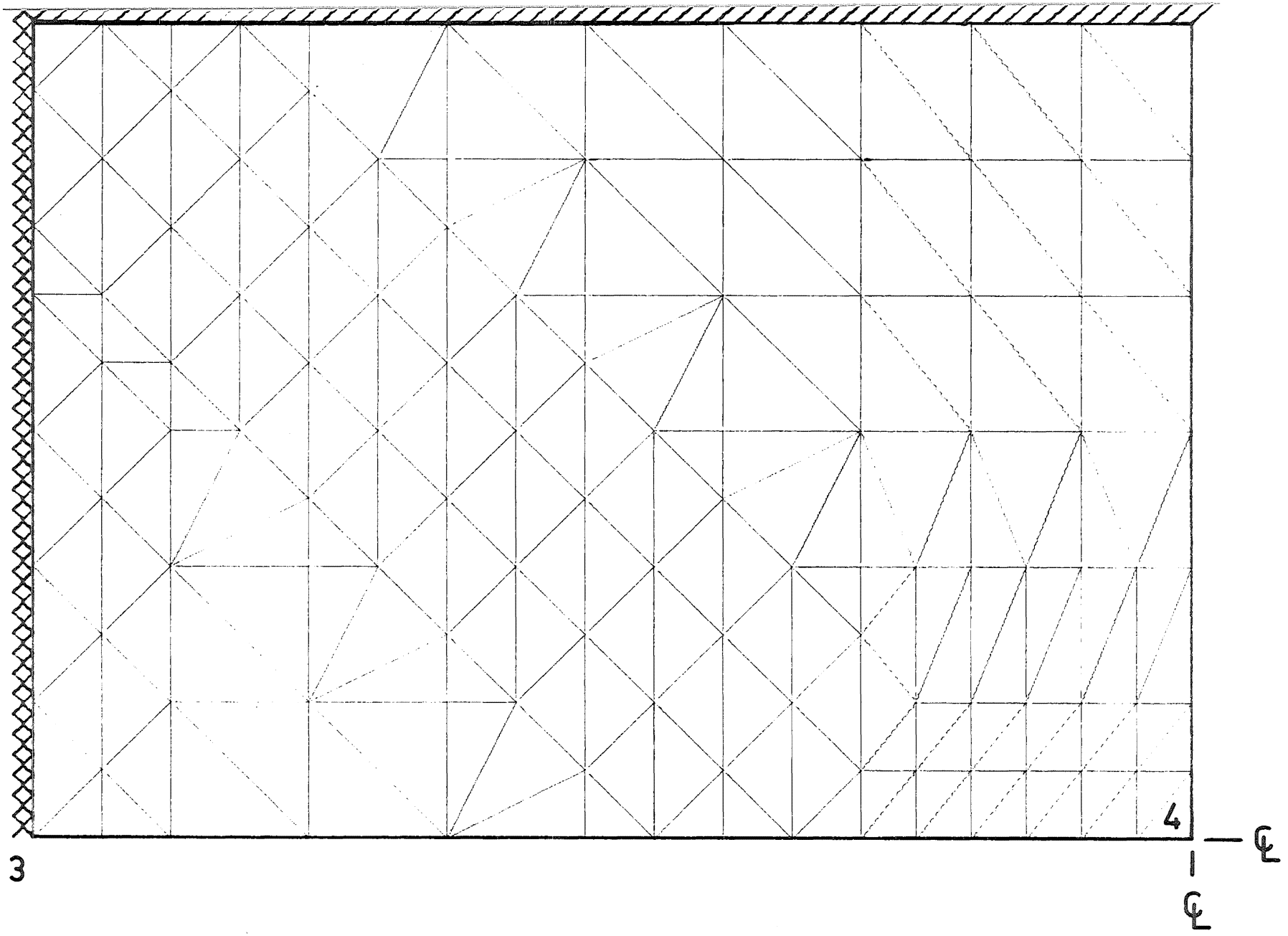

Fig. 7.2. Finite Element Mesh for Sharpe's Rectangular Slab

either totally cracked or totally uncracked. This does not appear to have had an adverse effect upon the results due to the phenomenon, mentioned previously in Section 6.2, of the nodes of elements that are about to be cracked (i.e. when redistribution is not complete) having high stresses. Thus the tendency is more towards overcracking rather than undercracking. To change the element mesh for each elastic analysis would be a tedious job because the cracking boundary changes with each redistribution; also, great care would have to be made to ensure that the element shapes were acceptable (again, a video-display unit and a light pen would ease this task). The most important feature is to ensure that the elements are small in the more sensitive regions wherein a change in stiffness would significantly affect the displacement pattern, i.e. at the centre and at the fixed boundaries.

The reinforcement $\frac{3}{8}$" Ø at 8" centres is equivalent to .0138 sq.in./in. and the reinforcement $\frac{3}{8}$" Ø at 9" centres is equivalent to .0122 sq.in./in. Because these two values do not differ much and because the other details of the material properties are only approximately known it was assumed that the slab was isotropically reinforced with $\frac{3}{8}$" Ø at 8½" centres, i.e. .0130 sq.in./in. (The inclusion of orthotropic reinforcement would not be too difficult: the two moment-curvature relationships in the reinforcement directions would have to be known and hence the moment across any section would be divided into the components acting

along the reinforcement. Therefore the flexural rigidities in the reinforcement directions could be determined as could the angle of cracking, i.e. corresponding to the principal strains, which in general would not equal the angle of the principal stresses.)

The first analysis of Sharpe's slab used a moment-curvature relationship which assumed a rectangular bond stress distribution and took the equivalent-displacement curvature. Fig. 7.3 shows this moment-curvature relationship together with the relationship that takes the curvature at a cracked section (both of these curves have been normalised to 1). It is seen that there is not a great difference between the two curves and this is due to the low maximum tensile stress assumed for the concrete.

The extent and directions of the cracked and yielded regions are shown in Figs 7.4 to 7.7 inclusive for the loads 500, 840, 1,320, 1,620 and 1,870 lb./sq.ft respectively. Fig. 7.4 shows the cracked region when the load was 500 lb./sq.ft, i.e. the slab had only just cracked. (This load is only 27.2% of the theoretical ultimate load.) The principal feature of this figure is the large area of the slab that has cracked. The principal crack directions are easily discernable although, as mentioned previously (Section 6.2), when a singly cracked element becomes cracked in two directions the angle of the second set of cracks is not as accurate as the angle for the first set of cracks

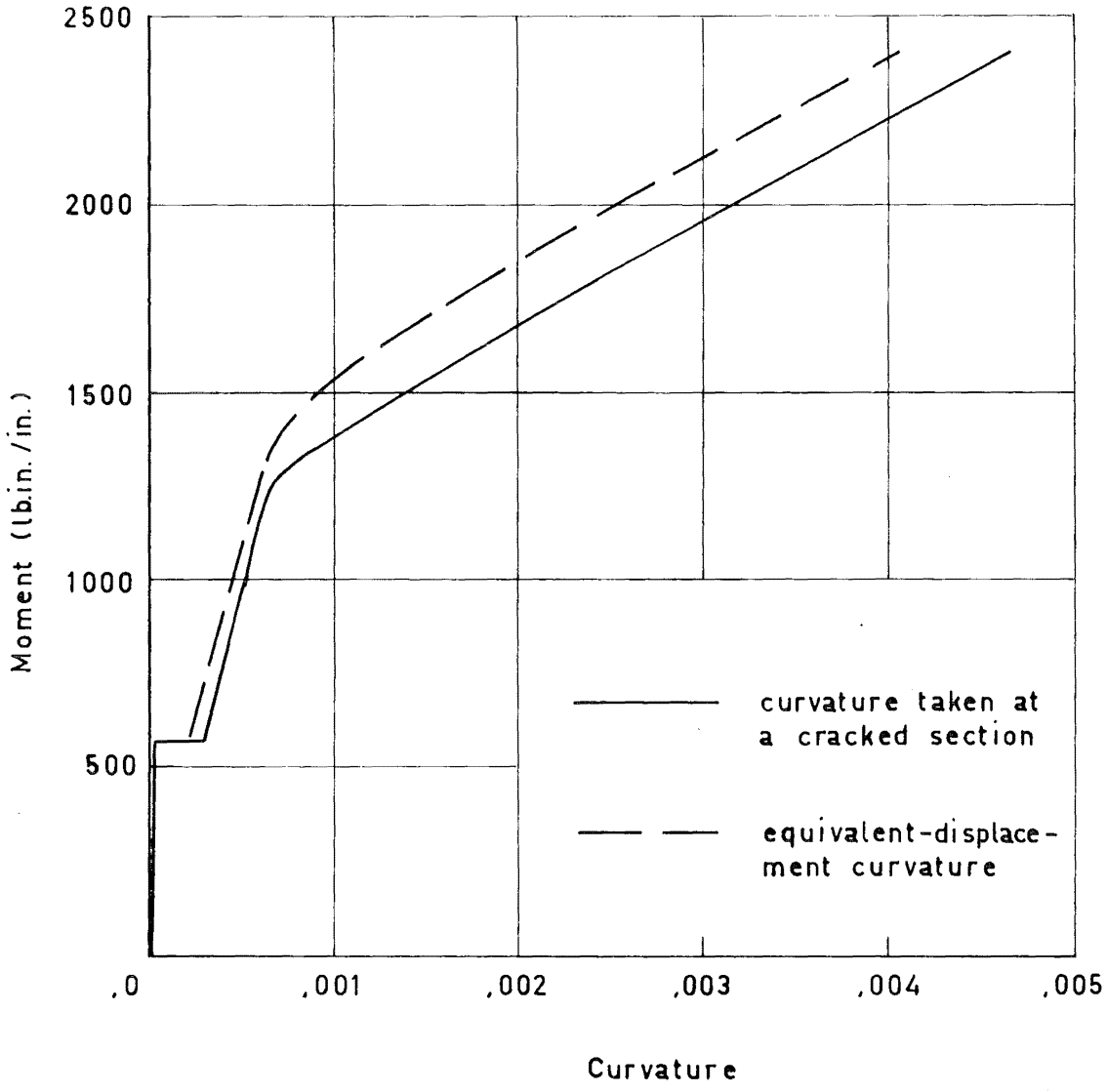

Fig. 7.3. Moment-Curvature Curves for Sharpe's Rectangular Slab

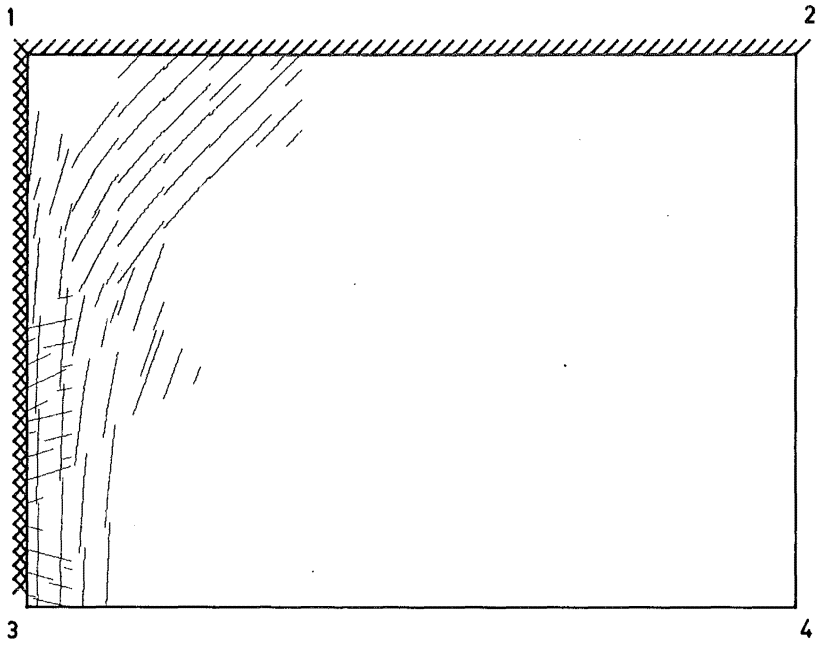

Top Surface

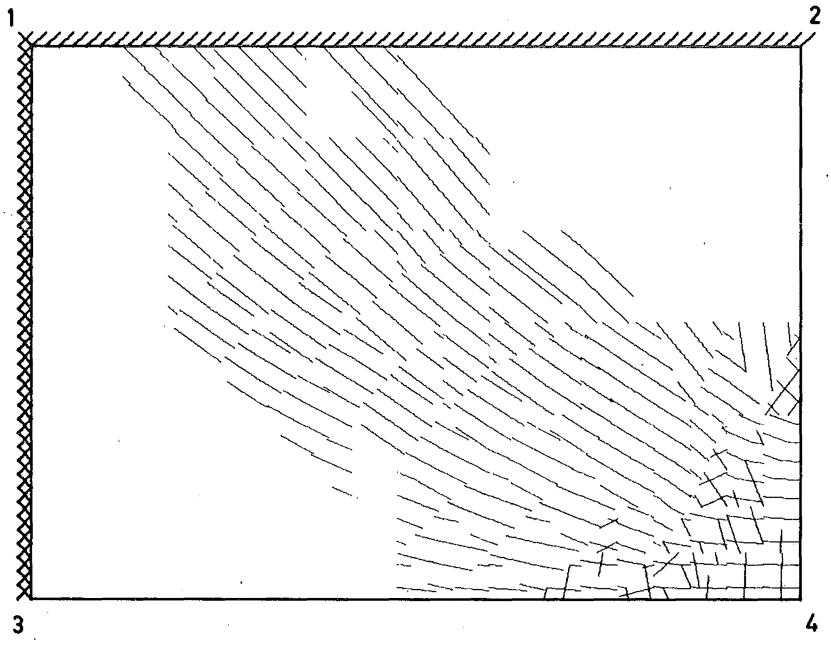

Bottom Surface

Fig. 7.4. Crack Patterns for Sharpe's Rectangular Slab - 500 lb./sq.ft

(this can be seen in both the elements near the centre of the slab and the elements on the built-in edge). The bottom surface cracking commenced at the centre of the slab and progressed along the longitudinal direction for a short distance before branching towards a point which is approximately ten inches from the corner support, i.e. point 1 (refer Fig. 7.2 for the numbering). This seems to indicate that the "hinge" along the line 1-3 would be between the line 1-3 and another line approximately ten inches from the line 1-3. The top surface cracks formed along the rigid edge and curved towards the simply supported edge. Both sets of cracks follow the pattern that the yield line theory depicts and the only variance is in the width of the cracked region. There are, however, some additional longitudinal cracks formed near the point 3 on the top surface. These have resulted from a transverse hogging moment acting along the rigid support.

The crack patterns at the load 840 lb./sq.ft, which is 45.0% of the theoretical ultimate load, are shown in Fig. 7.5. Cracking on the bottom surface covered approximately three quarters of the area. In the middle of this cracked region there is one element which has not cracked (although it would have in a real slab). Because all the surrounding elements have cracked the stresses within the element are not high enough to crack it and it is moving like a small rigid body. In the next load case, however, this element becomes cracked.

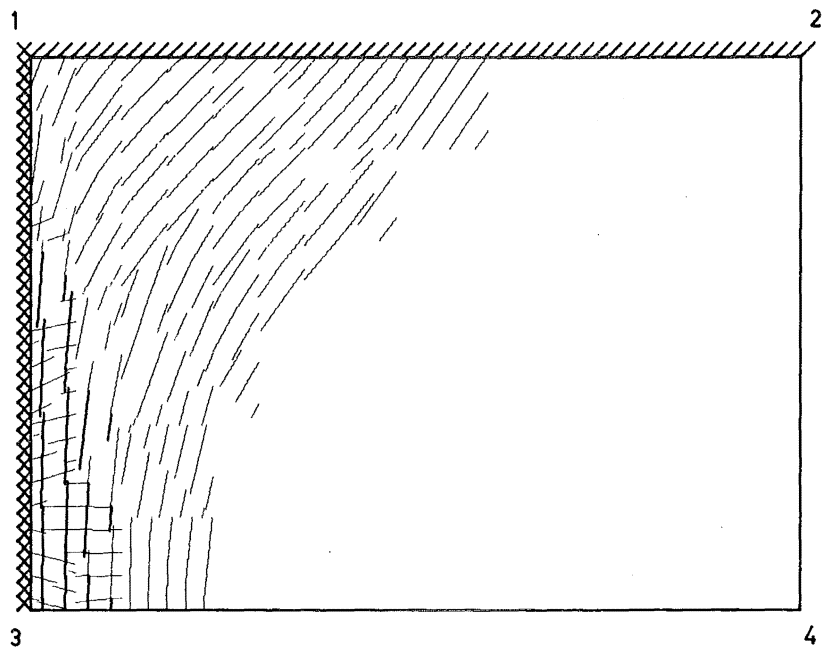

Top Surface

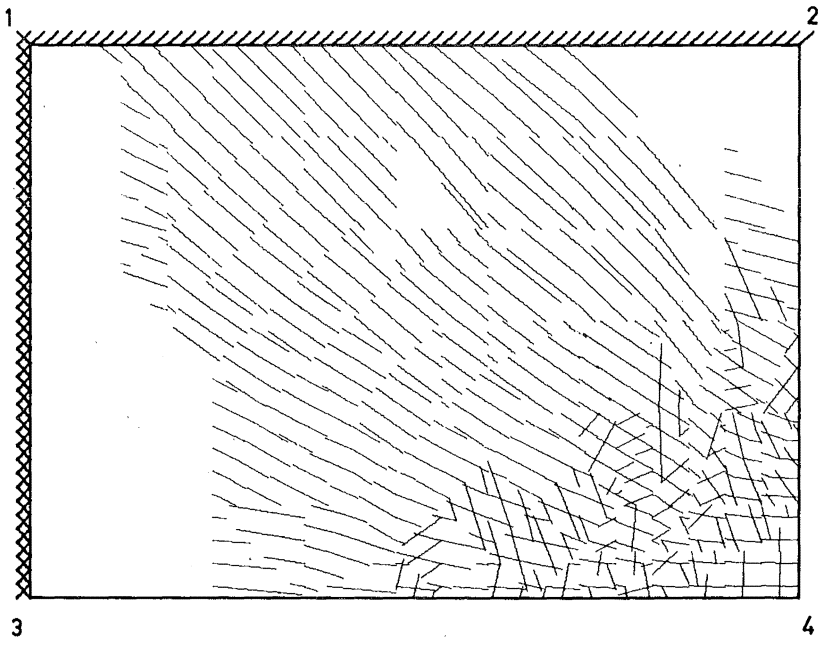

Bottom Surface

Fig. 7.5. Crack Patterns for Sharpe's Rectangular Slab - 840 lb./sq. ft

On the top surface the cracking has also expanded and some of the elements along the built-in edge have yielded.

Fig. 7.6 shows the cracked regions at the load 1,320 lb./sq.ft which is 70.7% of the theoretical ultimate load. The cracked regions have expanded and many elements have now yielded. On the bottom surface the yielded region is quite broad. There is substantial yielding around the centre of the slab, i.e. point 4, then the band progresses towards a point, approximately 10 inches from point 3, in a similar fashion to the initial cracking (shown in Fig. 7.4). On the top surface the band of yielding parallel to the rigid support has broadened and near the corner at point 1 this band curves towards the point where the bottom surface yield region meets the side 1-2. Hence in the region of this point there is a warping moment caused by the opposite curvatures on the bottom and top surfaces.

At a load of 1,620 lb./sq.ft, 86.8% of the theoretical ultimate load, the yielded regions have again expanded (Fig. 7.7). On the bottom surface there has been a slight increase in the cracked area though this cracked area was close to being fully cracked at the previous load. The region of yielding has broadened on both the bottom and the top surface. Along the fixed edge on the top surface some elements have failed (indicated by the double dark line), i.e. the theoretical moment within these elements is greater than the theoretical moment capacity of the section.

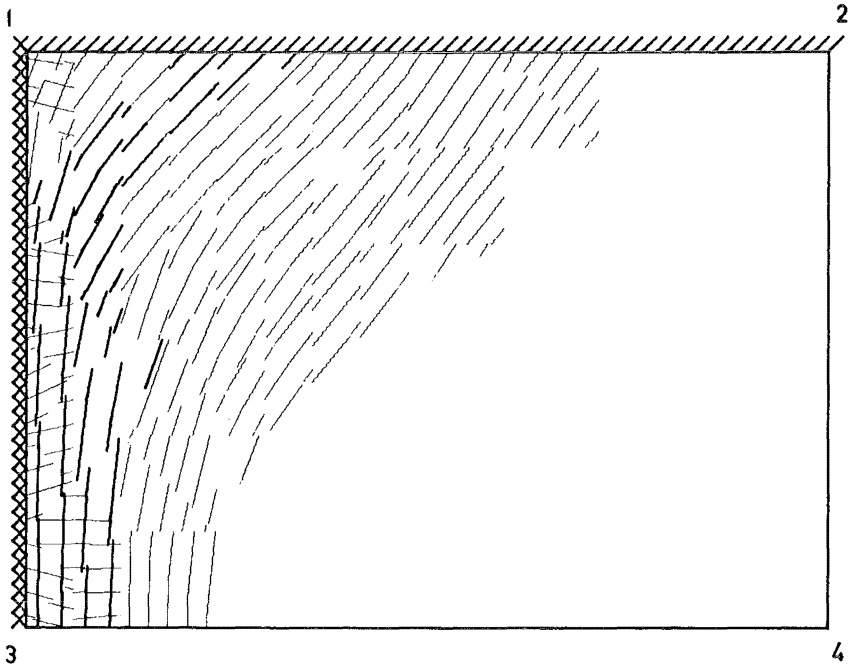

Top Surface

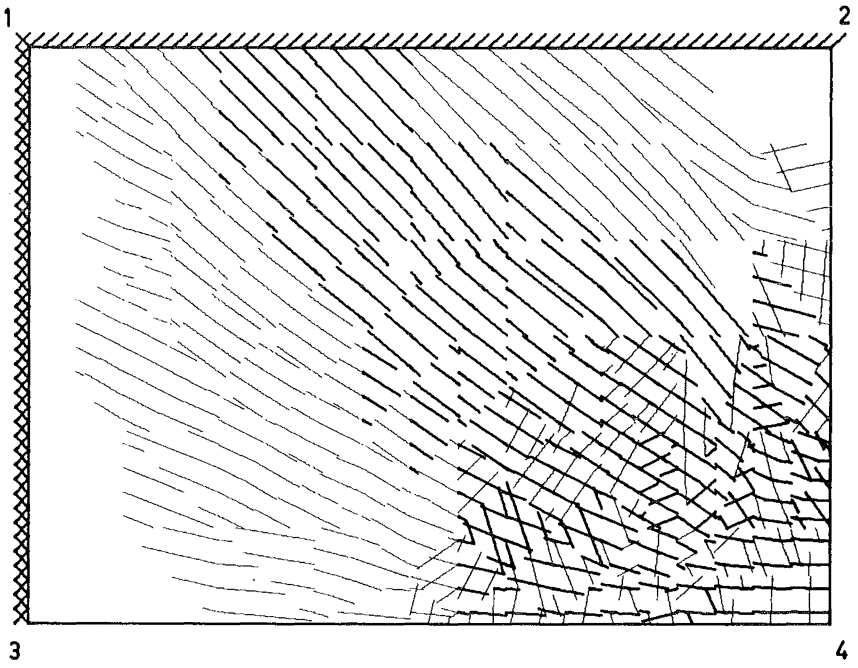

Bottom Surface

Fig. 7.6. Crack Patterns for Sharpe's Rectangular Slab - 1.320 lb./sq.ft

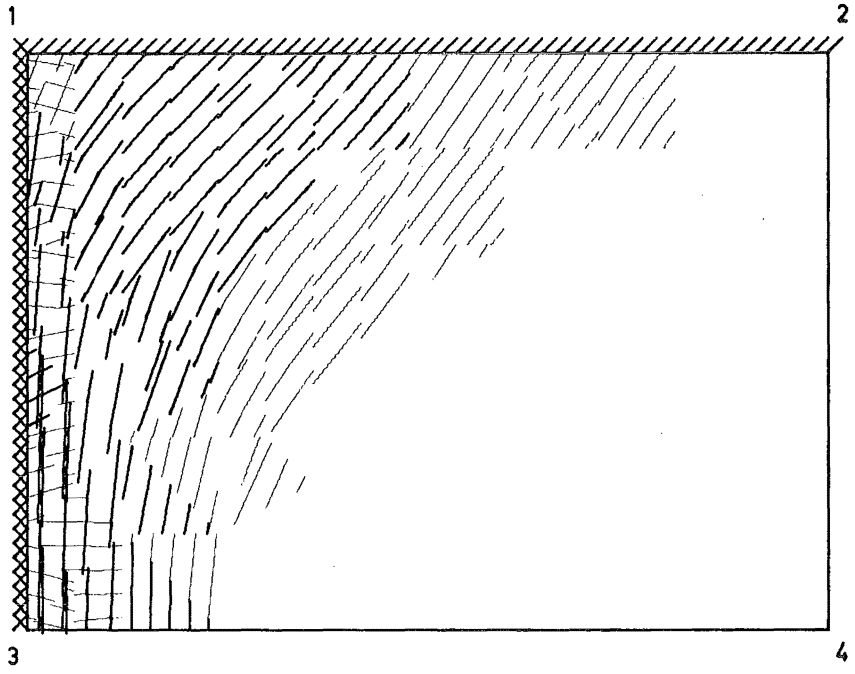

Top Surface

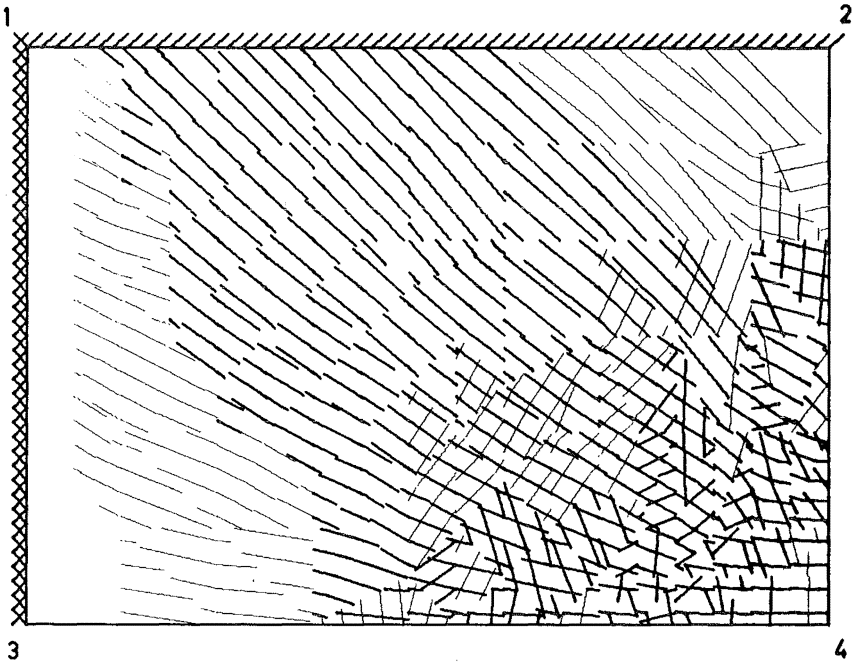

Bottom Surface

Fig. 7.7 Crack Patterns for Sharpe's Rectangular Slab - 1620 lb/sq ft

Fig. 7.8 shows the cracked regions at a load of 1,870 lb./sq.ft which is just below the theoretical ultimate load. The yielded regions have expanded slightly compared with the previous load case. The principal feature of this figure is the failure of most of the elements along the built-in edge (on the top surface). Without this restraint the slab's carrying capacity is greatly reduced and failure is imminent.

Sharpe only photographed the final cracking on the bottom surface and this photograph has been reproduced in Fig. 7.9. To obtain his end fixity he clamped the end of the slab and the line of fixity can be seen by the lines drawn on the slab. The experimental slab has more longitudinal cracking than the theory although it appears that the longitudinal cracking has occurred at the reinforcement where the weaker sections would have influenced the crack pattern. The longitudinal cracking stopped short of the rigid support and continued again after the support. Two of the cracked bands progressing towards the corners had one dominant crack going straight to the corner flanked by subsidiary cracks to either side; the other two cracked bands went to either side of the corner and it is impossible to tell whether or not the first crack progressed towards a point approximately 10 inches from the corner as they did in the theory (refer Figs 7.4 and 7.6).

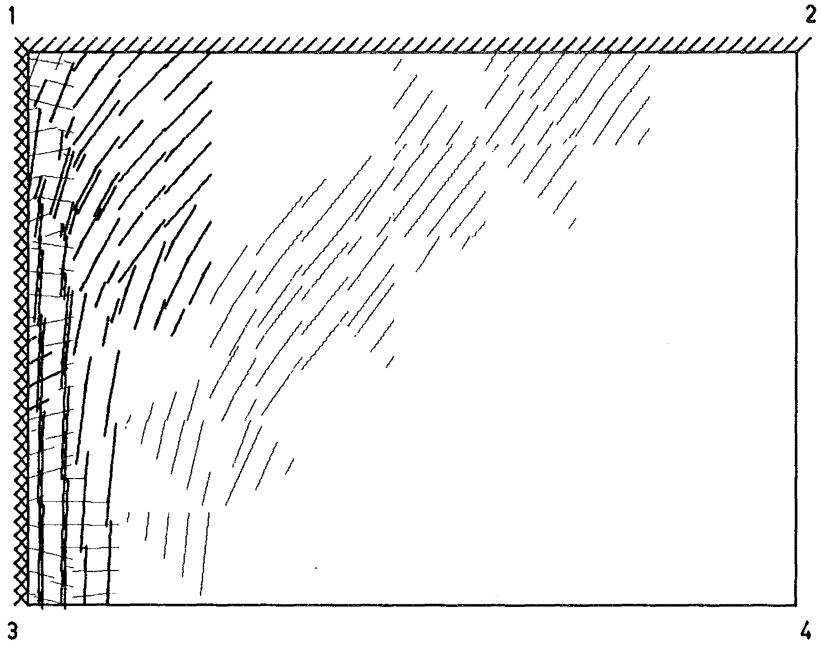

Top Surface

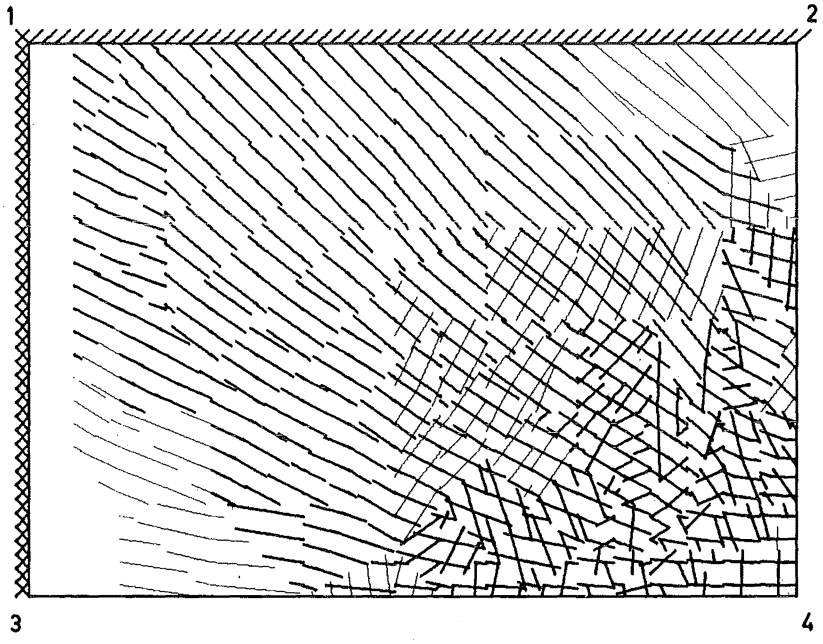

Bottom Surface

Fig. 7.8. Crack Patterns for Sharpe's Rectangular Slab - 1,870 lb./sq.ft

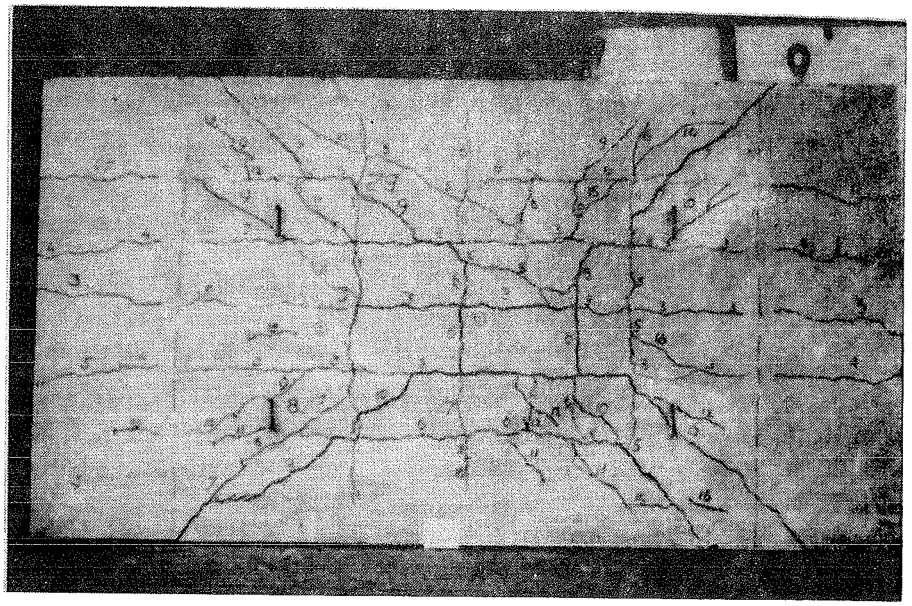

Bottom surface

Fig. 7.9. Experimental Crack Patterns

Fig. 7.10 shows the load-deflection curves for points A and B (refer Fig. 7.1 for the nomenclature). Considering the experimental curves first, Sharpe records a distinct step when the cracking moment is reached (this was not observed in Islam's slabs which had a mesh reinforcement, refer Figs 6.6 and 6.22). However, this step is to be expected considering the large region of the slab that cracked when the cracking load was reached (refer Fig. 7.4). The most notable feature about the experimental curves is the coincidence of the curves until a load which is 64% of the experimental ultimate load. Theoretically this is not feasible because point B has a large restraint caused by the built-in end and the simply supported sides; Sharpe did not comment upon this anomaly. A possible explanation, apart from faulty instrumentation, is that Sharpe's test frame underwent a rigid body rotation, caused possibly by a support deflection. This rotation would increase the displacement of point B and also, to a lesser extent, the displacement of point A. Thus both the experimental load-displacement curves would overestimate the true displacements.

The theoretical curve for point A shows that the theory has predicted a greater stiffness for the slab although the relative stiffnesses for the points are similar. The ratio of the theoretical displacement to the experimental displacement is shown for each load in Table 7.1 and, neglecting the first ratio, the experimental stiffness is approximately 75%

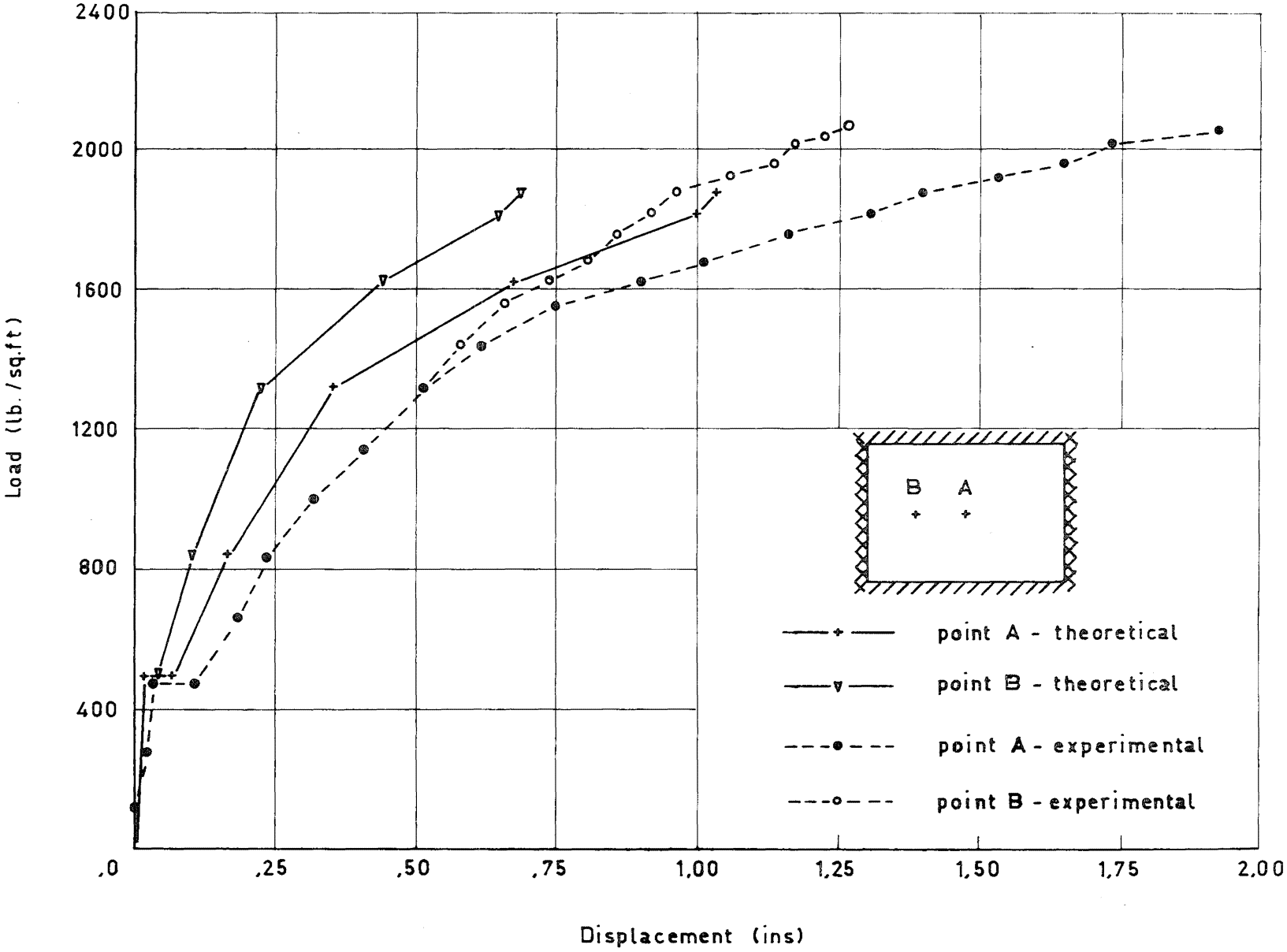

Fig. 7.10 Load Displacement Curves for Points A and B

of the theoretical stiffness, i.e. if the theoretical modulus of elasticity was 3.19×10^6 lb./sq.in. instead of 4.25×10^6 lb./sq.in. then the curves would be almost identical. From Eq. (7.1) the expected compressive strength of concrete which had a modulus of elasticity of 3.19×10^6 is 3,080 lb./sq.in. which is a reduction of 43% on the assumed experimental compressive strength of 5,450 lb./sq.in. This reduction is, however, much greater than could be expected.

Load lb./sq.ft	Displacement Ratio
500	.62
840	.72
1,320	.70
1,620	.77
1,820	.76
1,870	.75

Table 7.1 The Ratio of the Theoretical to the Experimental Displacements

Near the theoretical ultimate load (1,870 lb./sq.ft) the theoretical curve stiffens slightly before failure. However, this would not occur in an actual structure because spalling and creep would cause a smoother transition in which the stiffness would be constantly degrading.

The experimental ultimate load is greater than the theoretical ultimate load but this is to be expected because the theory does not take into account membrane forces which would enhance the load capacity of the slab. In this case the experimental ultimate load is 10% higher than the theoretical ultimate load.

Load lb./sq.ft	Displacement Ratio
500	.58
840	.60
1,320	.63
1,620	.65
1,820	.65
1,870	.65

Table 7.2 The Theoretical Displacement Ratio of Points A and B

Table 7.2 shows the ratio of the theoretical displacement of point B to the theoretical midpoint displacement and this illustrates the effect that the cracking and yielding has upon the displacements. This effect is also seen in Fig. 7.10a and Fig. 7.10b which show the displacement profiles (normalised to 1) along the longitudinal centreline (line 3-4) and the transverse centreline (line 2-4) respectively for the three load cases: before cracking, at a load

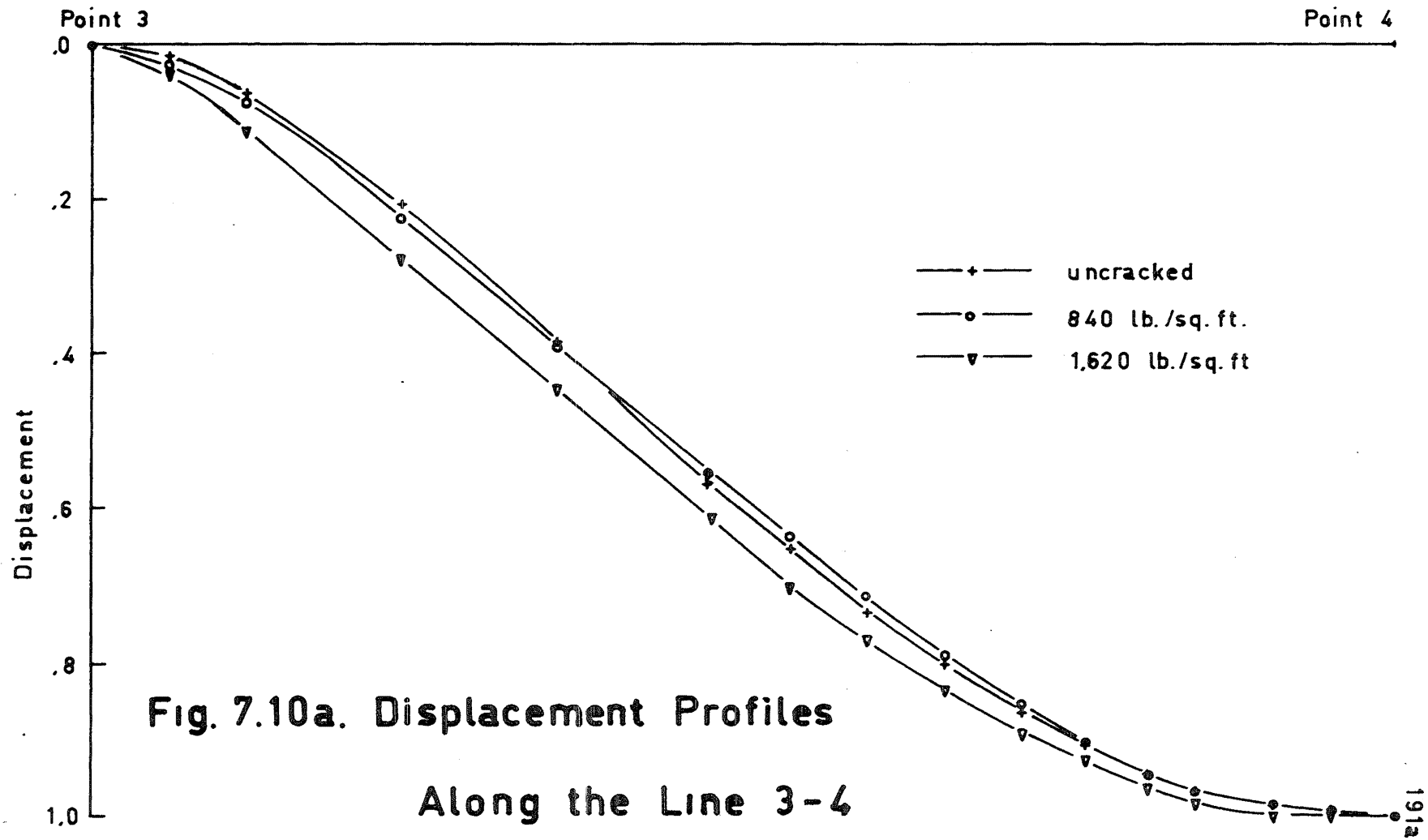

Fig. 7.10a. Displacement Profiles

Along the Line 3-4

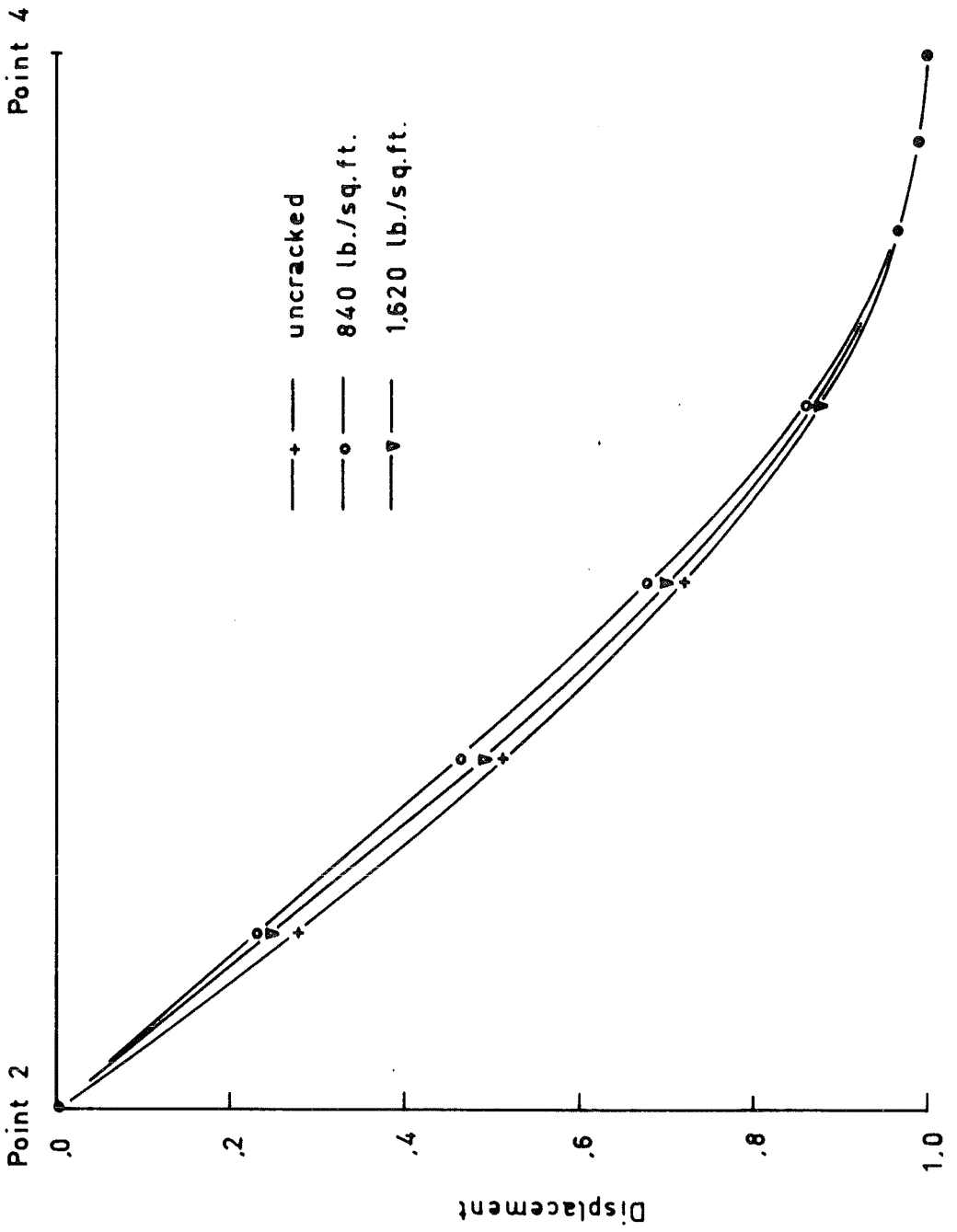

Fig. 7.10b. Displacement Profiles Along the Line 2-4

of 840 lb./sq.ft, and at a load of 1620 lb./sq.ft.

The displacement profile along the longitudinal centre-line (Fig. 7.10a) is altered quite substantially when cracked. In this example cracking increases the displacement of points near the centre of the slab, i.e. those within the cracked region, and cracking at the built-in edge weakens this edge which now behaves like a partially restrained edge. In between these two cracked regions the slab has deformed as a rigid body, i.e. the displacements are linearly related. As the load increases the yielded and cracked regions expand causing the fixed edge to become even less "fixed". Also, the portion of the slab which acts as a rigid body has decreased and is approximately 30% of the longitudinal centreline. Again, yielding has not been restricted to a small area which could be represented as a yield line because most of the slab has deformed elastically or inelastically and not as a rigid body.

The displacement profile along the transverse centre-line (Fig. 7.10b) changed when cracking initiated at the centre of the slab and then it returned towards the elastic profile. At first cracking there has again been a tendency for part of the slab to deform as a rigid body but as crack-ing and yielding progressed towards the simply supported edges the deflection profile tended to follow the elastic profile.

Sharpe's slab was reanalysed using the moment-curvature relationship that took the curvature at a cracked section (refer Fig. 7.3). The crack patterns for this analysis are almost identical with those shown in Figs. 7.4 to 7.7, the only difference being that at the lower loads the cracked areas were greater, although not by any significant quantity.

Load lb./sq.ft	Displacement Ratio
500	.80
840	.88
1,320	.88
1,620	.93
1,820	.85
1,870	.83

Table 7.3 The Ratio of the Theoretical to the Experimental Displacements

The theoretical and experimental load-displacement curves for points A and B, are shown in Fig. 7.11. The curves for point A are closer together in this diagram and the ratios of the theoretical displacement to the experimental displacement, for the loads at which the theoretical displacement are considered, are shown in Table 7.3. The ratio of the stiffnesses of the curves is approximately .88 and thus,

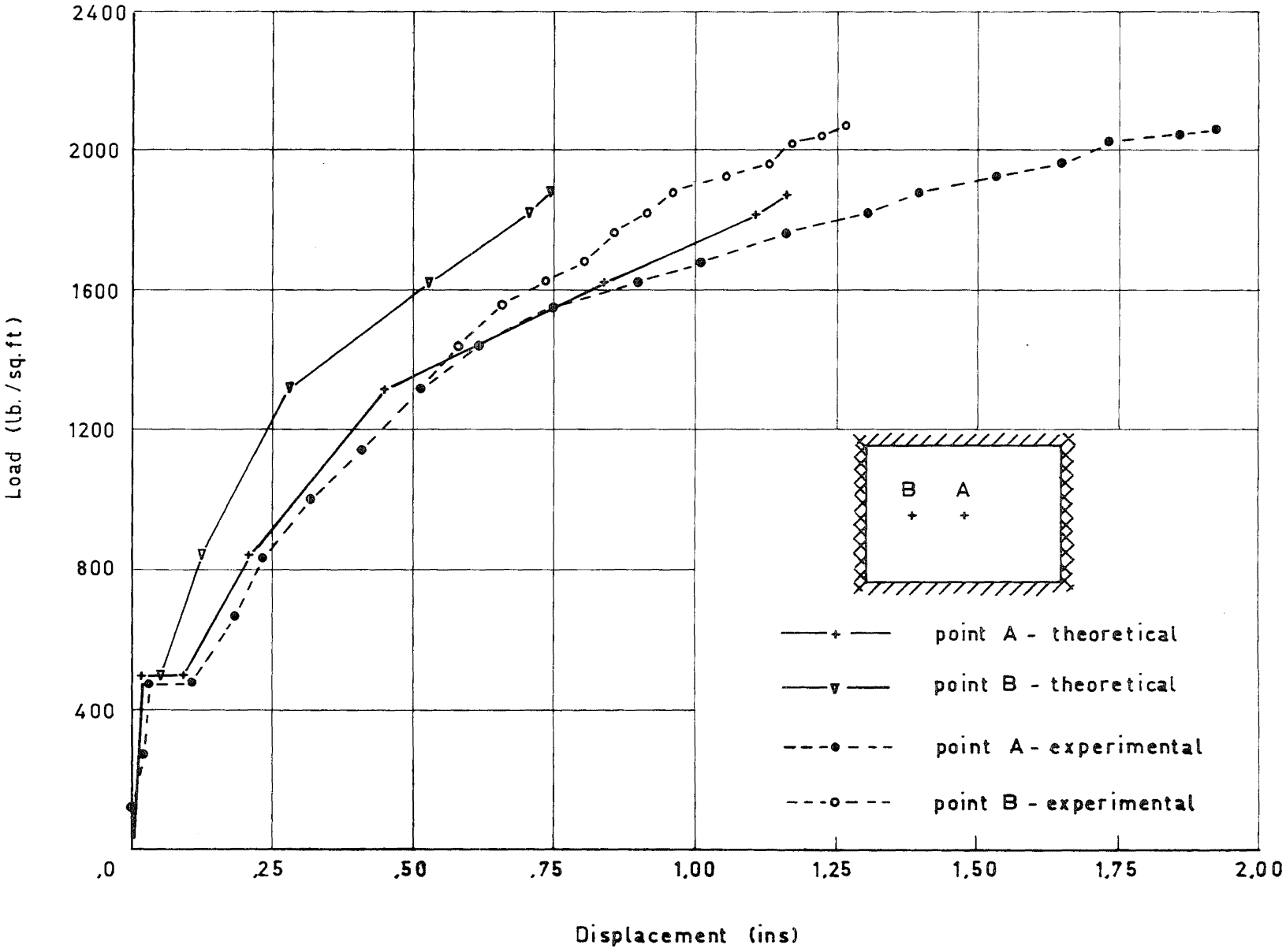

Fig. 7.11. Load Displacement Curves for Points A and B

if the modulus of elasticity was 3.74×10^6 lb./sq.in., the curves would be similar. This value for the modulus of elasticity corresponds to a crushing strength for the reinforced concrete of 4,230 lb./sq.in. which is a reduction of 22.2% on the experimental crushing strength of 5,450 lb./sq.in. However, this variation is approximately double the coefficient of variation that was determined for this concrete (refer Section 7.1). Comparing Tables 7.1 and 7.3 we see that the two theoretical load-deflection curves for point A are not similar which implies that the cracking and the redistribution of stresses occurred in a slightly different sequence. This is reasonable because the two moment-curvature curves were not linearly related.

Load lb./sq.ft	Displacement Ratio
500	.58
840	.60
1,320	.62
1,620	.63
1,820	.63
1,870	.63

Table 7.4 The Theoretical Displacement Ratio of Points A and B

Table 7.4 lists the ratios of the theoretical displacements of points A and B and we see that these are almost identical with those in the previous analysis shown in Table 7.2. Similarly, the displacement profiles for the elastic, cracked and yielded states have the same form as in Fig. 7.4.

It was stated in Section 4.3 that both Wood[60] and Kwiecinski[61] postulated that the yield moment across a crack which is inclined at a non-zero angle to the reinforcement would be greater than the yield moment given by Johansen's square-yield criterion due to a partial distortion of the reinforcement across the crack. To test this theory Sharpe's slab was reanalysed, again assuming that the reinforcement was isotropic. This assumption simplifies Eq. 4.15 to

$$\frac{m_n}{m} = \cos\alpha\sqrt{1 - A^2\sin^2\alpha} + \sin\alpha\sqrt{1 - A^2\cos^2\alpha} \qquad (7.2)$$

where

m_n is the yield moment across the crack,

m is the yield moment for $\alpha = 0^o$,

$1 \geqslant A = \sqrt{2-\mu^2} \geqslant 0$, and

$\mu = \frac{m_n}{m}$ $(\alpha = 45^o)$.

From a series of tests Kwiecinski proposed a value of 1.188 for μ and hence $A^2 = 0.589$. Fig. 7.12 shows the variation of m_n/m within one quadrant and also includes Johansen's square-yield criterion. The theory postulates large increases

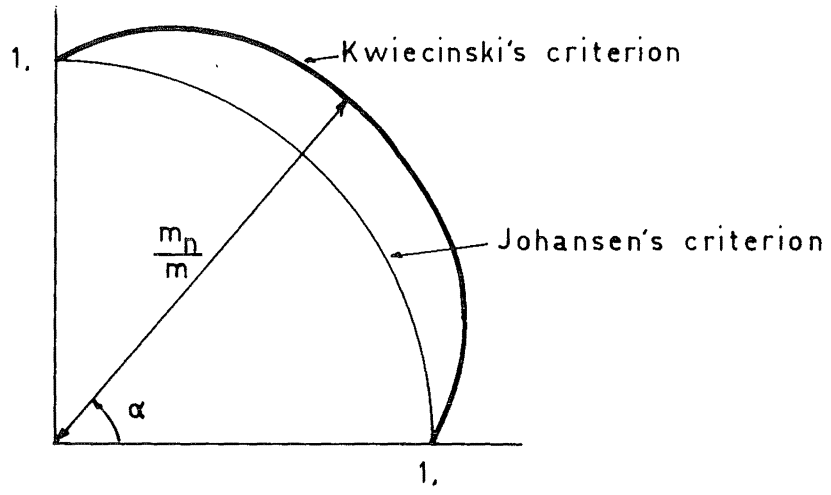

Fig. 7.12 Kwiecinski's and Johansen's Yield Criteria

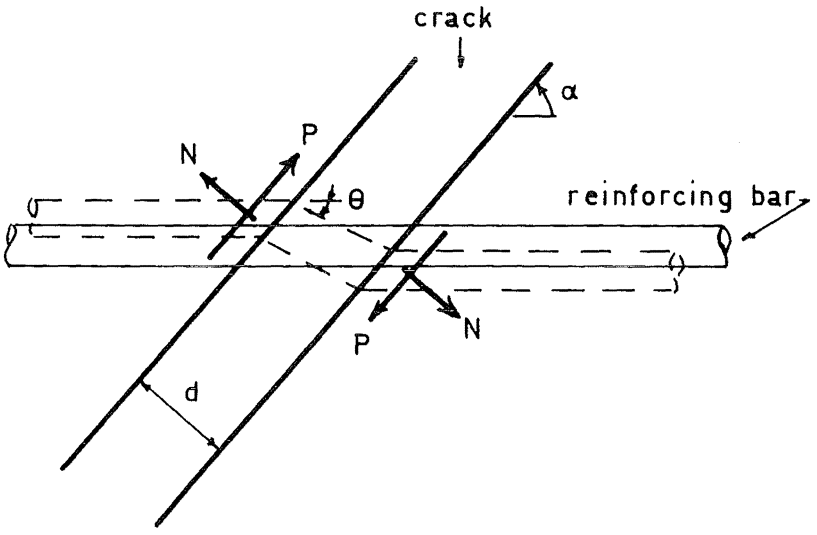

Fig. 7.13. Reinforcing Bar Inclined at an Angle α to a Crack

in strength even at small angles, for example, the maximum increase when $\alpha = 45^{o}$ is 18.8% and when $\alpha = 10^{o}$ the increase is 9.0%.

Fig. 7.13 shows a reinforcing bar inclined at an angle α to a crack. The forces acting on the bar and the possible distortion of the bar are also shown. The distortion of the bar is caused by the force P which is formed by the concrete being displaced in a direction normal to the crack. The amount of this deflection, assuming that the concrete does not crush, is d x θ where d is the crack width and θ the angle of distortion.

The amount of distortion will depend upon many factors including: the crack width, the amount of crushing of the concrete when it is compressed against the reinforcing bar, the angle that the crack makes with the reinforcing bar, and the size of the reinforcing bar. After the concrete cracks, the moment across the crack will become dependent upon the angle between the crack and the reinforcement and hence, to degrade the stiffness of such a section will require a moment that is greater than that postulated by a square section property diagram (refer Section 4.2). At the cracking load the cracks will be small and the force P will also be small but, as the load increases, the force will increase until at the ultimate load it will be a maximum. Unfortunately Kwiecinski did not give a complete load-deflection curve for any of his tests but only specified the failure load and

therefore the behaviour prior to yielding is unknown. One analysis was made, however, assuming that after a section is cracked the moment to further degrade the stiffness would be calculated according to the Kwiecinski criterion. This represents the maximum effect that partial distortion of the reinforcement would have on the complete analysis. Hence this analysis would represent one bound to the true solution, and the prior analysis that ignored the effect of distortion would represent the other bound. The moment-curvature relationship is represented as 100 stepped values (refer Section 6.3) and therefore the section property diagram (discussed in Section 4.2) will consist of 100 three dimensional surfaces similar to the surface shown in Fig. 7.14 (in this figure it has been assumed, for simplicity, that the negative moment is zero though this is not assumed in practice). Also shown, in dotted lines, is the surface which is independent of the angle of the reinforcement, i.e. Johansen's criterion.

The crack patterns for this analysis are shown in Figs 7.15 to 7.20 for the loads 500, 840, 1,320, 1,620, 1,820 and 2,100 lb./sq.ft respectively. In general, the comments made earlier in this section with respect to the crack patterns for the analysis that assumed the Johansen square-yield criterion will be relevant to this analysis too. The principal interest, however, is to compare these two sets of crack patterns and, subsequently, the load-deflection curves.

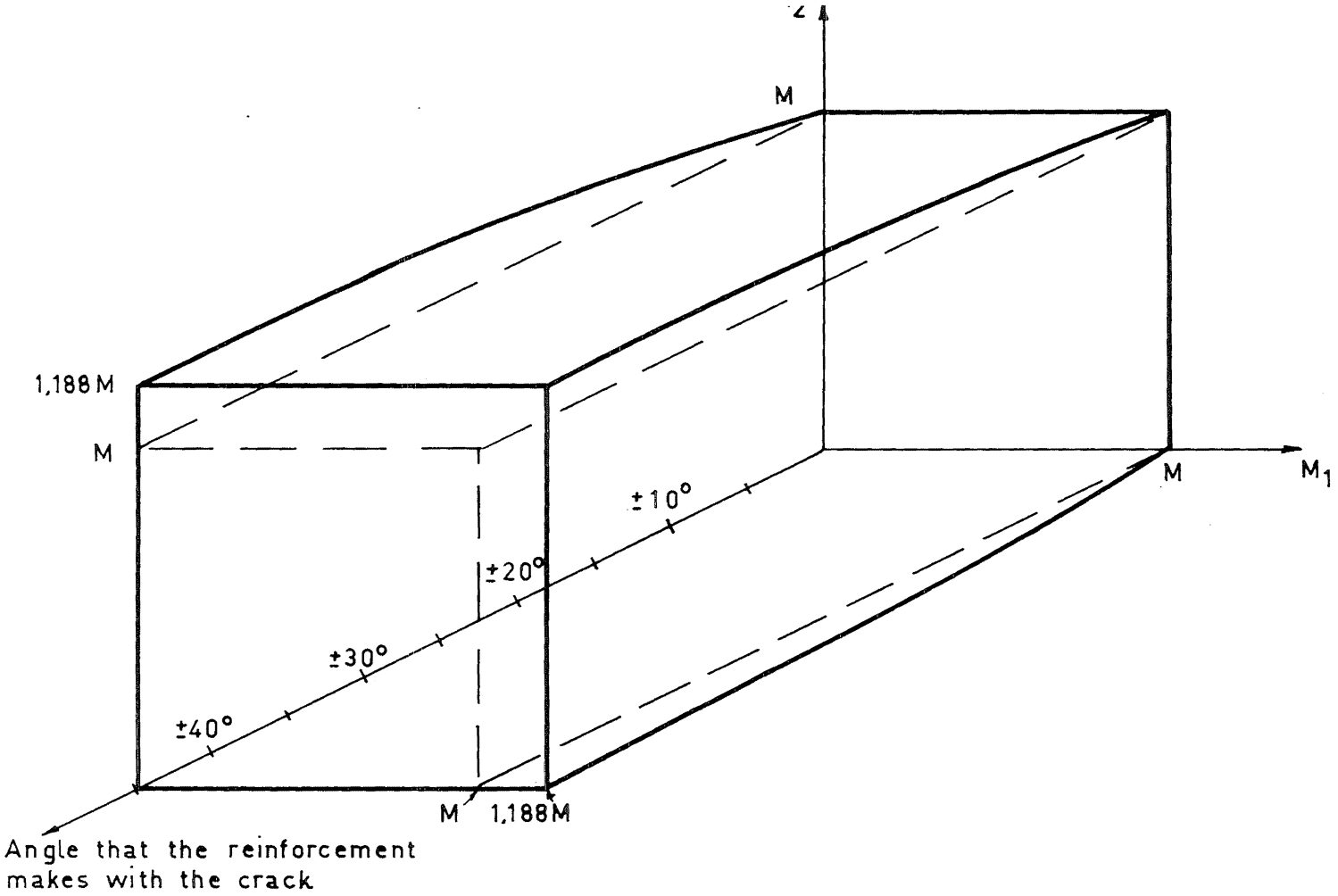

Fig. 7.14. Element of a Section Property Diagram

Fig. 7.15 shows the cracked pattern when the slab has just cracked, at a load of 500 lb./sq.ft which is 23.8% of the theoretical ultimate load. Comparison with Fig. 7.4 shows that there is very little difference between crack patterns. This is to be expected, however, because the additional strength of the simulated slab is not noticed until after the slab is cracked.

The crack pattern at the load 840 lb./sq.ft, which is 40.0% of the theoretical ultimate load, is shown in Fig. 7.16 and it does not vary much from its counterpart in Fig. 7.5. The additional strength of the simulated slab can be observed, however, by the smaller regions that have yielded on both the bottom and the top surfaces.

Fig. 7.17 shows the crack pattern at the load 1,320 lb./sq.ft, which is 62.9% of the theoretical ultimate load. This crack pattern deviates markedly from its counterpart shown in Fig. 7.6. As expected, the cracked regions are approximately equivalent but the yielded regions are quite different. On the bottom surface, in Fig. 7.17, yielding has commenced at the centre of the slab and also near the centre where the cracked region begins to branch towards the opposite corner. In Fig. 7.6, however, the bottom surface yielding has progressed along the diagonal yield region and it has met the opposite side. Similarly, the yielding on the top surface has advanced more in Fig. 7.6 where yielding has crossed the corner at the point 1.

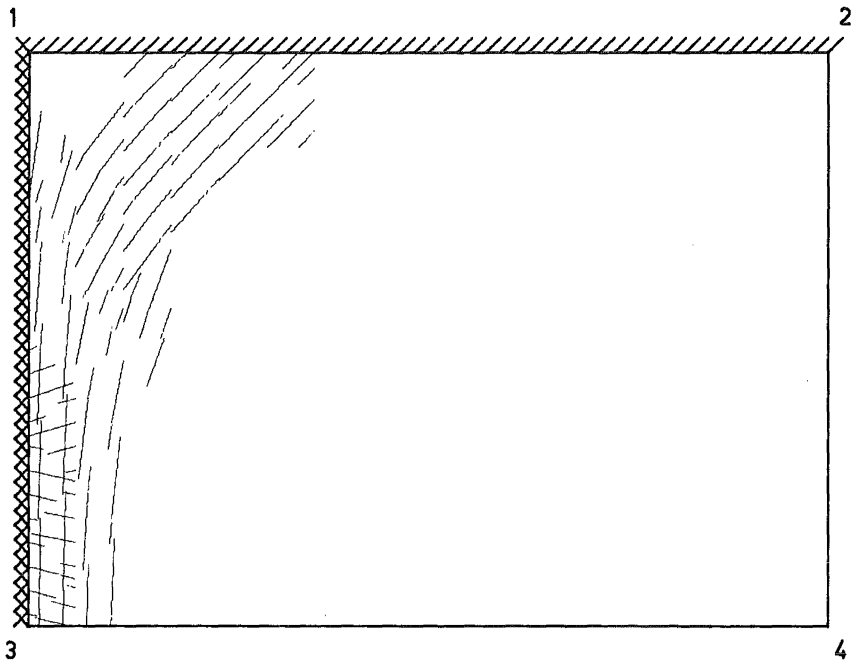

Top Surface

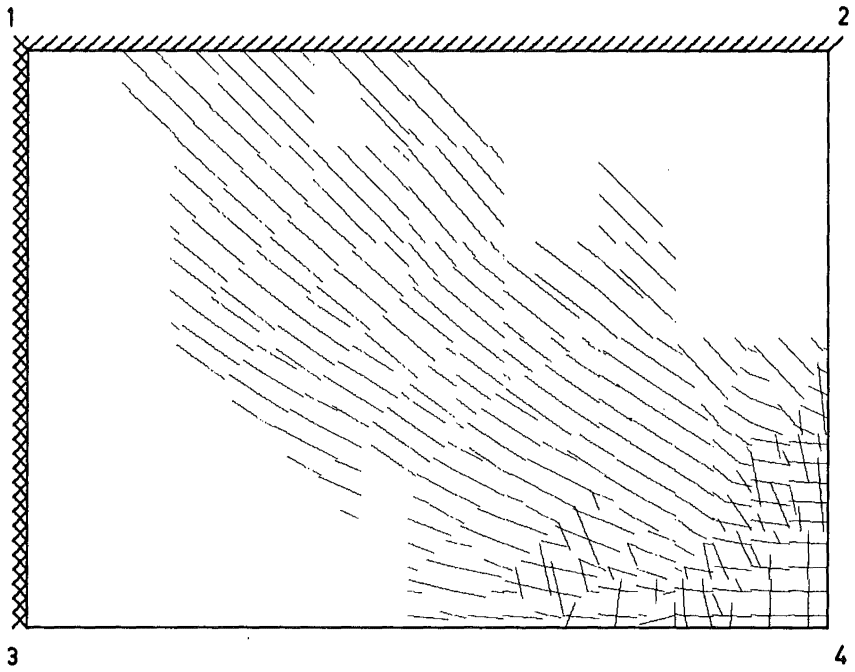

Bottom Surface

Fig. 7.15. Crack Patterns for Sharpe's Rectangular Slab - 500 lb./sq.ft

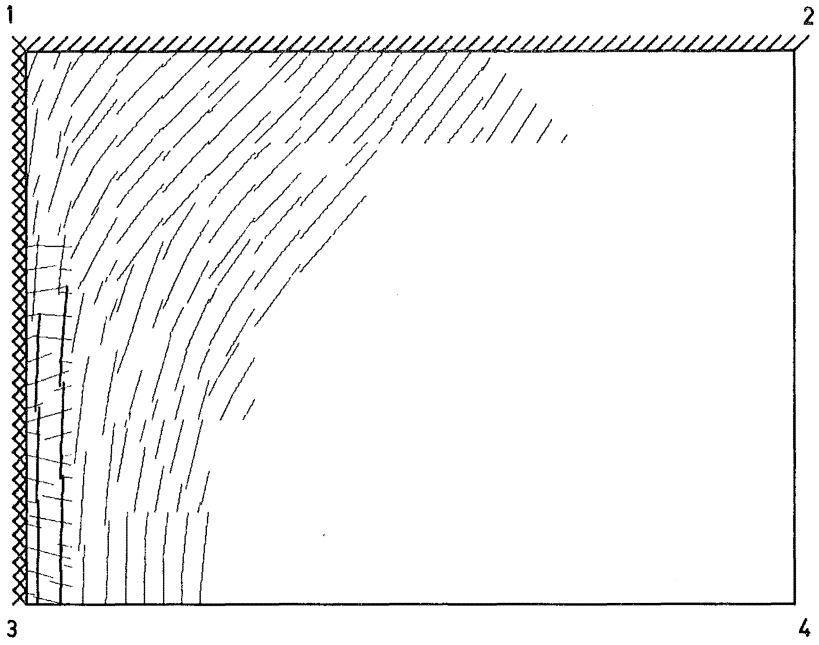

Top Surface

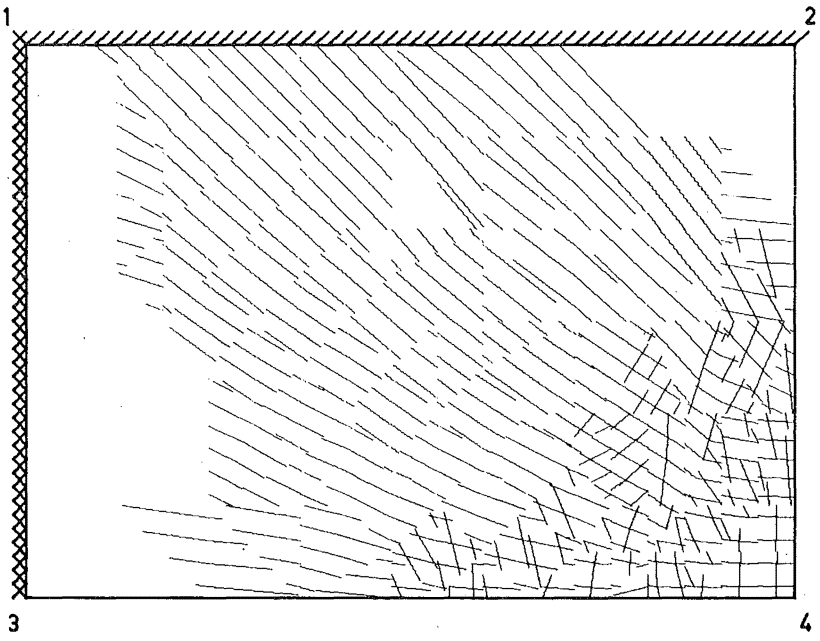

Bottom Surface

Fig. 7.16. Crack Patterns for Sharpe's Rectangular Slab - 840 lb./sq.ft

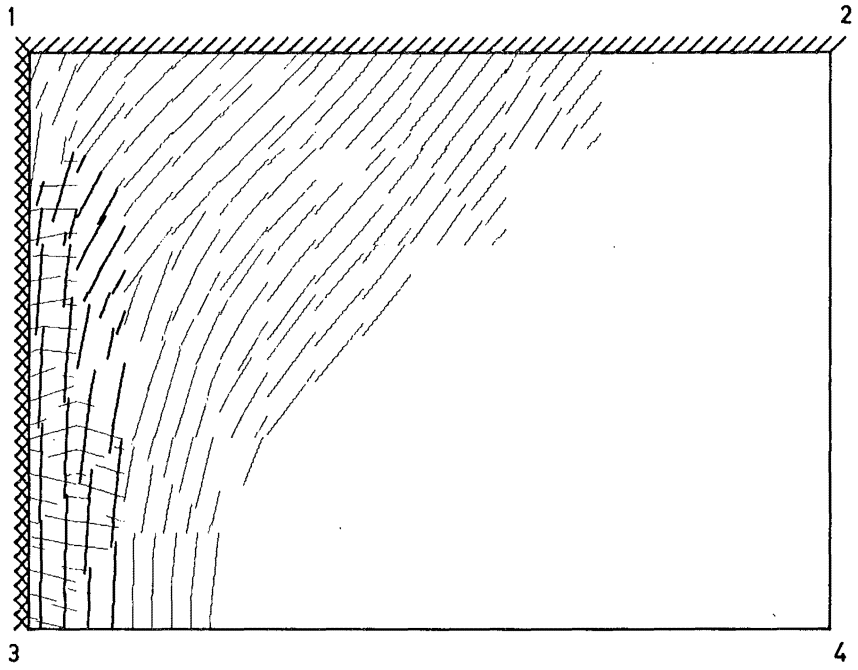

Top Surface

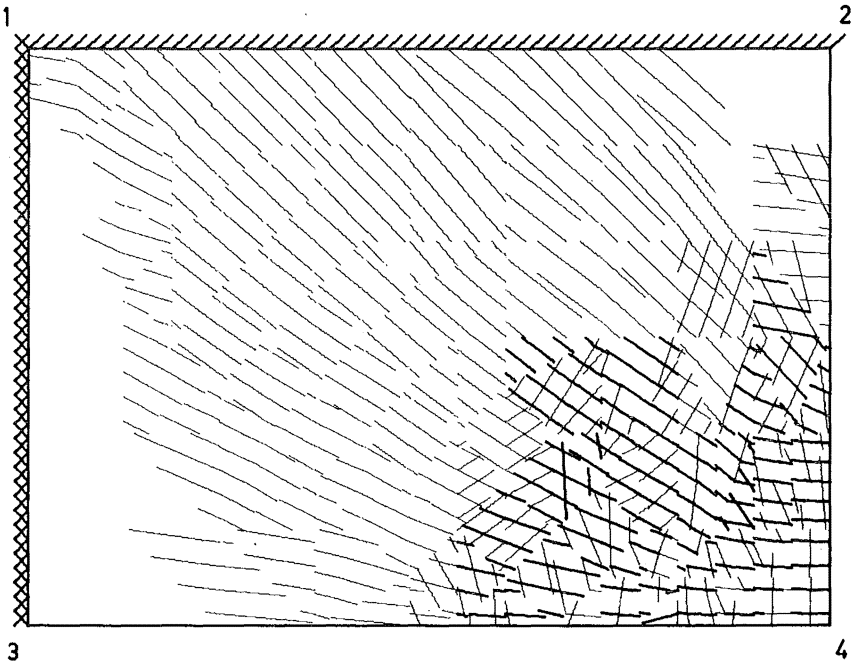

Bottom Surface

Fig. 7.17. Crack Patterns for Sharpe's Rectangular Slab - 1,320 lb./sq.ft

There are equally significant differences in the crack patterns at the load 1,620 lb./sq.ft which is 77.2% of the theoretical ultimate load. The simulated slab that assumes the Kwiecinski yield criterion is shown in Fig. 7.18 and the yielded regions are not as broad as those shown in Fig. 7.7 which assumed the Johansen yield criterion. Also, of importance to the structural behaviour, is the small number of elements that have failed on the top surface in Fig. 7.18 compared with the substantially greater amount in Fig. 7.7.

Fig. 7.19 shows the crack pattern at the load 1,870 lb./sq.ft which is 89.1% of the theoretical ultimate load. The corresponding pattern when the Johansen yield criterion was assumed is shown in Fig. 7.8 and this pattern occurred just before this slab failed. Again the widths of the cracked regions are smaller in Fig. 7.19 for both the bottom and the top surfaces. Also, the number of elements that have failed is greater in Fig. 7.8.

The cracked region at the load 2,100 lb./sq.ft, which is just prior to failure, is shown in Fig. 7.20 and, as expected, this pattern is very similar to the failure crack pattern in Fig. 7.8.

The load-deflection curves for points A and B are shown in Fig. 7.21 together with the theoretical curves which assume an equivalent-displacement curvature and the Johansen square-yield criterion (i.e. from Fig. 7.10). There is very little difference in the values at the loads 500 and 840

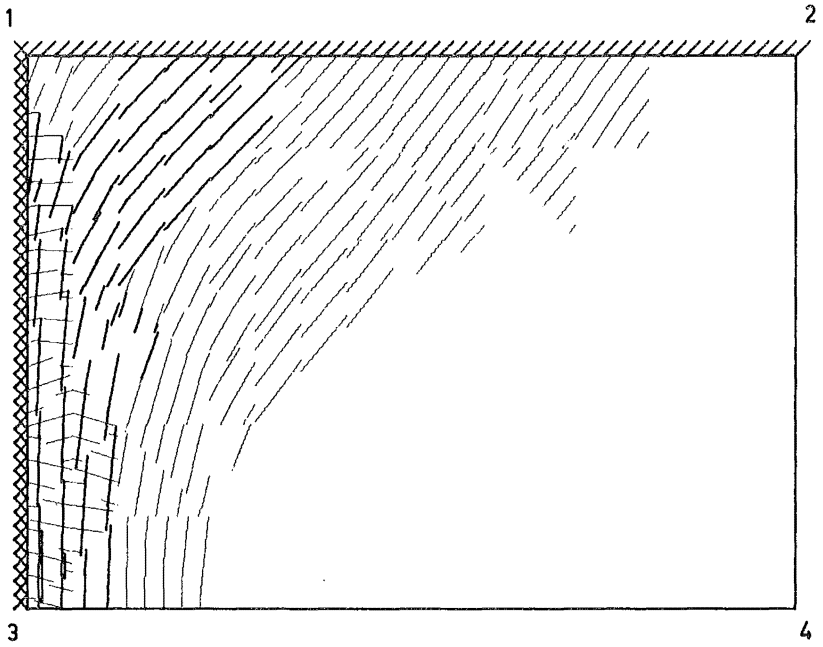

Top Surface

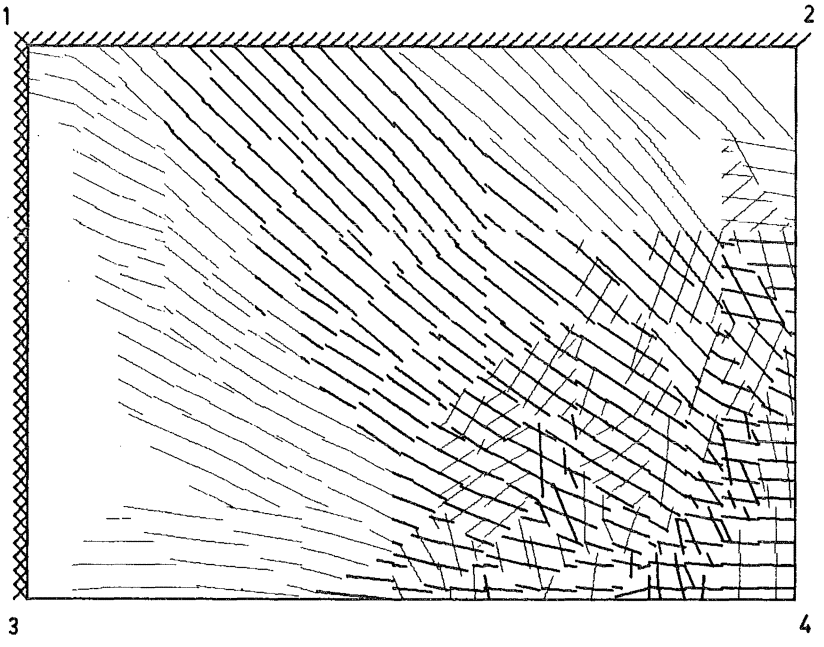

Bottom Surface

Fig. 7.18. Crack Patterns for Sharpe's Rectangular Slab - 1,620 lb./sq.ft

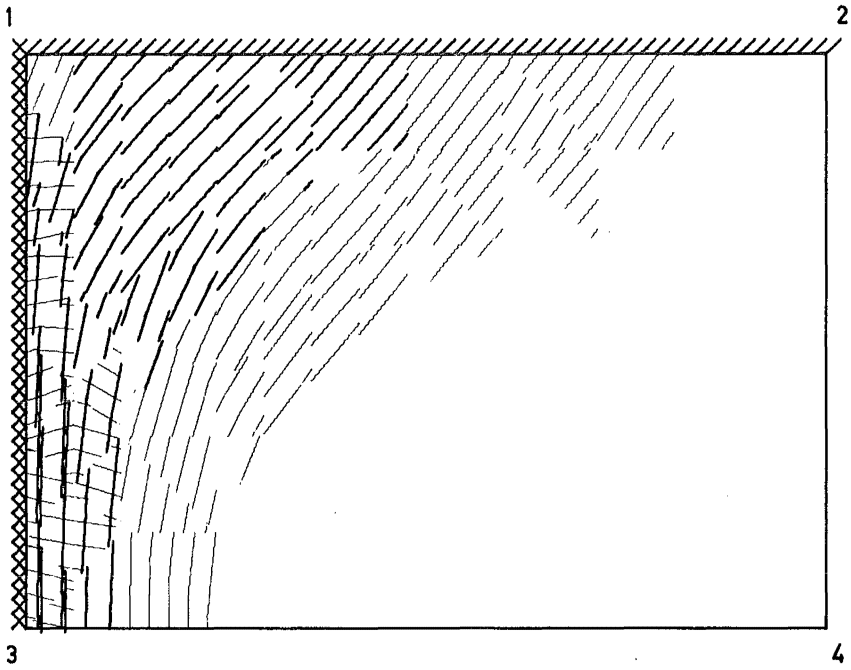

Top Surface

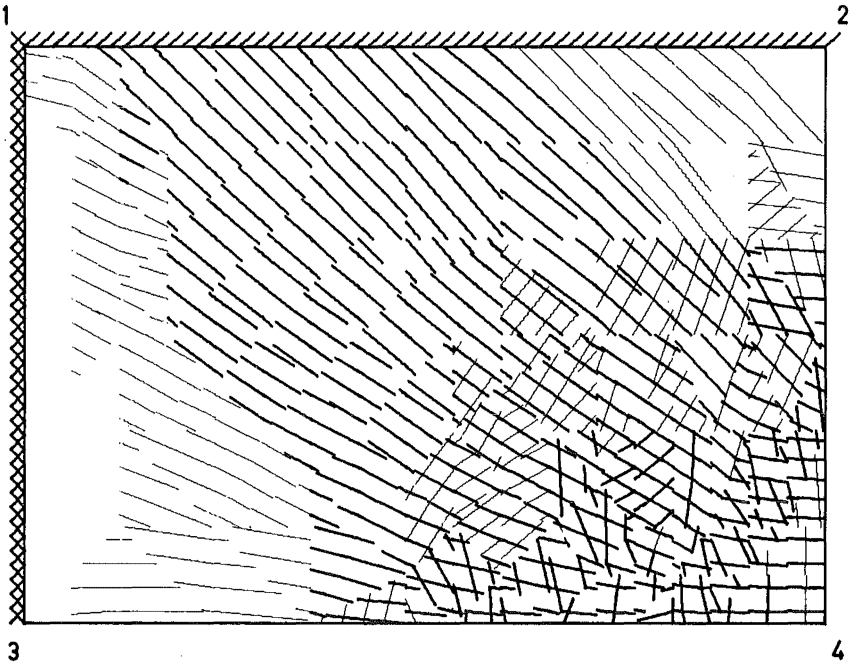

Bottom Surface

Fig. 7.19. Crack Patterns for Sharpe's Rectangular Slab - 1,870 lb./sq.ft

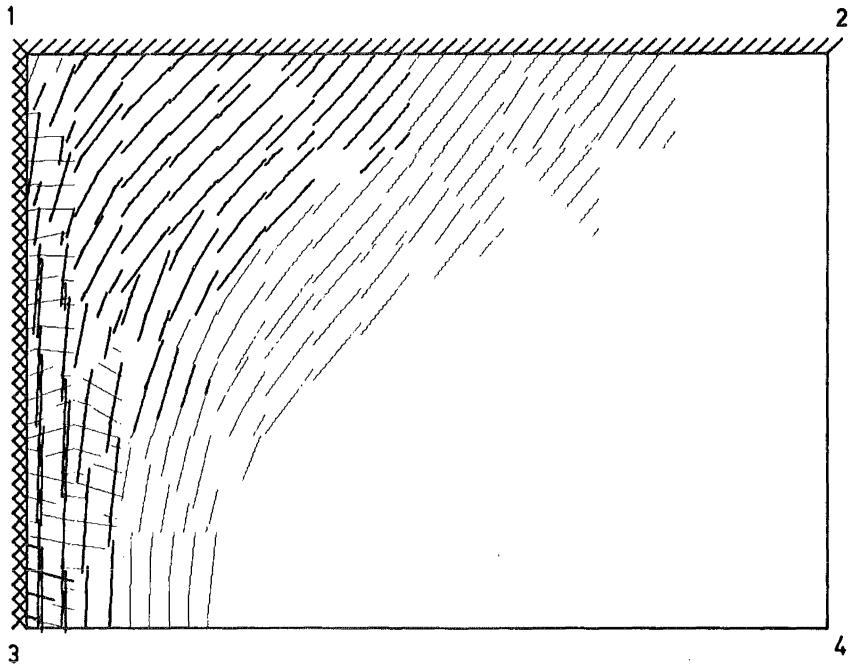

Top Surface

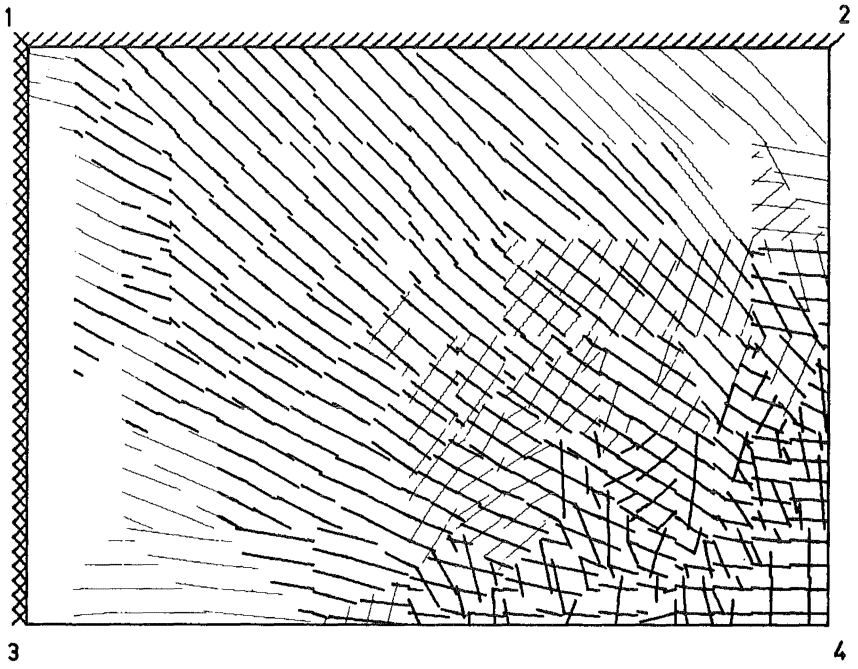

Bottom Surface

Fig. 7.20. Crack Patterns for Sharpe's Rectangular Slab - 2,100 lb./sq.ft

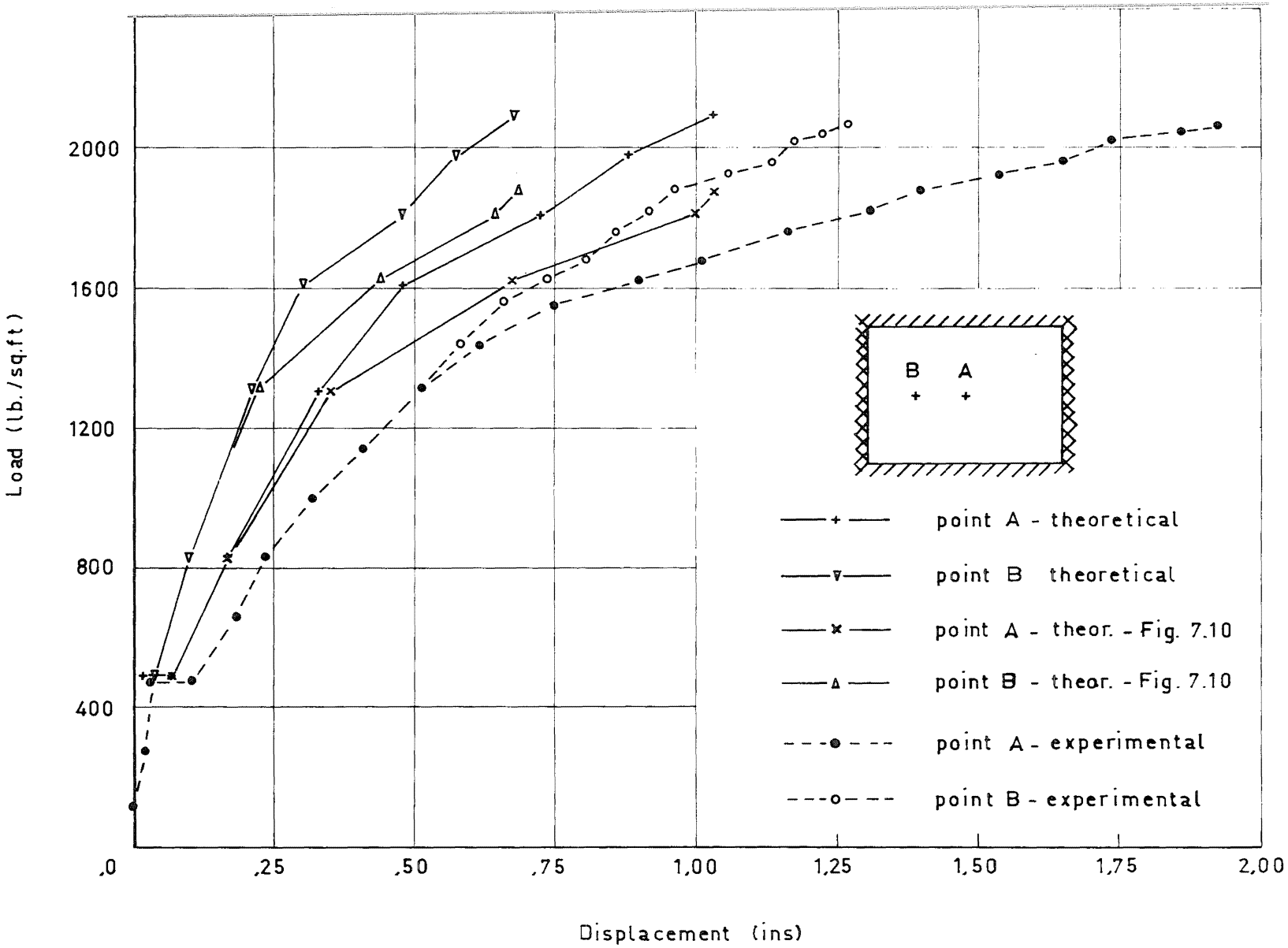

Fig. 7.21. Load -Displacement Curves for Points A and B

lb./sq.ft which is reasonable because there was very little difference between the crack patterns for these loads. From here on, however, the curves diverge although the displacements at the ultimate loads are almost identical which, again, arises from the equivalent crack patterns (Fig. 7.8 and Fig. 7.20).

The ultimate load assuming the Kwiecinski yield criterion is approximately 12% higher than when Johansen's yield criterion is used. This appears reasonable because, as stated previously, if the angle between the reinforcement and a crack is only 10^{o} there is a strength enhancement of 9.0% and hence, allowing for kinking we could expect an enhancement of approximately 12-15%.

7.3 Analysis of Sharpe's Rectangular Slab Using Elastic/Inelastic Finite Elements

Sharpe's rectangular slab was reanalysed using the two types of elastic/inelastic finite elements described in Sections 5.1 and 5.2, i.e. the elastic/inelastic element formed by a beam analogy, and the elastic/inelastic element formed by "integrating by parts". The formation of these elements took a substantial amount of computer time and it became apparent that if these elements were to be useful they would have to be capable of using a smaller mesh whilst having a similar accuracy to the method of analysis that used either totally cracked or totally uncracked elements. Because the elements

can contain both cracked and uncracked regions we do not have to have small elements in the regions of high stress, and hence a simple, regular mesh can be used. Two element meshes were used, one containing 60 elements and the other 144 elements (refer Fig. 7.22).

The method of analysis was altered slightly and made semi-automatic, i.e. at the end of each cycle the operator had the option of continuing the analysis or stopping it. If the analysis was to be stopped then the operator had another option of whether he wanted punched output giving data on the element properties. These facilities were included so that the output data did not have to be punched at each cycle (there was quite a lot of data giving the dimensions and conditions of each subelement).

The analysis used the material properties that were given in Section 7.1, and the moment-curvature relationship which took an equivalent-displacement curvature. The analyses predicted stiffer behaviour of the structures than did the former analyses which used either totally cracked or totally uncracked elements, and therefore only two load increments, 500 lb./sq.ft and 840 lb./sq.ft, were studied. We will consider the analyses which used the elastic/inelastic finite elements that were formed by a beam analogy (refer Section 5.1) first. At the load 500 lb./sq.ft the crack patterns using the 60 element mesh are shown in Fig. 7.23, and the

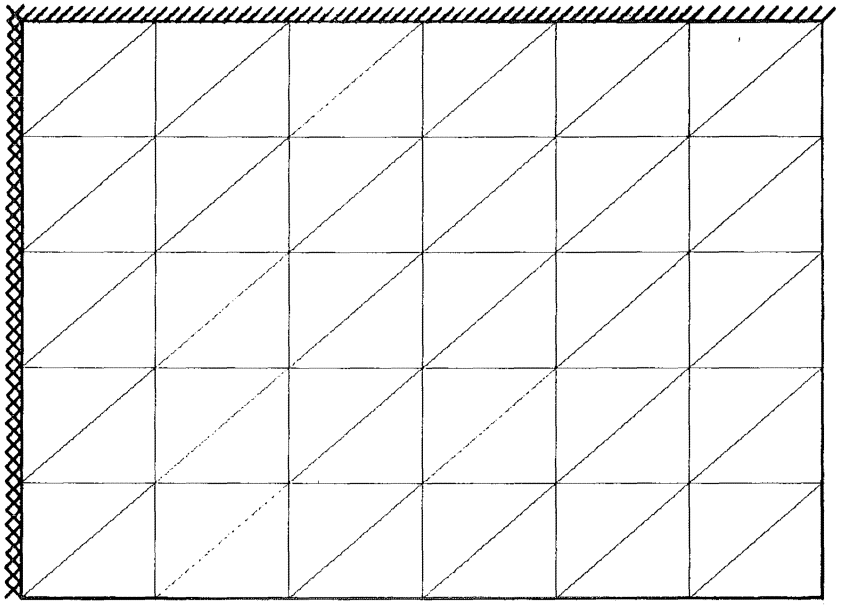

60 Element Mesh

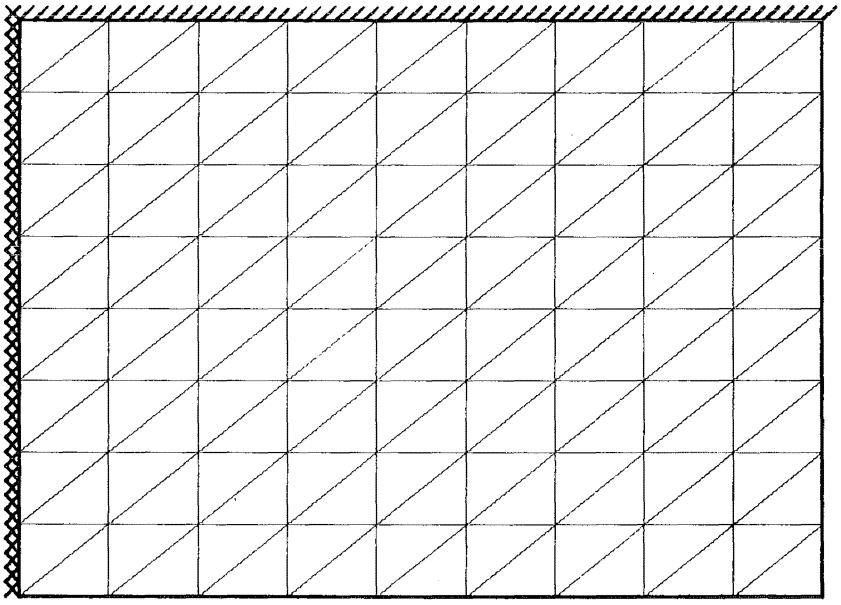

144 Element Mesh

Fig. 7.22. Finite Element Meshes for Sharpe's Slab

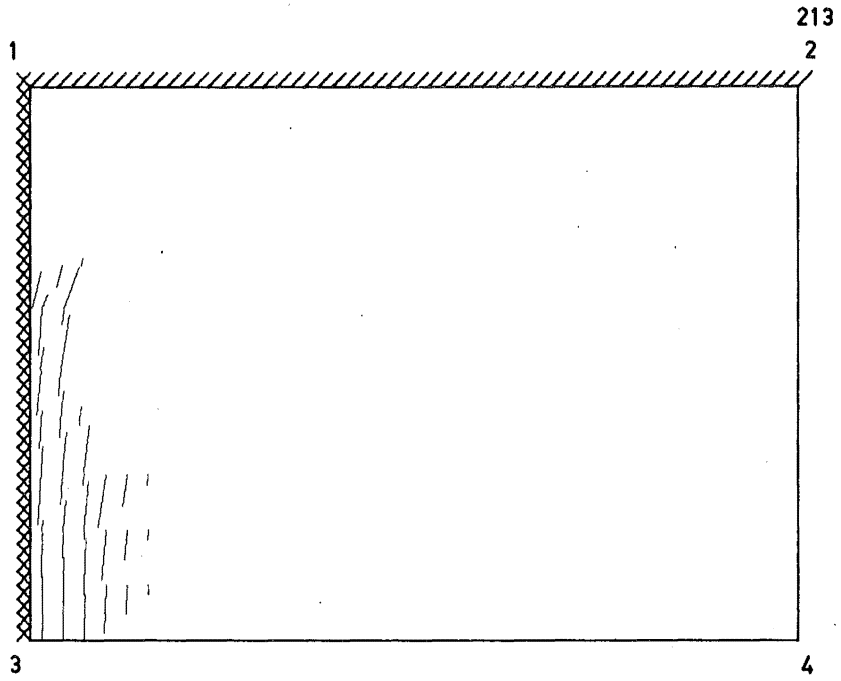

Top Surface

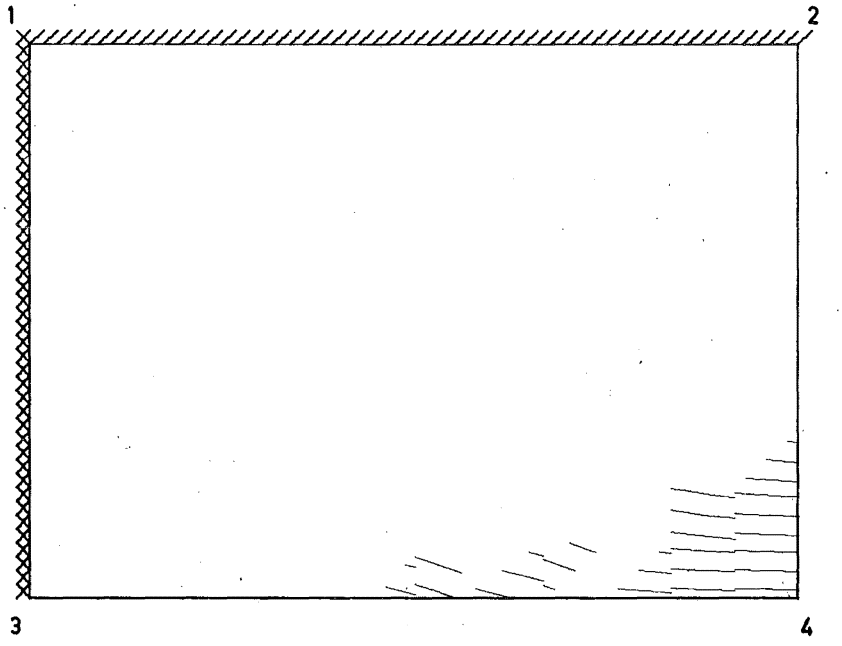

Bottom Surface

Fig. 7.23. Crack Patterns for Sharpe's Slab - 500 lb./sq.ft - 60 Element Mesh

crack patterns using the 144 element mesh are shown in Fig. 7.24. Both of these figures show substantially less cracking than was observed in the prior analysis (on a 196 element mesh - refer Fig. 7.2) which used elements that were either totally cracked or totally uncracked (Fig. 7.4). This can be partially explained by comparing the elastic displacements at the centre of the slab for these three cases, i.e.

for the 196 element mesh, δ = .01648

for the 60 element mesh, δ = .01600

and for the 144 element mesh, δ = .01633.

An approximate guide when analysing the same structure with different mesh configurations is that the greater the displacements, the greater are the surrounding stresses. Hence we would expect the proportions of cracking that have been observed, although, at a slightly larger load, we would expect the three cracking patterns to be equivalent.

An interesting point which is observed in the crack patterns which were formed using elastic/inelastic elements is that the crack boundary has become less smoothly continuous than in prior analyses which were formed using elements that were either totally cracked or totally uncracked. This is due to stress discontinuities which arose from the existing crack pattern.

The crack patterns at the load 840 lb./sq.ft. are shown in Fig. 7.25 for the 60 element mesh, and in Fig. 7.26 for the

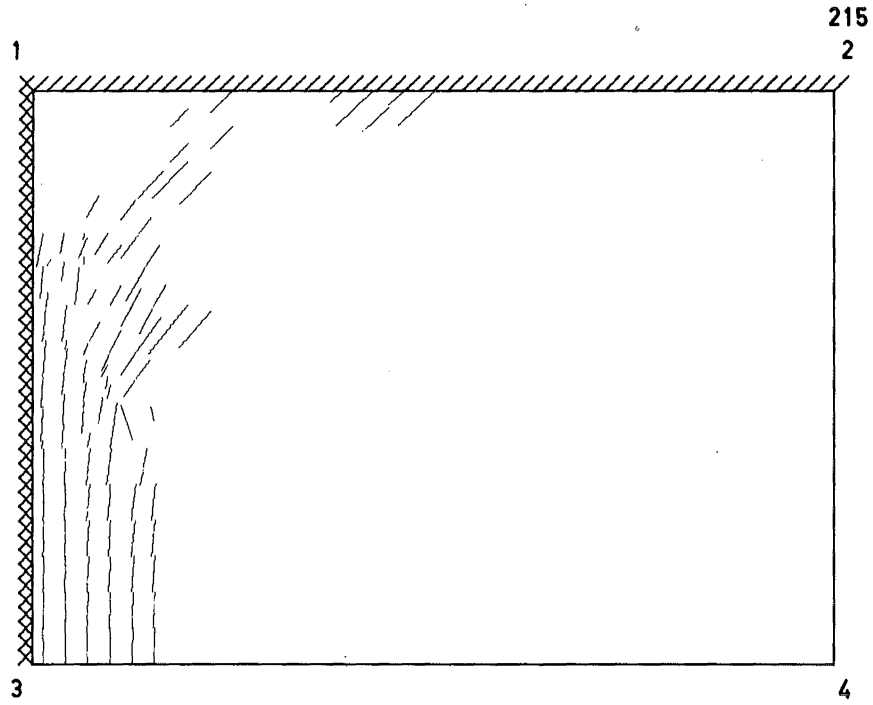

Top Surface

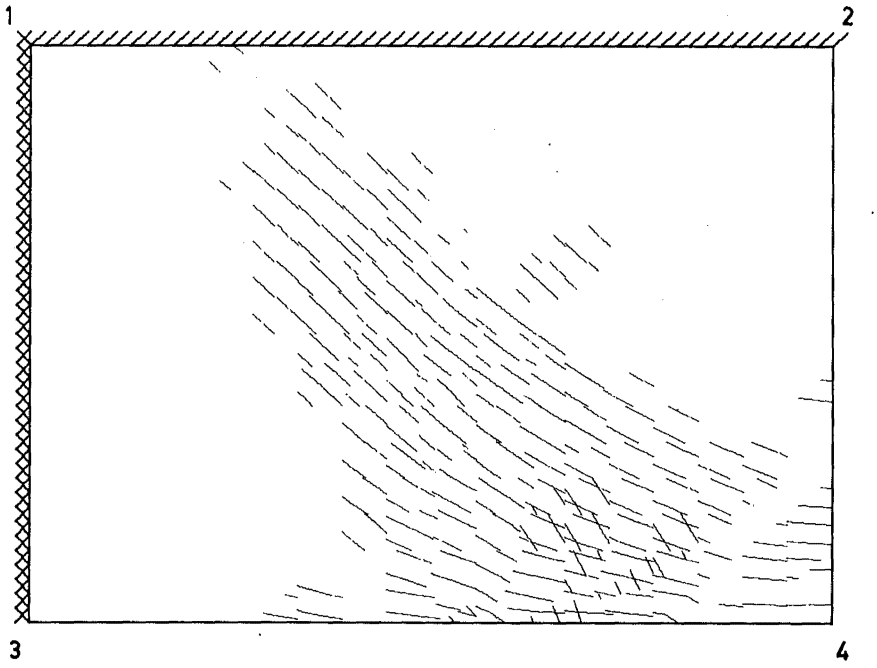

Bottom Surface

Fig. 7.24. Crack Patterns for Sharpe's Slab - 500 lb./sq.ft - 144 Element Mesh

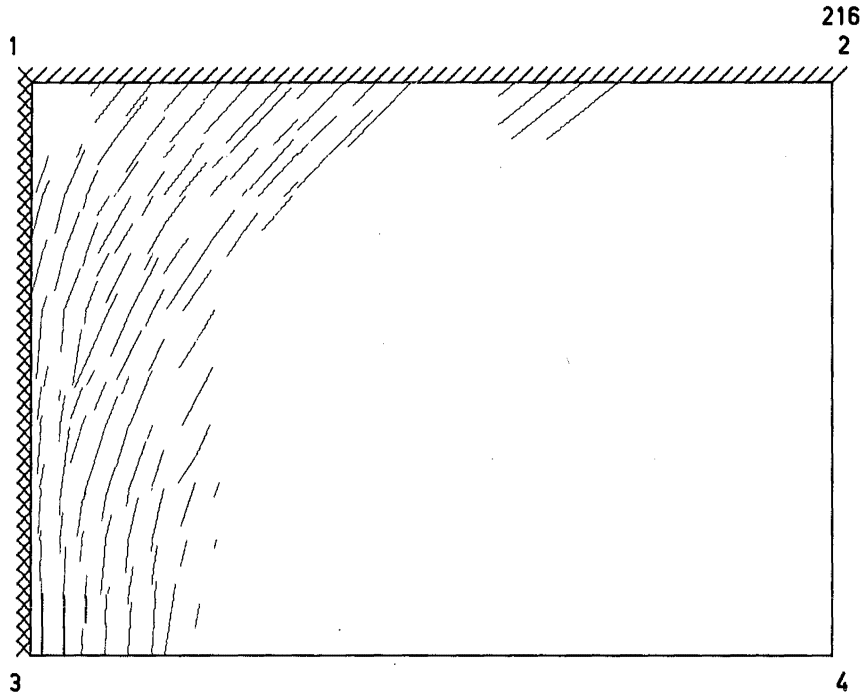

Top Surface

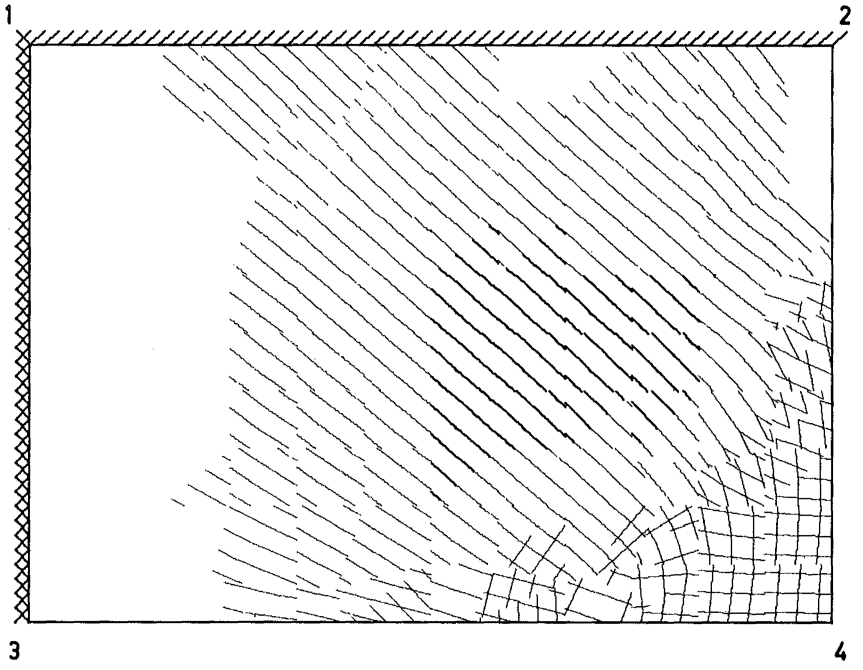

Bottom Surface

Fig. 7.25. Crack Patterns for Sharpe's Slab-
840 lb./sq.ft-60 Element Mesh

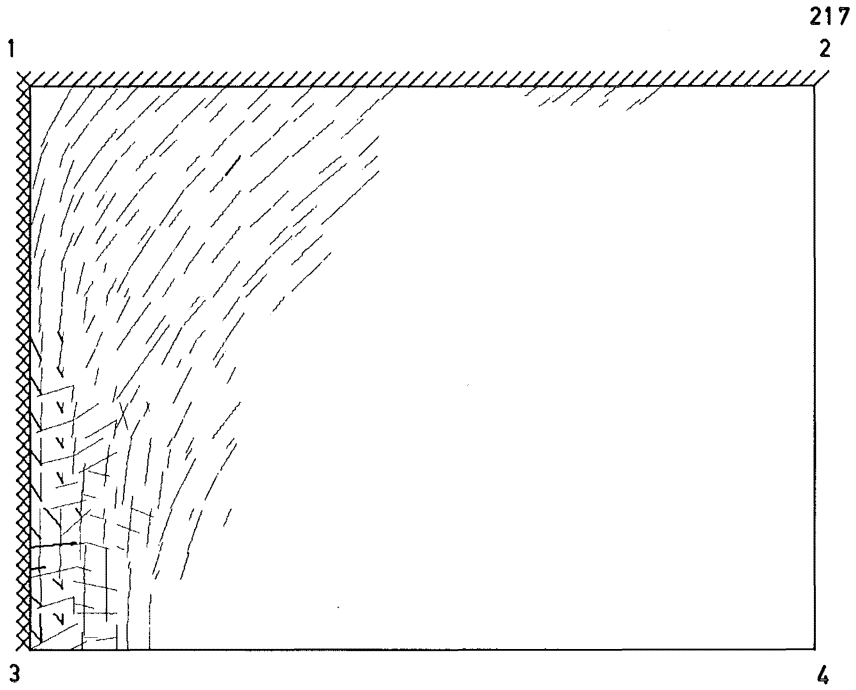

Top Surface

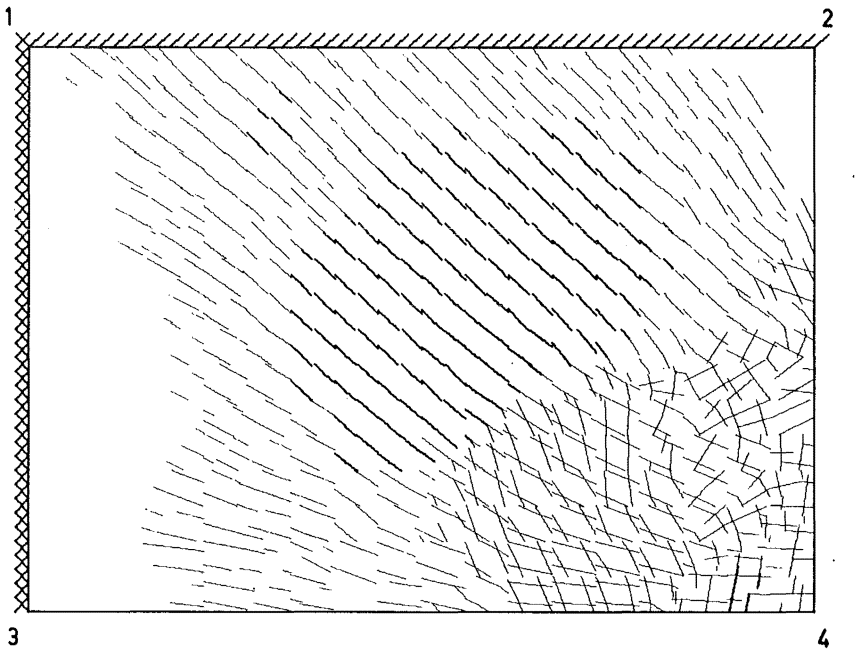

Bottom Surface

Fig. 7.26. Crack Patterns for Sharpe's Slab - 840 lb./sq.ft - 144 Element Mesh

144 element mesh. As expected, the proportion of the slab area that was cracked is similar to that of the prior analysis, shown in Fig. 7.5. Some important features can be observed from these figures. Firstly, the elements at the centre of the slab that were doubly cracked have more consistent crack directions than those shown in Fig. 7.5. This is probably due to the different sequence in cracking; also, the subelement crack angle is determined from the subtriangle nodes, and the angles at these nodes would often be similar because the nodes can be closer together than can many of the fixed nodal points shown in the element mesh in Fig. 7.2. The other feature that can be seen in the crack patterns is the region of yielding on the bottom surface which has not occurred at the centre of the slab but has occurred in between points 1 and 4. This region resulted from a high moment which formed from the crack patterns shown in Figs. 7.23 and 7.24. The reason for this becomes obvious when the displacement profiles are studied and therefore a fuller discussion will be postponed until later.

The cracking was not very regular; for example, the top surface cracking (Fig. 7.25) shows an isolated cracked region whose angle of cracking is correct but the region is not connected to the main region of cracking. Such isolated regions occurred from high localised stresses caused by both the sequence of cracking and the type of elements that were

formed after cracking. (If greater operator interaction had been provided these regions could have been eliminated and another cycle repeated to observe whether they reappeared or not.)

Yielding on the top surface occurred along the built-in edge but it is not as extensive in Fig. 7.25 and 7.26 as it is in Fig. 7.5. Therefore, when the elastic/inelastic elements are used, the built-in edge will provide a greater restraint than in the analysis which used elements that were either totally cracked or totally uncracked, though the effect of the large yield region on the bottom surface may make these simulated slabs more flexible.

A study of the displacement profiles helps to clarify the behaviour of the elastic/inelastic elements. At the load 500 lb./sq.ft Fig. 7.27 shows displacement profiles along the line 2 - 4, and Fig. 7.28 shows displacement profiles along the line 3 - 4. In both figures there are profiles taken from the 60 element mesh and the 144 element mesh; also, from the 196 element mesh there are two profiles showing the elastic displacements and the displacements at the load 500 lb./sq.ft. We see immediately that the cracked profiles using the elastic/inelastic finite elements resemble the shape of the elastic profile very closely and they are considerably stiffer than the cracked profile. We can, however, expect these profiles to be stiffer because the respective areas of

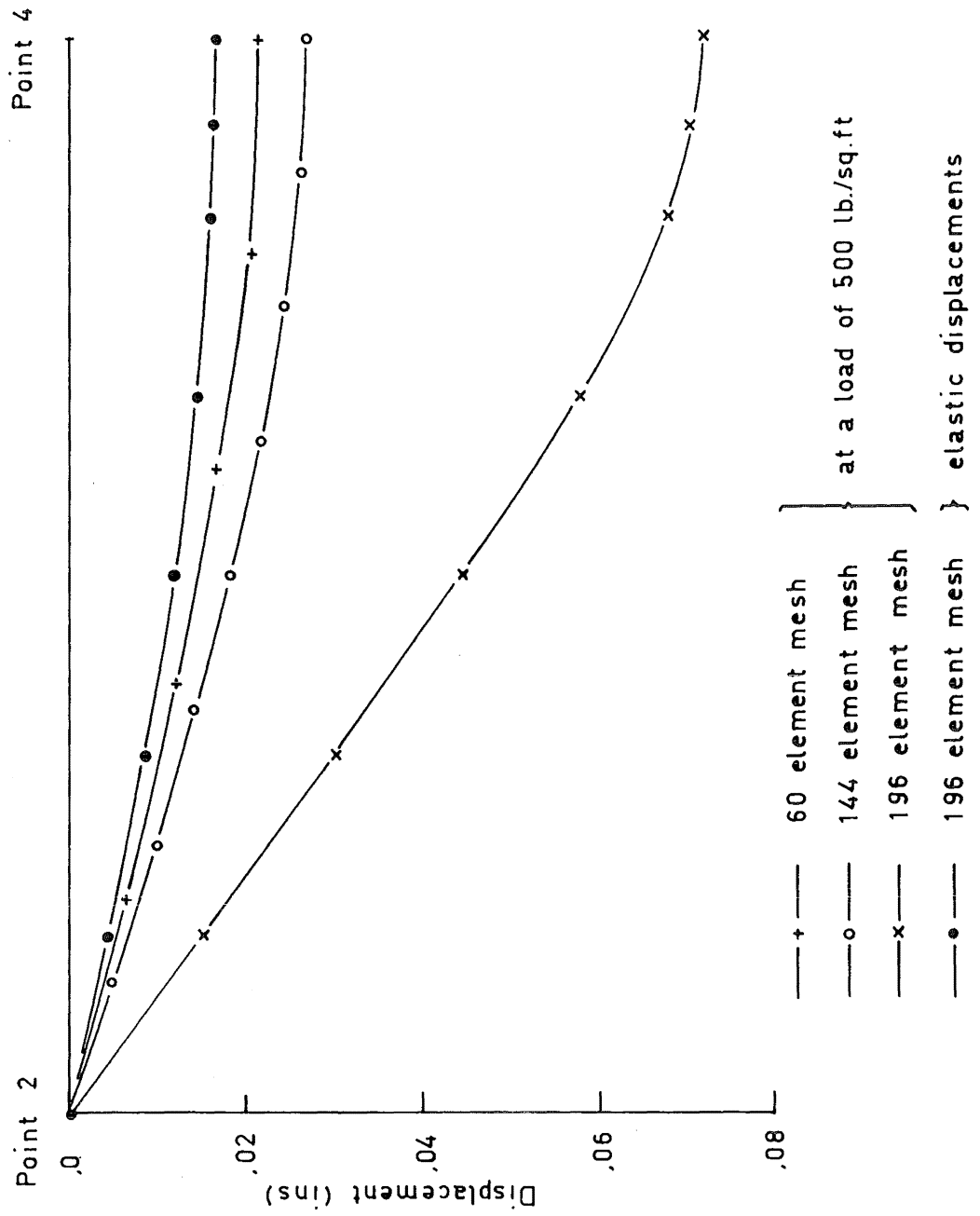

Fig. 7.27. Displacement Profiles Along the Line 2-4 - 500 lb./sq.ft

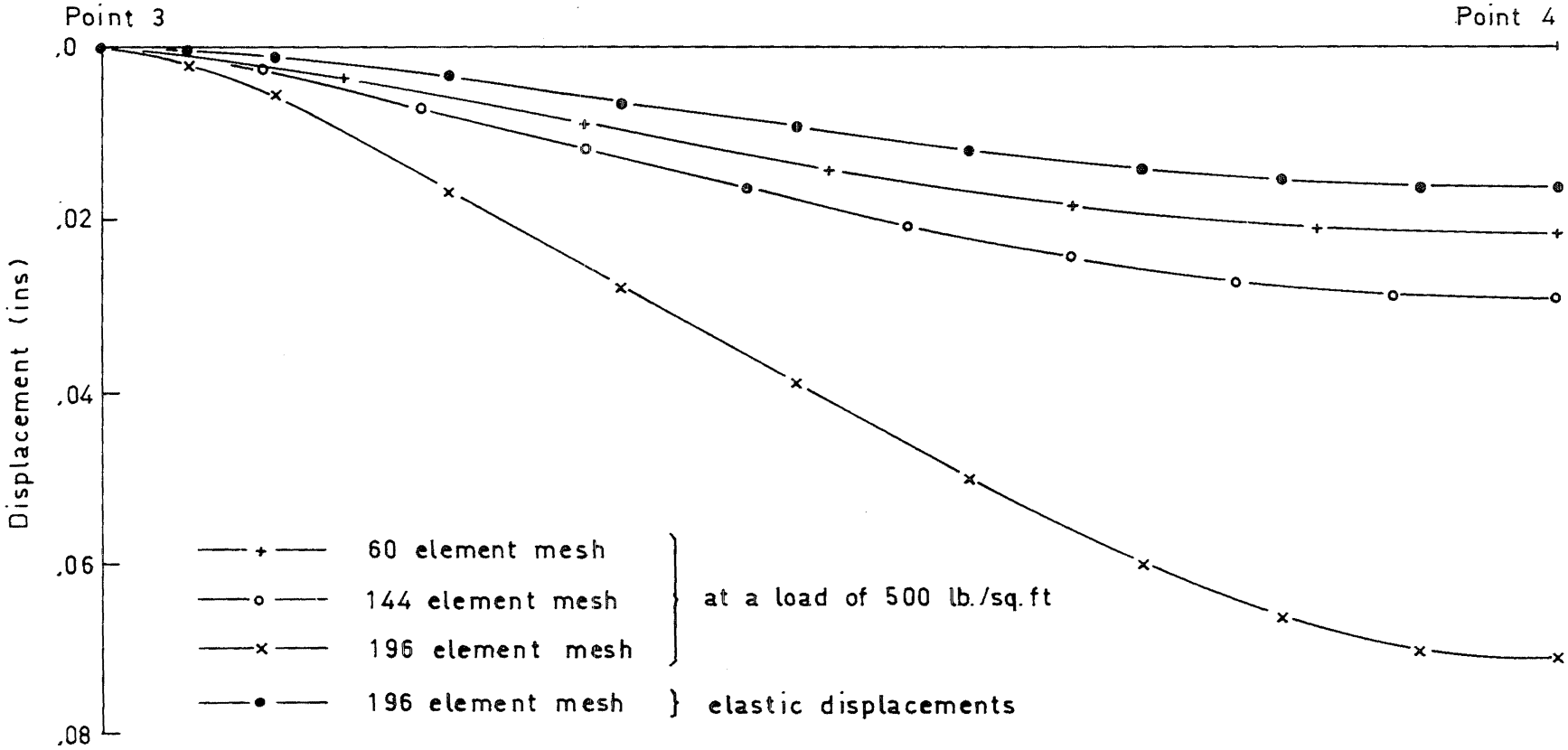

Fig. 7.28. Displacement Profiles Along the Line 3-4 - 500 lb./sq.ft

the slab that are cracked, differ considerably (Figs. 7.23, 7.24, and 7.4). However, the most significant feature is the resemblance of the profile using the elastic/inelastic finite elements to the elastic profile, especially within the central cracked region at point 4. The small deformations arising in this cracked region have produced low stresses in the region and correspondingly high stresses outside the cracked region. This effect has caused the yielded region to form on the bottom surface of the slab and it also prevented this region from extending to the centre of the slab.

Figs. 7.29 and 7.30 show the displacement profiles along the lines 2 - 4 and 3 - 4 respectively at the load 840 lb./sq.ft. Again the displacement profiles that were calculated using the elastic/inelastic elements are much stiffer than the displacement profiles that used elements which were either totally cracked or totally uncracked. The central regions near point 4 are still very stiff showing that they are deforming almost like rigid bodies. This type of deformation is very similar to that observed in the examples using the elastic/inelastic finite elements formed by "integrating by parts", which are described in Section 5.2. The deformation results from the elastic/inelastic stiffness matrix being formed with some of the off-diagonal coefficients being considerably larger than in the elastic stiffness matrix. This is a deficiency of the element formulation. (The cubic

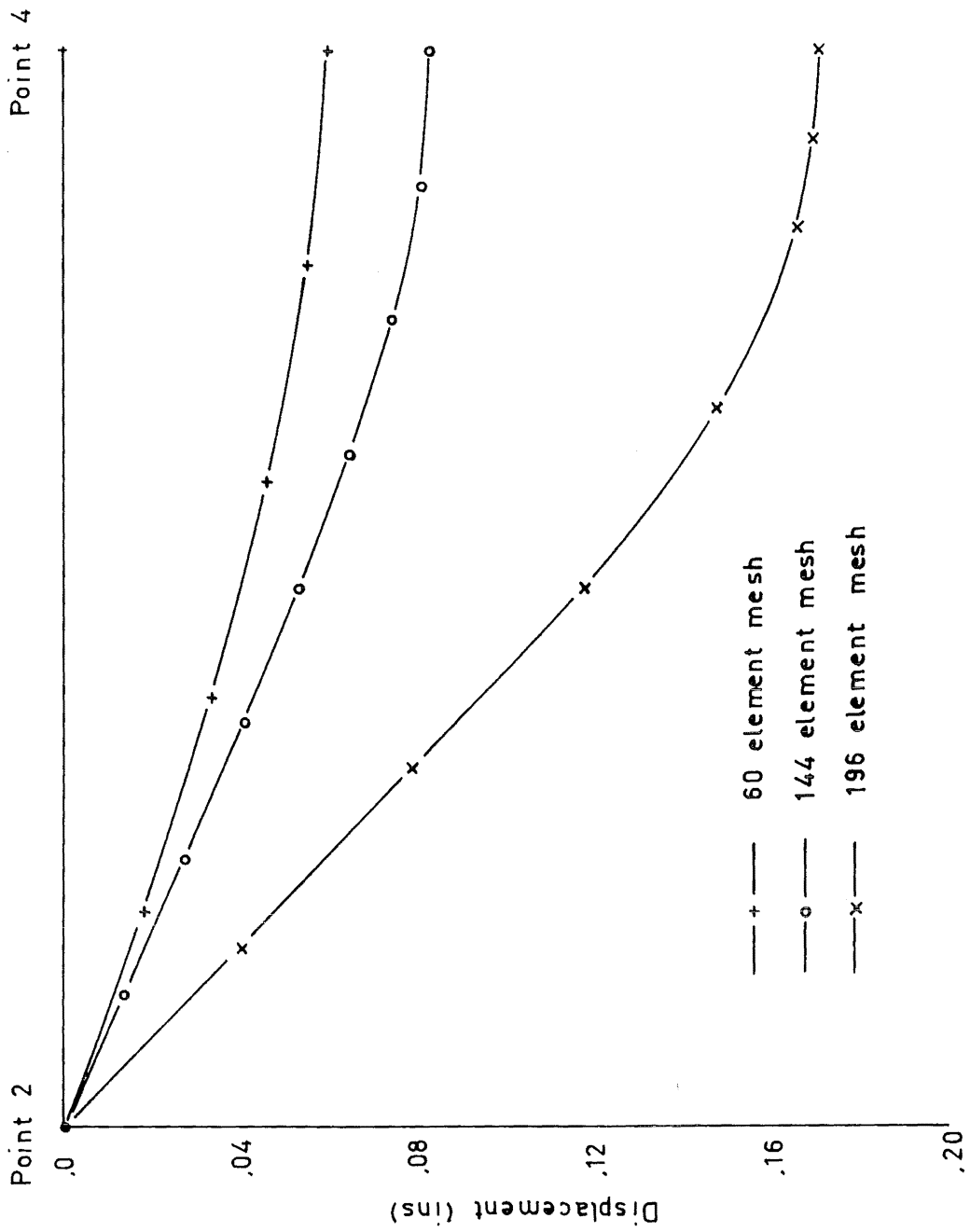

Fig. 7.29. Displacement Profiles Along the Line 2-4 - 840 lb./sq.ft

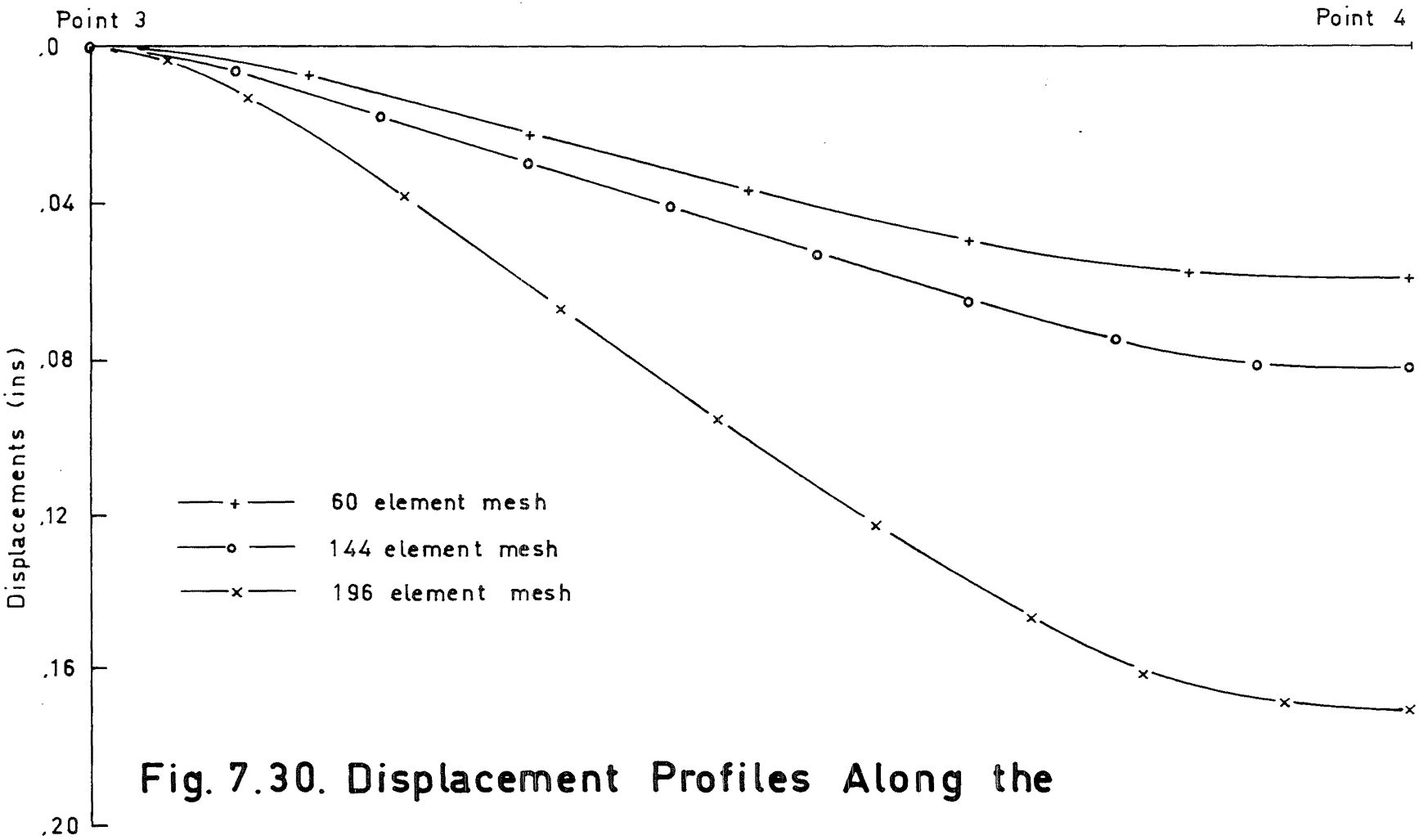

Fig. 7.30. Displacement Profiles Along the Line 3-4 - 840 lb./sq.ft

plate bending element is the simplest possible formulation and it is possible that a more accurate elastic/inelastic finite element could be developed using a plate bending finite element which possessed a quartic or a quintic transverse displacement variation.)

The above analyses were repeated using the elastic/inelastic finite element formed by "integrating by parts". The crack patterns at the load 500 lb./sq.ft. are shown in Fig. 7.31 for the 60 element mesh, and in Fig. 7.32 for the 144 element mesh. Many of the comments made above for the elastic/inelastic finite elements which were formed by a beam analogy are also applicable here. For example, the areas that are cracked are still governed by the displacement at point 4 which gives an indication of the stress intensity about that point. However, cracking has been more extensive with this finite element, though it is not as extensive as in the analysis which used elements that were totally cracked or totally uncracked (Fig. 7.4).

The crack patterns at the load 840 lb./sq.ft. are shown in Fig. 7.33 for the 60 element structure, and in Fig. 7.34 for the 144 element structure. Both of these patterns show the yielded regions on the bottom surface which has been caused by the central elements moving like rigid bodies and imposing high stresses away from the centre, and low stresses at the centre. In these two structures yielding along the built-

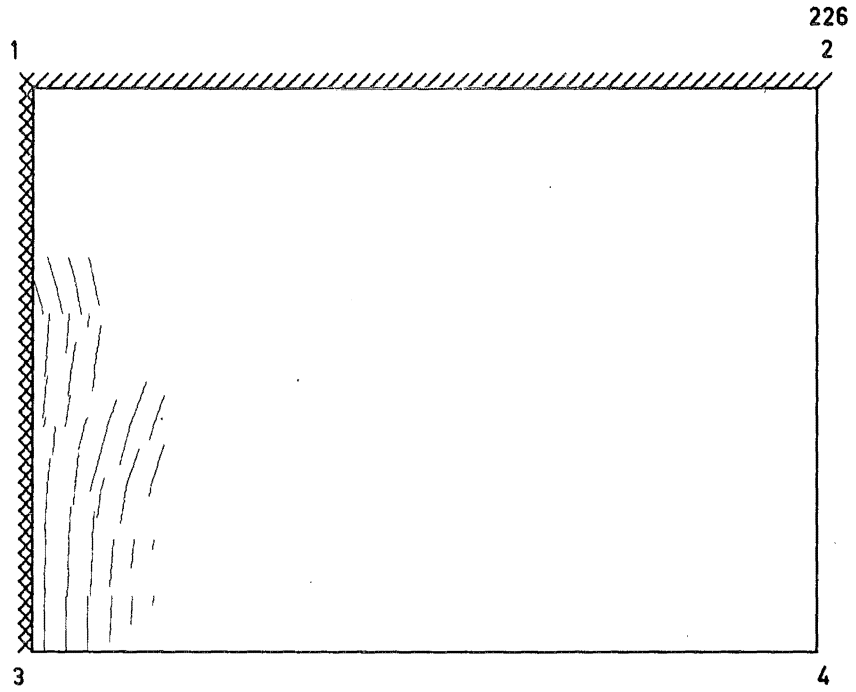

Top Surface

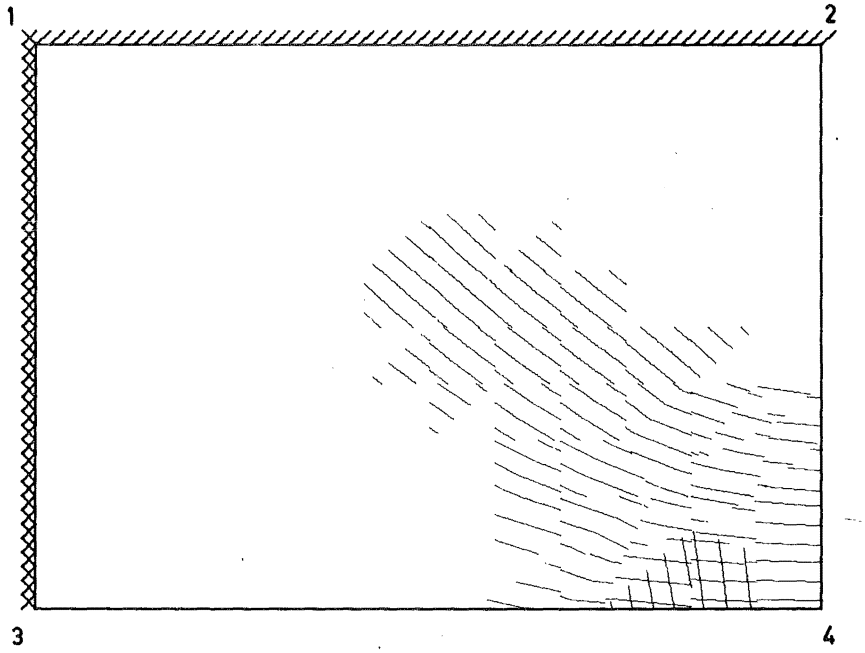

Bottom Surface

Fig. 7.31. Crack Patterns for Sharpe's Slab - 500 lb./sq.ft - 60 Element Mesh

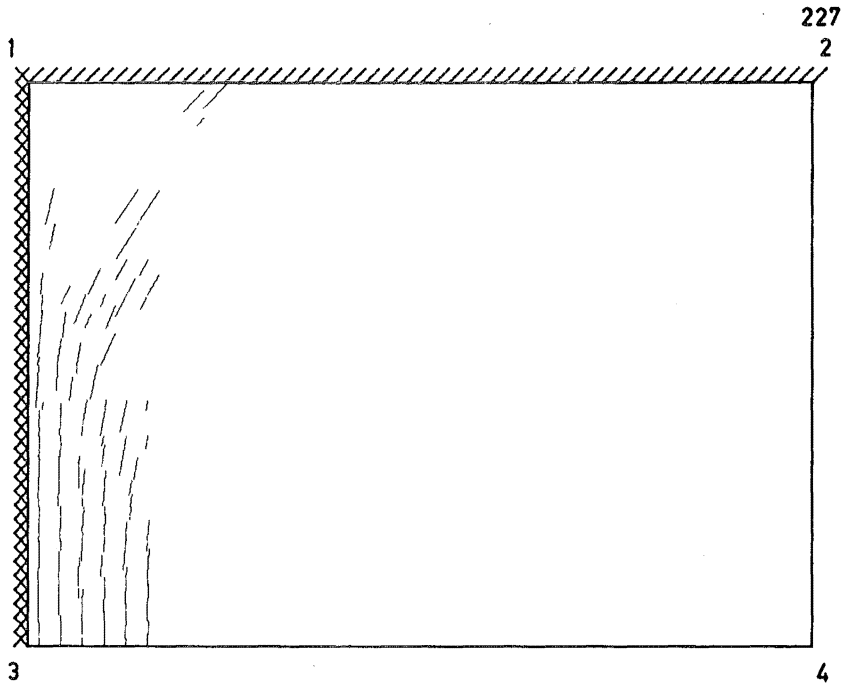

Top Surface

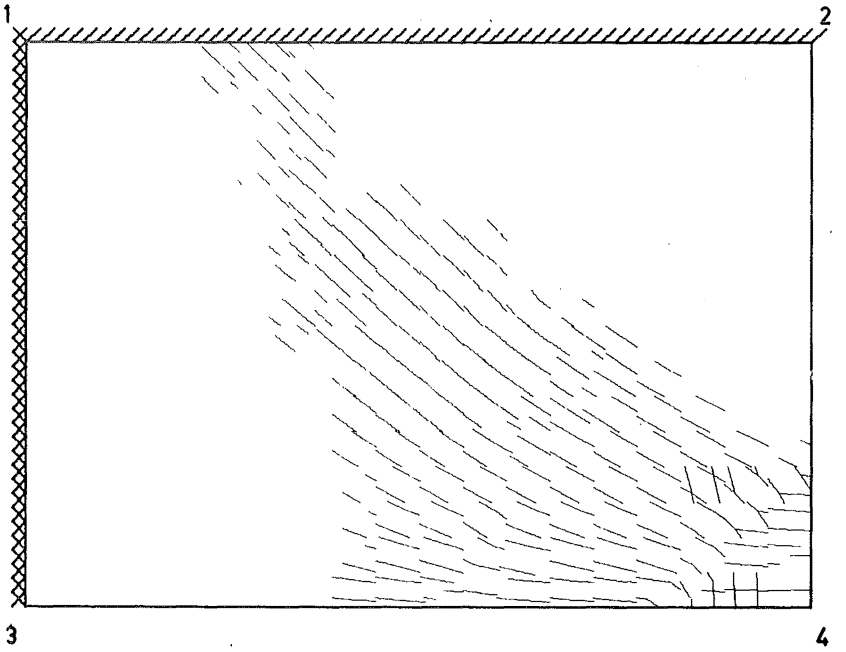

Bottom Surface

Fig. 7.32. Crack Patterns for Sharpe's Slab - 500 lb./sq.ft - 144 Element Mesh

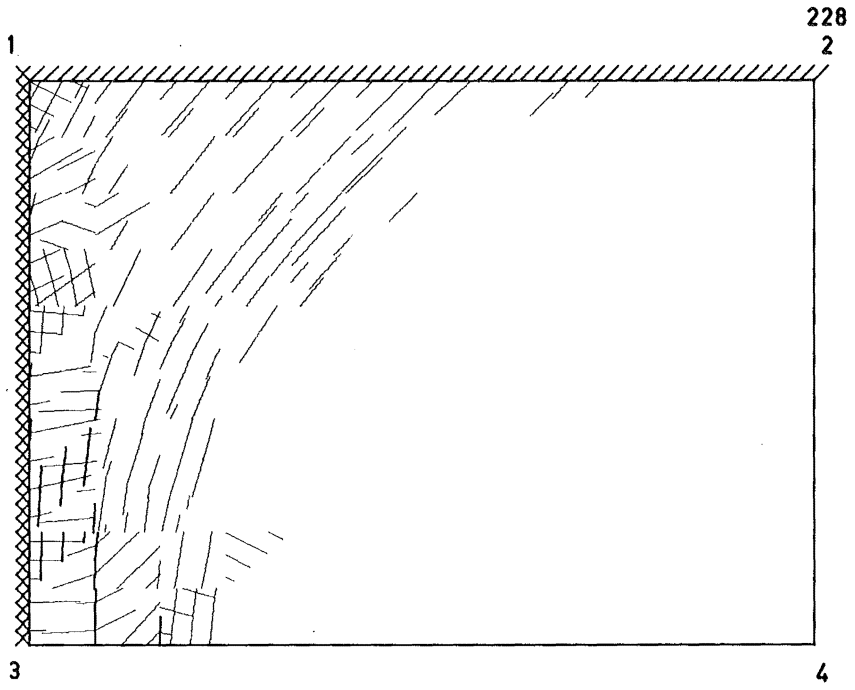

Top Surface

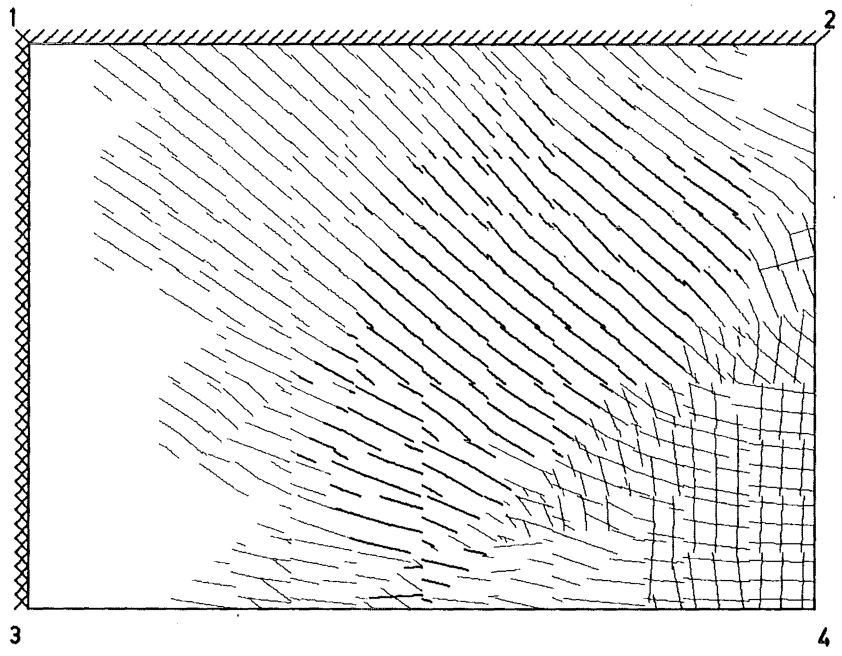

Bottom Surface

Fig. 7.33. Crack Patterns for Sharpe's Slab - 840 lb./sq.ft - 60 Element Mesh

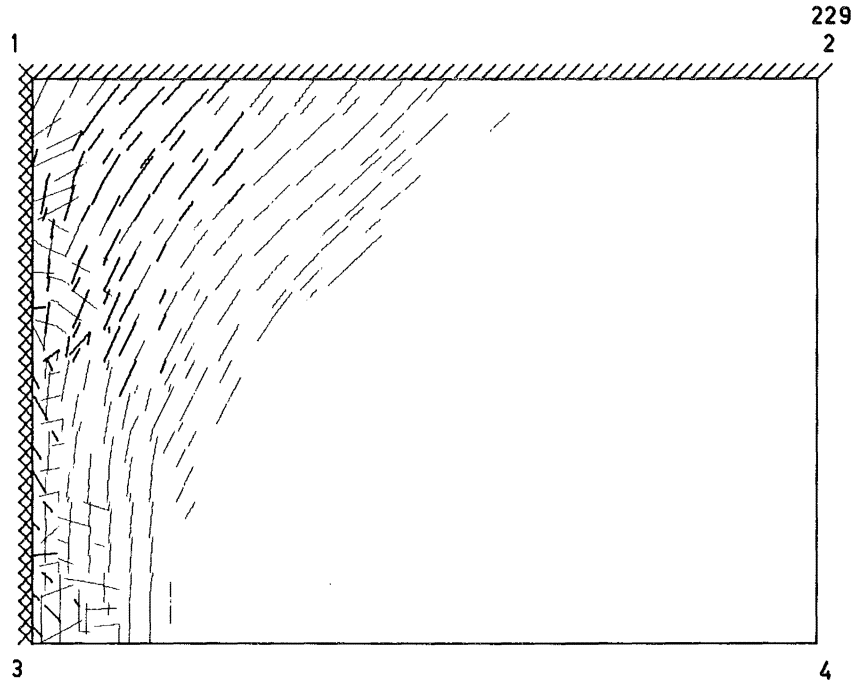

Top Surface

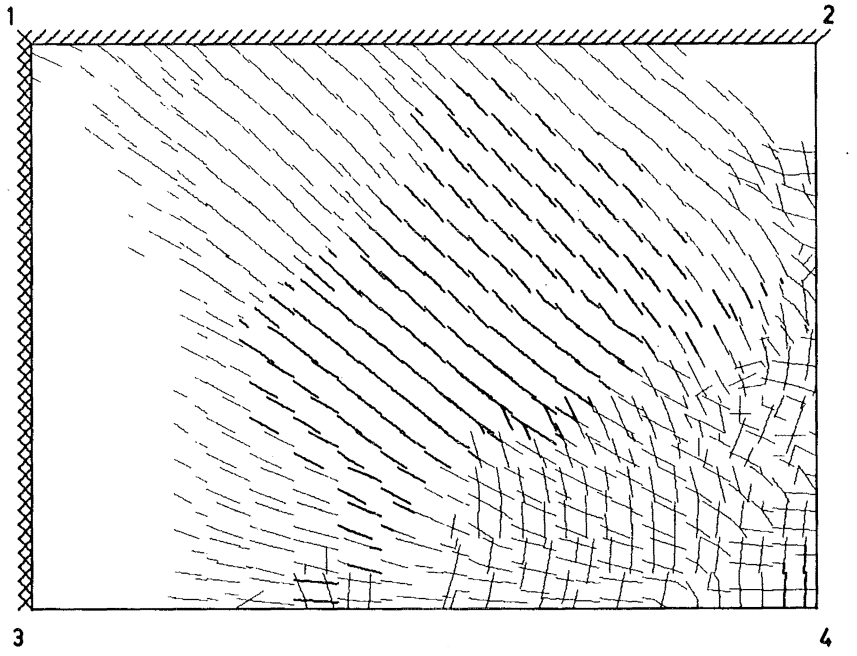

Bottom Surface

Fig. 7.34. Crack Patterns for Sharpe's Slab - 840 lb./sq.ft - 144 Element Mesh

in edge was quite different; the 60 element structure had a high transverse moment along this edge, and the 144 element structure had a high longitudinal moment about this edge though its yield region was formed by a twisting moment at point 1. This high twisting moment probably resulted from the crack patterns at the load 500 lb./sq.ft. (Fig. 7.32). The initial cracking for the 60 element structure was relatively complete in Fig. 7.31 and no stress discontinuities arose. However, the analysis of the 60 element structure showed the instability of these elements because on one cycle, after a degradation in some of the element stiffnesses, the structure became stiffer. This was a result of high off-diagonal coefficients distorting the distribution of the stiffness coefficients.

At the load 500 lb./sq.ft. the displacement profile along the line 2 - 4 is shown in Fig. 7.35, and the displacement profile along the line 3 - 4 is shown in Fig. 7.36. Again the elastic/inelastic element is too stiff though it is slightly more flexible than the elastic/inelastic element formed by a beam analogy. This is the reverse of the results from the simply supported beam example described in Sections 5.1 and 5.2. The present example, however, redistributes the stresses whereas the beam example did not, and this implies that the combination of stiffness and stress matrices for the elastic/inelastic finite element formed by

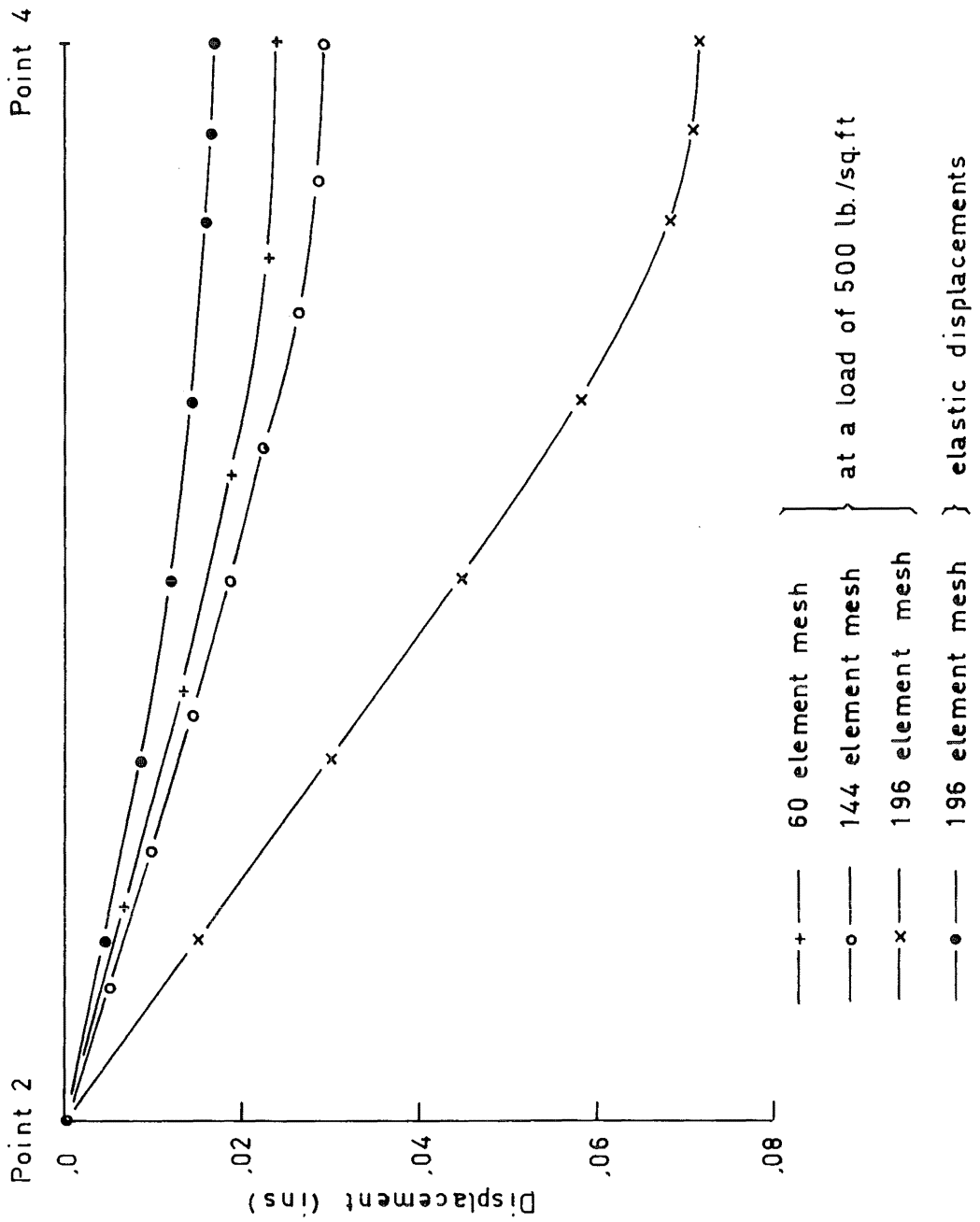

Fig. 7.35. Displacement Profiles Along the Line 2 - 4 - 500 lb./sq.ft

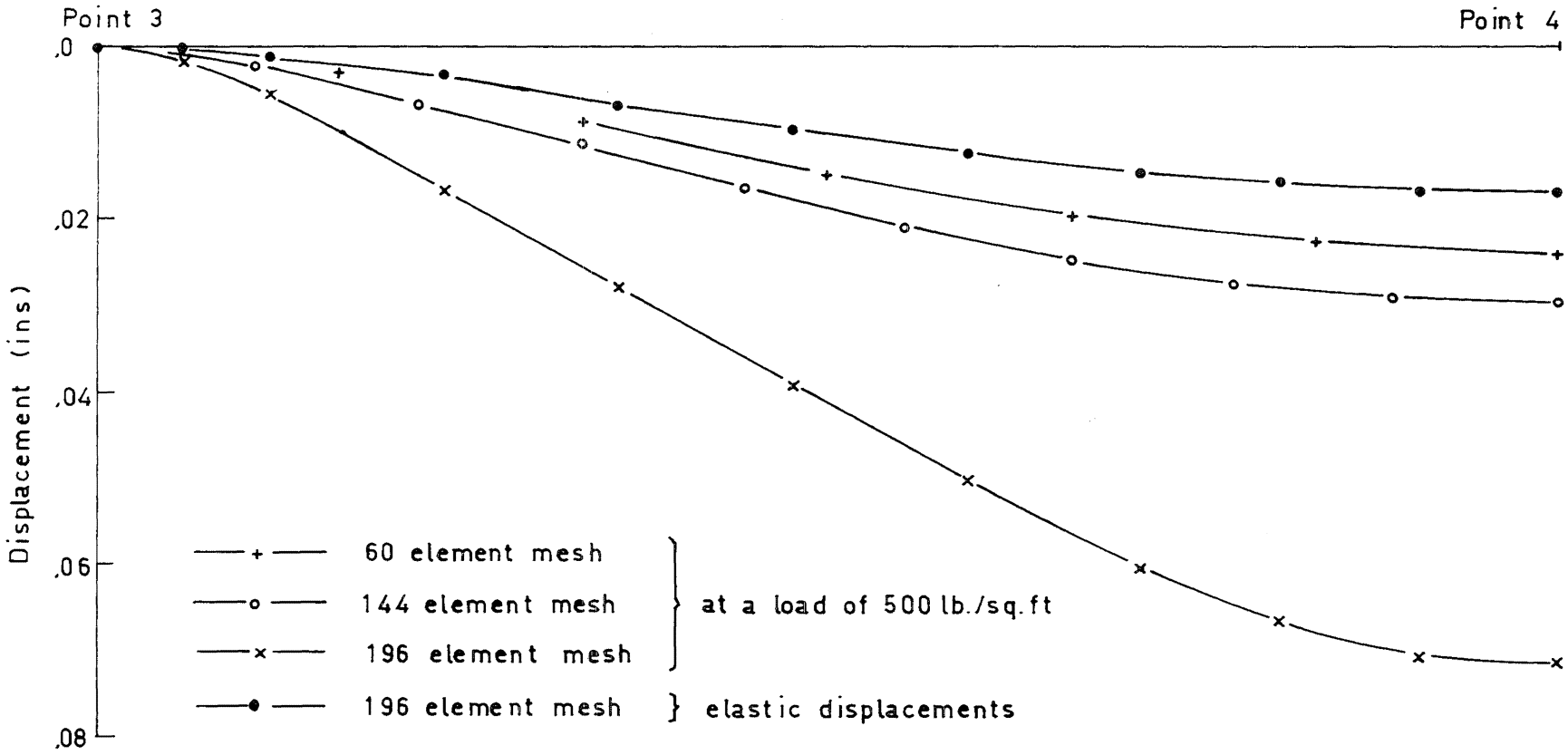

Fig. 7.36. Displacement Profiles Along the Line 3-4 - 500 lb./sq.ft

"integrating by parts" can represent the redistribution more accurately than can the finite element formed by a beam analogy.

At the load 840 lb./sq.ft. the displacement profile along the line 2 - 4 is shown in Fig. 7.37, and the displacement profile along the line 3 - 4 is shown in Fig. 7.38. The displacement profiles are similar although the profiles for the elastic/inelastic elements are still stiffer than those for the analysis which used elements that were either totally cracked or totally uncracked. The reason for the displacement profiles being similar is due to the large proportion of the slab which has cracked, and also the region of yielding on the bottom surface has helped to increase the central displacements. This cracking, however, does not agree with the more reliable theoretical crack pattern shown in Fig. 7.5. The regions of cracking are similar to those from the elastic/inelastic finite element formed by a beam analogy but the displacement profile of the latter is considerably stiffer; again implying that finite elements formed by "integrating by parts" are more flexible. An important feature of both Figs. 7.37 and 7.38 is the increased flexibility of the 60 element structure near the centre of the slab. This phenomenon is yet another example of the sensitivity of the simulated structure to their crack patterns.

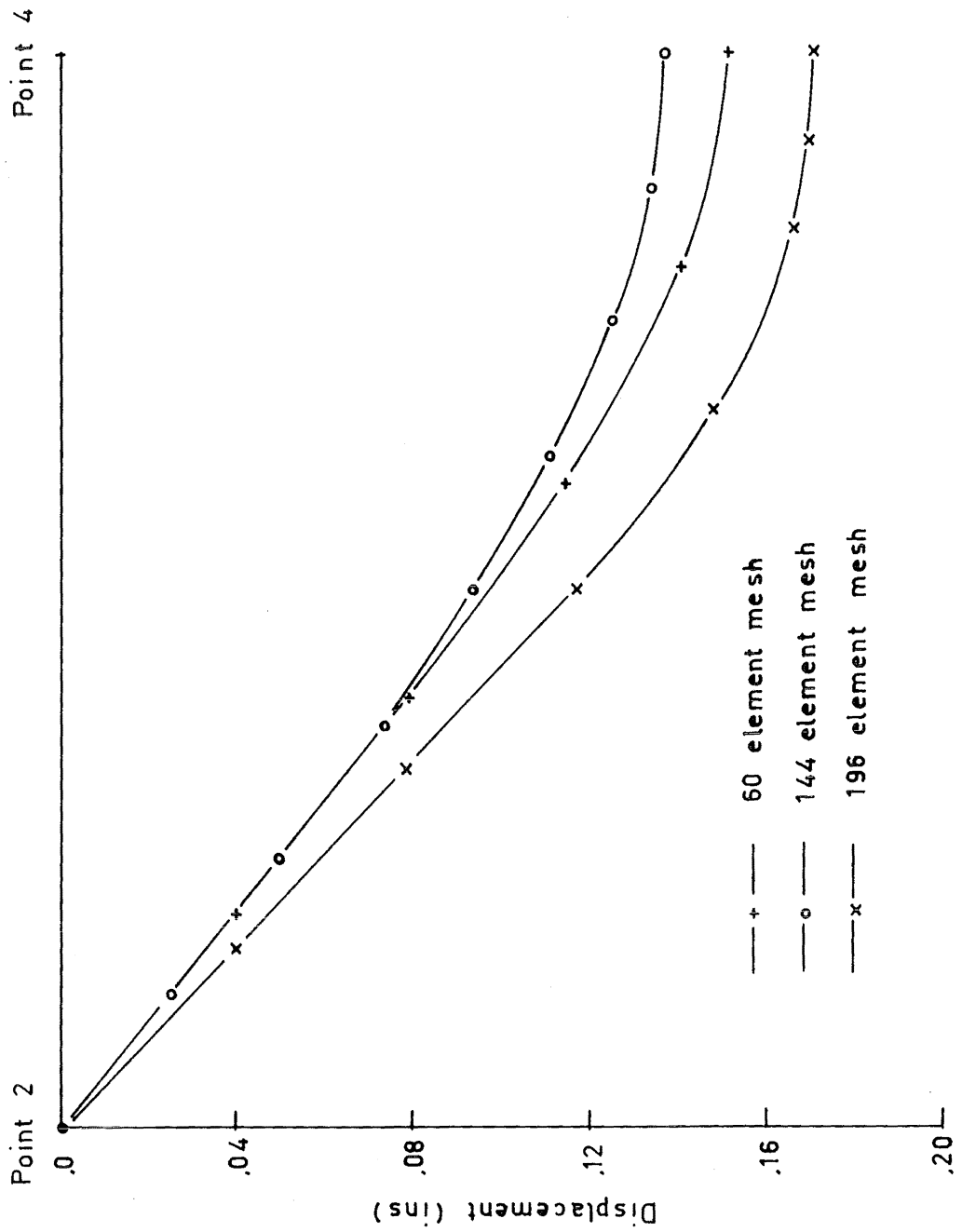

Fig. 7.37. Displacement Profiles Along the Line 2-4 - 840 lb./sq.ft

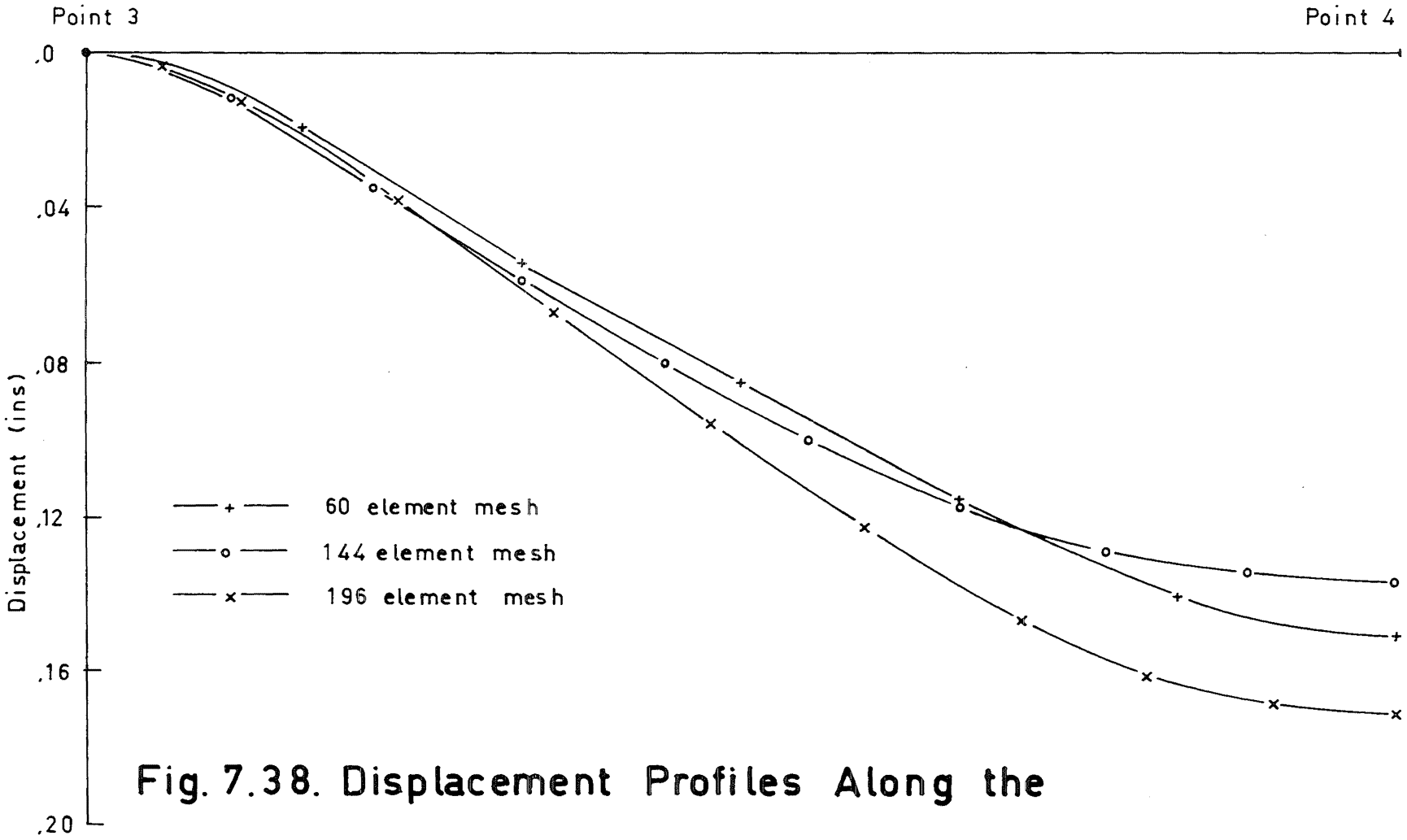

Fig. 7.38. Displacement Profiles Along the Line 3-4 - 840 lb./sq.ft

The behaviour of the elastic/inelastic finite elements is best understood from a comparison with an elastic finite element. Displacements determined from an elastic plate bending stiffness matrix are normally calculated as the difference between two large numbers (this is the reason why plate bending problems are more ill-conditioned than plane stress problems), and this also applies to the elastic/inelastic elements. It would appear that the inter-relationships between the stiffness coefficients have been destroyed in the two elastic/inelastic formulations that have been used. However, as mentioned previously, it may be possible to construct a more accurate elastic/inelastic element from a higher order element.

Summarising this chapter the principal results and conclusions are as follows:

1) the simulated slab was stiffer than the experimental slab though the experimental results seem to indicate that either the instrumentation was faulty or else the test frame underwent a rigid body rotation;

2) membrane forces may have enhanced the strength of the experimental slab (these forces were ignored in the simulated slab) because the experimental load was 10% higher than the theoretical ultimate load;

3) both the theoretical results and the experimental crack patterns at the failure load indicated that cracking and yielding covered most of the slab area;

4) the elastic/inelastic elements did not accurately depict the behaviour of an element that contains both cracked and uncracked regions.

CHAPTER 8

CYLINDRICAL SHELL ROOF MODEL TESTED BY HEDGREN

This chapter describes the analysis of a cylindrical shell roof model which was tested by Hedgren[15] at Princeton University in 1965. Hedgren was studying the analysis of translational shells and he tested the cylindrical shell model so that he could compare his theoretical and experimental results.

The first section of this chapter describes the cylindrical shell, and states the shell information that Hedgren gave and the shell information that had to be assumed. The second section begins with a description of the program that was used to analyse Hedgren's shell. This is followed by the results from the complete analysis which are compared with both the experimental results, and the results obtained by Riera and Billington[6] who also made a complete analysis of Hedgren's shell (refer Section 4.1).

8.1 Shell Information

The parabolic cylindrical shell (Fig. 8.1) was supported on end diaphragms and had free longitudinal edges. The rise to span ratio was 1:5.3 and the width to length ratio was 1:1.75.

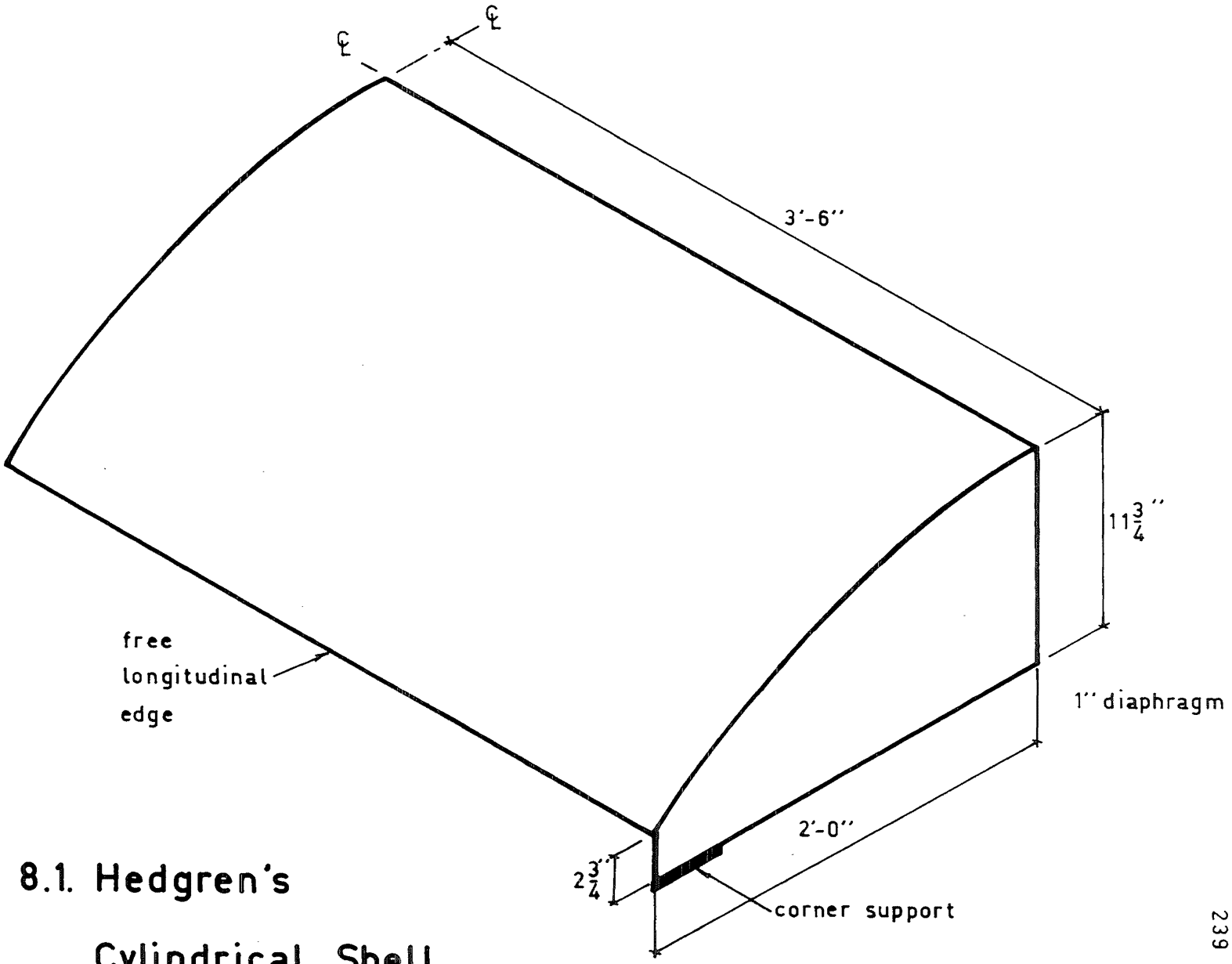

Fig. 8.1. Hedgren's Cylindrical Shell

The properties of the mortar that Hedgren gave were:

Mortar cylinder strength	=	4,390 lb./sq.in.
Poisson's ratio for the mortar	=	.145
Modulus of elasticity for the the mortar (in flexure)	=	3.0×10^6 lb./sq.in.
Tensile strength of the mortar	=	696 lb./sq.in.

Hedgren determined the value for the modulus of elasticity from four simply supported beam specimens. The moduli of elasticity for Islam's mortar slabs were calculated from results found by Magura (refer Table 6.2), and from these results the modulus of elasticity for Hedgren's mortar, i.e. corresponding to a compressive strength of 4,390 lb./sq.in., is 2.4×10^6 lb./sq.in. which is approximately 17% lower than Hedgren's value.

The drawings of the shell reinforcement have been reproduced in Fig. 8.2, and the properties of the reinforcement which Hedgren gave are shown in Table 8.1. The shell reinforcement was simplified for this analysis. Fig. 8.3 is a reproduction of a photograph that shows the cracking after failure on the bottom and top surfaces of the shell. A comparison of the crack patterns shown in Fig. 8.3 and the reinforcement layout shown in Fig. 8.2 shows that almost all of the cracking was perpendicular to the reinforcement, and that there were six distinct regions of cracking (these are shown in Fig. 8.4). Therefore isotropic reinforcement

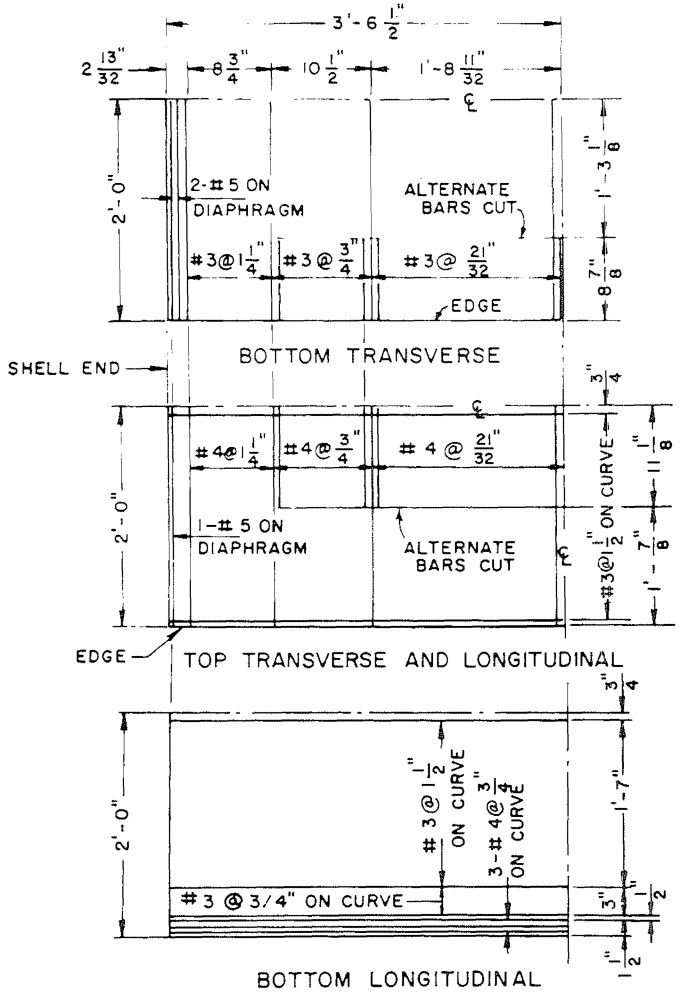

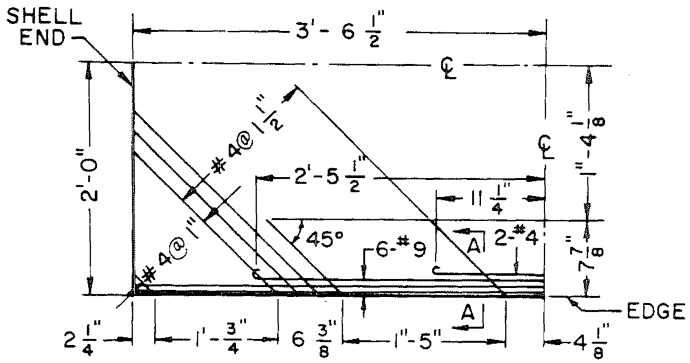

DIAGONAL AND EDGE

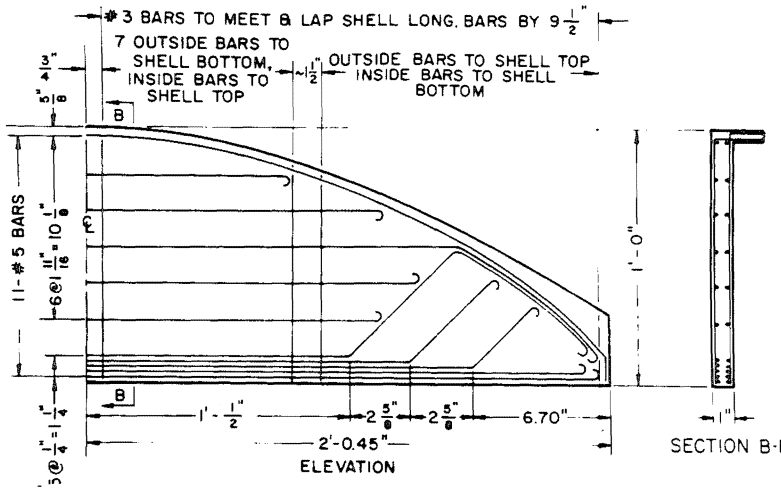

Fig. 8.2 Shell Reinforcement

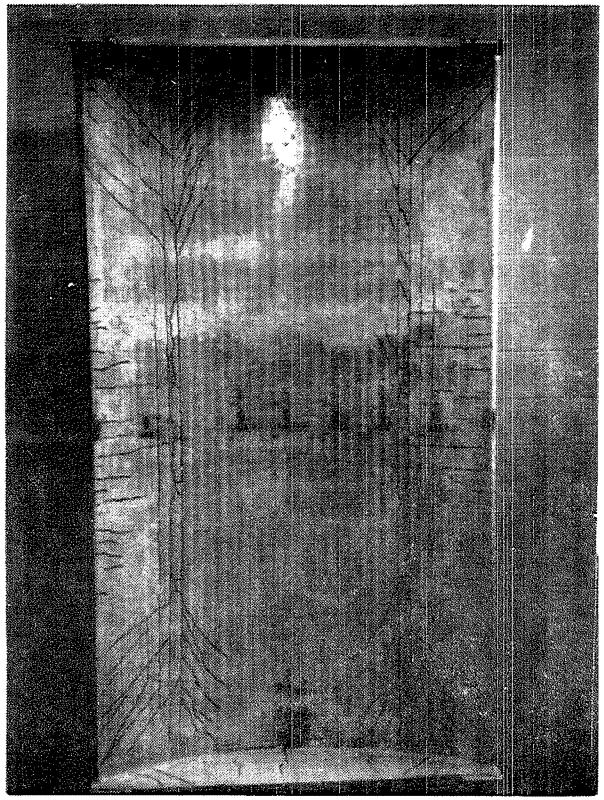

Bottom Surface

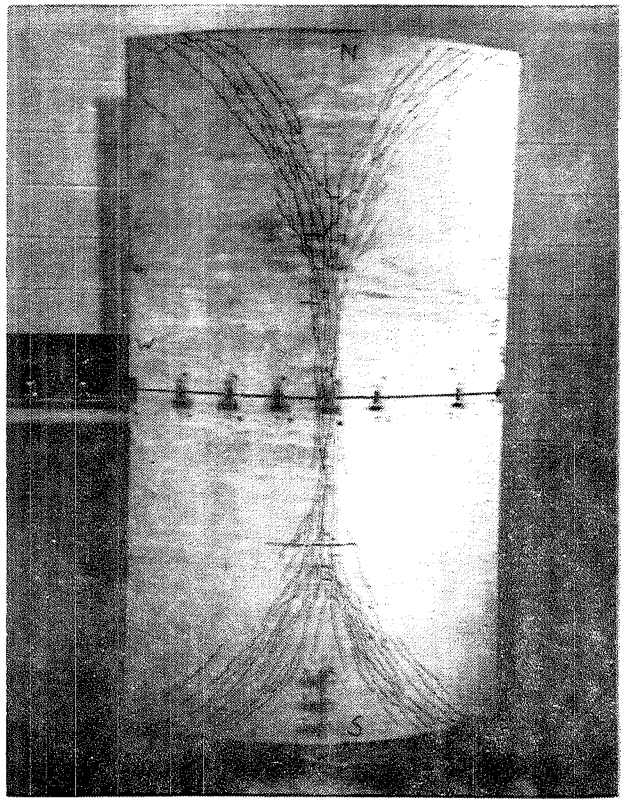

Top surface

Fig. 8.3. Experimental Crack Patterns

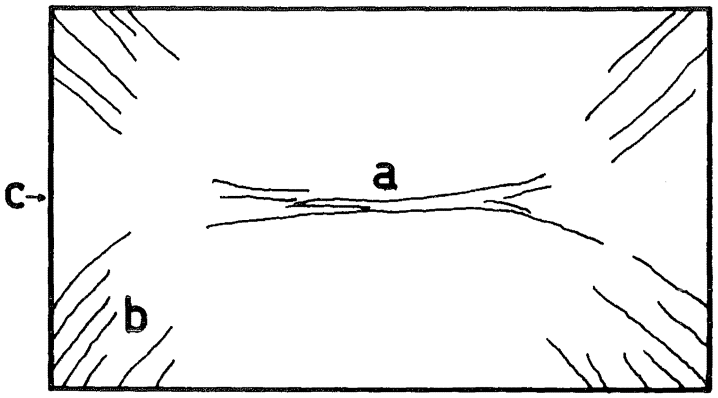

Top surface

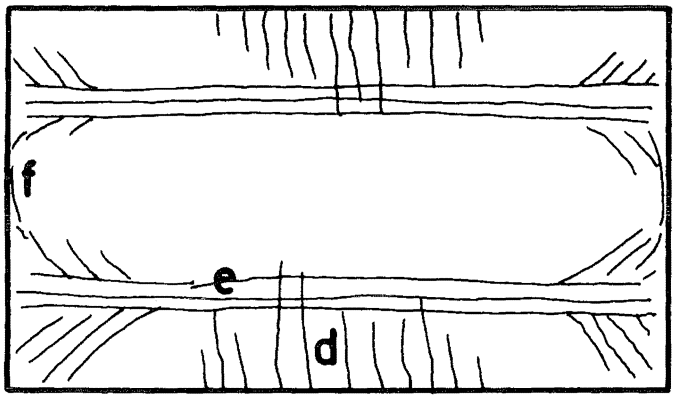

Bottom surface

Fig. 8.4. Regions of Cracking in the Shell

was assumed within each of these six regions, and the quantity and position of this reinforcement was made identical to the quantity and position of the shell reinforcement that was perpendicular to the respective band of cracks. From these six regions of cracking there arise eight different reinforcement patterns, and these are shown in Fig. 8.5. In the analysis every element was assigned a number which referred to one of these reinforcement patterns (refer Fig. 8.6).

Gage	Designation	Diameter in.	Area $in.^2$	σ_y $lb./in.^2$	σ_{ult} $lb./in.^2$
18	3	0.048	0.00181	36,700	52,800
16	4	0.062	0.00302	31,800	50,000
14	5	0.080	0.00503	36,400	51,700
10	9	0.135	0.0143	44,500	60,900

Table 8.1 Model Reinforcement[15]

Most of the shell reinforcement consisted of #3 and #4 reinforcing bars (approximately $\frac{1}{8}$ scale) and we see from Table 8.1 that the properties of these two bars are very similar. For this reason all the reinforcement was considered to have identical material properties, namely:

Yield stress of the reinforcement = 34,200 lb./sq.in.

Ultimate stress of the reinforcement = 51,400 lb./sq.in.

Elastic modulus of elasticity = 29.0×10^6 lb./sq.in.

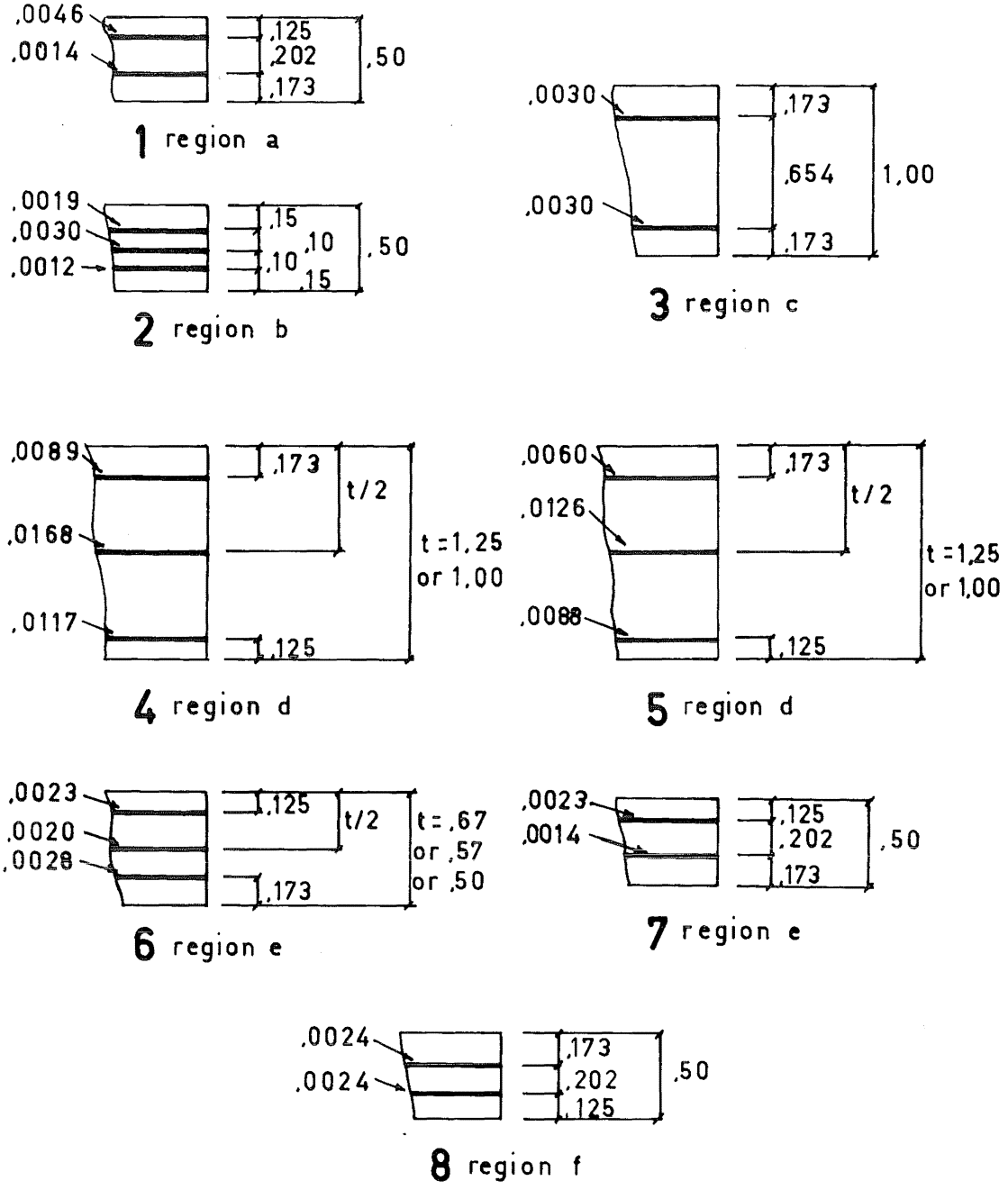

Units length - ins
reinforcement area - sq.in./in.

Fig. 8.5. Governing Reinforcement Regions

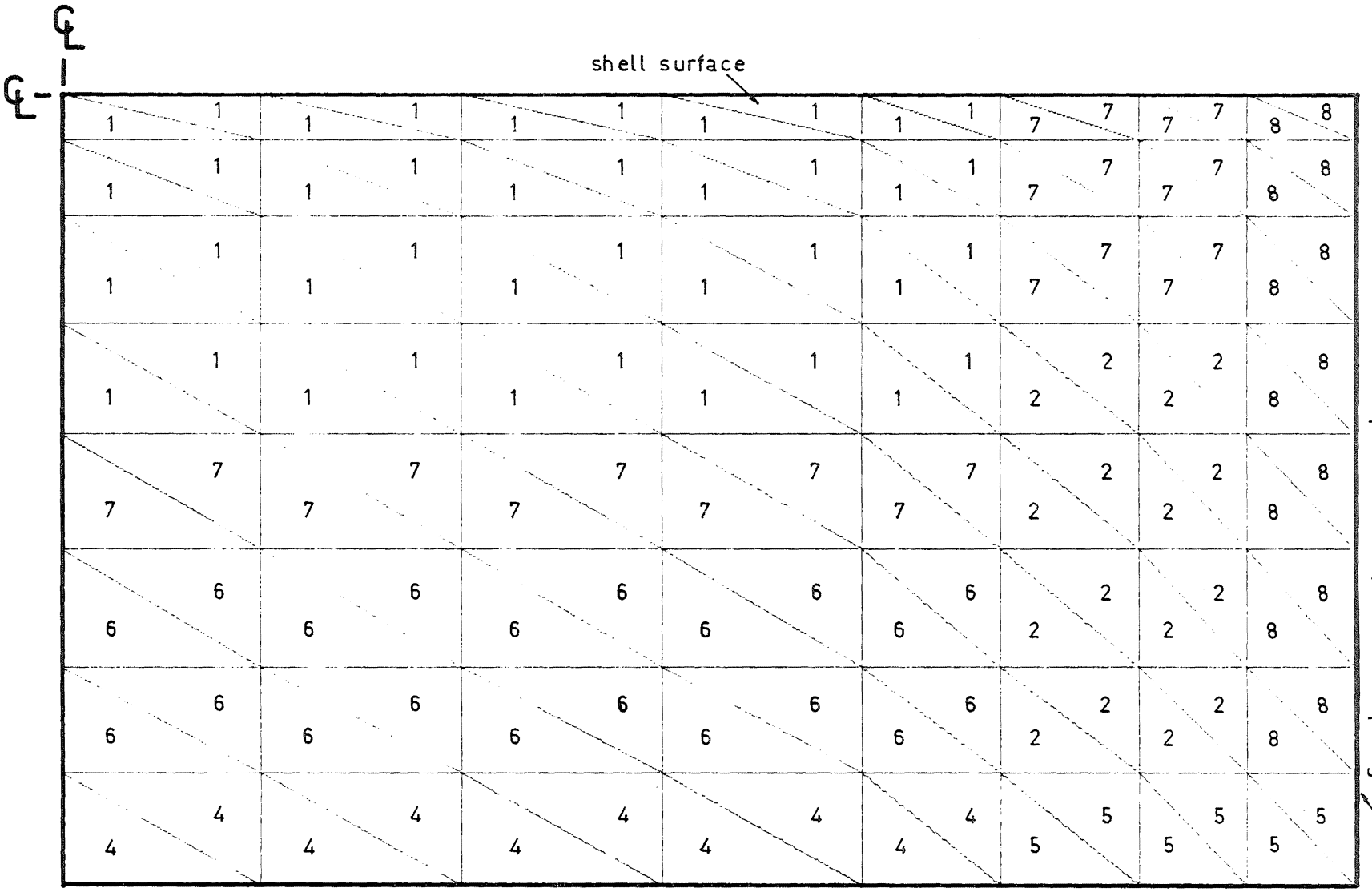

Fig. 8.6. Reinforcement Patterns in each Finite Element

Effective modulus of elasticity after yielding (determined by assuming that the ultimate reinforcement strain was .01) $= 1.95 \times 10^6$ lb./sq.in.

Along the longitudinal edges of the shell the thickness was increased, over a 5 inch horizontal distance, according to the variation

$$h = 0.5 + \left(\frac{y'}{5}\right)^{1.5}$$

where h is the thickness and y' is the horizontal distance. This variation is shown in Fig. 8.7 together with the position of the three outermost nodal points. Near the longitudinal edge each element has two nodes of one thickness and the third node a different thickness, and in the complete analysis each element thickness was determined from the average of its nodal thicknesses.

8.2 Analysis of Hedgren's Cylindrical Shell

Hedgren's cylindrical shell was analysed using a similar method of analysis to that used for the slab analyses (refer Section 4.6) though a few modifications were made, and these are discussed below.

In the slab analyses the degradation in stiffness of any section was determined from the equivalent degradation of a moment-curvature relationship whose variation was retained within the computer as a stepped function comprised

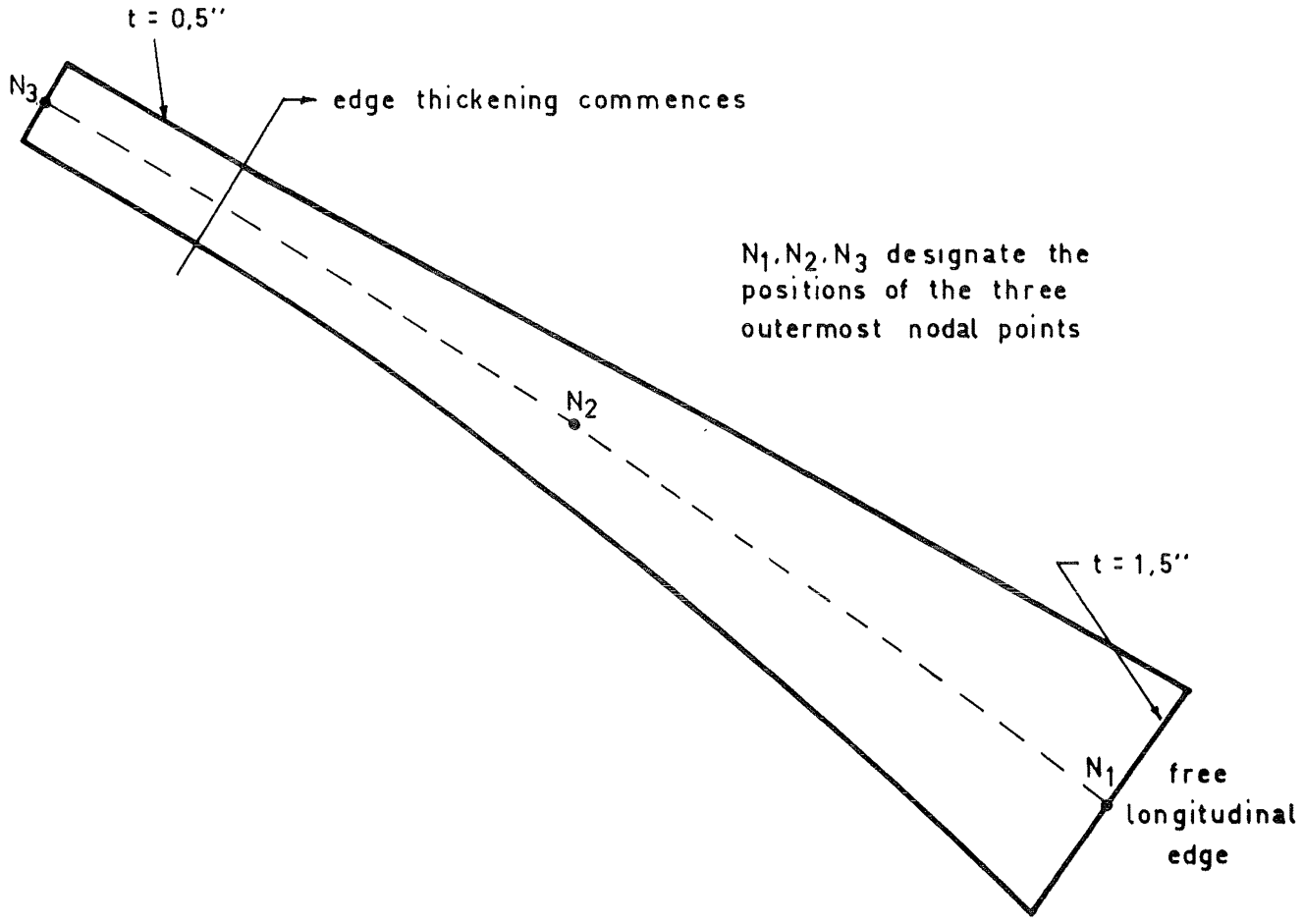

Fig. 8.7. Thickness Variation at the Longitudinal Edge

of 100 steps (refer Section 6.3). In a shell, however, the degradation in stiffness is determined from the equivalent degradation of the load-moment-curvature relationship and it is not practical to retain an image of this relationship within the computer because 40,000 words of core storage would be needed to depict the relationship to the same accuracy as that used for the slab moment-curvature relationship, and normally this storage would not be available. In the analysis of Hedgren's shell each element was analysed to determine its average nodal principal forces and principal moments, and these forces were applied to an equivalent beam section whose properties corresponded to one of the eight reinforcement patterns shown in Fig. 8.5. For a given load and moment, the beam section was analysed and any degradation of stiffness was determined.

The analysis of the equivalent beam section, referred to above, utilizes a trial and error solution technique (refer Appendix B), and because there are many possible force/moment combinations the concrete stress-strain curve was simplified because this in turn simplifies the trial and error solution. The load-moment-curvature relationships described in Appendix B used a concrete stress-strain curve that had a parabolic and a linear variation (Fig. B.2), and this was simplified in the load-moment-curvature relationships to a linear variation, i.e.

for $-\varepsilon_t \leqslant \varepsilon \leqslant \varepsilon_u$ $\qquad f_c = E_c \varepsilon$ $\qquad (8.3)$

where ε_t is the tensile strain at which the concrete will crack in flexure, ε is the concrete strain, ε_u is the ultimate compressive strain of the concrete, f_c is the concrete stress, and E_c is the modulus of elasticity for concrete.

In the complete analysis the strains at a section result from the combined action of an axial force and a bending moment, though the finite element analysis assumed that the plate bending and the plane stress stiffnesses are not related, i.e. that a rotation at a point does not affect the in-plane displacements at that point, etc. Hence, when an element was cracked two reduction factors were determined, one for the plate bending stiffness matrix and the other for the plane stress stiffness matrix. The reduction factor for the plate bending stiffness matrix was determined by the same method as in the slab analyses, i.e. by the curvature degradation, and for the cylindrical shell the curvature was taken at the cracked sections. (The equivalent-displacement curvature was not used because the analyses of Islam's mortar models had been too stiff - refer Sections 6.2 and 6.3.) Fig. 8.8a shows a cracked segment subjected to an axial tensile force, N . When determining the reduction factor for this segment two approximations were introduced; firstly the bending in the cracked segment caused by the axial force was ignored, and secondly, it was assumed that the concrete stress was

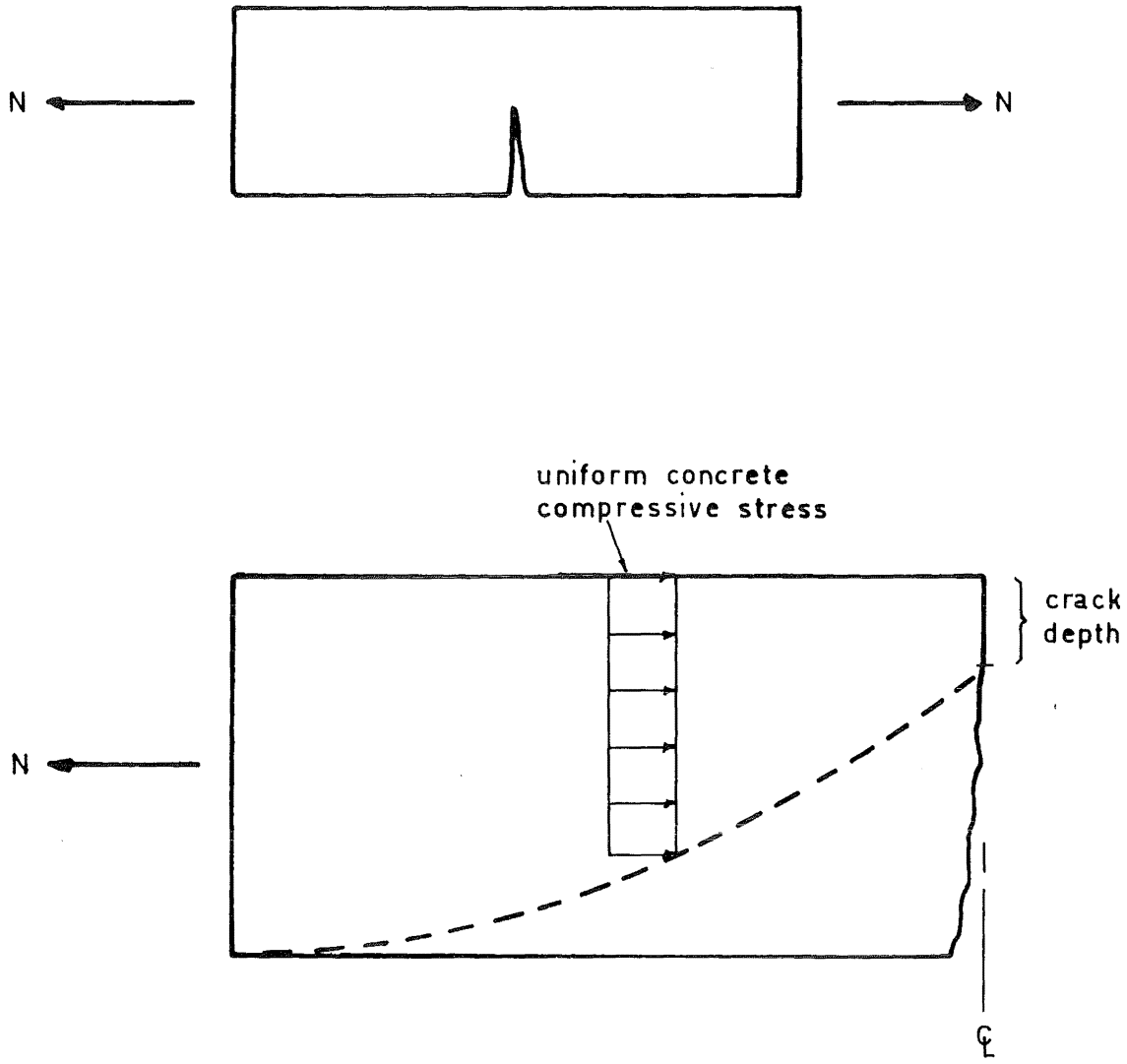

Fig. 8.8. Cracked Segment Subjected to an Axial Force

constant and that the depth of the stress block varied parabolically from the cracked section to the two end sections (refer Fig. 8.8b). Hence, the axial deformation of one half of the cracked segment is

$$\delta = \int_0^a \frac{N_1}{E_c(t-y) + \bar{E}_s}\, dx \qquad (8.4)$$

where $y = \frac{b}{a^2} x^2$ and $\bar{E}_s = E_s(a_{st} + a_{sm} + a_{sb})$ and a_{st}, a_{sm}, and a_{sb} are the steel areas in the top, middle, and bottom layers respectively. Solving Eq. (8.4) and rearranging it to obtain the force for a unit displacement we get

$$N_1 = \frac{bE_c}{\frac{1}{2m} \log_e \frac{m+1}{m-1}} \qquad (8.5)$$

where $m = \frac{t}{b} + \frac{\bar{E}_s}{bE_c}$.

If the section is uncracked then, for a unit displacement

$$N_2 = E_c t + \bar{E}_s \qquad (8.6)$$

and the reduction factor is given by the ratio N_1/N_2. A pessimistic case is when the crack height $b = \frac{3}{4}t$, and substituting this value into Eqs. (8.5) and (8.6) for the $\frac{1}{2}$ inch shell we obtain a reduction factor of 0.633. Because this factor does not vary significantly as the crack height changes any element whose plane stress stiffness had to be reduced was reduced by the factor of 0.633.

Free edged cylindrical shells are very flexible structures and an attempt was made in the complete analysis to consider the effect of large deformations. With large deformations there are two sources of non-linearity;

a) the strain-displacement equations contain non-linear terms, e.g. those introduced by a rotation of the element, and

b) the equilibrium equations and boundary conditions should be formulated in the deformed geometry.

The inclusion of the first source of geometric non-linearity requires the formation of additional stiffness matrices[19,47,79] and was not included in the analysis of Hedgren's shell. The second source of geometric non-linearity, however, can easily be taken into account. In each cycle the nodal displacements were automatically punched onto cards and the nodal dimensions were calculated at each cycle as the sum of the original dimensions and the displacements calculated from the previous cycle.

One further modification was made to the program. Initially when an element failed it was given a modulus of elasticity of 1.0 lb./sq.in., but this was changed to give the modulus of elasticity that would result if the limiting concrete and reinforcement strains were ignored. The reason for making this change is described below. At a load which was approximately 45% of the experimental failure load some elements contained reinforcement that had reached

its theoretical ultimate strain of .01. Because the elements were all doubly reinforced, and some had an additional layer of reinforcing in the middle of the section, it was decided that a modulus of elasticity of 1.0 lb./sq.in. would be unduly pessimistic. More important, however, because a shell had a considerable capability of redistributing its stresses the probability is that, as the section is degrading in stiffness, the stresses will redistribute and thus relieve the stresses on the degrading element. Hence, failure of the element could be prevented. Due to the low effective modulus of elasticity of the reinforcement after it has yielded this procedure formed moduli of elasticity that varied approximately from 1/10 to 1/100 of the elastic modulus of elasticity depending on how large the stresses were at the section.

The crack patterns, load-displacement curves, and displacement profiles from the experimental and theoretical results will now be considered. Hedgren recorded the cracks that could be observed with the naked eye for four load cases, and they are shown in Fig. 8.9. He also made some comments on the sequence of cracking which will be briefly summarised below. Because the shell was loaded by a vacuum Hedgren could not see the cracking on the bottom surface of the shell and his deductions on the bottom surface cracking have been made from his strain readings. Initial cracking

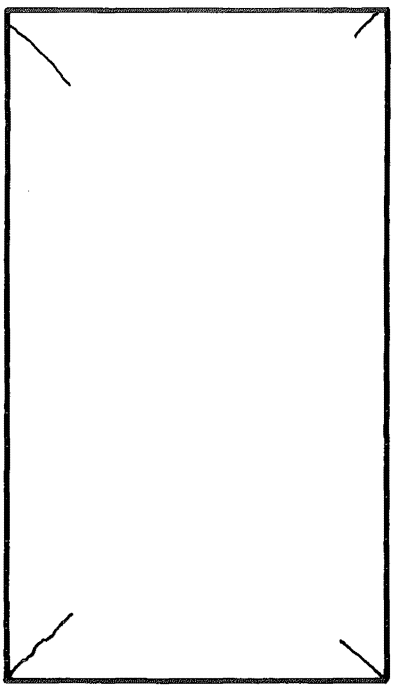

120 lb./sq.ft

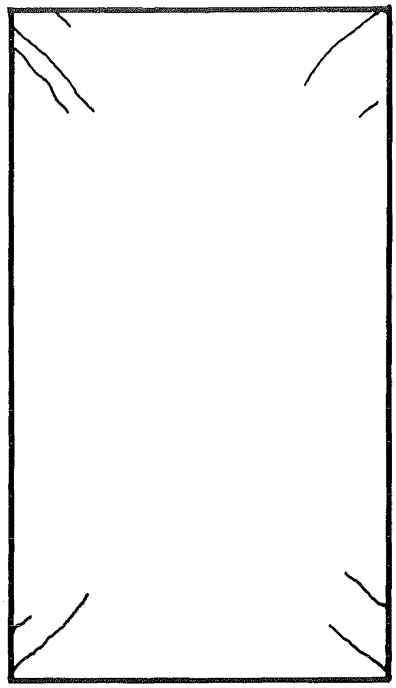

180 lb./sq.ft

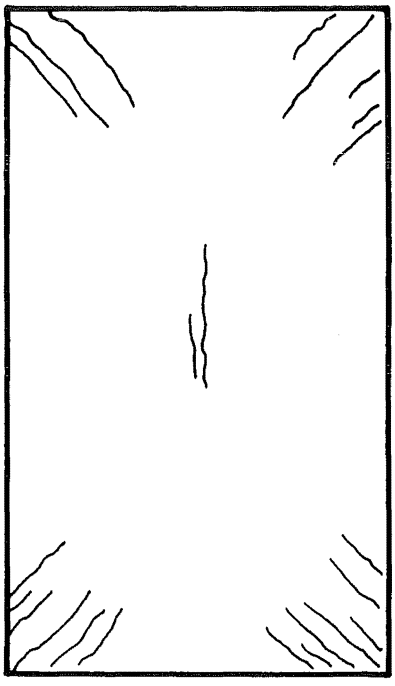

240 lb./sq.ft

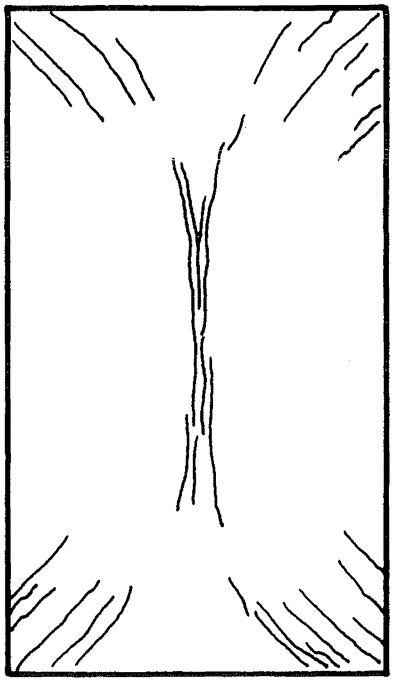

300 lb./sq.ft

Fig. 8.9. Experimental Crack Patterns

occurred at a load of 37.5 lb./sq.ft. and they formed on the bottom surface and at the longitudinal edges. Flexural cracking formed on the top surface, at the centre of the shell, at a load of approximately 60 lb./sq.ft. All these cracks, however, could not be seen with the naked eye. At a load of 120 lb./sq.ft. cracking was observed at the shell corners (refer Fig. 8.9). This cracking had increased when the load was 180 lb./sq.ft. and cracking and yielding of the reinforcement at the crown of the shell became apparent at a load of 240 lb./sq.ft. When the load was 300 lb./sq.ft. the corner and crown cracks propagated but did not meet. At failure, 330 lb./sq.ft. these two crack bands had become one and, in conjunction with the bottom longitudinal cracks, a failure mechanism formed. The photographs of the final crack patterns are shown in Fig. 8.3.

Hedgren recorded flexural cracking at the crown of the shell at a load of approximately 60 lb./sq.ft. and from the experimental strain readings he calculated that the bending moment at the crown was -24 lb.in/in. and the axial force was -20 lb.in./in. (i.e. a compressive force). The author analysed these results and determined that the theoretical value of the cracking strain was 0.000184, and therefore the theoretical maximum concrete tensile stress was 890 lb./sq.in., which is approximately 27% greater than the value of 696 lb./sq.in. that Hedgren determined from testing beam specimens

(refer Section 8.1). In the analysis the maximum concrete tensile stress of 696 lb./sq.in. was used because it was calculated by a more accurate and reliable method.

The theoretical crack patterns of the shell roof are given below. When these patterns were plotted it was assumed that the shell was unfolded and therefore the width of these diagrams corresponds to the arc length of the shell. The equivalent unfolded shell mesh is shown in Fig. 8.10.

The theoretical crack patterns at the load 120 lb./sq.ft. are shown in Fig. 8.11. On the top surface the initial cracking formed at the crown and was caused by a high transverse bending moment. Elements on the crown were also subjected to large longitudinal compressive forces and small transverse compressive forces. The initial crown cracking was longitudinal but near the diaphragm the cracks have curved towards the corner of the shell at point 4 (refer Fig. 8.10 for the numbering) because of a high twisting stress that was encountered in this region. Another region of cracking occurred on the top surface near point 4, and this was caused by a principal moment formed from both a longitudinal and twisting moment. Counteracting this cracking is a compressive stress of approximately 300 lb./sq.in.

Hedgren recorded the visible top surface cracking at this load (Fig. 8.9), and it consisted of cracking at the shell corners, i.e. at point 4. In the theory, however,

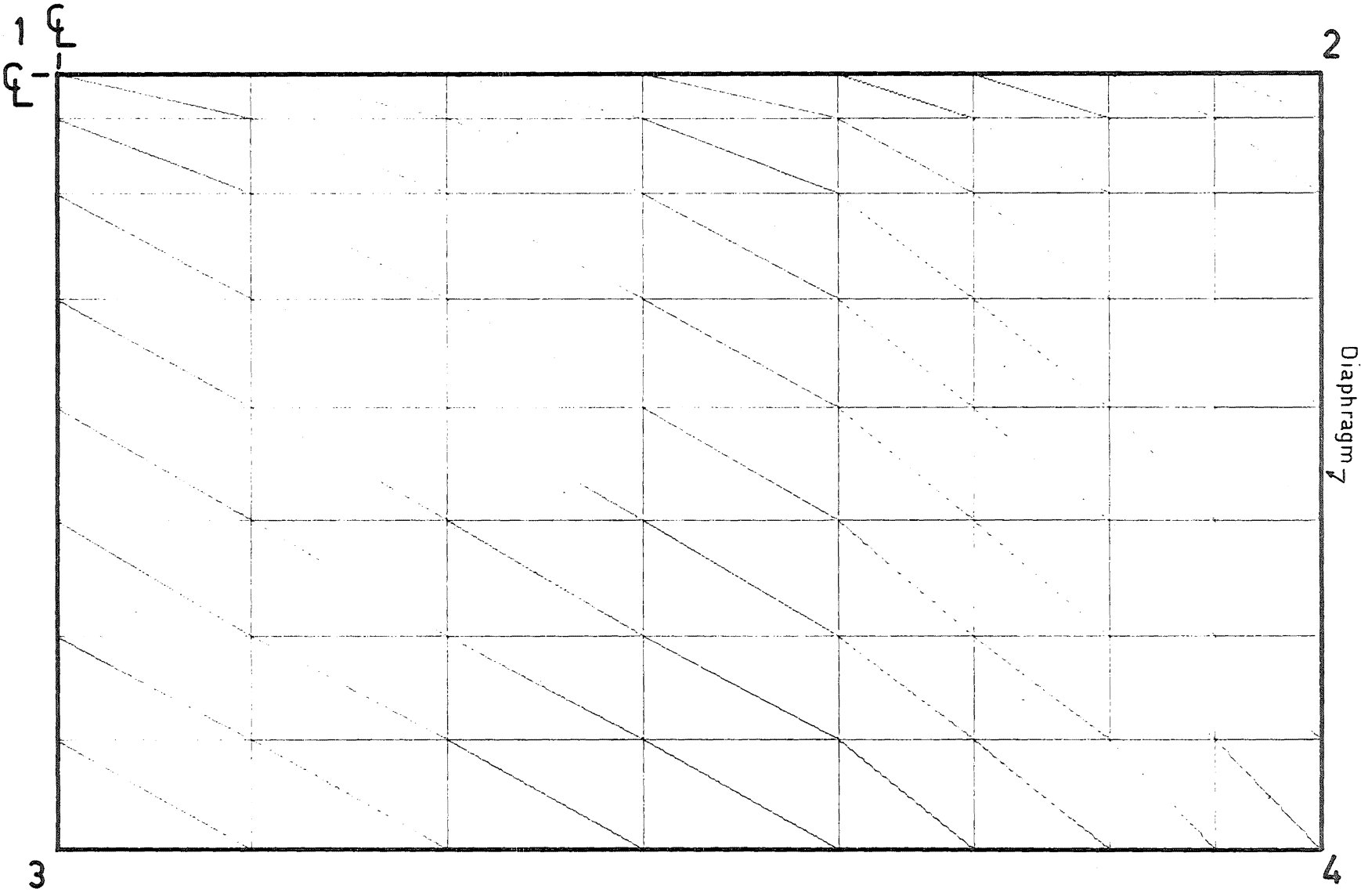

Fig. 8.10. Unfolded Finite Element Shell Mesh

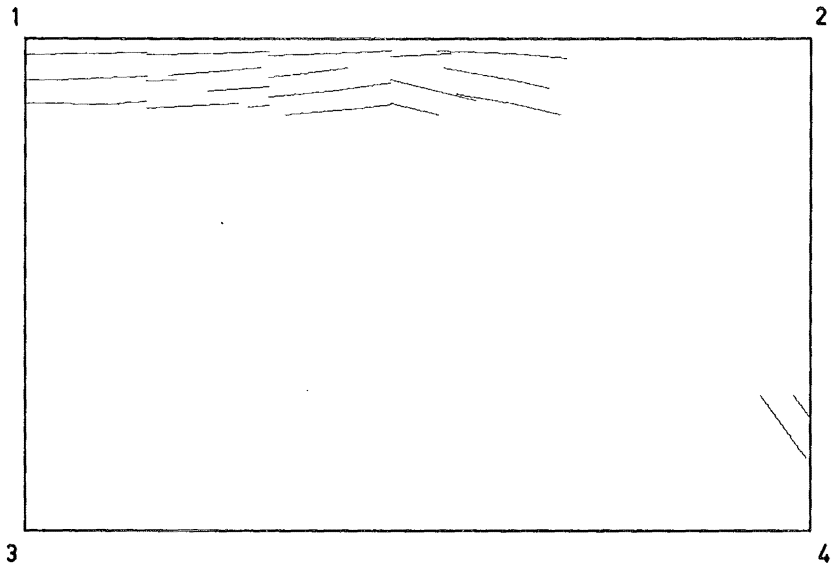

Top Surface

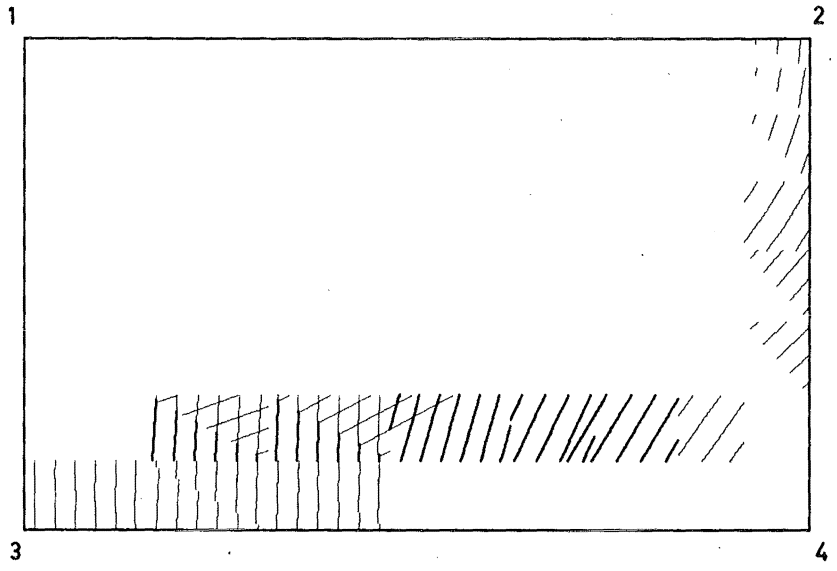

Bottom Surface

Fig. 8.11. Crack Patterns for Hedgren's Cylindrical Shell - 120 lb./sq.ft

the reinforcement at these cracks had not yielded and therefore they would probably not be visible.

On the bottom surface there are two regions of cracking. The first region occurred along the intersection of the shell and the diaphragm, and has been caused by the outward displacement of the diaphragm. This movement can be seen in the displacement profile of the longitudinal centre-line (Fig. 8.25). The cracking by the free longitudinal edge, i.e. line 3-4, is comprised of two linear cracked regions. The region nearest the free edge shows transverse cracking which was caused predominantly by high tensile forces. The second row of cracking had crack angles that were inclined at approximately 50°-60° to the free edge. The reason for the inclined cracking can be seen in Fig. 8.12a which shows 6 nodal points near the free edge: both the angle that the cracks at each nodal point would make with the free longitudinal edge, and the average angle for each element, are shown. Because the cracks are formed predominantly by high tensile forces and because they are propagating into the shell away from the free edge, the average angle of these cracks was changed to equal the average of the two angles closest to the free edge. These new average element crack angles are shown in Fig. 8.12b. Towards point 4 the twisting stresses have an increasing influence, and the angle that the cracks make with the longitudinal edge decreases. No cracking

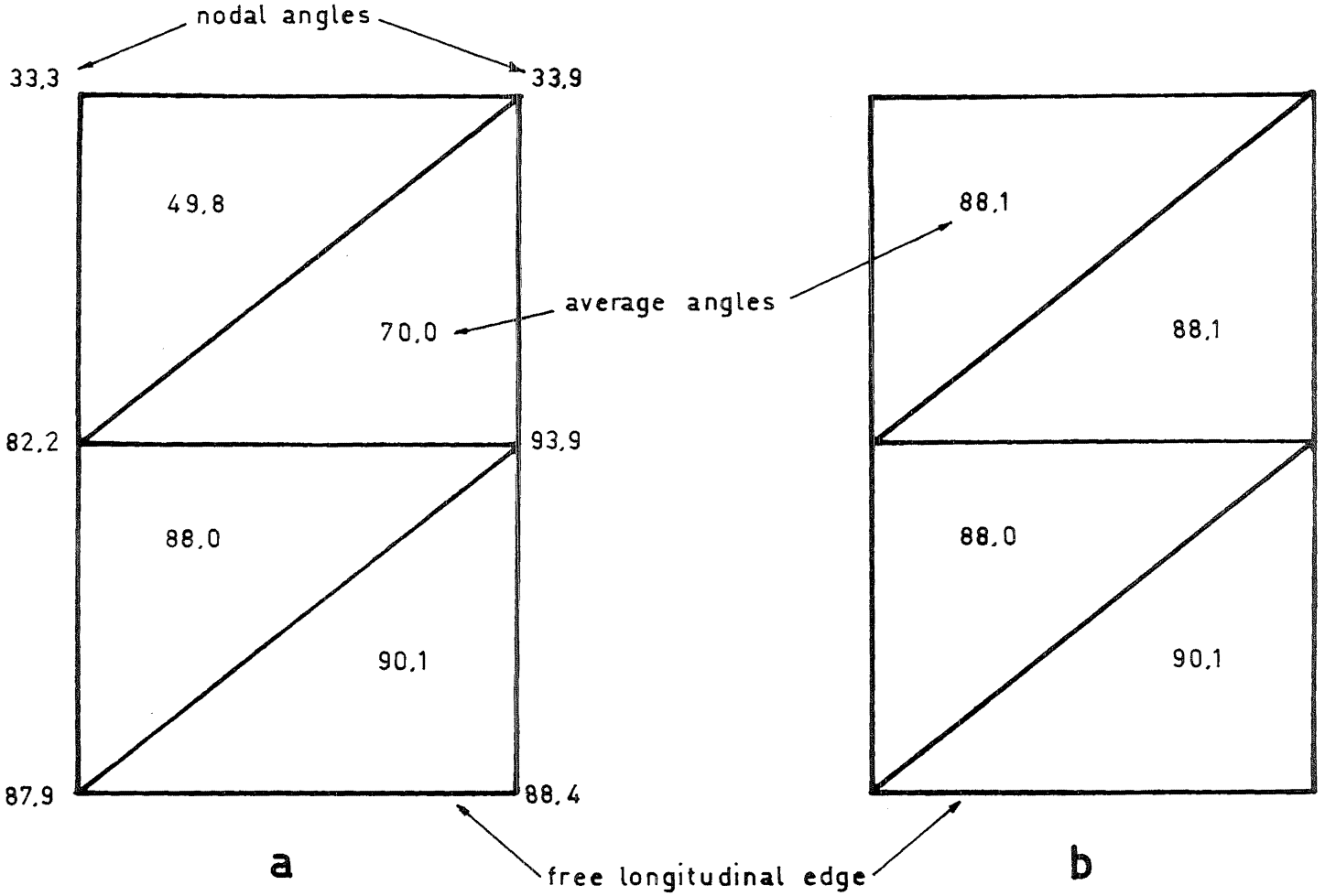

Fig. 8.12. Angle of the Principal Forces Near Line 3-4

occurred near point 3 even though the tensile force is highest in this region. This is because the principal force has been formed by a combination of the tensile and shear force resultants (though the crack angles were changed to make them into tensile cracks), and at the centre of the longitudinal span the shear force resultant was zero and the principal forces were not large enough for cracks to form. The reinforcement at some of these cracks has yielded (this is indicated in the crack patterns by a darker line), though the yielding is not continuous due to some elements being more highly stressed than their adjacent element. Thus, the element stiffnesses would be on either side of the yield stiffness (shown for a one-dimensional case in Fig. 6.5). This non-continuous cracking occurred quite often and therefore it is studied briefly below. The shell element configuration, shown in Fig. 8.10, utilizes elements that are parallel to both the free edge and the diaphragm edge, and near the centre of the longitudinal span the forces and moments decrease transversely. Therefore, the stresses in an element are often governed by the stresses at the two longitudinal nodes, and thus adjacent elements can be quite differently stressed. This problem was alleviated to some extent with the elements close to the longitudinal edge because they were given different thicknesses (refer Section 8.1). However, the method of deriving the different element thicknesses was only approximate, and in places may

cause the elements to be over-stressed. At the longitudinal edge the axial forces are predominant, and, considering an element where N_1, N_2, and N_3 are the three nodal forces and t_1, t_2, and t_3 are the true thicknesses at these nodes, then the average element strain is

$$\varepsilon_{av} = \frac{1}{3}\,(N_1/t_1 + N_2/t_2 + N_3/t_3). \qquad (8.7)$$

Also, if the element is given an average thickness of t then the average element strain is

$$\varepsilon_{av} = \frac{1}{3}\,(N_1 + N_2 + N_3)\,/\,t\,. \qquad (8.8)$$

Equating Eqs. 8.7 and 8.8 we obtain

$$t = \frac{N_1 + N_2 + N_3}{N_1/t_1 + N_2/t_2 + N_3/t_3} \qquad (8.9)$$

We can consider two limits on the average thickness, firstly, if the three forces are approximately equivalent then $t = \frac{1}{3}(t_1 + t_2 + t_3)$ which is the value used in the analysis. The second limit occurs if two of the forces are approximately equivalent and they are substantially greater than the third force, in which case $t = \frac{1}{2}(t_1 + t_2)$. The second limit is more predominant near point 3, and because the average of the three thicknesses was taken in the analysis higher stresses result. Though it was not done in this analysis it would be possible to determine the element's thickness by substituting into Eq. (8.9) at each cycle.

Two elements on the bottom surface have been doubly cracked, and the second set of cracks corresponds to the longitudinal cracking which can be observed in Hedgren's shell (Fig. 8.3). The cracks shown in Fig. 8.11 are not longitudinal due to the influence of the in-plane shear stresses, though Hedgren notes that the location of the bottom longitudinal cracks in the experiment were determined by the position of the bottom longitudinal reinforcement, and hence the reinforcement probably enforced the cracks to be longitudinal rather than inclined.

At this load there was no theoretical cracking in the diaphragm.

The theoretical crack patterns at the load 150 lb./sq.ft. are shown in Fig. 8.13. On the top surface there has been further longitudinal cracking at the crown of the shell, and again the effect of the nodal configuration has produced triangular cracking rather than continuous cracking. (No attempt was made in the analysis to change the element configuration.) The new cracks curved toward point 4 due to the increasing effect of the in-plane shear stresses both as the diaphragm and the free longitudinal edge were approached. The top surface cracking at point 4 has also increased, though the reinforcement at these cracks has still not yielded.

On the bottom surface the transverse cracking has increased, and on the line 3-4 some of the elements have

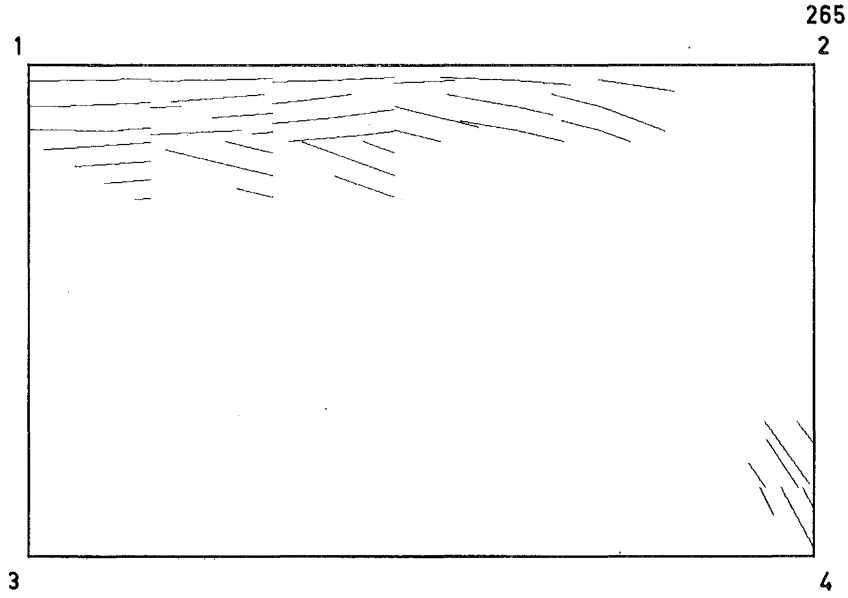

Top Surface

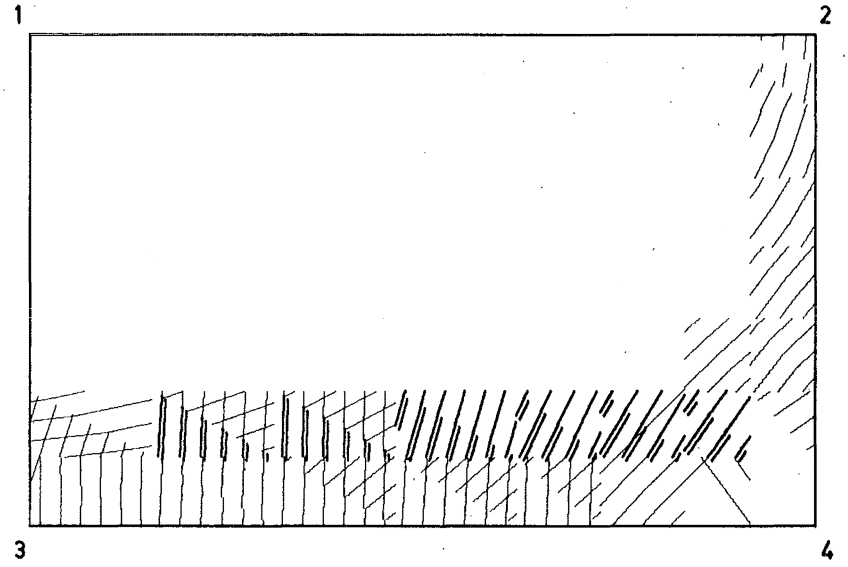

Bottom Surface

Fig. 8.13. Crack Patterns for Hedgren's Cylindrical Shell - 150 lb./sq.ft

been doubly cracked due to the presence of high in-plane shear stresses. These cracks are an extension of the cracks above them, many of which are shown by double dark lines, i.e. their reinforcement has reached its theoretical ultimate strain. As explained in the beginning of this section these elements were given a stiffness that was calculated as if the reinforcement had no ultimate strain. Therefore the double dark line shown in Fig. 8.13 signifies that the reinforcement has undergone a large strain but the section has not failed. Failure of the simulated structure is now defined by the formation of a failure mechanism or by excessively large displacements. The elements that are doubly cracked are cracked in a longitudinal direction near the line 1-3 because the in-plane shear stresses are zero at this line. However, further away from this line the crack angles become increasingly inclined due to the increasing in-plane shear stresses. The cracking in the shell at the diaphragm junction, line 2-4, has now met the region of cracking along the free longitudinal edge.

There was no cracking in the diaphragm at this load.

The theoretical crack patterns at the load 180 lb./sq.ft. are shown in Fig. 8.14. On the top surface the cracking at the crown has become more continuous and the new crack directions curve markedly towards the corner at point 4. The cracking in the corner, at point 4, has also expanded

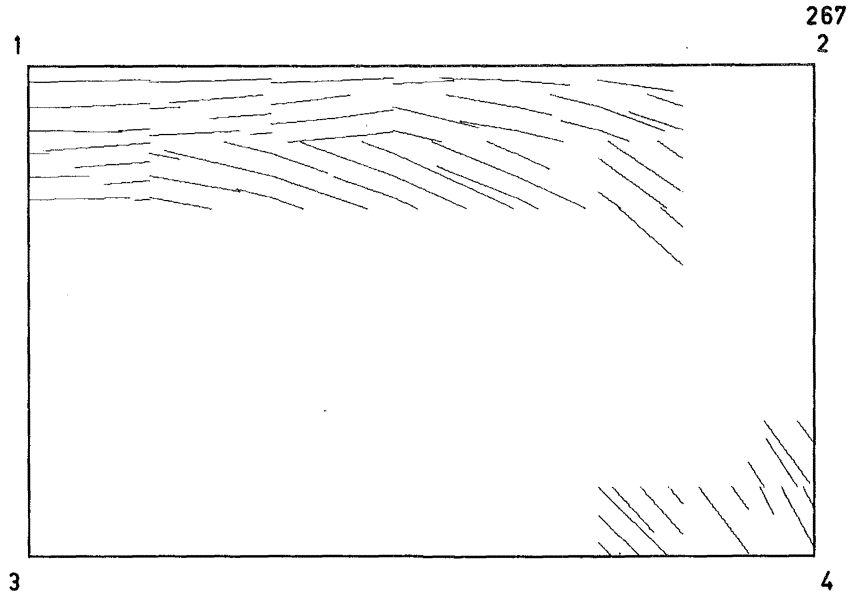

Top Surface

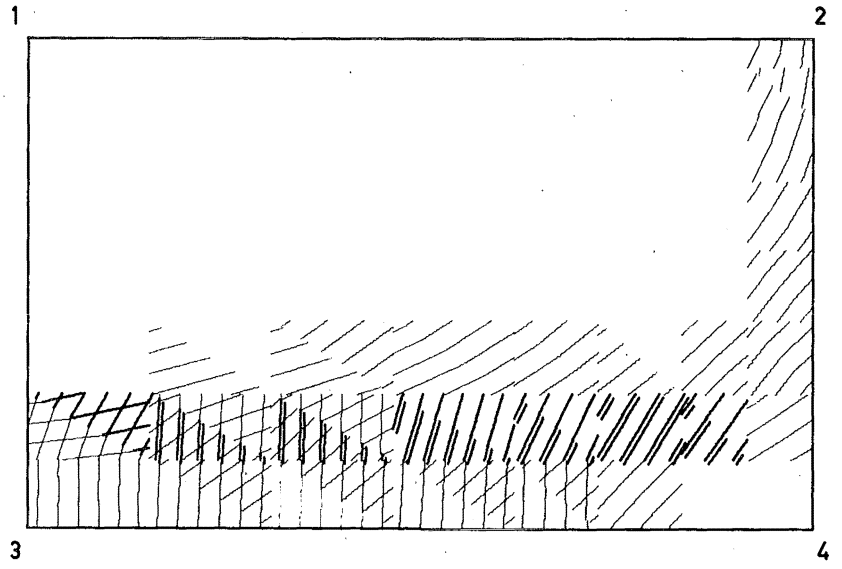

Bottom Surface

Fig. 8.14. Crack Patterns for Hedgren's Cylindrical Shell - 180 lb./sq.ft

although it has not progressed very far into the shell. The reason for this is that there were very high longitudinal and in-plane shear stresses near the longitudinal edge but, moving into the shell, these stresses rapidly decreased.

On the bottom surface of the shell the cracking that is next to the diaphragm has not altered. Parallel to the free longitudinal edge the cracking has increased, and again the region near the centre of the longitudinal span has not cracked. As before, this is because the absence of in-plane stresses at the midspan means that the principal stresses are higher at points closer to the diaphragm. This phenomenon can also be observed in the failure crack patterns of the cylindrical shell, shown in Fig. 8.3. These cracks have been formed by bending and twisting moments because the region contains a high longitudinal compressive force and a smaller transverse compressive force.

In the diaphragm vertical cracks have formed near the crown of the shell. These cracks were formed by both high bending moments and tensile forces which would result from the outward arching of the diaphragm.

Comparing the theoretical top surface cracking with that observed by Hedgren (Fig. 8.9) we see that the theoretical corner cracking, at point 4, has still not yielded, and presumably would not be visible.

The theoretical crack patterns at the load 210 lb./sq.ft are shown in Fig. 8.15. On the top surface the cracking at the crown has extended down towards the corner at point 4, and some of the elements on the crown and near the centre have yielded. Along the crown there is a small transverse compressive force, and the longitudinal force is also a small compressive force except near the diaphragm where it is a small tensile force. The longitudinal compressive force has been reducing as the cracking at the crown increased. Fig. 8.16 shows the longitudinal force distribution (normalised to 1) at the centre of the longitudinal span, i.e. along line 1 - 3; for the uncracked state, at a load of 160 lb./sq.ft., and at the present load of 210 lb./sq.ft. Hedgren did not record such small forces at the crown though his strain readings may have been affected by the cracking at the crown. Fig. 8.16 illustrates the differing methods that the shell adapts to carry the load; with the onset of cracking the length of the lever arm, joining the centroids of the tensile and compressive regions, decreases, and thus the load-carrying capacity of the shell is reduced. This, however, is offset to some degree by the contraction of the shell cross-section which makes the shell deeper. Bouma[80] also records a decrease of the longitudinal compressive force, though like Hedgren, he does not obtain a tensile stress at the crown. The cracking at point 4 has not altered because the high in-plane shear stresses still decrease quickly as we move

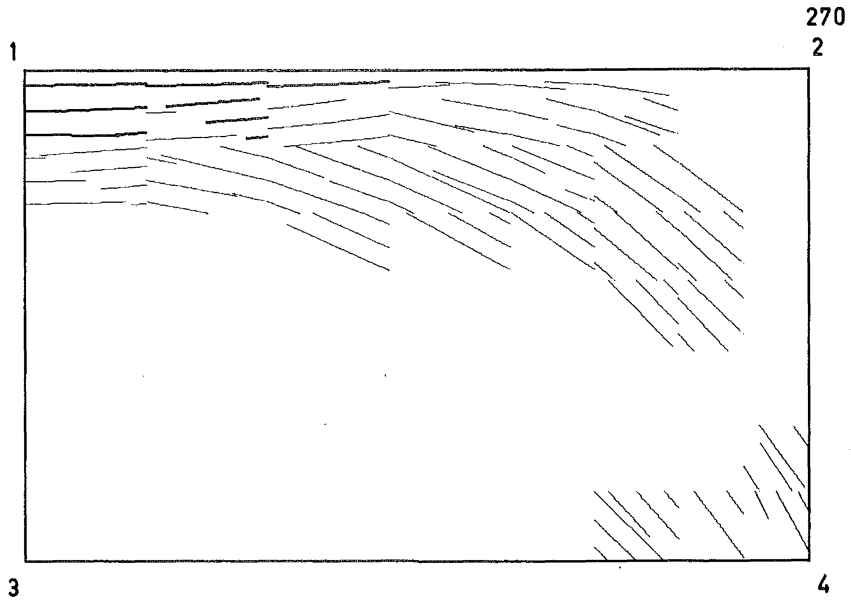

Top Surface

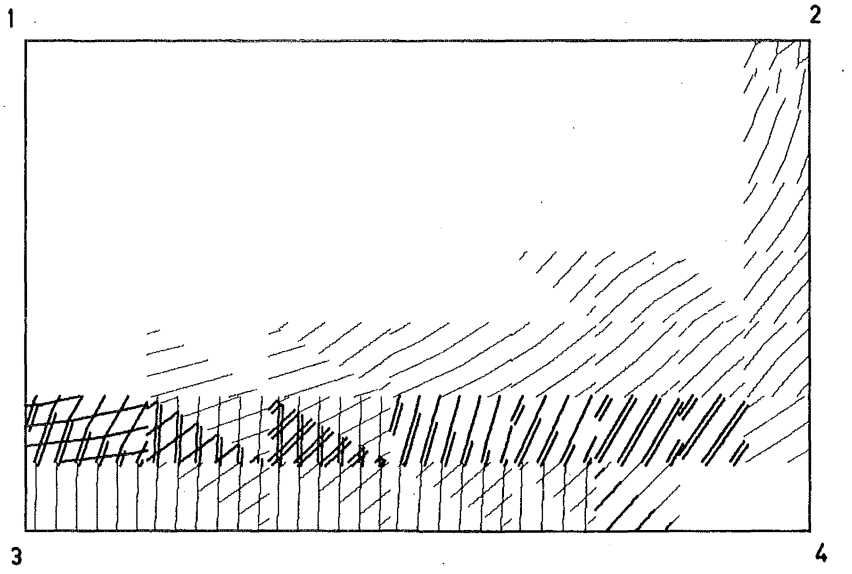

Bottom Surface

Fig. 8.15. Crack Patterns for Hedgren's Cylindrical Shell - 210 lb./sq.ft

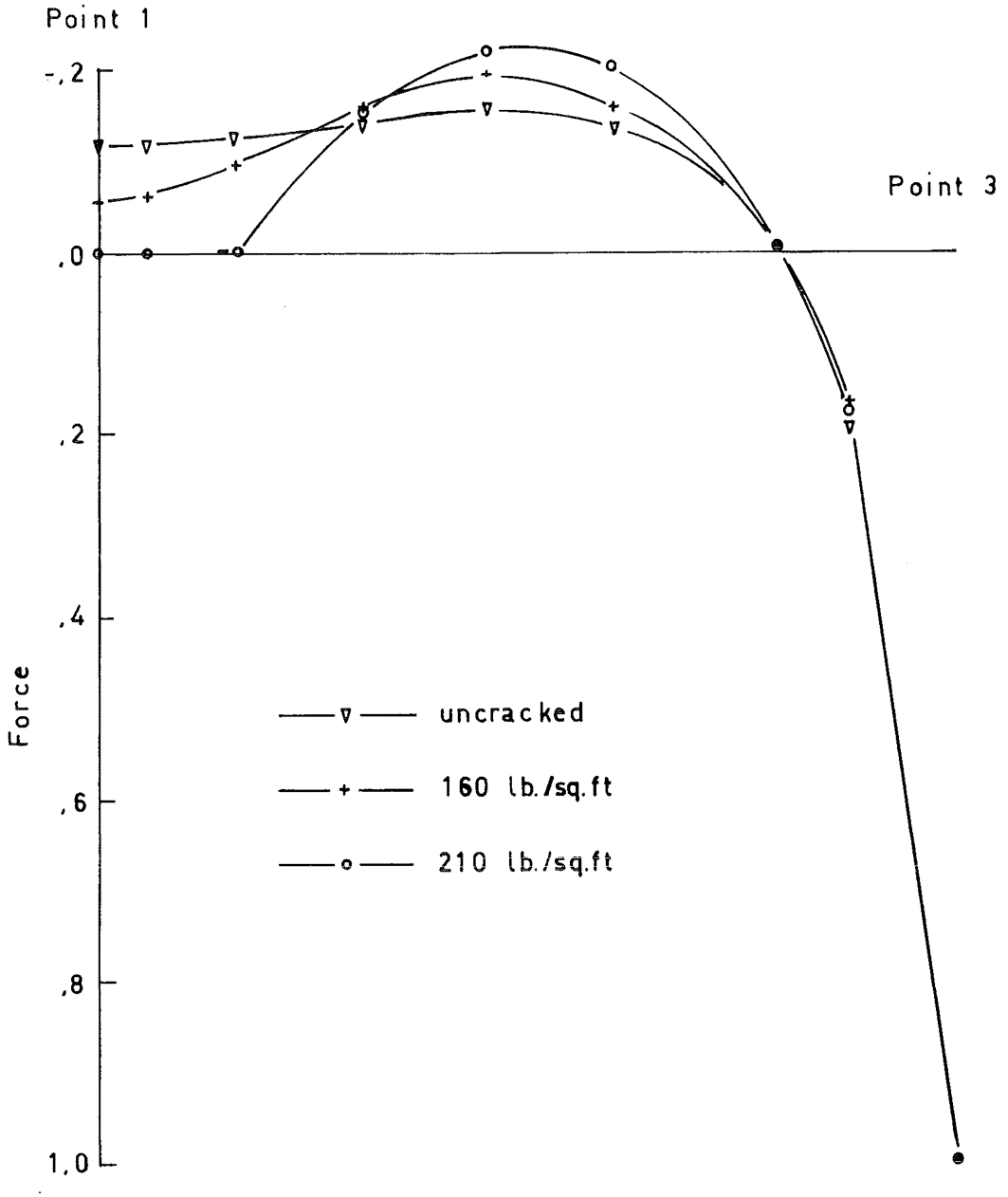

Fig. 8.16. Longitudinal Force Distribution Along the Line 1 - 3

into the shell, away from point 4.

On the bottom surface, cracking has increased slightly due to high in-plane stresses, which have even caused one of the elements at the free longitudinal edge to yield. An element at the crown of the shell and next to the diaphragm, i.e. at point 2, has been doubly cracked, and this is because higher stresses have formed in this region as a result of the cracking in the diaphragm.

At the present load of 210 lb./sq.ft. additional cracking occurred in the diaphragm, approximately at the third points, and again near the shell-diaphragm connection. Again, this cracking resulted from large tension forces combined with bending which resulted from the outward arching of the diaphragm.

The theoretical crack patterns at the load 240 lb./sq.ft are shown in Fig. 8.17. On the top surface the yielding along the crown has increased, though the cracking in this region has remained constant. Two separate regions of yielding can be observed, and this is due to the change in the reinforcement, which is lower in the region near the diaphragm (refer Figs. 8.5 and 8.6). In an actual shell we would expect these regions to merge into one. The cracking at the bottom corner has also remained constant. A new region of cracking has occurred on the top surface as a result of the diaphragm cracking. At the previous load of

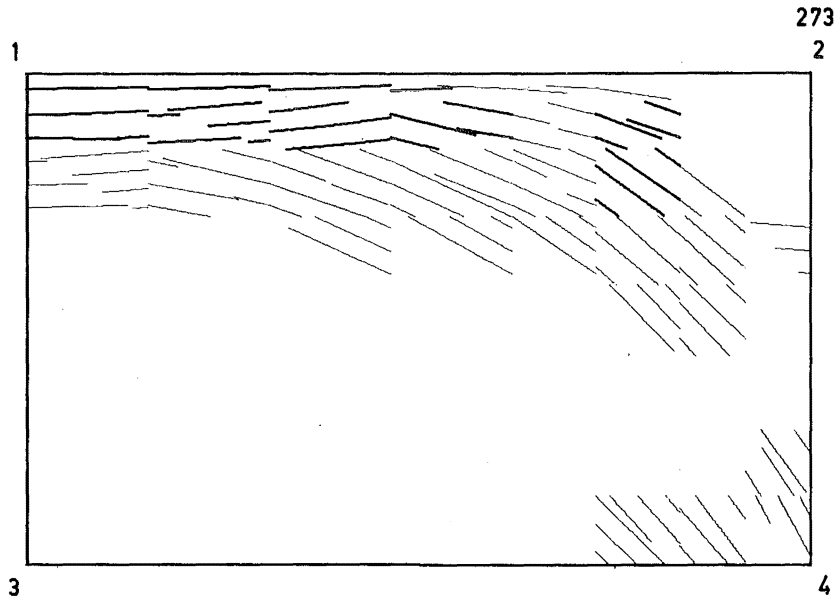

Top Surface

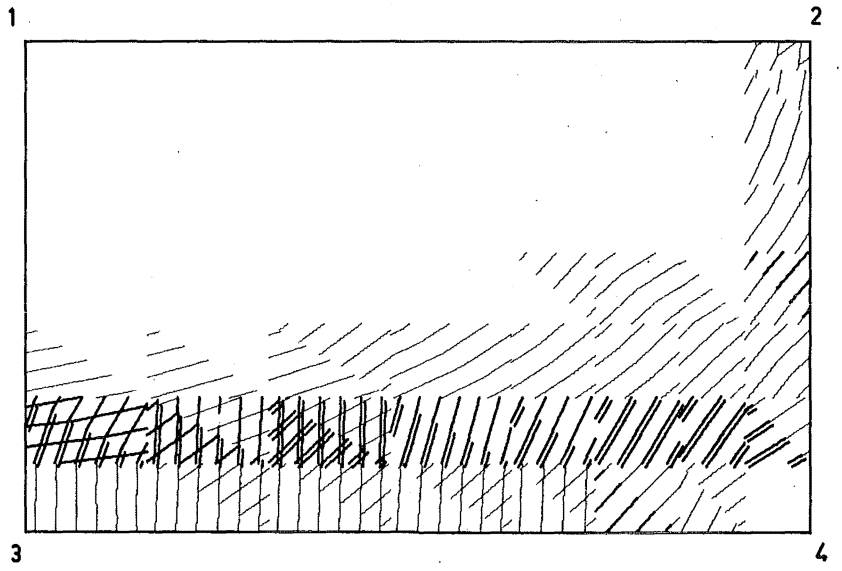

Bottom Surface

Fig. 8.17. Crack Patterns for Hedgren's Cylindrical Shell - 240 lb./sq.ft

210 lb./sq.ft the element at the crown of the shell and next to the diaphragm became doubly cracked due, predominantly, to a high tensile force combined with a positive bending moment. The new cracking, however, has been formed predominantly by a high negative bending moment, and hence the two cracked regions are on opposite surfaces of the shell.

Comparing the theoretical top surface cracking with that observed in the experiment (Fig. 8.9) we note that the theoretical corner cracking has still not yielded. In the experiment the corner cracking has increased in width, though, similar to the theory, it has not progressed very far into the shell. Longitudinal cracking along the crown was also observed in the experiment though not as much as was recorded in the theory.

On the bottom surface the only additional cracking occurred in one element at the centre of the longitudinal span, and in two elements at point 4. At the shell-diaphragm junction an element's reinforcement has yielded, and this was due to the high stresses produced by the cracks in the diaphragm. Parallel to the free longitudinal edge the reinforcement in some of the elements near point 4 has reached its theoretical ultimate strain. Also, some of the reinforcement across the transverse cracks near point 3 has either yielded or reached its theoretical ultimate strain.

In the diaphragm cracking and yielding and theoretical

failure of the reinforcement continued in cracked regions which, at this load, covered the central area near the shell junction.

The theoretical crack patterns at the load 270 lb./sq.ft are shown in Fig. 8.18. On the top surface the two cracked regions on the crown in which the reinforcement had yielded have expanded, though they are still separated. Three elements contain reinforcement that has reached its theoretical ultimate strain. It would appear that this "failure" has been a result of a high localised stress caused, possibly, because the element on the crown which had its reinforcement at the theoretical ultimate strain at the present load, was uncracked at the previous load. This high stress has also caused one of the elements to become doubly cracked. However, at subsequent loads the stresses in this region decreased substantially. At the bottom corner, point 4, the cracked region has expanded along the free longitudinal edge and the reinforcement in two of these elements has yielded. This additional cracking resulted from high twisting stresses close to the free longitudinal edge. Cracking at the shell-diaphragm junction has also increased due to the equivalent proportion of the diaphragm having cracked. However, this diaphragm cracking did not propagate into the shell very far.

On the bottom surface the cracking has increased and it covers approximately 50% of the shell area. One element in

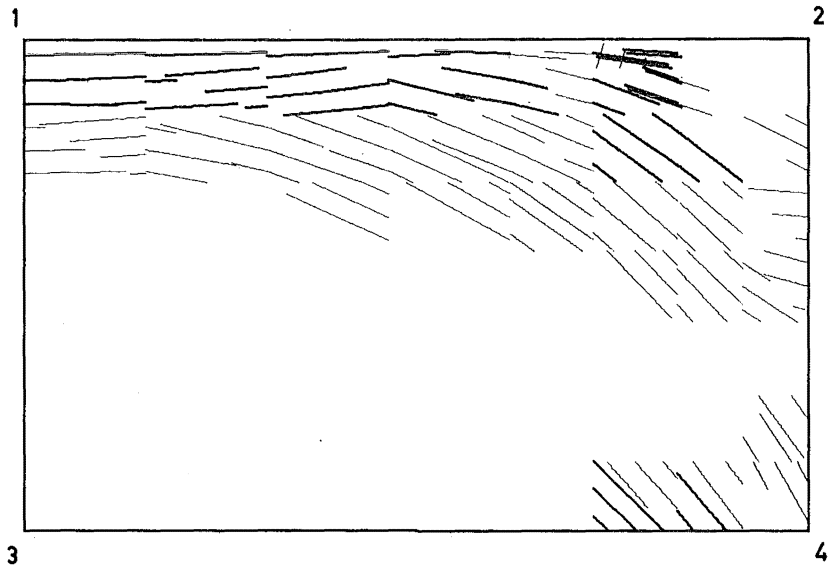

Top Surface

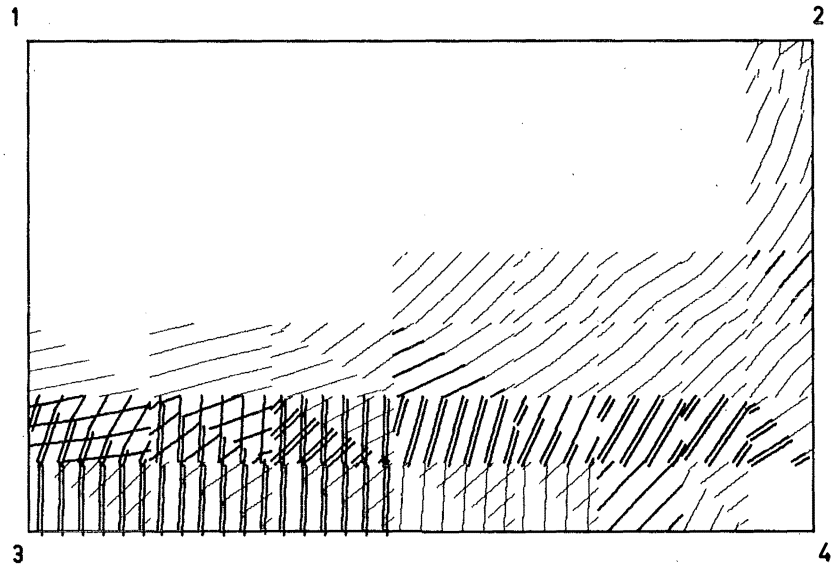

Bottom Surface

Fig. 8.18. Crack Patterns for Hedgren's Cylindrical Shell - 270 lb./sq.ft

the interior of the shell has had its reinforcement yielded due to high in-plane shear stresses in this region. The most important feature of the cracking is the large region of elements along the free longitudinal edge, and near point 3, in which the concrete has reached its theoretical ultimate tensile strain. On consideration, however, it was decided that this theoretical cracking was too pessimistic. At point 3 the axial tensile force was 2,526 lb./in. and at the next node, approximately 3 inches away, the tensile force was 463 lb./in., i.e. 18.4% of the force at point 3. This reduction in tensile force can also be seen in Fig. 8.16 which shows the distribution of the longitudinal axial force across the shell. In Section 8.1 the reinforcement in the elements at the longitudinal edge was calculated as the sum of the reinforcement divided by the width of the element. If, however, we consider the first ½ inch at the longitudinal edge, the reinforcement (refer Fig. 8.2) is

$$a_{st} = .0178 \text{ sq.in./in.}$$

$$a_{sm} = .0286 \text{ sq.in./in.}$$

$$a_{sb} = .0178 \text{ sq.in./in.}$$

which is approximately double the reinforcement assumed in the analysis. Hence, it is possible that some splitting of the concrete occurred at the free longitudinal edge but, due to the rapid decrease in the longitudinal tensile force, thissplitting action would not propagate very far from the

edge of the shell. Hence, the reduction factor, for reducing the elastic modulus for the plane stress stiffness matrix, was retained at 0.633, i.e. it was assumed that this region did not fail, though the crack patterns are shown with this failure region included. This example illustrates an inadequacy of the shell nodal mesh that was used in this analysis (refer Fig. 8.10). The mesh used the smallest elements at the crown of the shell whereas a better mesh would utilize the smallest elements at the free longitudinal edge.

Cracking in the diaphragm had now extended into the corner, near point 4, and the only uncracked region was at the bottom of the diaphragm underneath the crown.

The theoretical crack patterns at the load 300 lb./sq.ft are shown in Fig. 8.19. On the top surface some more elements on the crown have had their reinforcement reach either the yield strain or the theoretical ultimate strain. On the whole, however, the crack patterns do not vary much from the previous load case.

Comparing the theoretical top surface cracking with that of the experiment (Fig. 8.9) we see that the cracking at the crown is very similar though the experiment still shows more visible cracking at the corner, i.e. at point 4.

On the bottom surface more elements failed, and this was due to high tensile stresses at point 3, and high in-plane shear stresses at point 4. Similar to the previous load

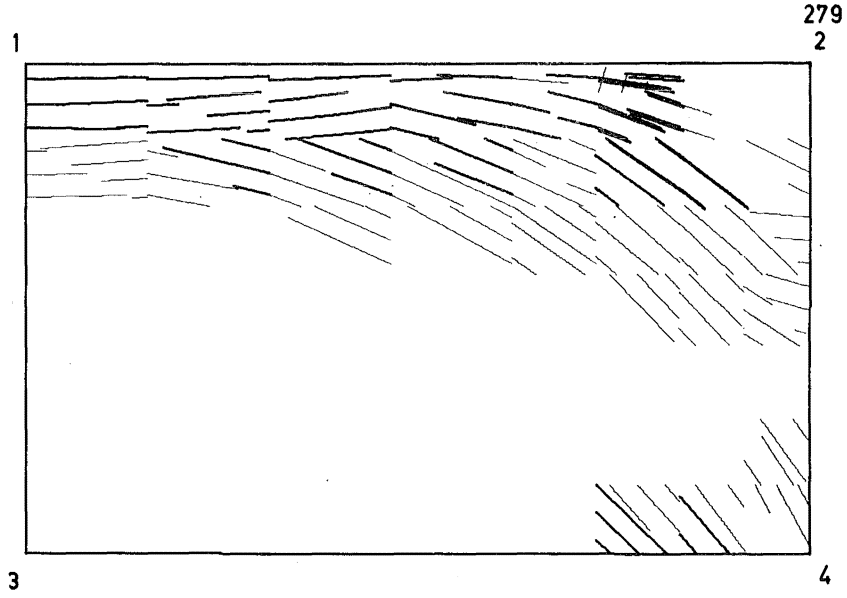

Top Surface

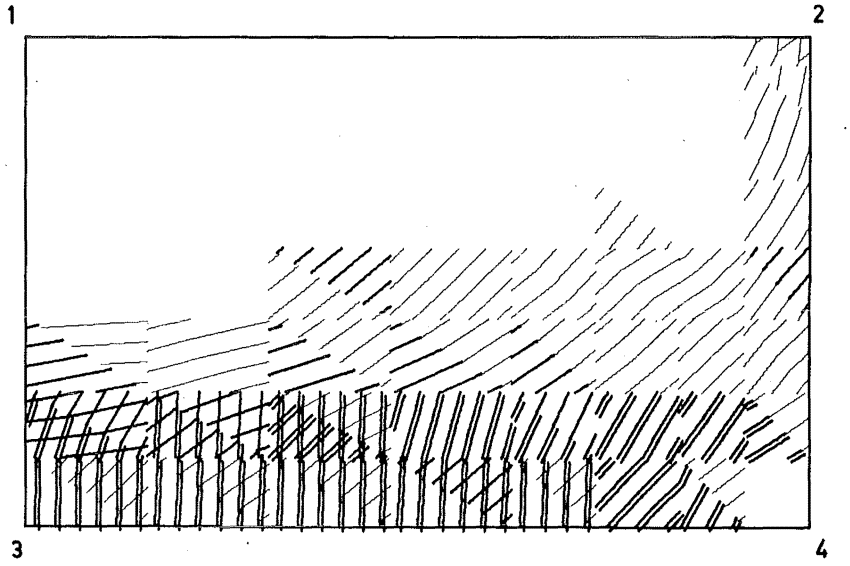

Bottom Surface

Fig. 8.19. Crack Patterns for Hedgren's Cylindrical Shell - 300 lb./sq.ft

case, the stresses were not high enough to cause such widespread failure of the concrete and therefore the in-plane reduction factor was not reduced. If, however, failure was by flexure then the bending reduction factor was automatically reduced. There was substantial cracking which was longitudinally inclined near point 3, and then it curved towards point 2 at the top of the diaphragm.

Cracking in the diaphragm had not extended very far at this load, though the stiffness of some of the sections had been further reduced.

The theoretical crack patterns at the load 330 lb./sq.ft are shown in Fig. 8.20. On the top surface, elements along the crown have had their reinforcement reach its theoretical ultimate strain, and with this reduction in stiffness the shell would soon fail. The crack patterns shown in Fig. 8.20 represent the state of the simulated shell after six cycles of redistribution, but it is possible that if more cycles were executed then further cracking would occur. The regions of cracking near point 4, and at the shell-diaphragm junction, have remained constant.

On the bottom surface there has been increased cracking near point 2. The cracking is isolated from the main cracking, and this is a result of high stresses forming at the bottom of the region, i.e. closest to the free longitudonal edge. However, the stresses at the existing cracked region

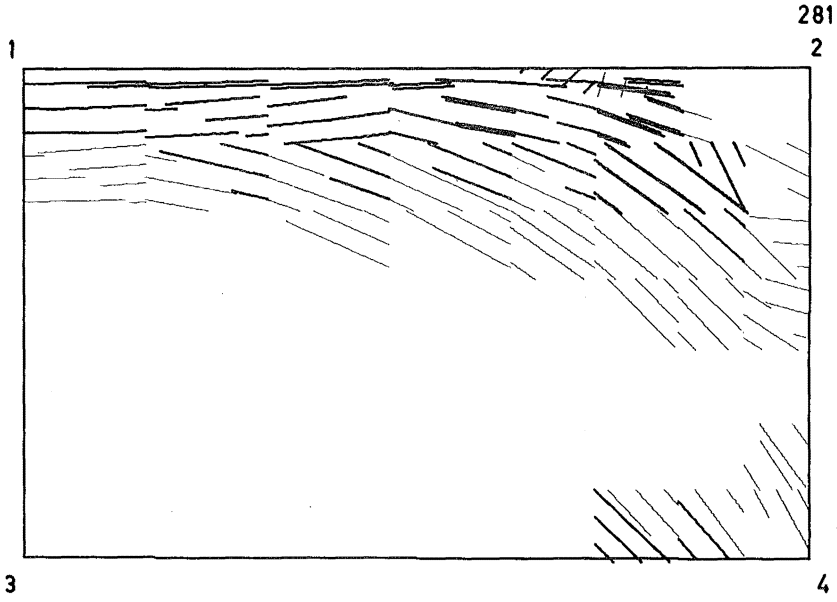

Top Surface

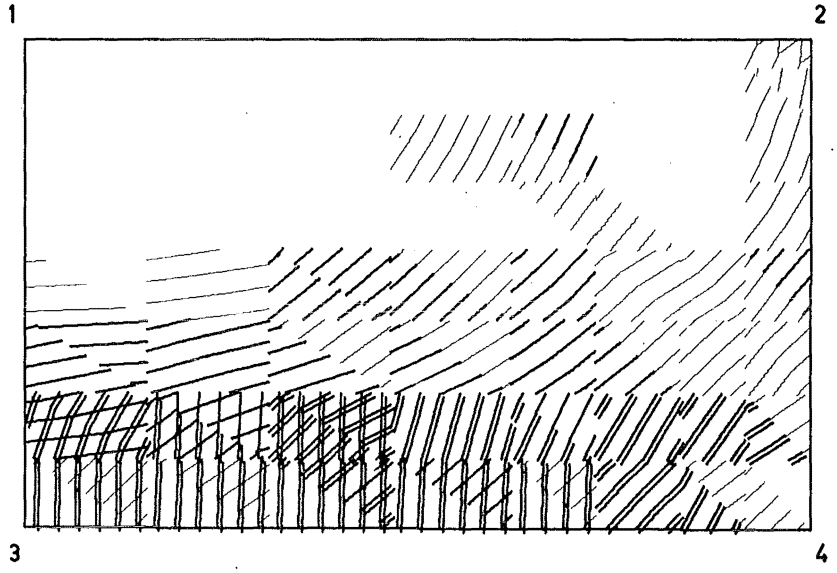

Bottom Surface

Fig. 8.20. Crack Patterns for Hedgren's Cylindrical Shell - 330 lb./sq.ft

were not high enough to produce cracking within the intermediate region. The cracking that is equivalent to Hedgren's longitudinal cracking has developed further. It is difficult to distinguish this region of cracking in Fig. 8.20 because of the large number of transverse double lines, and also the "longitudinal" crack angles vary substantially from element to element. This latter difficulty is partially due to these cracks being formed after the transverse cracking, and, as explained in Section 6.2, the angle of the second angle of cracking is not as accurate as the first angle because localised stresses form during redistribution of the stresses. This causes the adjacent element stiffnesses to be lower than they should be, and hence subsequent stresses are affected by these low stiffness regions. Greater yielding and failure in this "longitudinal" crack region, combined with the longitudinal failure region at the crown, forms the collapse mechanism.

The variation of the normal displacement at point 3 with the applied load is shown in Fig. 8.21. Four curves are shown and they represent; the experimental results (from two points on either side of the shell cross-section), the theoretical results, and the theoretical results obtained by Riera and Billington[6]. Up to a load of 180 lb./sq.ft the experimental slab was more flexible than the simulated structure, which in turn was more flexible than Riera and

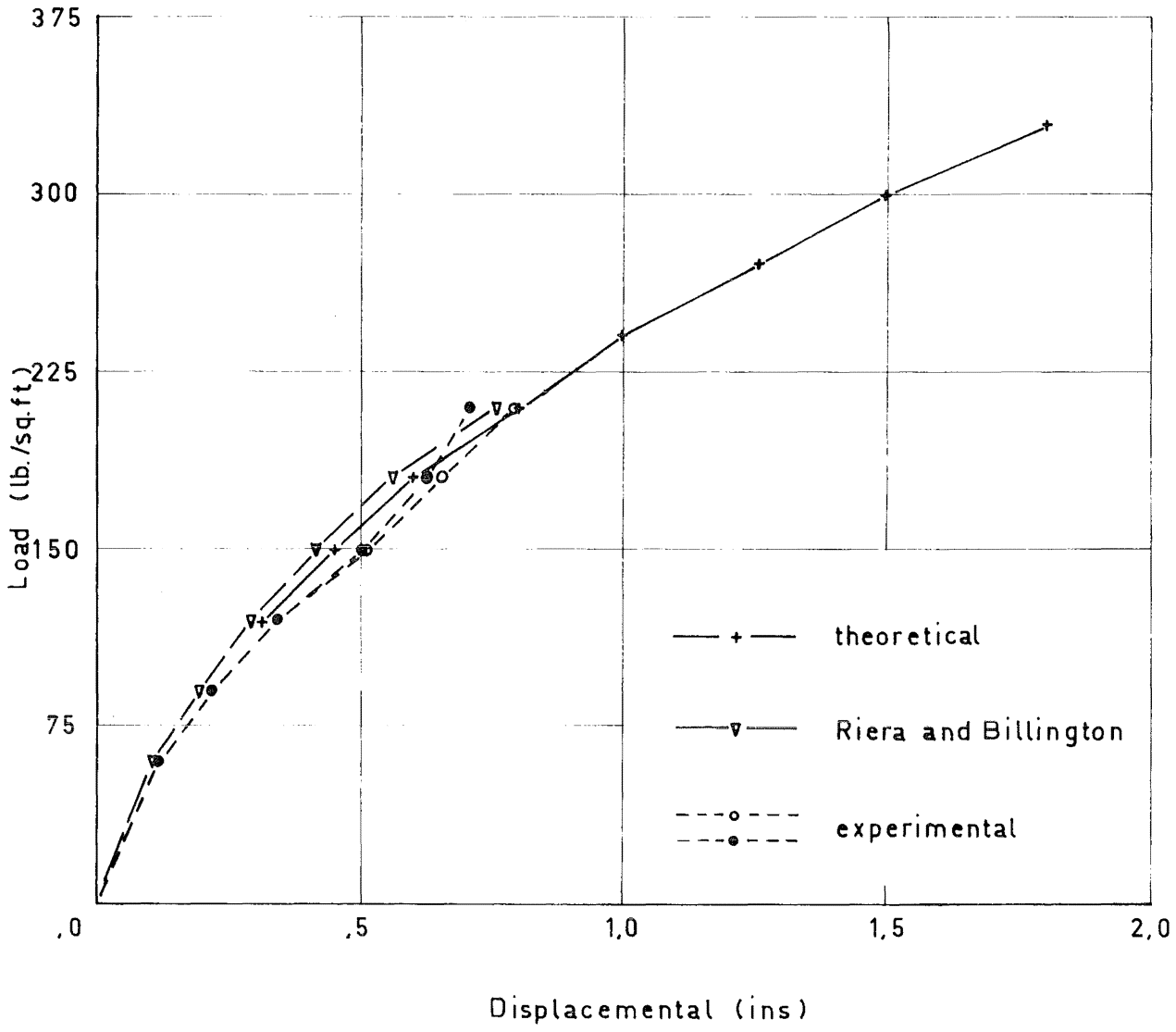

Fig. 8.21. Load-Displacement Curves for Point 3

Billington's simulated structure. At the next load increment, i.e. 210 lb./sq.ft, one side the experimental shell has become stiffer than the other side. From here on Hedgren could not measure the normal displacement because his dial gauges had reached their full extent. In their report Riera and Billington did not give any additional values, and therefore only the values for the simulated structure are shown. We see that there is not a rapid degradation in the structure; this represents a basic difference from the behaviour of the slabs (Figs. 6.8, 6.26, and 7.10) which, once a mechanism is formed, had very little reserve strength. This is to be expected, however, due to the greater capability of a shell to redistribute its stresses. At the load 330 lb./sq.ft Hedgren stated that the shell was failing by creep and that the free longitudinal edges came to rest on the braced plywood frame which was used to enclose the model when it was loaded. The theoretical displacement at the load 330 lb./sq.ft was 1.78 inches, which represents a vertical displacement of 1.51 inches, i.e. the edge was 1.24 inches above the ground level.

The variation of the normal displacement at point 1 with the applied load is shown in Fig. 8.22. There are three curves shown in the figure, one from the experiment, one from the simulated structure, and the other from Riera and Billington's simulated structure. The two theoretical curves

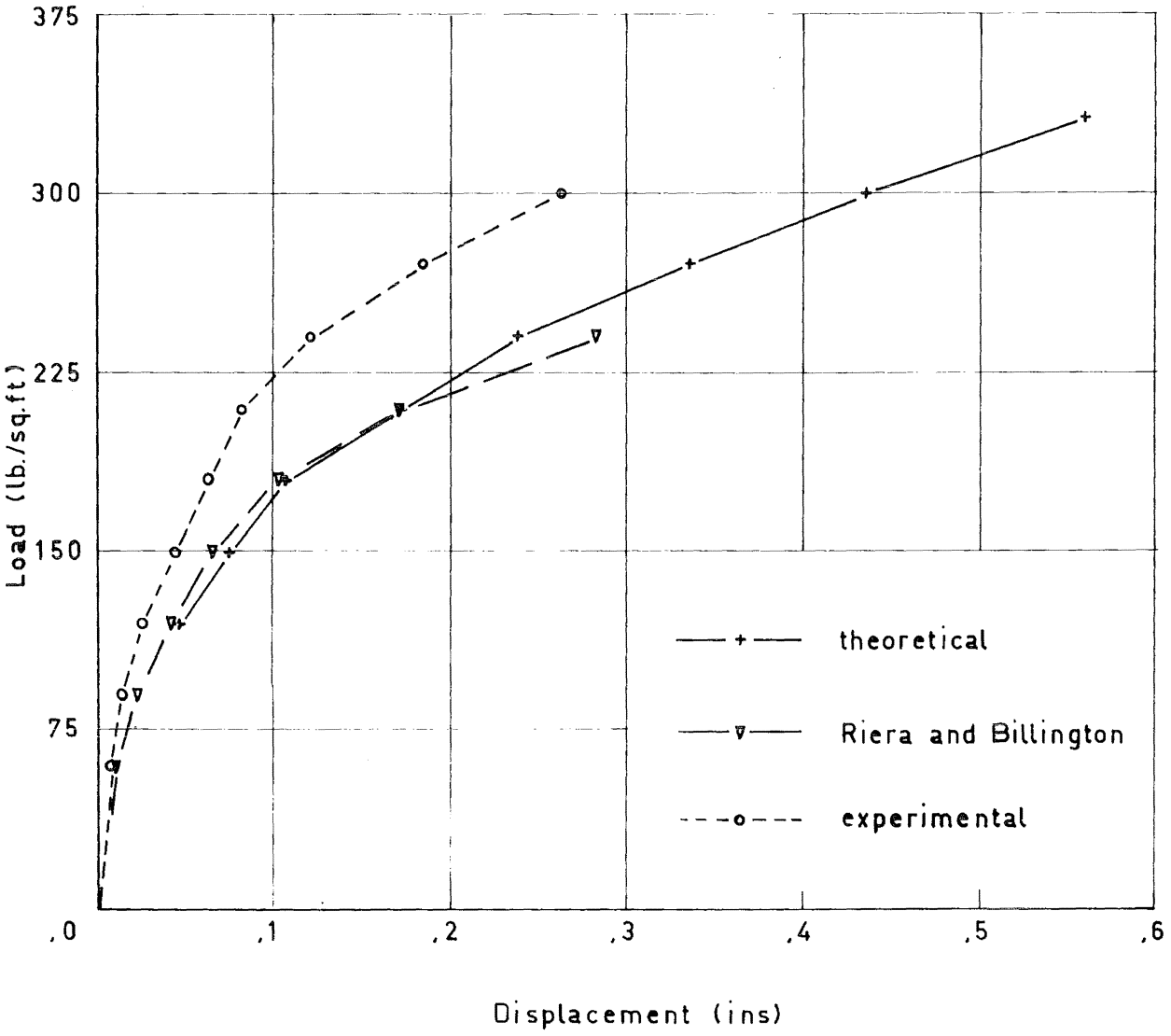

Fig. 8.22. Load-Displacement Curves for Point 1

are similar until a load of 210 lb./sq.ft but at the next load increment, 240 lb./sq.ft, the simulated structure becomes stiffer. Again, Riera and Billington's results are not known after this load. Until a load of 180 lb./sq.ft the theoretical structures were approximately 50% more flexible than the experiment. This increase is accentuated in the next two load increments but then the curves become approximately parallel until a load of 300 lb./sq.ft is reached. No experimental displacement is given at a load of 330 lb./sq.ft because of the creep failure. The reasons for the divergence of these two curves are discussed below, because a similar occurrence is observed in the displacement profile along the transverse centreline.

Fig. 8.23 shows the displacement profile (normalised to 1) along the transverse centreline. This figure shows the vertical displacement plotted from a horizontal base line; the actual deformed shape of the shell cross-section is shown in the following figure. Fig. 8.23 shows three theoretical displacement profiles; in the uncracked state, at a load of 210 lb./sq.ft, and at a load of 330 lb./sq.ft. Also shown are the experimental values for the uncracked state, and at a load of 210 lb./sq.ft. The values near the load of 330 lb./sq.ft are not shown because the displacements near the free edge were not known. We will consider the theoretical profiles first. At the load of 210 lb./sq.ft

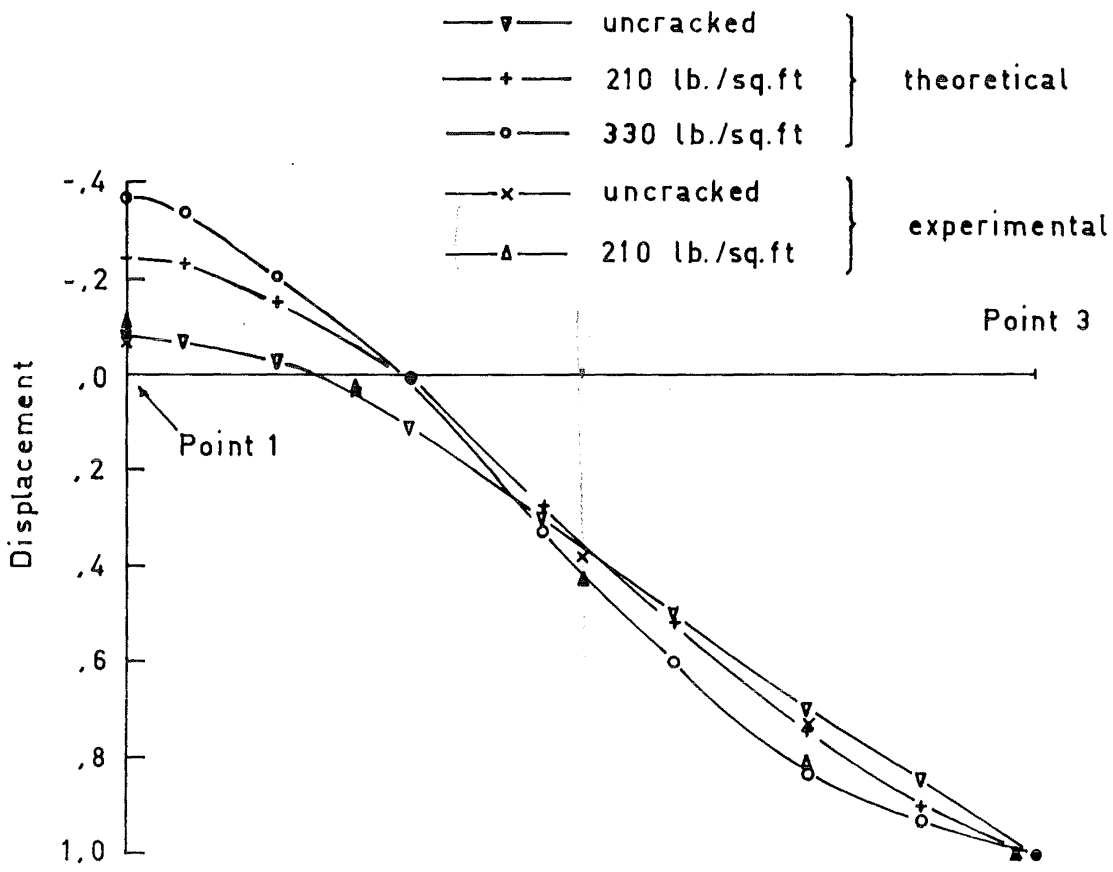

Fig. 8.23. Displacement Profiles Along the Line 1 - 3

the displacement at the crown of the shell has increased markedly, and also, near the free edge, the profile has deflected inwards. Both of these changes from theelastic profile have been caused by both the longitudinal cracking at the crown and the cracking parallel to the free longitudinal edge. At the load of 330 lb./sq.ft these two phenomena have increased, and they represent the failure mechanism, i.e. a longitudinal yield line forms at both of these positions. The experimental values for the uncracked profile correspond approximately to the theoretical profile. At a load of 210 lb./sq.ft, however, the experimental displacement profile is similar to the theoretical displacement profile at a load of 330 lb./sq.ft for the downward displacements, i.e. near the free edge. At the crown, however, the experimental displacement profile gives displacements which are approximately 50% less than the corresponding theoretical displacements. The experimental and theoretical load-displacement curves at the free edge, i.e. point 3, were very similar (Fig. 8.21), and hence we can assume that the longitudinal cracking in the experimental shell produced a lower transverse stiffness than in the theory. This could have been a result of the weaker sections imposed by the longitudinal reinforcement (refer to the discussion of the crack patterns in Fig. 8.11). A lower transverse stiffness near the free edge would alter the deformed shape of the transverse profile, and would cause the experimental displace-

ments at the crown of the shell to be smaller than the corresponding theoretical displacements.

The shell profiles along the transverse centreline is shown in Fig. 8.24 for: the unloaded state, at a load of 210 lb./sq.ft, and at a load of 330 lb./sq.ft. The deformed shapes show that there is a substantial horizontal, as well as vertical, movement of most nodes. To determine the effect of accounting for large displacements one additional cycle was executed, at the load of 330 lb./sq.ft, using the initial, unloaded, structural geometry. The results from this cycle showed that the simulated structure became more flexible. For example, the vertical displacement at the centre of the free longitudinal edge increased from 1.51 inches to 1.97 inches, i.e. an increase of 30%. At the crown, however, the vertical displacement decreased slightly, from .56 inches to .55 inches, i.e. a decrease of 2%. Some of the stresses resulting from the more flexible structure were substantially increased, sometimes by 100% or more. Hence, the incorporation of a large displacement analysis is necessary to obtain accurate results.

Displacement profiles (normalised to 1) along the longitudinal centreline are shown in Fig. 8.25 for the three cases: in the uncracked state, at a load of 210 lb./sq.ft, and at a load of 330 lb./sq.ft. In the uncracked state the displacement is a maximum at the crown and it decreases as the diaphragm is approached. The diaphragm enforces a rigid

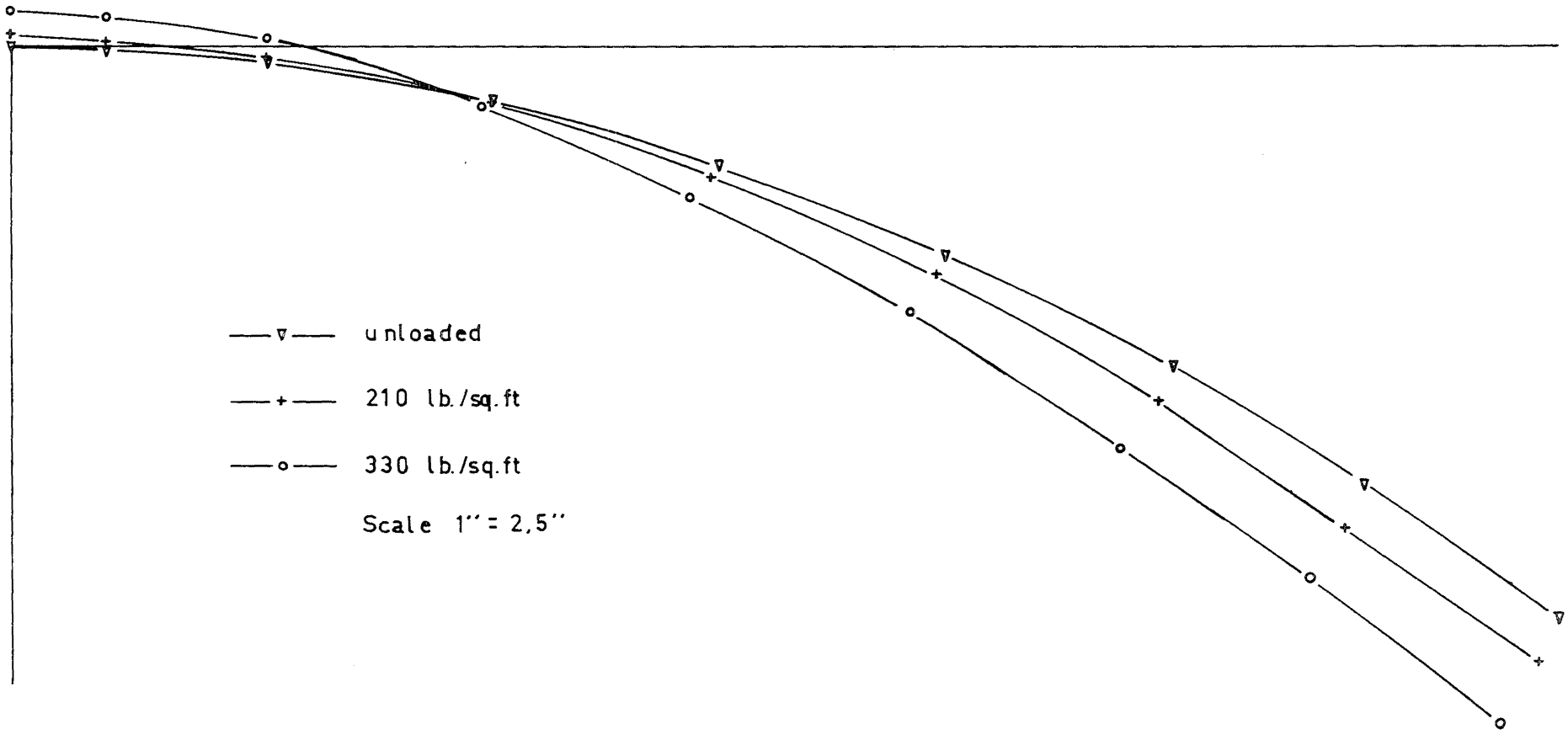

Fig. 8.24. Shell Profiles

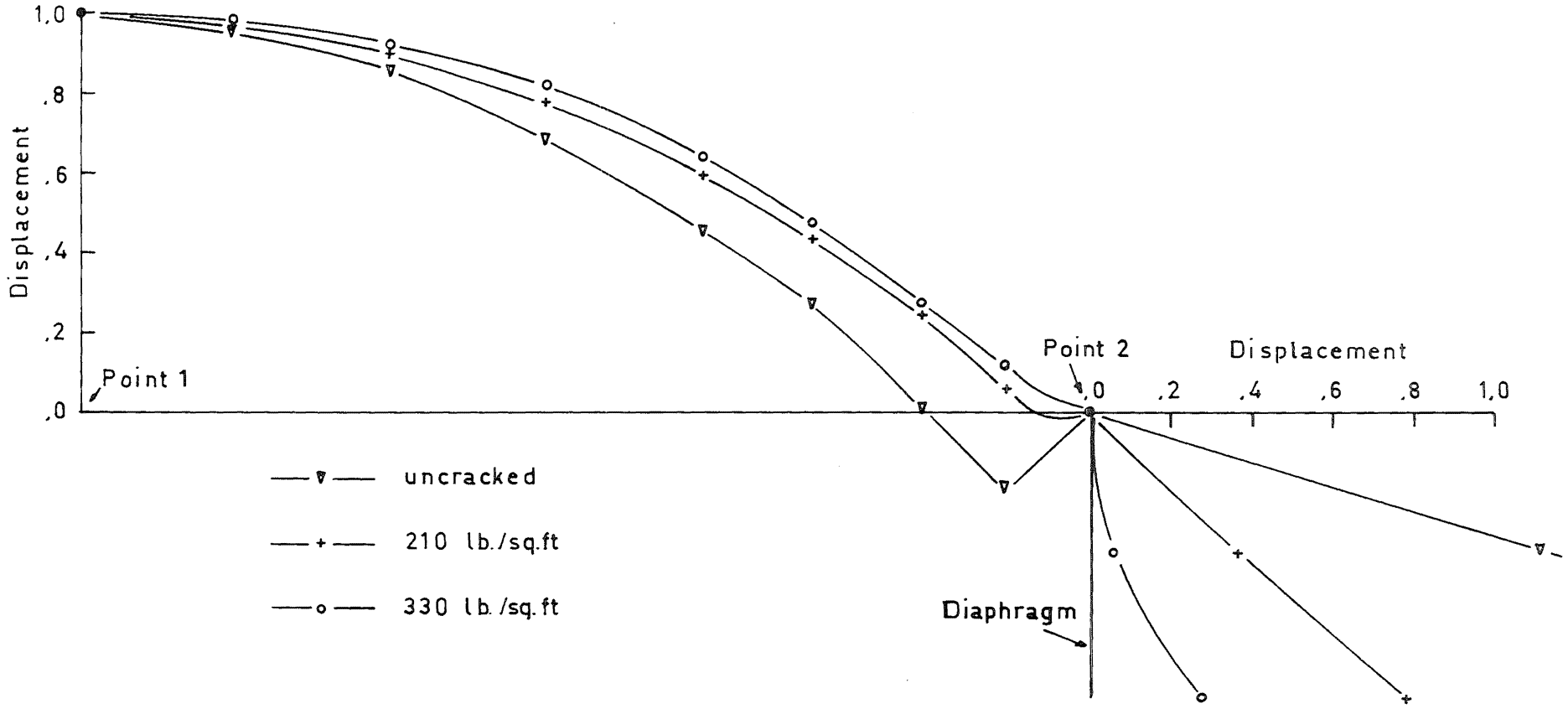

Fig. 8.25. Displacement Profiles Along the Line 1 - 2

connection with the shell, and thus large curvature changes result at this junction. The displacement at the base of the diaphragm is considerably larger than the crown displacement. At the load of 210 lb./sq.ft. the shell-diaphragm connection has cracked and this cracking relieves the restraint in this region: thus the profile along the crown has become flatter, and also the diaphragm has not displaced outwards as far. At the load of 330 lb./sq.ft cracking had increased and the fixity at the shell-diaphragm junction has decreased, and the aforementioned results have been accentuated.

Summarising the analysis of Hedgren's shell, the principal points are:

a) although many approximations were introduced the overall theoretical behaviour was very similar to the experimental behaviour;

b) the theoretical edge displacements were similar to the experimental value, though the theoretical crown displacements were large, and sometimes double the experimental crown displacements,

c) in the experiments the position of the reinforcement affected the cracking in the shell,

d) the shell geometry should be changed to coincide with its deformed shape, i.e. the effect of large displacements should be taken into account otherwise large stresses and erroneous deflections result.

CONCLUSIONS AND SUGGESTIONS FOR FURTHER STUDY

I. The finite element method.

1. The finite element method will normally provide an accurate analysis of structures. Possible sources of error in the displacement method of finite element analysis can arise from the following:

   a) an incorrect mesh idealization,

   b) very large stress or geometric discontinuities,

   c) violation of the conditions imposed within the Rayleigh-Ritz method, and

   d) loss of precision in the computer solution.

II. The complete analysis of two-dimensional structures.

1. It is possible to construct theoretical load-moment-curvature relationships which can take into account most of the actual properties of reinforced concrete including the bond stress distribution between two cracks, and the method of determining an "average" curvature for a cracked segment.

2. A complete analysis for reinforced concrete slabs and shells can be developed, and it can incorporate changes both in the cross-section properties and in the method of determining the load-moment-curvature relationship.

3. The method gives a realistic, phenomenological approach to the complete analysis for reinforced concrete slabs and shells.

4. For anisotropic finite elements an approximation can be introduced to determine the shear modulus from both the two moduli of elasticity and the two Poisson's ratios, and therefore the material constants for any element can be automatically determined if both the initial isotropic modulus of elasticity and Poisson's ratio are known.

5. It is possible to form finite elements which contain both cracked and uncracked regions. Two such formulations are proposed and, for plate bending elements, tested.

6. Some of the effects of geometrical non-linearity can easily be taken into account by changing the shape of the structure at each cycle.

III. A comparison of the theory with existing experimental results.

1. The method of analysis that uses elements which are either totally cracked or totally uncracked gives better results than the method of analysis that uses elastic/inelastic elements, i.e. elements that contain both cracked and uncracked regions.

2. When the method of analysis that uses elements which are either totally cracked or totally uncracked is used greater care has to be taken in selecting an element mesh than if the method of analysis that uses elastic/inelastic elements is used.

3. Operator interaction is desirable between cycles in the analysis so that, if necessary, his or her engineering knowledge can be used to alter the output data.

4. Pictorial crack patterns, displacement profiles, and load-displacement curves are normally sufficient to obtain a knowledge of a structure's behaviour.

5. When elements that are singly cracked become doubly cracked then the second angle of cracking is normally not as accurately represented as the first angle.

6. The theoretical load-displacement curves logically reflect the load-moment-curvature relationships that they are based upon.

7. Displacement profiles show that after cracking has commenced the uncracked regions displace like rigid bodies. Also, the regions that are almost totally cracked have an approximately constant stiffness and

their displacement profile is similar to the uncracked displacement profile.

8. It is possible to account for the additional load-enhancement that partial distortion of the reinforcement may cause.

9. The method of analysis is not very accurate close to the ultimate load because spalling and creep are not taken into account.

10. The results of analyses predict failure due to folding mechanism similar to those predicted by the yield-line method with the exception that the theoretical yield-lines have a substantial width.

11. Failure about a narrow yield region is not desirable because spalling of the concrete in the compression zone above the cracks is more likely to occur, and this causes the structure to become more flexible and it also reduces the ultimate load that the structure can support.

12. The theory appears to give acceptable results for both slabs and shells though further comparisons with experimental results are desirable.

13. There is a great variance shown in some of the experimental results which became apparent when a test was repeated, when results should have been

symmetrical, and when some of the results were not very credible.

14. As the cost of computer time decreases and larger computers become available the method would be of assistance to designers.

IV. Suggestions for further research.

1. For the theory, more research would be useful in the following areas:

   a) the construction of a shell finite element whose plane-stress and plate-bending stiffnesses are interrelated,

   b) the construction of higher order plate bending finite elements that contain both cracked and uncracked regions, and

   c) for slabs, the theory could be extended to include both tensile and membrane forces.

2. More research would be useful with the present program in the following areas:

   a) on symmetrical structures assuming that the symmetrical portions have different stiffnesses,

   b) for different structures the theory could be compared with the yield-line method of analysis, and

c) to decrease the time of computation, principally by investigating the possibility of using an iterative method, and to expand the program as additional computer facilities become available.

3. Experimental research that would be useful includes the following:

a) additional information upon the tensile strength of reinforced concrete slabs and shells in flexure, including the effect of the position and size of the reinforcement for both bars and mesh,

b) sensitivity studies, i.e. statistical variation on repetitive tests, the effects of using different types of reinforcing, and a comparison of scale effects between models and their prototypes,

c) any slab or shell loaded to failure and with comprehensive displacement readings and crack patterns recorded.

APPENDIX A

This appendix contains a summary of the plane stress and plate bending stiffness matrix derivations which were developed by Felippa and Carr at Berkeley[8,9,19].

The first section describes the triangular coordinate system which is used in many element derivations and this is followed by a section describing the development of interpolation functions. The final sections describe the plane stress and plate bending derivations.

A.1 Triangular Coordinate System

We saw in Section 3.2 that the initial plate bending triangular elements used a simplified displacement shape which was dependent upon the orientation of their rectangular coordinate system. When two sides of a triangle are parallel to the x and y axes respectively some of the terms of the interpolation vector are linearly dependent and a stiffness matrix cannot be formed. This problem can be circumvented by defining the displacement shape as a function of a "triangular" coordinate system which is independent of the position and orientation of the rectangular coordinate system (the triangular coordinate system is also termed a "natural" coordinate system[47] and an "area" coordinate system[28].

Fig. A.1a illustrates a triangle 1-2-3 described by a rectangular coordinate system and Fig. A.1b shows the same triangle described by the triangular coordinate system. Other dimensions that are used within this appendix are shown, for side 3, in Fig. A.2.

The coordinates of a point $P(\zeta_1,\zeta_2,\zeta_3)$ in the triangular coordinate system are

$$\begin{aligned} \zeta_1 &= \frac{A_1}{A} \\ \zeta_2 &= \frac{A_2}{A} \\ \zeta_3 &= \frac{A_3}{A} \end{aligned} \tag{A.1}$$

where the areas A_1, A_2 and A_3 are formed by joining the point P to the corners of the triangle and the subscript of each area is defined by the opposite corner node number. The total area of the triangle is A, therefore

$$\zeta_1 + \zeta_2 + \zeta_3 = 1. \tag{A.2}$$

The relations between the two coordinate systems are,

$$\begin{Bmatrix} 1 \\ x \\ y \end{Bmatrix} = \begin{bmatrix} 1 & 1 & 1 \\ x_1 & x_2 & x_3 \\ y_1 & y_2 & y_3 \end{bmatrix} \begin{Bmatrix} \zeta_1 \\ \zeta_2 \\ \zeta_3 \end{Bmatrix} \tag{A.3}$$

and

$$\begin{Bmatrix} \zeta_1 \\ \zeta_2 \\ \zeta_3 \end{Bmatrix} = \frac{1}{2A} \begin{bmatrix} 2A_{23} & b_1 & a_1 \\ 2A_{31} & b_2 & a_2 \\ 2A_{12} & b_3 & a_3 \end{bmatrix} \begin{Bmatrix} 1 \\ x \\ y \end{Bmatrix} \tag{A.4}$$

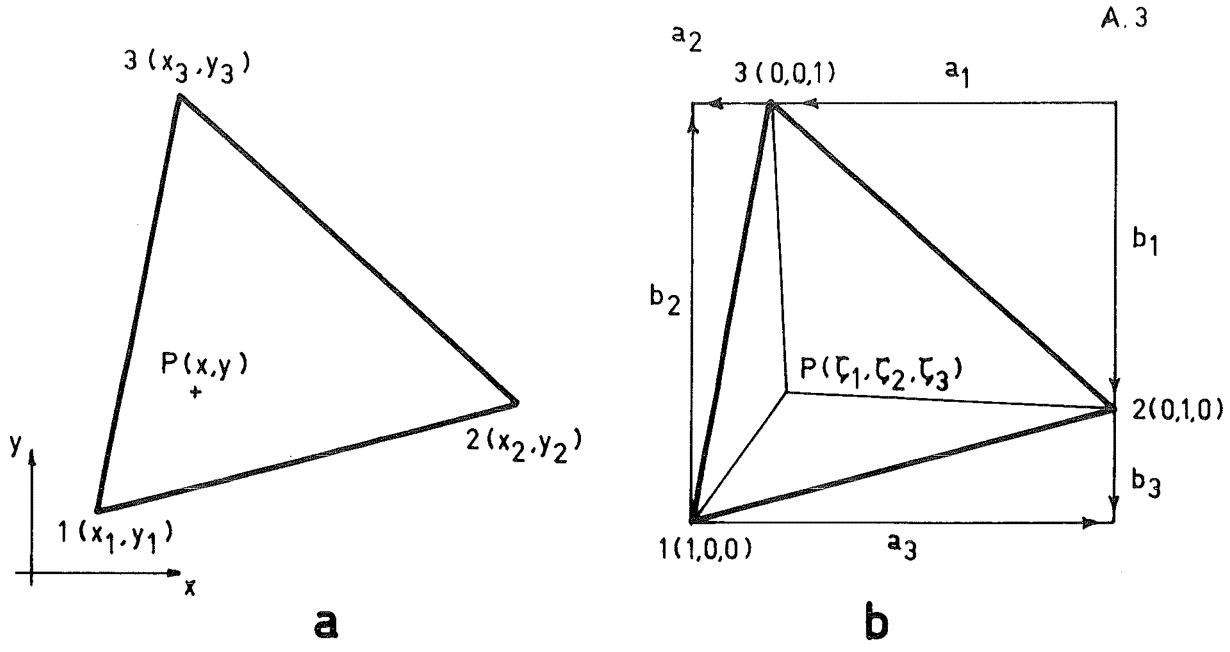

Fig. A.1. Rectangular and Triangular Coordinate Systems

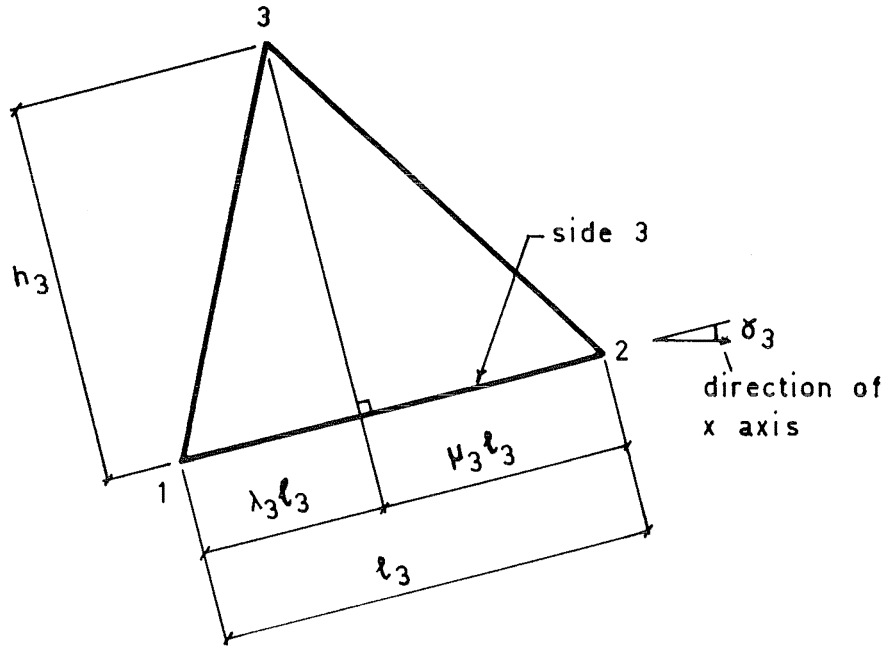

Fig. A.2. Additional Notation in the Trianglar Coordinate System

where A_{ij} is the area subtended by the corners i, j and the origin of the rectangular coordinate system.

A.2 Interpolation Functions in Triangular Coordinates

A general interpolation equation is

$$F = \{\phi\}^T \{f\} \tag{A.5}$$

where F is the value of a function at a point $P(\zeta_1,\zeta_2,\zeta_3)$, $\{\phi\}$ is the interpolation vector, and $\{f\}$ is a vector of known values of the function F. Hence, knowing several values of a function we can describe its variation between these known values by an appropriate interpolation vector.

Some of the linear, quadratic and cubic interpolation functions that are used within the next two sections are listed below so that their development and interdependence can be readily seen.

a) Linear Interpolation Vector

For the element nodal system shown in Fig. A.3a,

$$\{f_1\}^T = \langle f_1 \; f_2 \; f_3 \rangle \tag{A.6}$$

and

$$\{\phi_1\} = \begin{Bmatrix} \zeta_1 \\ \zeta_2 \\ \zeta_3 \end{Bmatrix}. \tag{A.7}$$

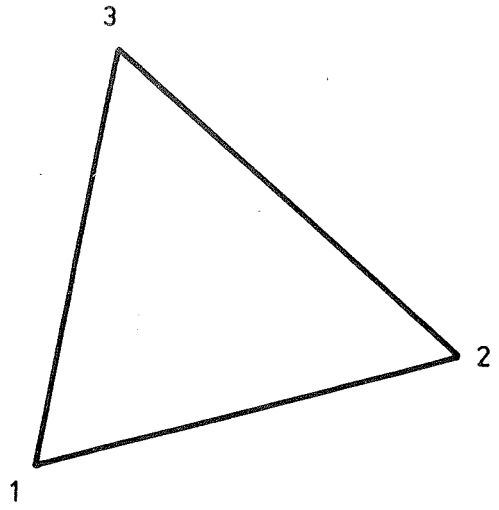

a

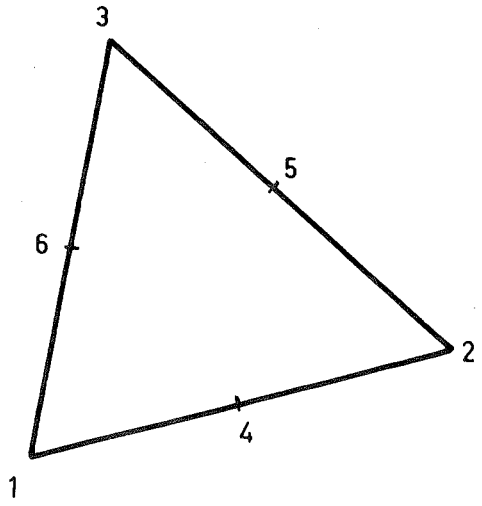

b

Fig. A.3. Nodal Configurations for Linear and Quadratic Interpolation Vectors

The plate bending element possesses a cubic transverse displacement shape and therefore the interpolation vector of Eq. (A.7) will describe the linear variation of both the moments and the curvatures over the element.

b) Quadratic Interpolation Vector

For the element nodal system shown in Fig. A.3b,

$$\{f_2\}^T = \langle f_1 \; f_2 \; f_3 \; f_4 \; f_5 \; f_6 \rangle \tag{A.8}$$

and

$$\{\phi_2\} = \begin{Bmatrix} \zeta_1(2\zeta_1-1) \\ \zeta_2(2\zeta_2-1) \\ \zeta_3(2\zeta_3-1) \\ 4\zeta_1\zeta_2 \\ 4\zeta_2\zeta_3 \\ 4\zeta_3\zeta_1 \end{Bmatrix} \tag{A.9}$$

The plane stress element possesses a cubic in-plane displacement shape and therefore the interpolation vector of Eq. (A.9) will describe the quadratic variation of both the stresses and the strains over the element.

c) Cubic Interpolation Vector

For the element nodal system shown in Fig. A.4a,

$$\{f_1\}^T = \langle f_1 \; f_2 \; f_3 \; f_4 \; f_5 \; f_6 \; f_7 \; f_8 \; f_9 \; f_{10} \rangle \tag{A.10}$$

and

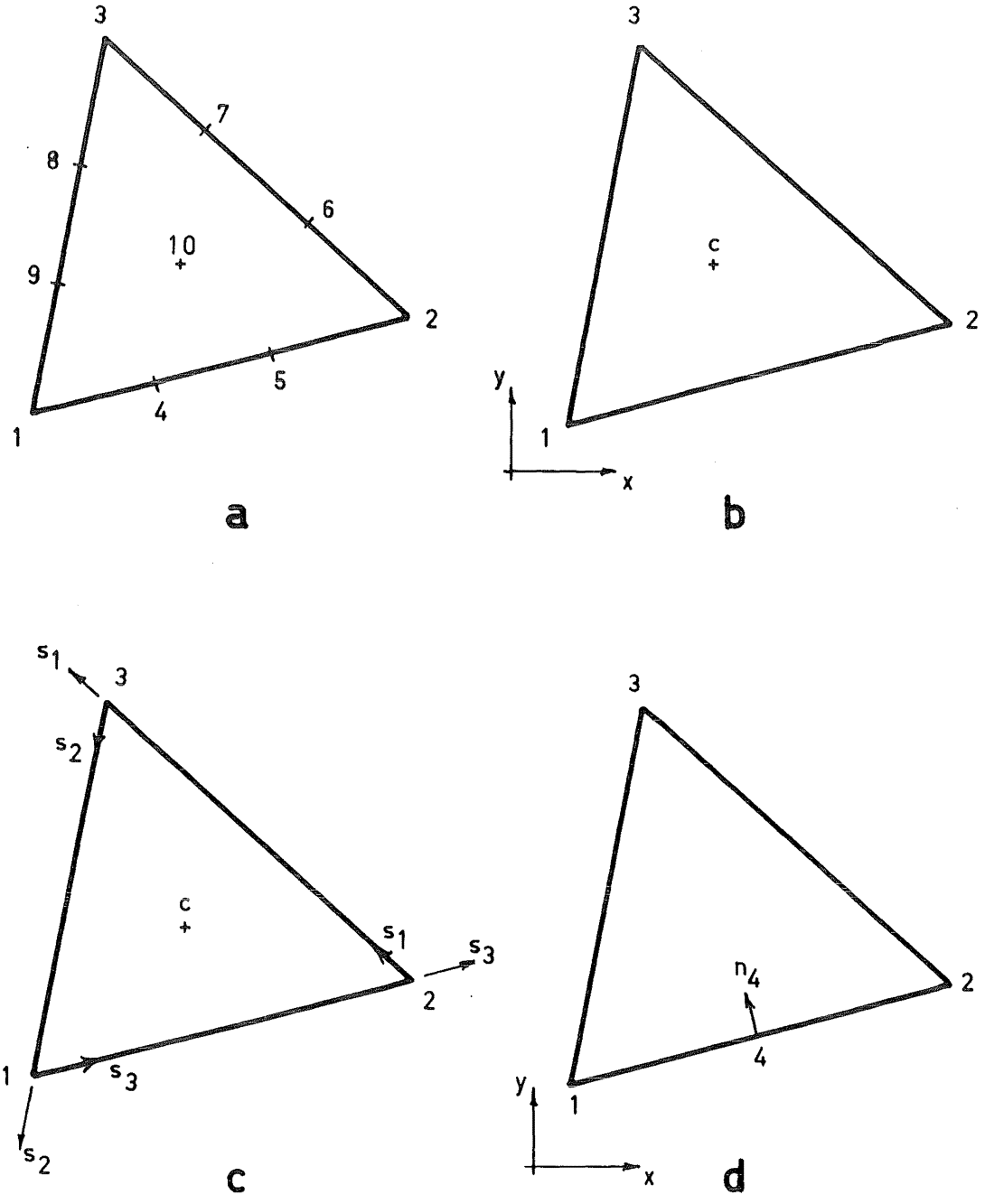

Fig. A.4. Nodal Configurations for Cubic Interpolation Vectors

$$\{\phi_3\} = \tfrac{1}{2}\begin{Bmatrix} \zeta_1(3\zeta_1-1)(3\zeta_1-2) \\ \zeta_2(3\zeta_2-1)(3\zeta_2-2) \\ \zeta_3(3\zeta_3-1)(3\zeta_3-2) \\ 9\zeta_1\zeta_2(3\zeta_1-1) \\ 9\zeta_1\zeta_2(3\zeta_2-1) \\ 9\zeta_2\zeta_3(3\zeta_2-1) \\ 9\zeta_2\zeta_3(3\zeta_3-1) \\ 9\zeta_3\zeta_1(3\zeta_3-1) \\ 9\zeta_3\zeta_1(3\zeta_1-1 \\ 54\zeta_1\zeta_2\zeta_3 \end{Bmatrix} \qquad \text{(A.11)}$$

A more useful nodal system, containing only a centroidal node and three corner nodes, is shown in Fig. A.4b. For this system

$$\{f_4\}^T = \langle f_1 \; f_{x1} \; f_{y1} \; f_2 \; f_{x2} \; f_{y2} \; f_3 \; f_{x3} \; f_{y3} \; f_c \rangle \qquad \text{(A.12)}$$

where

$$f_{x1} = \left(\frac{\partial f}{\partial x}\right)_1 \quad \text{and} \quad f_{y1} = \left(\frac{\partial f}{\partial y}\right)_1, \text{ etc.}$$

The interpolation vector for this nodal system can be determined by transforming the interpolation vector of Eq.(A.11), i.e.

$$F = \{\phi_3\}^T \{f_3\}$$

$$= \{\phi_3\}^T [A]\{f_4\}$$

where [A] is a transformation matrix relating $\{f_3\}$ to $\{f_4\}$. Hence

$$\{\phi_4\} = [A]^T \{\phi_3\}. \qquad \text{(A.13)}$$

The easiest method of determining the transformation matrix [A] is through an intermediate nodal system which is shown in Fig. A.4c and where

$$\{f_i\}^T = \langle f_1 \; f_{21} \; f_{31} \; f_2 \; f_{32} \; f_{12} \; f_3 \; f_{13} \; f_{23} \; f_c \rangle$$

with $f_{21} = (\frac{\partial f}{\partial s_2})_1$ etc. For this system

$$\{f_3\} = [A_1]\{f_i\}, \tag{A.14}$$

i.e.

$$\begin{Bmatrix} f_1 \\ f_2 \\ f_3 \\ f_4 \\ f_5 \\ f_6 \\ f_7 \\ f_8 \\ f_9 \\ f_c \end{Bmatrix} = \frac{1}{27} \begin{bmatrix} 27 & & & & & & & & & \\ & 27 & & & & & & & & \\ & & 27 & & & & & & & \\ 20 & & & 4\ell_3 & 7 & -2\ell_3 & & & & \\ 7 & & & 2\ell_3 & 20 & -4\ell_3 & & & & \\ & & & & & & 20 & & 4\ell_1 & 7 & -2\ell_1 \\ & & & & & & 7 & & 2\ell_1 & 20 & -4\ell_1 \\ & 7 & -2\ell_2 & & & & & 20 & & & 4\ell_2 \\ & 20 & -4\ell_2 & & & & & 7 & & & 2\ell_2 \\ & & & & & & & & & & & 27 \end{bmatrix} \begin{Bmatrix} f_1 \\ f_{21} \\ f_{31} \\ f_2 \\ f_{32} \\ f_{12} \\ f_3 \\ f_{13} \\ f_{23} \\ f_c \end{Bmatrix}$$

where ℓ_1, ℓ_2 and ℓ_3 are the lengths of sides 1, 2 and 3 respectively. Also,

$$\{f_i\} = [A_2]\{f_4\}$$

i.e.

$$\begin{Bmatrix} f_1 \\ f_{21} \\ f_{31} \\ f_2 \\ f_{32} \\ f_{12} \\ f_3 \\ f_{13} \\ f_{23} \\ f_c \end{Bmatrix} = \begin{bmatrix} 1 & & & & & & & & & \\ & \cos\gamma_2 & \sin\gamma_2 & & & & & & & \\ & \cos\gamma_3 & \sin\gamma_3 & & & & & & & \\ & & & 1 & & & & & & \\ & & & & \cos\gamma_3 & \sin\gamma_3 & & & & \\ & & & & \cos\gamma_1 & \sin\gamma_1 & & & & \\ & & & & & & 1 & & & \\ & & & & & & & \cos\gamma_1 & \sin\gamma_1 & \\ & & & & & & & \cos\gamma_2 & \sin\gamma_2 & \\ & & & & & & & & & 1 \end{bmatrix} \begin{Bmatrix} f_1 \\ f_{x1} \\ f_{y1} \\ f_2 \\ f_{x2} \\ f_{y2} \\ f_3 \\ f_{x3} \\ f_{y3} \\ f_c \end{Bmatrix}$$

where γ_1, γ_2 and γ_3 are the angles, measured anticlockwise from the x-axis, to the sides 1, 2, and 3 respectively.

The transformation matrix is given by

$$[A] = [A_1][A_2].$$

and the interpolation vector for the nodal system shown in Fig. A.4b is

$$\{\phi_4\} = \begin{Bmatrix} \zeta_1^2(\zeta_1 + 3\zeta_2 + 3\zeta_3) - 7\zeta_1\zeta_2\zeta_3 \\ \zeta_1^2(a_3\zeta_2 - a_2\zeta_3) + (a_2 - a_3)\zeta_1\zeta_2\zeta_3 \\ \zeta_1^2(b_2\zeta_3 - b_3\zeta_2) + (b_3 - b_2)\zeta_1\zeta_2\zeta_3 \\ \zeta_2^2(\zeta_2 + 3\zeta_3 + 3\zeta_1) - 7\zeta_1\zeta_2\zeta_3 \\ \zeta_2^2(a_1\zeta_3 - a_3\zeta_1) + (a_3 - a_1)\zeta_1\zeta_2\zeta_3 \\ \zeta_2^2(b_3\zeta_1 - b_1\zeta_3) + (b_1 - b_3)\zeta_1\zeta_2\zeta_3 \\ \zeta_3^2(\zeta_3 + 3\zeta_1 + 3\zeta_2) - 7\zeta_1\zeta_2\zeta_3 \\ \zeta_3^2(a_2\zeta_1 - a_1\zeta_2) + (a_1 - a_2)\zeta_1\zeta_2\zeta_3 \\ \zeta_3^2(b_1\zeta_2 - b_2\zeta_1) + (b_2 - b_1)\zeta_1\zeta_2\zeta_3 \\ 27\zeta_1\zeta_2\zeta_3 \end{Bmatrix} \qquad (A.15)$$

This is the interpolation vector used to describe the displacement shape of the plane-stress element (Section A.3).

For the plate bending element the nodal system shown in Fig. A.4d is the most convenient (this becomes apparent in Section A.4), with

$$\{f_5\} = \langle f_1 \; f_{y1} \; -f_{x1} \; f_2 \; f_{y2} \; -f_{x2} \; f_3 \; f_{y3} \; -f_{x3} \; f_{n4} \rangle \qquad (A.16)$$

where

$$f_{y1} = \left(\frac{\partial f}{\partial y}\right)_1 \quad \text{and} \quad -f_{x1} = -\left(\frac{\partial f}{\partial x}\right)_1,$$

similarly for f_{y2}, $-f_{x2}$, f_{y3} and $-f_{x3}$.

The interpolation vector is again determined most easily by transforming the nodal system shown in Fig. A.4c.

$$\{f_i\} = [A_3]\{f_5\} \qquad (A.17)$$

i.e.

$$\begin{Bmatrix} f_1 \\ f_{21} \\ f_{31} \\ f_2 \\ f_{32} \\ f_{12} \\ f_3 \\ f_{13} \\ f_{23} \\ f_c \end{Bmatrix} = \begin{bmatrix} 1 & & & & & & & & & \\ \sin\gamma_2 & -\cos\gamma_2 & & & & & & & & \\ \sin\gamma_3 & -\cos\gamma_3 & & & & & & & & \\ & & 1 & & & & & & & \\ & & & \sin\gamma_3 & -\cos\gamma_3 & & & & & \\ & & & \sin\gamma_1 & -\cos\gamma_1 & & & & & \\ & & & & & 1 & & & & \\ & & & & & & \sin\gamma_1 & -\cos\gamma_1 & & \\ & & & & & & \sin\gamma_2 & -\cos\gamma_2 & & \\ a_1 & a_2 & a_3 & a_4 & a_5 & a_6 & a_7 & a_8 & a_9 & a_{10} \end{bmatrix} \begin{Bmatrix} f_1 \\ f_{y1} \\ -f_{x1} \\ f_2 \\ f_{y2} \\ -f_{x2} \\ f_3 \\ f_{y3} \\ -f_{x3} \\ f_{n4} \end{Bmatrix}$$

where

$$a_1 = (7 + 6\mu_3)/27 \qquad a_2 = -b_3(2 + \mu_3)/27$$

$$a_3 = -a_3(2 + \mu_3)/27 \qquad a_4 = (7 + 6\lambda_3)/27$$

$$a_5 = b_3(2 + \lambda_3)/27 \qquad a_6 = a_3(2 + \lambda_3)/27$$

$$a_7 = 7/27 \qquad a_8 = (b_1 - b_2)/27$$

$$a_9 = (a_1 - a_2)/27, \quad \text{and} \quad a_{10} = 4h_3/27$$

Transforming the interpolation vector of Eq. (A.11) by the transformation matrices in Eqs (A.13) and (A.17) we obtain the interpolation vector for the nodal system shown in Fig. A.4d,

$$\{\phi_5\} = \begin{Bmatrix} \zeta_1^2(\zeta_1 + 3\zeta_2 + 3\zeta_3) + 6\mu_3\zeta_1\zeta_2\zeta_3 \\ \zeta_1^2(b_2\zeta_3 - b_3\zeta_1) + (b_1 - b_3\mu_3)\zeta_1\zeta_2\zeta_3 \\ \zeta_1^2(a_2\zeta_3 - a_3\zeta_1) + (a_1 - a_3\mu_3)\zeta_1\zeta_2\zeta_3 \\ \zeta_2^2(\zeta_2 + 3\zeta_2 + 3\zeta_1) + 6\lambda_3\zeta_1\zeta_2\zeta_3 \\ \zeta_2^2(b_3\zeta_1 - b_1\zeta_3) + (b_3\lambda_3 - b_2)\zeta_1\zeta_2\zeta_3 \\ \zeta_2^2(a_3\zeta_1 - a_1\zeta_3) + (a_3\lambda_3 - a_2)\zeta_1\zeta_2\zeta_3 \\ \zeta_3^2(\zeta_3 + 3\zeta_1 + 3\zeta_2) \\ \zeta_3^2(b_1\zeta_2 - b_2\zeta_1) \\ \zeta_3^2(a_1\zeta_2 - a_2\zeta_1) \\ 4h_3\zeta_1\zeta_2\zeta_3 \end{Bmatrix}. \qquad \text{(A.18)}$$

A.3 The Plane-Stress Finite Element

Corresponding to the nodal system shown in Fig. A.5 we select the nodal displacement vector

$$\{\bar{r}\} = \begin{Bmatrix} \bar{u} \\ \bar{v} \end{Bmatrix} \tag{A.19}$$

where $\{\bar{u}\}^T = \langle u_1\ u_{x1}\ u_{y1}\ u_2\ u_{x2}\ u_{y2}\ u_3\ u_{x3}\ u_{y3}\ u_c \rangle$,

and $\{\bar{v}\}^T = \langle v_1\ v_{x1}\ v_{y1}\ v_2\ v_{x2}\ v_{y2}\ v_3\ v_{x3}\ v_{y3}\ v_c \rangle$.

(The bar on top of the vectors differentiates them from the final displacement vector which contains different terms.)

At any point, the displacements u and v are defined as

$$\begin{aligned} u &= \{\phi_4\}^T\{\bar{u}\} \\ v &= \{\phi_4\}^T\{\bar{v}\} \end{aligned} \tag{A.20}$$

where $\{\phi_4\}$ is the interpolation vector given in Eq. (A.15).

Strain Displacement Relations: The strains at any point can be formed by differentiating Eqs (A.20)

$$\begin{aligned} \varepsilon_n &= \frac{\partial u}{\partial x} = \{\phi_{4x}\}^T\{\bar{u}\} \\ \varepsilon_y &= \frac{\partial v}{\partial y} = \{\phi_{4y}\}^T\{\bar{v}\} \\ \gamma_{xy} &= \frac{\partial u}{\partial y} + \frac{\partial v}{\partial x} = \{\phi_{4y}\}\{\bar{u}\} + \{\phi_{4x}\}\{\bar{v}\}, \end{aligned} \tag{A.21}$$

where $\{\phi_{4x}\}$ and $\{\phi_{4y}\}$ are the vectors formed from the appropriate derivatives of the interpolation vector $\{\phi_4\}$, i.e.

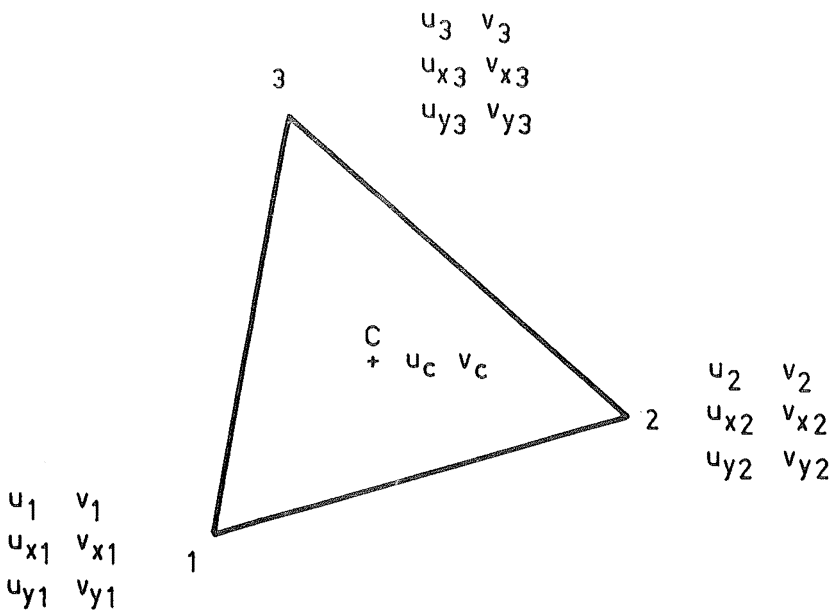

Fig. A.5. Displacement Nodal System for the Plane-Stress Finite Element

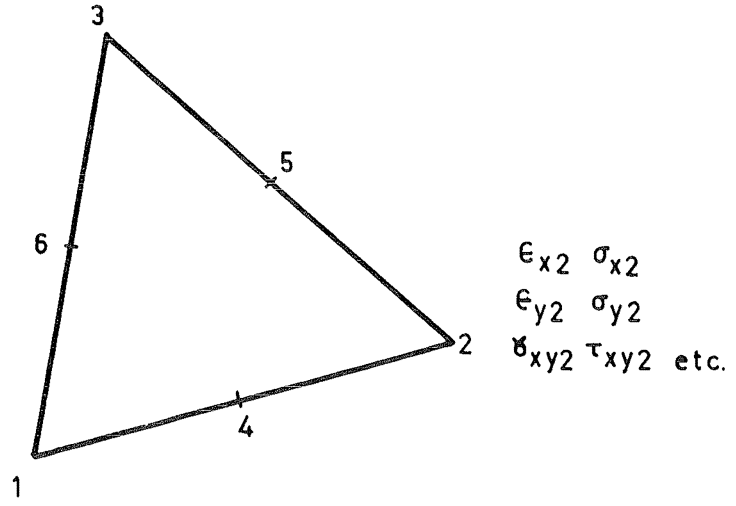

Fig. A.6. Stress and Strain Nodal System for the Plane-Stress Finite Element

$$\{\phi_{4x}\} = \{\frac{\partial \phi_4}{\partial x}\} = \frac{1}{2A} \begin{Bmatrix} 6\zeta_1(1-\zeta_1)b_1 - 7H_a \\ 2\zeta_1 b_1(a_3\zeta_2 - a_2\zeta_3) + 2\zeta_1{}^2 A + (a_2-a_3)H_a \\ 2\zeta_1 b_1(b_2\zeta_3 - b_3\zeta_2) + (b_3-b_2)H_a \\ 6\zeta_2(1-\zeta_2)b_2 - 7H_a \\ 2\zeta_2 b_2(a_1\zeta_3 - a_3\zeta_1) + 2\zeta_2{}^2 A + (a_3-a_1)H_a \\ 2\zeta_2 b_2(b_3\zeta_1 - b_1\zeta_3) + (b_1-b_3)H_a \\ 6\zeta_3(1-\zeta_3)b_3 - 7H_a \\ 2\zeta_3 b_3(a_2\zeta_1 - a_1\zeta_2) + 2\zeta_3{}^2 A + (a_1-a_2)H_a \\ 2\zeta_3 b_3(b_1\zeta_2 - b_2\zeta_1) + (b_2-b_1)H_a \\ 27H_a \end{Bmatrix} \quad (A.22)$$

and

$$\{\phi_{4y}\} = \{-\frac{\partial \phi_4}{\partial y}\} = \frac{1}{2A} \begin{Bmatrix} 6\zeta_1(1-\zeta_1)a_1 - 7H_b \\ 2\zeta_1 a_1(a_3\zeta_2 - a_2\zeta_3) + (a_2-a_3)H_b \\ 2\zeta_1 a_1(b_2\zeta_3 - b_3\zeta_2) + 2\zeta_1{}^2 A + (b_3-b_2)H_b \\ 6\zeta_2(1-\zeta_2)a_2 - 7H_b \\ 2\zeta_2 a_2(a_1\zeta_3 - a_3\zeta_1) + (a_3-a_1)H_b \\ 2\zeta_2 a_2(b_3\zeta_1 - a_1\zeta_3) + 2\zeta_2{}^2 A + (b_1-b_3)H_b \\ 6\zeta_3(1-\zeta_3)a_3 - 7H_b \\ 2\zeta_3 a_3(a_2\zeta_1 - a_1\zeta_2) + (a_1-a_2)H_b \\ 2\zeta_3 a_3(b_1\zeta_2 - b_2\zeta_1) + (b_2-b_1)H_b \\ 27H_b \end{Bmatrix}$$

where $H_a = \zeta_1\zeta_2 b_3 + \zeta_2\zeta_3 b_1 + \zeta_3\zeta_1 b_2$

$H_b = \zeta_1\zeta_2 a_3 + \zeta_2\zeta_3 a_1 + \zeta_3\zeta_1 a_2$.

Eq. (A.21) can be written in the matrix form,

$$\{\tilde{\varepsilon}\} = \begin{Bmatrix} \tilde{\varepsilon}_x \\ \tilde{\varepsilon}_y \\ \tilde{\gamma}_{xy} \end{Bmatrix} = \begin{bmatrix} \phi_{4x} & \cdot \\ \cdot & \phi_{4y} \\ \phi_{4y} & \phi_{4x} \end{bmatrix} \begin{Bmatrix} \bar{u} \\ \bar{v} \end{Bmatrix} = [\tilde{B}]\{\tilde{r}\} \quad (A.23)$$

$(3\times20)\,(20\times1)$

where the tilde on the strain vector denotes the vector of strains at any point (distinct from the nodal strain vector $\{\varepsilon\}$).

The strains (and hence the corresponding stresses) vary quadratically over the element, and therefore we can describe their variation by the interpolation vector $\{\phi_2\}$, as in Eq. (A.9), corresponding to the nodal system shown in Fig. A.6. Hence, the strains and the stresses at any point in the element are

$$\{\tilde{\varepsilon}\} = \{\phi_2\}^T\{\varepsilon\}$$

and (A.24)

$$\{\tilde{\sigma}\} = \{\phi_2\}^T\{\sigma\}$$

where $\{\varepsilon\}$ is the nodal strain vector,

$$\{\varepsilon\} = \begin{Bmatrix} \varepsilon_x \\ \varepsilon_y \\ \gamma_{xy} \end{Bmatrix} \quad (A.25)$$

with $\{\varepsilon_x\}^T = \langle \varepsilon_{x1} \ \varepsilon_{x2} \ \varepsilon_{x3} \ \varepsilon_{x4} \ \varepsilon_{x5} \ \varepsilon_{x6} \rangle$,

similarly for $\{\varepsilon_y\}$ and $\{\gamma_{xy}\}$.

The nodal stress vector is

$$\{\sigma\} = \begin{Bmatrix} \sigma_x \\ \sigma_y \\ \sigma_{xy} \end{Bmatrix} \tag{A.26}$$

where $\{\sigma_x\}^T = \langle \sigma_{x1} \ \sigma_{x2} \ \sigma_{x3} \ \sigma_{x4} \ \sigma_{x5} \ \sigma_{x6} \rangle$,

similarly for $\{\sigma_y\}$ and $\{\tau_{xy}\}$.

Evaluating Eq. A.21 at the nodal points we obtain

$$\{\varepsilon\} = \begin{bmatrix} U & \cdot \\ \cdot & V \\ V & U \end{bmatrix} \begin{Bmatrix} \bar{u} \\ \bar{v} \end{Bmatrix} = [\bar{B}]\{\bar{r}\} \tag{A.27}$$

where the submatrices [U] and [V] are given overleaf. From these submatrices we see that the corner nodal strains are directly related to the corresponding corner nodal displacements but the midside nodal strains are dependent upon all the nodal displacements. Therefore the strains will not be compatible along the interelement boundaries.

Constitutive Law: The constitutive law is

$$\{\tilde{\sigma}\} = [C]\{\tilde{\varepsilon}\} \tag{A.28}$$

and for isotropic materials,

$$[U] = \frac{1}{8A}\begin{bmatrix}
\cdot & 8A & \cdot & \cdot & \cdot & \cdot & \cdot & \cdot & \cdot & \cdot \\
\cdot & \cdot & \cdot & \cdot & 8A & \cdot & \cdot & \cdot & \cdot & \cdot \\
\cdot & \cdot & \cdot & \cdot & \cdot & \cdot & \cdot & 8A & \cdot & \cdot \\
6b_1-7b_3 & (b_1-2b_3)a_3 & (2b_3-b_1)b_3 & 6b_2-7b_3 & (2b_3-b_2)a_3 & (b_2-2b_3)b_3 & -7b_3 & (a_1-a_2)b_3 & (b_2-b_1)b_3 & 27b_3 \\
-7b_1 & (a_2-a_3)b_1 & (b_3-b_2)b_1 & 6b_2-7b_1 & (b_2-2b_1)a_1 & (2b_1-b_2)b_1 & 6b_3-7b_1 & (2b_1-b_3)a_1 & (b_3-2b_1)b_1 & 27b_1 \\
6b_1-7b_2 & (2b_2-b_1)a_2 & (b_1-2b_2)b_2 & -7b_2 & (a_3-a_1)b_2 & (b_1-b_3)b_2 & 6b_3-7b_2 & (b_3-2b_2)a_2 & (2b_2-b_3)b_2 & 27b_2
\end{bmatrix}$$

$$[V] = \frac{1}{8A}\begin{bmatrix}
\cdot & \cdot & 8A & \cdot & \cdot & \cdot & \cdot & \cdot & \cdot & \cdot \\
\cdot & \cdot & \cdot & \cdot & \cdot & 8A & \cdot & \cdot & \cdot & \cdot \\
\cdot & \cdot & \cdot & \cdot & \cdot & \cdot & \cdot & \cdot & 8A & \cdot \\
6a_1-7a_3 & (a_1-2a_3)a_3 & (2a_3-a_1)b_3 & 6a_2-7a_3 & (2a_3-a_2)a_3 & (a_2-2a_3)b_3 & -7a_3 & (a_1-a_2)a_3 & (b_2-b_1)a_3 & 27a_3 \\
-7a_1 & (a_2-a_3)a_1 & (b_3-b_2)a_1 & 6a_2-7a_1 & (a_2-2a_1)a_1 & (2a_1-a_2)b_1 & 6a_3-7a_1 & (2a_1-a_3)a_1 & (a_3-2a_1)b_1 & 27a_1 \\
6a_1-7a_2 & (2a_2-a_1)a_2 & (a_1-2a_2)b_2 & -7a_2 & (a_3-a_1)a_2 & (b_1-b_3)a_2 & 6a_3-7a_2 & (a_3-2a_2)a_2 & (2a_2-a_3)b_2 & 27a_2
\end{bmatrix}$$

$$\begin{Bmatrix} \sigma_x \\ \sigma_y \\ \tau_{xy} \end{Bmatrix} = \frac{E}{1-\nu^2} \begin{bmatrix} 1 & \nu & \cdot \\ \nu & 1 & \cdot \\ \cdot & \cdot & \frac{1-\nu}{2} \end{bmatrix} \begin{Bmatrix} \varepsilon_x \\ \varepsilon_y \\ \gamma_{xy} \end{Bmatrix} .$$

Strain Energy Integration: For an element of thickness h the strain energy integral is

$$U = \tfrac{1}{2}h \int_A \tilde{\sigma}^T \tilde{\varepsilon} \, d\, A. \qquad (A.29)$$

and, substituting Eqs (A.24) and (A.28) into Eq. (A.29), we get

$$U = \tfrac{1}{2}\{\varepsilon\}^T [Q][D]\{\varepsilon\} \qquad (A.30)$$

where $[Q] = h \int_A \{\phi_2\}\{\phi_2\}^T dA$, and [D] is a matrix comprising the terms of the constitutive law corresponding to the order of the strains as given in Eq. (A.25).

Hence, incorporating Eq. (A.27)

$$U = \tfrac{1}{2}\{\bar{r}\}^T[\bar{k}]\{r\} \qquad (A.31)$$

where

$$[\bar{k}] = [\bar{B}]^T[Q][D][\bar{B}]$$

and the stiffness matrix $[\bar{k}]$ corresponds to the order of $\{\bar{r}\}$ as given in Eq. (A.19).

A more meaningful stiffness matrix can be obtained however by rearranging the order of $\{\bar{r}\}$ to obtain $\{r^*\}$ where,

$$\{r^*\} = \begin{Bmatrix} r_1 \\ r_2 \\ r_3 \\ r_0 \end{Bmatrix} = \begin{Bmatrix} r \\ -- \\ r_0 \end{Bmatrix} \tag{A.32}$$

with $\{r_0\}^T = \langle u_0 \; v_0 \rangle$ and

$$\{r_1\}^T = \langle u_1 \; v_1 \; \varepsilon_{x1} \; \varepsilon_{y1} \; \varepsilon_{xy1} \; \omega_1 \rangle,$$

and $\varepsilon_{x1} = u_{x1}$, $\varepsilon_{y1} = v_{y1}$ the direct strains,

$\varepsilon_{xy1} = \frac{1}{2}\gamma_{xy1} = \frac{1}{2}(v_{x1} + u_{y1})$ the shear strain, and

$\omega_1 = \omega_{xy1} = \frac{1}{2}(v_{x1} - u_{y1})$ the average rotation of an element fibre about the z axis. Similarly for $\{r_2\}$ and $\{r_3\}$.

After appropriately rearranging the rows and columns of $[\overline{k}]$ we obtain,

$$U = \frac{1}{2}\{r^*\}^T \underset{(20x20)}{[k^*]} \{r^*\}. \tag{A.33}$$

The stiffness matrix $[k^*]$ can be reduced by condensing out the centroidal displacements,

$$\begin{Bmatrix} P \\ P_0 \end{Bmatrix} = \begin{bmatrix} K_{11} & K_{12} \\ K_{21} & K_{22} \end{bmatrix} \begin{Bmatrix} r \\ r_0 \end{Bmatrix}$$

hence

$$\{P\} = [K]\{r\} \tag{A.34}$$

where

$$[K] = [K_{11}] - [K_{12}][K_{12}^{-1}][K_{21}]$$

is the final (18x18) plane stress stiffness matrix.

A.4 The Plate Bending Finite Element

The plate bending element has a cubic displacement function and two quadratically varying rotations; thus, to maintain interelement compatability along a side, the displacement and rotations must be defined uniquely by the degree of freedom at the nodes on the side being considered. This condition means that, to define the transverse rotation we must include an additional node possessing one rotational degree of freedom. The interpolation formula of Eq. (A.18) corresponding to the nodal system shown in Fig. A.4d contains only one midside node; therefore, referring to Fig. A.7, the triangular element 1-2-3 is divided into three subtriangles 1-2-0, 2-3-0 and 3-1-0 where each subtriangle has the nodal system shown in Fig. A.4d. We apply the cubic interpolation formula of Eq. (A.18) over each subtriangle which is renumbered according to Fig. A.2d so that the interior node is always node 3. Each subtriangle has its own properties associated with a superscript corresponding to the subelement number which is determined from the opposite nodal number. Fig. A.8 shows some of the properties of subelement 1 which has been taken from the triangle 1-2-3 shown in Fig. A.7.

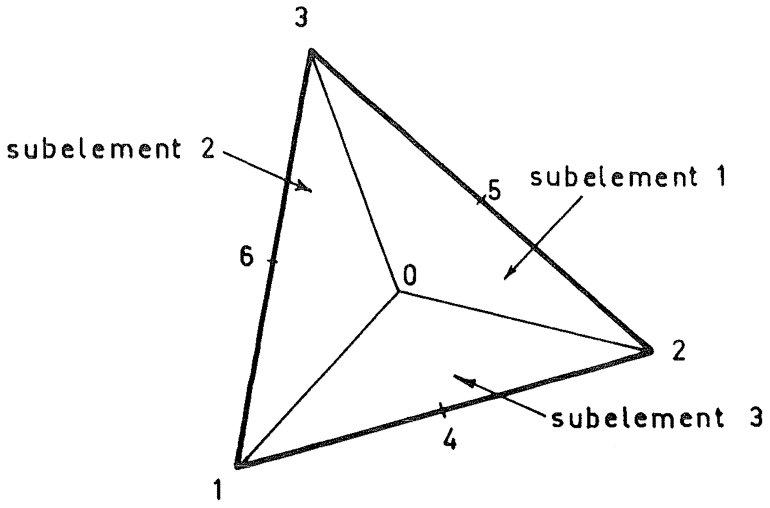

Fig. A.7. Plate Bending Finite Element

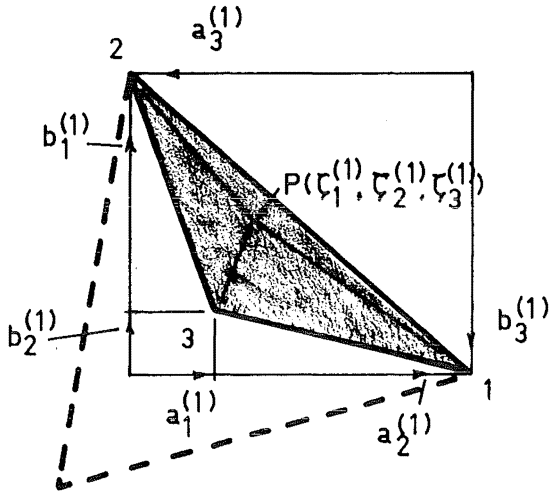

Fig. A.8. Notation for Subelement 1

Interpolation Formula: We may write the interpolation formula $\{\phi_5\}$ as a function of the fifteen degrees of freedom by inserting zeros in the appropriate positions, for example, in subelement 1,

$$w^{(1)} = \underset{(1\times15)}{\{\phi_p^{(1)}\}^T} \underset{(15\times1)}{\{\bar{r}\}}$$

$$= \{\phi_e^{(1)T} \quad \phi_o^{(1)T}\} \begin{Bmatrix} r \\ r_o \end{Bmatrix} \tag{A.35}$$

where

$$\{r\}^T = \langle w_1 \ \theta_{x1} \ \theta_{y1} \ w_2 \ \theta_{x2} \ \theta_{y2} \ w_3 \ \theta_{x3} \ \theta_{y3} \ \theta_{n4} \ \theta_{n5} \ \theta_{n6} \rangle$$

$$\theta_{xi} = \left(\frac{\partial w}{\partial y}\right)_i$$

$$\theta_{yi} = -\left(\frac{\partial w}{\partial x}\right)_i$$

$$\theta_{ni} = \left(\frac{\partial w}{\partial n}\right)_i$$

and the direction n is always normal to the edge and towards the interior of the triangle,

$$\{r_o\}^T = \langle w_o \ \theta_{xo} \ \theta_{yo} \rangle$$

and

$$\{\phi_p\} = \begin{Bmatrix}
\zeta_1^{(1)2}(3-2\zeta_1^{(1)}) + 6\mu_3^{(1)}\zeta_1^{(1)}\zeta_2^{(2)}\zeta_3^{(1)} \\
\zeta_1^{(1)2}(b_2^{(1)}\zeta_3^{(1)}-b_3^{(1)}\zeta_2^{(1)})+(b_1^{(1)}-b_3^{(1)}\mu_3^{(1)})\zeta_1^{(1)}\zeta_2^{(1)}\zeta_3^{(1)} \\
\zeta_1^{(1)2}(a_2^{(1)}\zeta_3^{(1)}-a_3^{(1)}\zeta_2^{(1)})+(a_1^{(1)}-a_3^{(1)}\mu_3^{(1)})\zeta_1^{(1)}\zeta_2^{(1)}\zeta_3^{(1)} \\
\zeta_2^{(1)2}(3-2\zeta_2^{(1)})+6\lambda_3^{(1)}\zeta_1^{(1)}\zeta_2^{(1)}\zeta_3^{(1)} \\
\zeta_2^{(1)2}(b_3^{(1)}\zeta_1^{(1)}-b_1^{(1)}\zeta_3^{(1)})+(b_3^{(1)}\lambda_3^{(1)}-b_2^{(1)})\zeta_1^{(1)}\zeta_2^{(1)}\zeta_3^{(1)} \\
\zeta_2^{(1)2}(a_3^{(1)}\zeta_1^{(1)}-a_1^{(1)}\zeta_3^{(1)})+(a_3^{(1)}\lambda_3^{(1)}-a_2^{(1)})\zeta_1^{(1)}\zeta_2^{(1)}\zeta_3^{(1)} \\
0 \\
0 \\
0 \\
0 \\
4h_3^{(1)}\zeta_1^{(1)}\zeta_2^{(1)}\zeta_3^{(1)} \\
0 \\
\zeta_3^{(1)2}(3-2\zeta_3^{(1)}) \\
\zeta_3^{(1)2}(b_1^{(1)}\zeta_2^{(1)} - b_2^{(1)}\zeta_1^{(1)}) \\
\zeta_3^{(1)2}(a_1^{(1)}\zeta_2^{(1)} - a_2^{(1)}\zeta_1^{(1)})
\end{Bmatrix}$$

The first twelve rows of $\{\phi_p\}$ correspond to $\{\phi_e\}$, the remaining three rows to $\{\phi_o\}$. If five zero terms are omitted from $\{\phi_p\}$ we are left with the interpolation formula $\{\phi_5\}$ of Eq. (A.18).

Internal Compatability Requirements: We require compatability of the displacement and the rotations along the interior boundaries of the subelements so we match the

rotations normal to these boundaries at the internal mid-points 7, 8 and 9 (refer Fig. A.7). i.e.

$$\theta_7^{(2)} = \frac{\partial w^{(2)}}{\partial n_1^{(2)}} = -\frac{\partial w^{(3)}}{\partial n_2^{(3)}} = -\theta_7^{(3)}$$

$$\theta_8^{(3)} = \frac{\partial w^{(3)}}{\partial n_1^{(3)}} = -\frac{\partial w^{(1)}}{\partial n_2^{(1)}} = -\theta_8^{(1)} \qquad \text{(A.36)}$$

$$\theta_9^{(1)} = \frac{\partial w^{(1)}}{\partial n_1^{(1)}} = -\frac{\partial w^{(2)}}{\partial n^{(2)}} = -\theta_9^{(2)}$$

where the directions of n_1 and n_2 for i = 1,2,3 are shown in Fig. (A.9).

From Eqs (A.36), setting $\theta_7^{(2)} + \theta_y^{(3)} = 0$, etc., we obtain a set of equations which can be expressed as,

$$\underset{(3x3)}{[Q_0]}\ \underset{(3x1)}{\{r_0\}} + \underset{(3x12)}{[Q]}\ \underset{(12x1)}{\{r\}} = \{0\}$$

or, $$\{r_0\} = [G]\ \{r\} \qquad \text{(A.37)}$$

where $\underset{(3x12)}{[G]} = -\underset{(3x3)}{[Q_0^{-1}]}\ \underset{(3x12)}{[Q]}$.

Eq. (A.37) gives a constraining equation with which we can relate the centroidal displacements to the boundary displacements. Hence, Eq. (A.35) can be rewritten as

$$w^{(1)} = \underset{(1x12)}{(\{\phi_e^{(1)}\}^T} + \underset{(1x3)}{\{\phi_0^{(1)}\}}\ \underset{(3x12)}{[G]}\ )\ \underset{(12x1)}{\{r\}} \qquad \text{(A.38)}$$

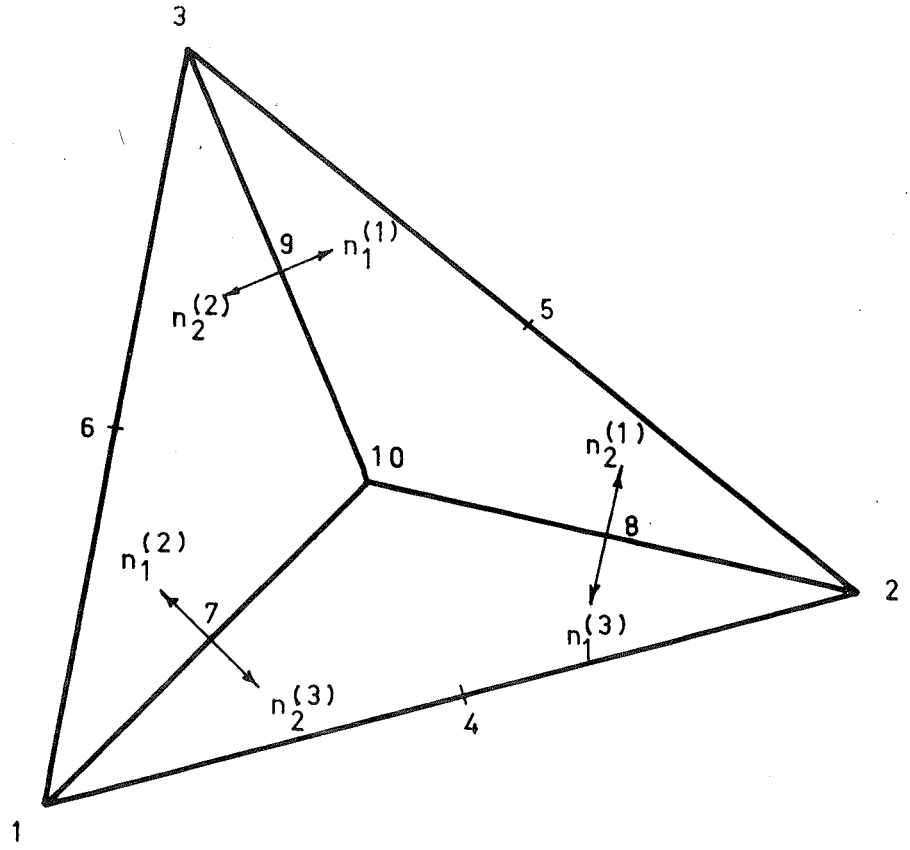

Fig. A.9. Nodal System for the Plate Bending Finite Element

Curvature-Displacement Relations: From the three subtriangles we obtain three curvature components at each node

$$\chi_{xx} = -\frac{\partial^2 w}{\partial x^2}$$

$$\chi_{yy} = -\frac{\partial^2 w}{\partial y^2} \qquad \text{(A.39)}$$

$$\chi_{xy} = -\frac{\partial^2 w}{\partial x \partial y}$$

giving a total of twenty-seven curvatures. These are reduced to 21 distinct values as the internal compatability requirements impose equivalent curvatures at the centroid. Hence the curvature vector is

$$\{\chi\} = \begin{Bmatrix} \chi_{xx} \\ \chi_{yy} \\ \chi_{xy} \end{Bmatrix} \qquad \text{(A.40)}$$

(21x21)

where $\{\chi_{xx}\}^T = \langle \chi^{(3)}_{xx1} \ \chi^{(3)}_{xx2} \ \chi^{(1)}_{xx2} \ \chi^{(1)}_{xx3} \ \chi^{(2)}_{xx3} \ \chi^{(2)}_{xx1} \ \chi_{xx0} \rangle$

and similarly for $\{\chi_{yy}\}$ and $\{\chi_{xy}\}$.

By differentiating Eq. (A.35) we can relate the nodal curvatures to the nodal displacements, i.e. for subelement k,

$$\{\chi^{(k)}_{xx}\} = \{\phi^{(k)}_{pxx}\}^T\{\bar{r}\}$$

$$= (\{\phi^{(k)}_{exx}\}^T + \{\phi^{(k)}_{oxx}\}^T[G])\{r\} \qquad \text{(A.41)}$$

and similarly for $\{\chi^{(k)}_{yy}\}$ and $\{\chi^{(k)}_{xy}\}$.

Hence we can write

$$\{\chi\} = [\bar{B}]\{\bar{r}\} = [B_e \; B_o] \begin{Bmatrix} r \\ r_o \end{Bmatrix} \tag{A.42}$$

i.e. $$\{\chi\} = [B]\{r\} \tag{A.43}$$

where $[B] = [B_e] + [B_o][G]$.

As the curvature variation is linear over each sub-triangle we can define the curvature at any point within subtriangle k as,

$$\underset{(3x1)}{\{\tilde{\chi}^{(k)}\}} = \begin{Bmatrix} \tilde{\chi}^{(k)}_{xx} \\ \tilde{\chi}^{(k)}_{yy} \\ \tilde{\chi}^{(k)}_{xy} \end{Bmatrix} = \underset{(3x9)}{\begin{bmatrix} \phi_1^{(k)T} & & \\ & \phi_1^{(k)T} & \\ & & \phi_1^{(k)T} \end{bmatrix}} \underset{(9x1)}{\{\chi^{(k)}\}} \tag{A.44}$$

$$= \{\psi\}^T \{\chi\}^{(k)}$$

where,

$$\{\chi^{(1)}_{xx}\} = \begin{Bmatrix} \chi^{(1)}_{xx2} \\ \chi^{(1)}_{xx3} \\ \chi^{(1)}_{xx0} \end{Bmatrix}, \text{ etc.,}$$

and $\{\phi_1\}$ is the linear interpolation formula of Eq. (A.7). Thus Eq. (A.44) yields

$$\{\tilde{\chi}^{(1)}_{xx}\} = \{\zeta_1^{(1)} \; \zeta_2^{(1)} \; \zeta_3^{(1)}\} \begin{Bmatrix} \chi^{(1)}_{xx2} \\ \chi^{(1)}_{xx3} \\ \chi^{(1)}_{xx0} \end{Bmatrix} \text{ etc..}$$

The Constitutive Law: The constitutive law is

$$\{\tilde{M}\} = [C]\{\tilde{\chi}\} \tag{A.45}$$

and, for isotropic materials,

$$\begin{Bmatrix} \tilde{M}_{xx} \\ \tilde{M}_{yy} \\ \tilde{M}_{xy} \end{Bmatrix} = \frac{Eh^3}{12(1-\nu^2)} \begin{bmatrix} 1 & \nu & \cdot \\ \nu & 1 & \cdot \\ \cdot & \cdot & (1-\nu)/2 \end{bmatrix} \begin{Bmatrix} \chi_{xx} \\ \chi_{yy} \\ 2\chi_{xy} \end{Bmatrix} .$$

The Strain Energy Integration: The strain energy of subelement k is

$$U = \tfrac{1}{2} \int_{A^{(k)}} \tilde{M}^T \tilde{\chi} \, dA^{(k)} \tag{A.46}$$

where the tilde again denotes the value at any point. Substituting Eqs (A.44) and (A.55),

$$U = \tfrac{1}{2}\{\chi^{(k)}\}^T \left(\int_{A^{(k)}} \{\psi\} [D] \{\psi\}^T \, dA^{(k)} \right) \{\chi^{(k)}\} \tag{A.47}$$

$$= \tfrac{1}{2}\{\chi^{(k)}\}^T [N^{(k)}] \{\chi^{(k)}\}$$

where [D] is formed from the appropriate portions of the constitutive law corresponding to the order of $\{\chi^{(k)}\}$; and the curvature stiffness matrix

$$[N] = \int_{A^{(k)}} \{\psi\}[D]\{\psi\}^T \, dA^{(k)} .$$

Substituting Eq. (A.43) we obtain

$$U = \tfrac{1}{2}\{r\}^T [k] \{r\}$$

where the stiffness matrix

$$[k] = [B]^T [N] [B].$$

Eliminating the Midside Nodal Points: The presence of midside nodal points is not desirable because they introduce a second type of node containing one rotational degree of freedom and these are not consistent with the corner nodes which contain three degrees of freedom.

We can eliminate the midside nodes by constraining the transverse rotation to a linear variation, e.g. for node 4 we set

$$\theta_{n4} = \tfrac{1}{2}(\theta_{n1} + \theta_{n2})$$

$$= \tfrac{1}{2}[(\theta_{x1} + \theta_{x2})\cos\theta_3 + (\theta_{y1} + \theta_{y2})\sin\theta_3)] \quad \text{(A.49)}$$

where θ_3 is the angle between the n axis and side 3 which includes the nodes 1, 2 and 4. A similar procedure will eliminate the midside nodes 5 and 6.

APPENDIX B

Theoretical Load-Moment-Curvature Relationships For a Reinforced Concrete Beam Section

After assuming material properties for both the reinforcement and the concrete, theoretical load-moment-curvature relationships are determined for a reinforced concrete beam section which is in a region of constant moment. Three cases are studied:

a) before cracking and at any section,

b) after cracking and at a cracked section, also,

c) after cracking and in between cracked sections.

In each example equilibrium of horizontal forces and equilibrium of moments provide two equations which are solved most easily by a trial and error solution.

B.1 Material Properties

For the steel reinforcement a bi-linear stress-strain curve was adopted (Fig. B.1) such that

$$\text{for } -\varepsilon_y \leq \varepsilon \leq \varepsilon_y \qquad \sigma = E_{s1}\varepsilon$$

$$\text{for } -\varepsilon_{su} \leq \varepsilon \leq -\varepsilon_y \qquad \sigma = -\sigma_y + E_{s2}(\varepsilon+\varepsilon_y) \qquad \text{(B.1)}$$

$$\text{and for } \varepsilon_y \leq \varepsilon \leq \varepsilon_{su} \qquad \sigma = \sigma_y + E_{s2}(\varepsilon-\varepsilon_y)$$

where ε_y is the yield strain of the reinforcement corresponding to the yield stress σ_y, ε_{su} is the ultimate strain

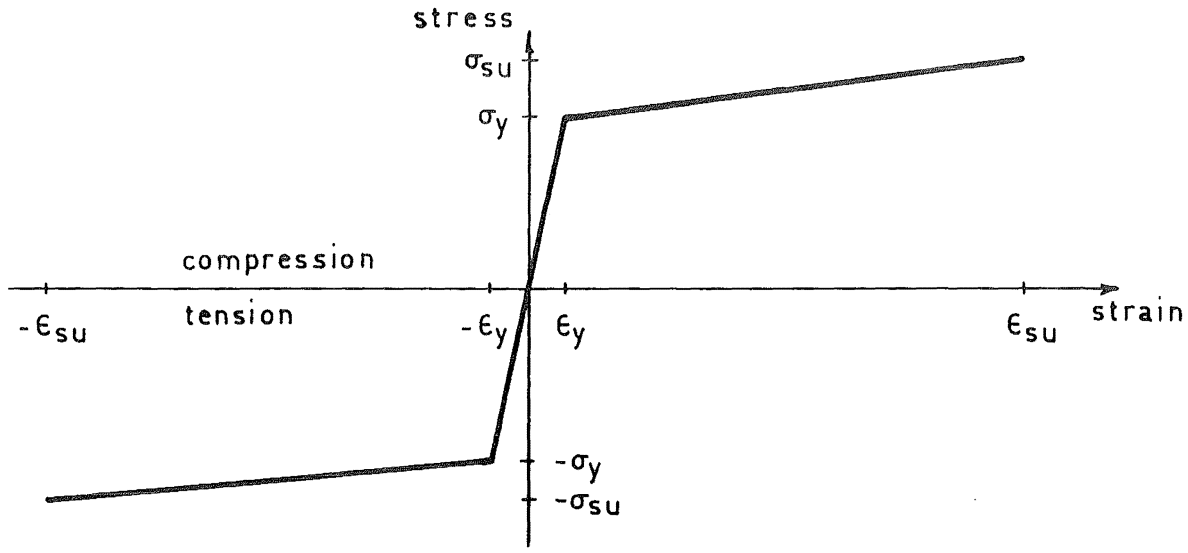

Fig. B.1. Theoretical Stress-Strain Curve for the Reinforcement

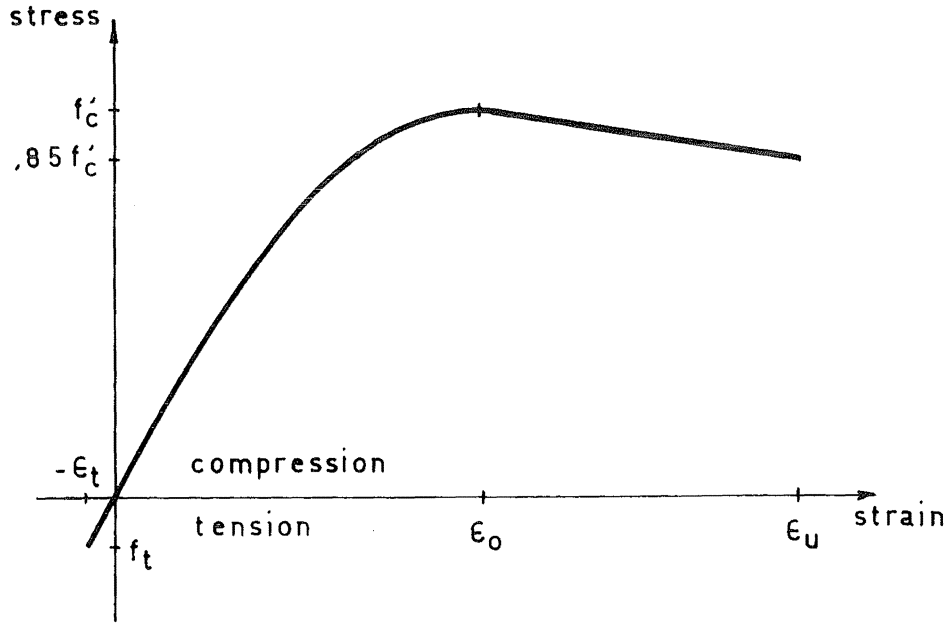

Fig. B.2. Theoretical Stress-Strain Curve for the Concrete

of the reinforcement corresponding to the ultimate stress σ_{su}, and E_{s1} and E_{s2} are the slopes of the bi-linear stress-strain relationship. Of these six parameters four are independent and have to be determined either from tables or by an experimental test. Most specimens possess a distinct yield strain and therefore the yield stress will be well defined. However, although the ultimate stress can be determined, the ultimate strain is often not defined very accurately. When in doubt, or if it is not stated, an ultimate steel strain of .01 was assumed.

The concrete stress-strain curve in compression (Fig. B.2) has a similar shape to that proposed by Hognestad[48]. The first portion is parabolic until, at a strain ε_0, the maximum concrete stress is reached, and from this point on the curve falls linearly until, at the ultimate concrete strain ε_u, the concrete stress is .85 times the maximum concrete stress. For the maximum concrete stress Hognestad took the value of .85 times the crushing stress of concrete. However, because his investigation was restricted to the eccentric loading of short columns, this value was considered to be too conservative for flexural members and the maximum concrete stress was assumed to equal the crushing-stress, f_c' (which concurs with the maximum stress for flexural members specified in Whitney's stress block). Hence, the stress-strain equations for concrete in compression are:

for $0 \leq \varepsilon \leq \varepsilon_0$ $\quad f_c = f_c'[2(\varepsilon/\varepsilon_0) - (\varepsilon/\varepsilon_0)^2]$

and for $\varepsilon_0 \leq \varepsilon \leq \varepsilon_u$ $\quad f_c = f_c'[1 - .15(\varepsilon-\varepsilon_0)/(\varepsilon_u-\varepsilon_0)]$

(B.2)

where ε_u is the ultimate strain of the concrete (normally taken as .0035 or .004).

In tension the stress-strain curve is assumed to be linear, for $-\varepsilon_t \leq \varepsilon \leq 0$ $\quad f_c = E_c\varepsilon$ (B.3)

where E_c is Young's Modulus for concrete, and ε_t is the tensile strain at which the concrete will crack in flexure.

B.2 Reinforced Concrete Section before Cracking

Consider the reinforced concrete section, shown in Fig. B.3, which is subjected to an axial load N and a bending moment M. Horizontal equilibrium on a unit width implies that,

$$CC + CS + TS + TC - N = 0 \qquad (B.4)$$

where

CC is the top concrete force (compressive forces and strains are positive)

and $CC = p\, f_c'(e - \frac{1}{3}e^2)$

with $e = \varepsilon_c/\varepsilon_o$,

CS is the top steel force and

$$CS = E_{sl}\,\frac{p-d_t}{p}\,\varepsilon_c a_{st}',$$

TS is the bottom steel force, and

$$TS = E_{sl}\,\frac{p-d_b}{p}\,\varepsilon_c a_{sb}',$$

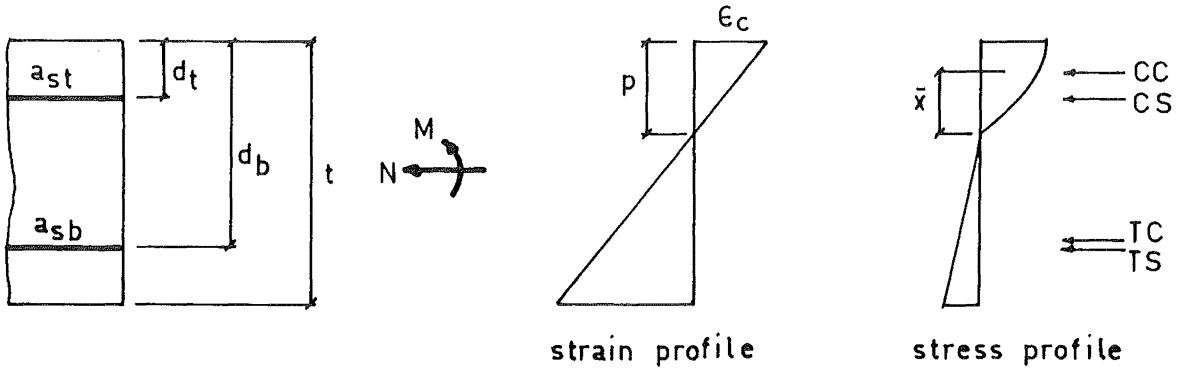

Fig. B.3. Reinforced Concrete Section - before Cracking

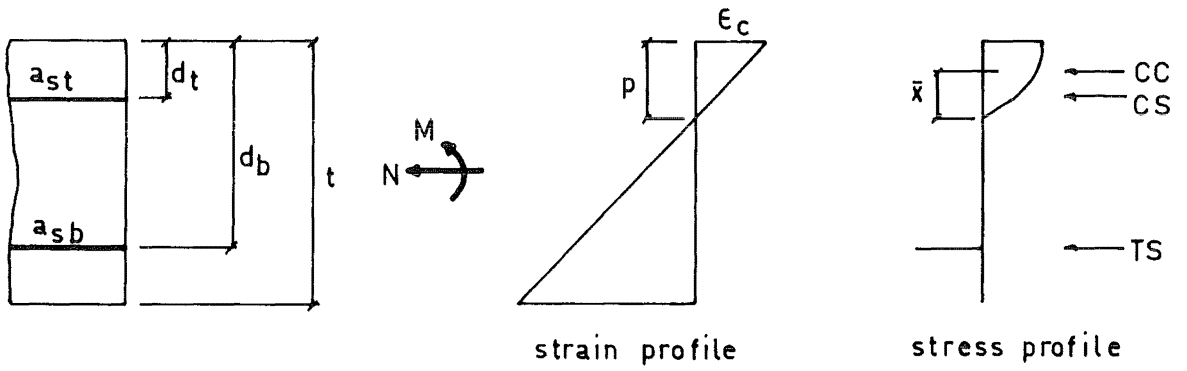

Fig. B.4. Reinforced Concrete Section - at a Crack

TC is the bottom concrete force, and

$$TC = -\tfrac{1}{2} E_c \frac{(t-p)^2}{p} \varepsilon_c .$$

Taking moments about the neutral axis,

$$CC(t/2 - p + \bar{x}) + CS(t/2 - d_t) + TS(t/2 - d_b) - TC(t/6 + p/3) = M \qquad (B.5)$$

where the lever arm of the concrete compressive force CC, is

$$\bar{x} = p \frac{(\frac{2}{3}e - \frac{1}{4}e^2)}{e - \frac{1}{3}e^2} \quad \text{with } e = \varepsilon_c/\varepsilon_o .$$

Hence we can solve for the unknowns ε_c and p using Eqs (B.4) and (B.5).

B.3 Reinforced Concrete Section at a Crack

Firstly consider the case of the top concrete stress being parabolic only. For the section shown in Fig. B.4. horizontal equilibrium for a unit width implies that,

$$CC + CS + TS - N = 0 \qquad (B.6)$$

where

$$CC = p f_c(e - \tfrac{1}{3}e^2) \text{ and } e = \varepsilon_c/\varepsilon_o ,$$

if $\varepsilon_{ts} \leqslant \varepsilon_y$ then $CS = E_{s1} \frac{p-d_t}{p} \varepsilon_c a_{st}$

where ε_{ts} is the strain of the top steel, and if

$$\varepsilon_{ts} > \varepsilon_y \text{ then } CS = [\sigma_y + E_{s2}(\frac{p-d_t}{p} \varepsilon_c - \varepsilon_y)]a_{st} ,$$

if $\varepsilon_{bs} \geq -\varepsilon_y$ then $TS = E_{sl} \frac{p-d_b}{p} \varepsilon_c a_{sb}$

where ε_{bs} is the strain of the bottom steel, and if

$\varepsilon_{bs} < -\varepsilon_y$ then $TS = [-\sigma_y + E_{s2}(\frac{p-d_b}{p} \varepsilon_c + \varepsilon_y)]a_{sb}$.

Taking moments about the neutral axis we obtain

$$CC(t/2 - p + \bar{x}) + CS(t/2 - d_t) + TS(t/2 - d_b) = M \qquad (B.7)$$

where

$$\bar{x} = \frac{p(\frac{2}{3}e - \frac{1}{4}e^2)}{e - \frac{1}{3}e^2} \quad \text{with } e = \varepsilon_c/\varepsilon_o.$$

The unknowns ε_c and p can be found from Eqs (B.6) and (B.7)

The second case is when the top concrete stress block is parabolic and linear. For the section shown in Fig. B.5, horizontal equilibrium for a unit width implies that,

$$C1 + C2 + CS + TS - N = 0 \qquad (B.8)$$

where

$$C1 = \frac{2}{3} p f_c' \frac{\varepsilon_o}{\varepsilon_c}$$

$$C2 = p f_c'(1 - \varepsilon_o/\varepsilon_c)[1 - 0.075(\varepsilon_c - \varepsilon_o)/(\varepsilon_u - \varepsilon_o)]$$

and the values of CS and TS are identical to those in Eq. (B.6). Taking moments about the neutral axis,

$$C1(t/2 - p + \bar{x}_1) + C2(t/2 - p + \bar{x}_2) + CS(t/2 - d_t)$$

$$+ TS(t/2 - d_b) = M \qquad (B.9)$$

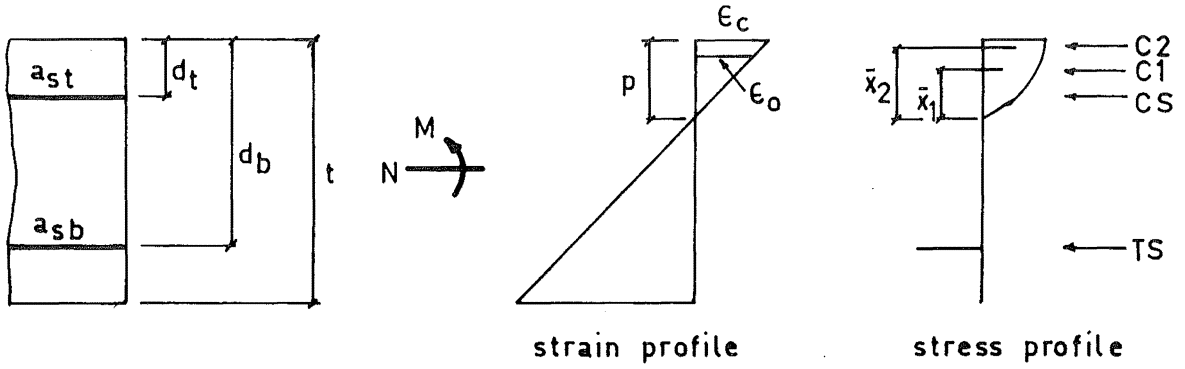

Fig. B.5. Reinforced Concrete Section - at a Crack

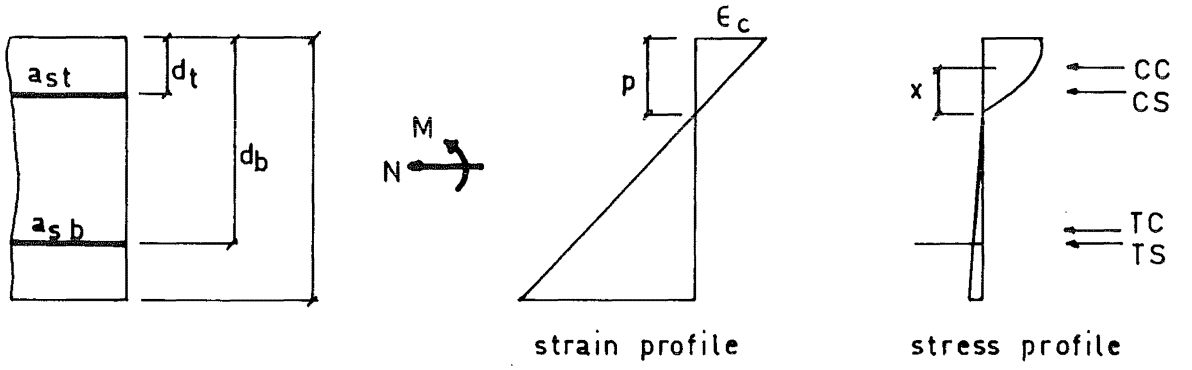

Fig. B.6. Reinforced Concrete Section - Distance l_b from a Crack

where

$$\bar{x}_1 = \frac{5}{8}\frac{\varepsilon_o}{\varepsilon_c} p,$$

and

$$\bar{x}_2 = \frac{\varepsilon_o}{\varepsilon_c} p + p\left(1 - \frac{\varepsilon_o}{\varepsilon_c}\right) \frac{.5 + .05\bar{\varepsilon}}{1. + .075\bar{\varepsilon}}$$

with

$$\bar{\varepsilon} = \frac{\varepsilon_c - \varepsilon_o}{\varepsilon_u - \varepsilon_o}.$$

The unknowns ε_c and p can be determined from Eqs (B.8) and (B.9).

B.4 Reinforced Concrete Section Between Two Cracked Sections

Consider a reinforced concrete beam, within a constant moment region, that has just cracked. As we move away from the cracked section, the concrete tensile force increases until, at a distance ℓ_b (called the bond length) from the crack, the concrete tensile force is capable of forming a new crack. Fig. B.6 shows a section distance ℓ_b from a crack. Horizontal equilibrium gives,

$$CC + CS\ TS + TC - N = 0 \qquad (B.10)$$

where the values of CC, CS and TS are given in Section B.3, and

$$TC = -\tfrac{1}{2}E_c\varepsilon_t(t - p).$$

Taking moments about the neutral axis,

$$C(t/2 - p + \bar{x}) + CS(t/2 - d_t) + TS(t/2 - d_b)$$

$$- TC(t/6 + p/3) = M \qquad \text{(B.11)}$$

and from Eqs (B.10) and (B.11) the unknowns ε_c and p can be determined.

In between the section at a crack and the section distance ℓ_b from a crack the steel tensile force is reduced from its value at the cracked section and this force loss is transferred to the concrete. If the steel tensile stress at a cracked section is f_{sa} and the stress at a section distance ℓ_b from the cracked section is f_{sb} then the total reduction in steel force = $(f_{sa} - f_{sb})a_{sb}$ and this equals the average bond stress times the surface area of the reinforcement times ℓ_b. In between these sections the reduction in the steel force, for the bond stress distributions assumed in Section 4.2, is listed in Table B.1.

Bond Stress Distribution	Reduction in Steel Force
Triangular	$2(f_{sa} - f_{sb})\, a_{sb}\, (X - \frac{1}{2}X^2)$
Rectangular	$(f_{sa} - f_{sb})\, a_{sb}\, X$
Sinusoidal	$(f_{sa} - f_{sb})\, a_{sb}\, (1 - \cos \pi X)/2$

where $X = x/\ell_b$ and x = the distance from the cracked section.

Table B.1 Reduction in Steel Force Between Cracked Sections

For applied moments that are greater than the moment which just causes cracking the reduction in the tensile steel force for sections in between two cracked sections will be the value given in Table B.1. The unknowns are now p and TC and they can be determined from Eqs (B.10) and (B.11).

APPENDIX C

Formation of the Connective Matrix

This appendix describes how the connective matrix, of Eq. (5.3), is constructed. Basically, the deflection of a point p, which separates the two elastic regions of a bi-elastic beam (Fig. C.1), is related to all the possible deflection modes of the beam and, with this information, the connective matrix can be formed. All the examples cited below can be solved using the moment-area method. Because this method is straightforward in its application and because, in these examples, it involves some lengthy algebraic manipulations, only the initial conditions and the final result have been recorded.

For the flexural behaviour of the beam there are four cases to consider, namely a displacement and a rotation at nodes i and j. A coordinate system s-n-z is taken at node i (refer Fig. C.1) and the positive rotations are defined as,

$$\theta_s = \frac{\partial w}{\partial n}$$

$$\theta_n = -\frac{\partial w}{\partial s}. \qquad \text{(C.1)}$$

Consider first a displacement at node i; the deflection curve and the moment diagram are shown in Fig. C.2. The rotation of the tangent at node i with respect to the tangent at node j is zero, hence,

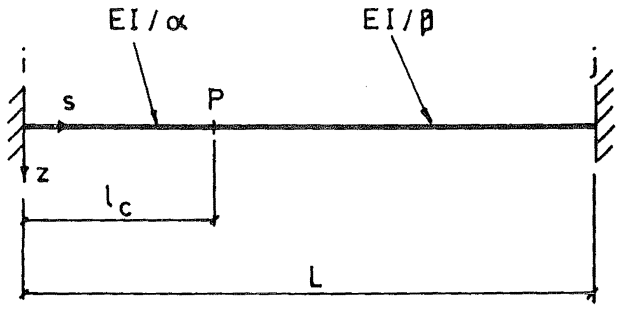

Fig. C.1. Bi-Elastic Beam

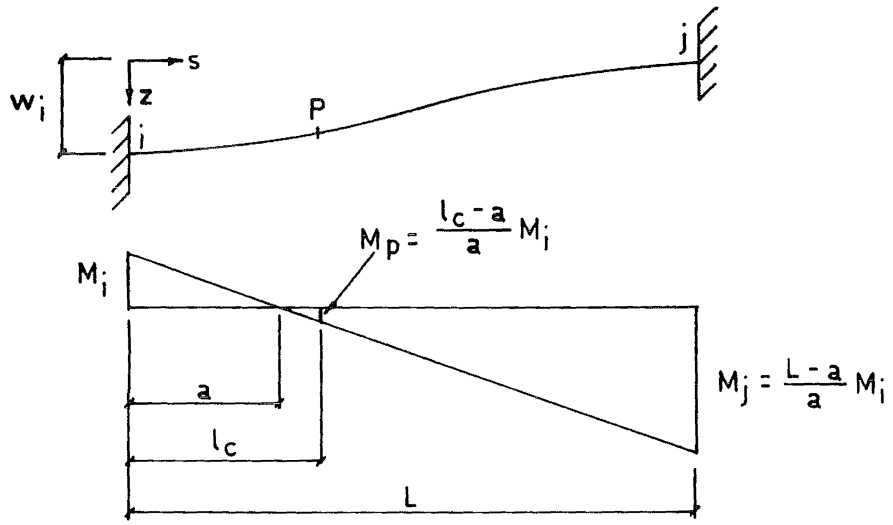

Fig. C.2. Deflection Curve and Moment Diagram for a Displacement at Node i

$$a = \tfrac{1}{2} \frac{(\alpha-\beta)\ell_c^2 + \beta L^2}{(\alpha-\beta)\ell_c + \beta L} \qquad (C.2)$$

Also, the displacement of node i with respect to the tangent at node j is w_i, so that we obtain

$$\frac{M_i}{EI} = 6qw_1 \qquad (C.3)$$

where

$$\frac{1}{q} = -a^2\alpha + \frac{(\ell_c-a)^2}{a}(\alpha-\beta)(a+2\ell_c) + \frac{(L-a)^2}{a}(a+2L),$$

and therefore the rotation and displacement at node p is

$$\theta_{np} = 3q\alpha\left[a - \frac{(\ell_c-a)^2}{a}\right] w_i \qquad (C.4)$$

and

$$w_p = \left[1 - q\alpha\left\{a(3\ell_c-a) - \frac{(\ell_c-a)^3}{a}\right\}\right] w_i.$$

If we consider a displacement w_j, the deflection curve and moment diagram (shown in Fig. C.3) are similar to that of Fig. C.2, and therefore the rotation and displacement at node p can be taken from Eqs (C.4), i.e.

$$\theta_{np} = -3q\alpha\left[a - \frac{(\ell_c-a)^2}{a}\right] w_j \qquad (C.5)$$

and

$$w_p = q\alpha\left[a(3\ell_c-a) - \frac{(\ell_c-a)^3}{a}\right] w_j$$

where q is given in Eq. (C.3).

Fig. C.4 shows the deflection curve and moment diagram for the next case which is a rotation at node i. The displacement of node i, with respect to the tangent at node

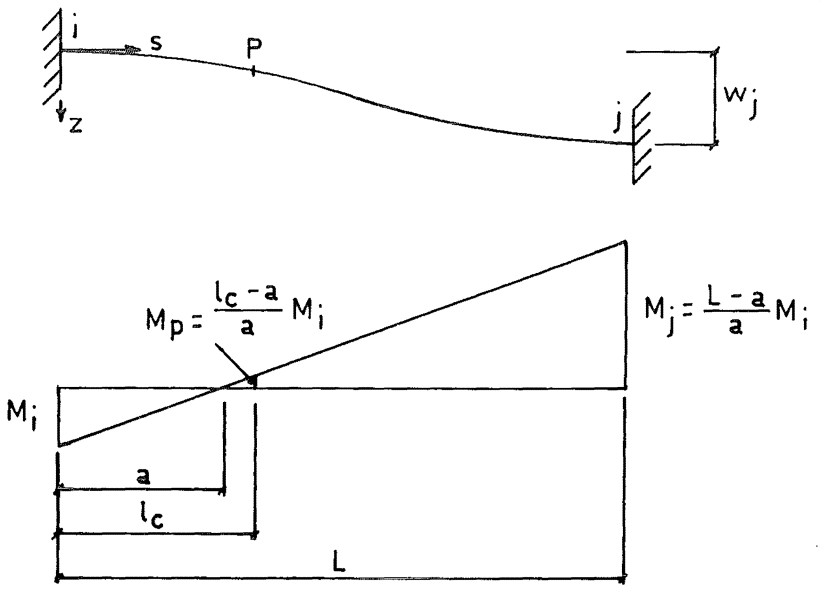

Fig. C.3. Deflection Curve and Moment Diagram for a Displacement at Node j

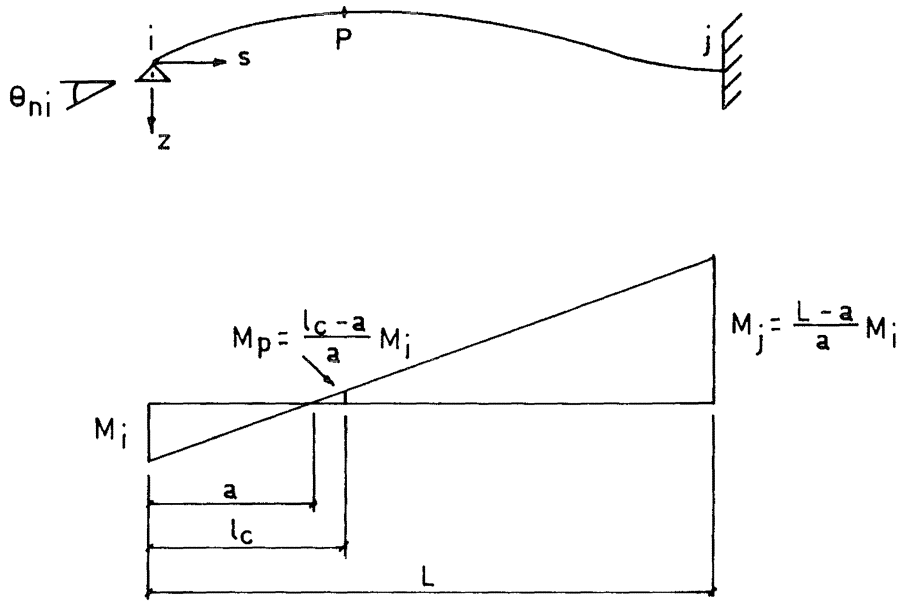

Fig. C.4. Deflection Curve and Moment Diagram for a Rotation at Node i

j, is zero, from which

$$a = \frac{2}{3} \frac{(\alpha-\beta)\ell_c^3 + \beta L^3}{(\alpha-\beta)\ell_c^2 + \beta L^2} . \qquad (C.6)$$

Also, the rotation of node i, with respect to the tangent at node j, is θ_{ni}, so that

$$\frac{M_i}{EI} = 4q\theta_{ni} \qquad (C.7)$$

where

$$\frac{1}{q} = 2\left[\alpha a - (\alpha-\beta)\frac{(\ell_c-a)^2}{a} - \beta\frac{(L-a)^2}{a}\right] ,$$

and therefore the rotation and displacement at node p is

$$\theta_{np} = -2q\beta \frac{L+\ell_c-2a}{a} (L-\ell_c)\theta_{ni}$$

and,

$$w_p = -\frac{2}{3}q\beta \frac{(L-\ell_c)^2}{} [\ell_c + 2L - 3a]\theta_{ni} . \qquad (C.8)$$

The fourth case is a rotation at node j; the deflection curve and moment diagram for this is shown in Fig. C.5.

The displacement of node j, with respect to the tangent at node i, is zero, therefore

$$a = L - \frac{2}{3} \frac{(\beta-\alpha)(L-\ell_c)^3 + \alpha L^3}{(\beta-\alpha)(L-\ell_c)^2 + \alpha L^2} . \qquad (C.9)$$

Also, the rotation of node j, with respect to the tangent at node i, is θ_{nj}, so that

$$M_i = 4q\theta_{nj} \qquad (C.10)$$

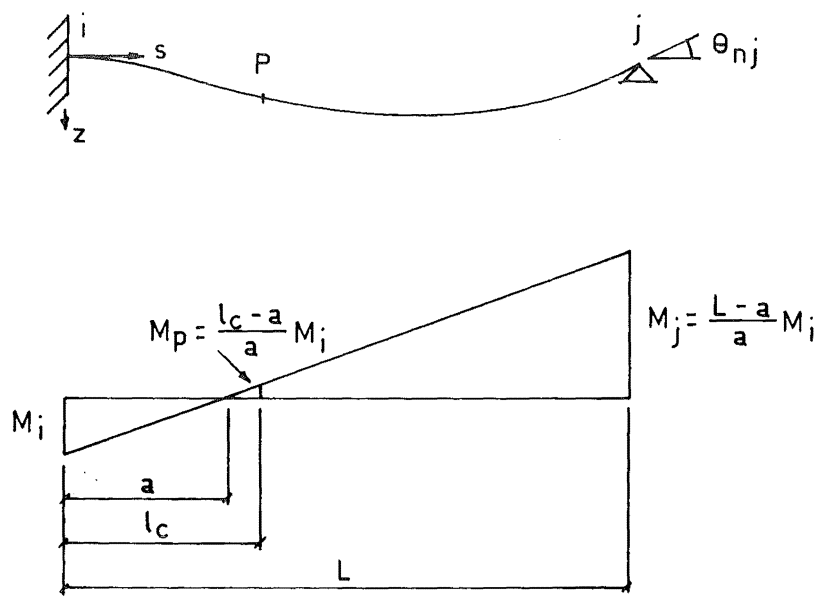

Fig. C.5. Deflection Curve and Moment Diagram for a Rotation at Node j

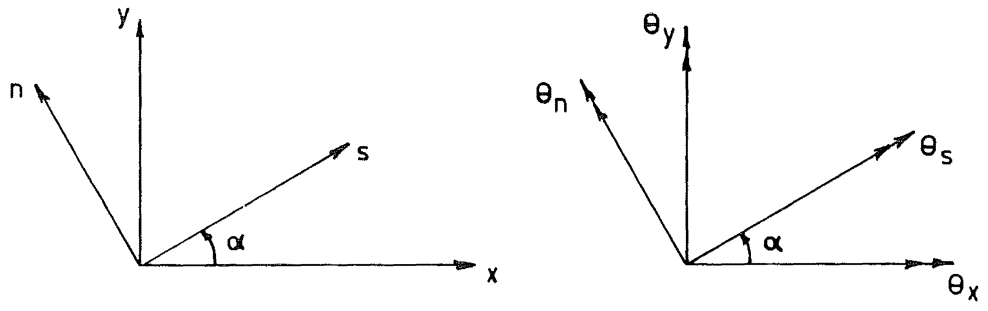

Fig. C.6. Coordinate Transformation

where

$$\frac{1}{q} = -2\left[\alpha a - (\alpha-\beta)\frac{(\ell_c-a)^2}{a} - \beta\frac{(L-a)^2}{a}\right]$$

and therefore the rotation and displacement at node p is

$$\theta_{np} = -2q\alpha\left[\alpha a - \frac{(\ell_c-a)^2}{a}\right]\theta_{nj}. \qquad (C.11)$$

and

$$w_p = q\alpha\left[2a(\ell_c - \tfrac{1}{3}a) - \frac{2}{3}\frac{(\ell_c-a)^3}{a}\right]\theta_{nj}.$$

Considering the torsional behaviour of the beam, for a fully elastic beam, we have

$$\phi = \frac{TL}{GJ} \qquad (C.12)$$

where T is the torque applied to the beam, ϕ is the total angle of twist over the distance L, and GJ is the shear rigidity. If we assume that the shear rigidity varies as the flexural rigidity varies then, for node p,

$$\theta_{sp} = \frac{\beta(L-\ell_c)}{(\alpha-\beta)\ell_c + \beta L}\theta_{si} + \frac{\alpha\ell_c}{(\alpha-\beta)\ell_c + \beta L}\theta_{sj}. \qquad (C.13)$$

The deflection of the point p can now be related to the deflections of the corner nodes i and j by incorporating Eqs (C.4), (C.5), (C.8), and (C.11). Having obtained this relationship in the coordinate system s-n-z we can transform it to a common coordinate system x-y-z (Fig. C.6) by using the transformation,

$$\begin{Bmatrix} W \\ \theta_s \\ \theta_n \end{Bmatrix} = \begin{bmatrix} 1 & 0 & 0 \\ 0 & \cos\alpha & \sin\alpha \\ 0 & -\sin\alpha & \cos\alpha \end{bmatrix} \begin{Bmatrix} w \\ \theta_x \\ \theta_y \end{Bmatrix} . \qquad \text{(C.14)}$$

APPENDIX D

Subdivision of Plate Bending Element and Numerical Integration

This appendix contains details of how the plate bending element described in Appendix A was divided into elastic and inelastic regions, and also how the numerical integration was performed over partial areas.

The plate bending element is shown divided into three subelements in Fig. A.5. When the element is divided into two regions, for example, by a line 5-6, the subelements can be divided into subtriangles where the additional side node is assumed to be at the midside and the nodes on the internal lines, if not intersected by the line 5-6, are also assumed to be at the midsides. Fig. D.1 shows the two possible configurations of such a divided element.

We wish to integrate Eq. (5.8), which is

$$[N_i] = [D_i]_{A_i} \int [\psi][\psi]^T \, dA_i, \qquad (D.1)$$

over a partial area and this is most easily done by a numerical procedure.

Consider subelement 3 (Fig. D.1), comprising the four subtriangles 1-4-7, 4-2-8, and 4-8-7. The first three subtriangles have two sides common with the subelement and therefore the area can be subdivided by lines formed by the equations

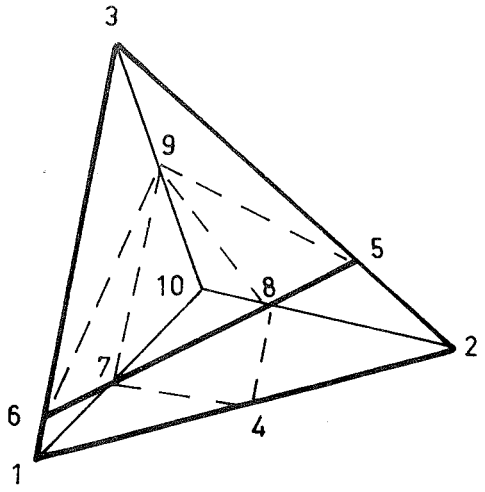

a

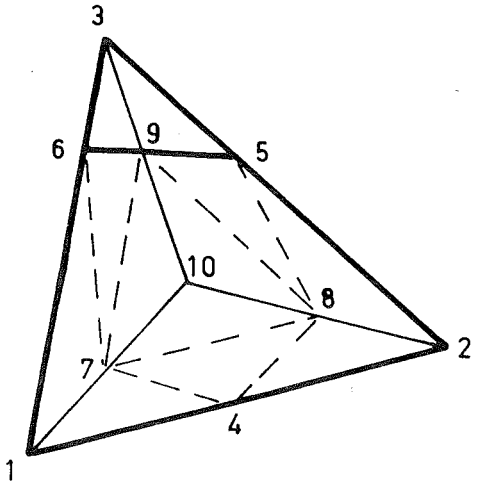

b

Fig. D.1. Subdivision of the Plate Bending Element

$$\zeta_i^{(p)} = c_1$$
$$\zeta_j^{(p)} = c_2 \qquad (D.2)$$

where p is the subelement number, i and j are the values of the common sides $\ell_i^{(p)}$ and $\ell_j^{(p)}$, i.e. they have the value 1, 2 or 3, and c_1 and c_2 are constants.

As an example, consider subtriangle 1-4-7 of Fig. D.1a. The two common sides of the subtriangle and the subelement are $\ell_2^{(3)}$ and $\ell_3^{(3)}$ (i.e. 1-10 and 1-2 respectively), and, assuming that the point 7 is the quarterpoint, Fig. D.2 shows the subtriangle divided by the two sets of lines which divide the lines 1-4 and 1-7 into three equal portions, i.e. by

$$\zeta_2^{(3)} = \frac{2}{3}, \frac{5}{6} \text{ and } 1,$$

$$\zeta_3^{(3)} = \frac{1}{2}, \frac{3}{4} \text{ and } 1,$$

also, a third set of lines is shown which divide the subtriangle into smaller triangles.

Assuming that the constitutive matrix within subtriangle 1-4-7 is constant, we can determine the contribution to the curvature stiffness matrix N_i by replacing the integral of Eq. (D.1) by a summation, i.e.

$$[\Delta N_i] = [D_i] \frac{A_i}{n} \sum_{j=1}^{n} [\psi][\psi]^T \qquad (D.2)$$

where n is the number of equal triangles that the subtriangle is divided into, and the function $[\psi]$ is calculated at the

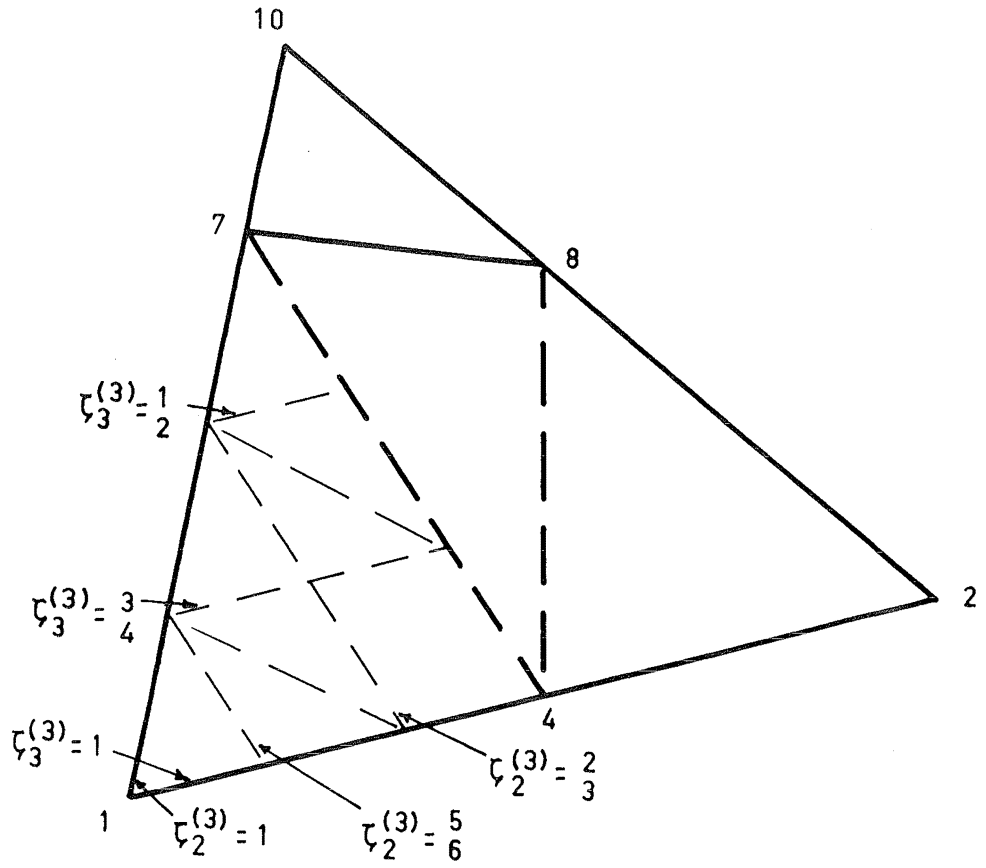

Fig. D.2. Subdivision of Subtriangle 1-4-7

centroid of the triangle and thence summed over the sub-triangle.

This process can be used for the three corner triangles, 1-4-7, 4-2-8 and 7-8-10 using any number of divisions within each area.

The interior subtriangle 4-7-8 does not have any sides common with the subelement and another method is used to determine this integration. The integration over the complete subelement is known[8] and therefore the integration of the interior subtriangle is determined by subtracting from the complete subelement integration the sum of the three corner triangle integrations (which are summed independently of their constitutive matrices).

REFERENCES

1. Bach, C., Elasticitat und Festigkeit, 3rd ed., Julius Springer, Berlin, 1898, pp. 552-564.

2. Ingerslev, A., "The Strength of Rectangular Slabs", Journal of the Institute of Structural Engineers, Vol.1, No.1, Jan. 1923, pp.3-14.

3. Johansen, K.W., "The Ultimate Strength of Reinforced Concrete Slabs", 3rd Congress, International Association for Bridge and Structural Engineering, Liege, Belgium, Sept. 1948, pp. 565-570.

4. Hognestad, E., "Yield-Line Theory for the Ultimate Flexural Strength of Reinforced Concrete Slabs", Proceedings of the American Concrete Institute, Vol.49, No.7, Mar. 1953, pp. 637-656.

5. Bhaumik, A.K., and Hanley, J.T., "Elasto-Plastic Plate Analysis by Finite Differences", Proceedings of the American Society of Civil Engineers, Vol.93, No.ST5, Oct., 1967, pp.279-294.

6. Riera, J.D., and Billington, D.P., "Non-Linear Analysis for Thin-Shell Concrete Structures", Research Report No. 68-3, Princeton University, New Jersey, Aug. 1968.

7. McNeice, G.M. and Kemp, K.O., "Comparison of Finite Element and Unique Limit Analysis Solutions for Certain Reinforced Slabs", Proceedings of the Institute of Civil Engineers, Vol.43, Aug. 1969, pp. 629-640.

8. Felippa, C.A., "Plate Bending Finite Elements", Ph.D. Thesis, University of California, Berkeley, 1966.

9. Carr, A.J., "A Refined Finite Element Analysis of Thin Shell Structures Including Dynamic Loading", Ph.D. Thesis, University of California, Berkeley, 1967.

10. Hrennikoff, A., "Solution of Problems of Elasticity by the Framework Method", Journal of Applied Mechanics, Vol.8, No.4, Dec. 1941, pp. A169-A175.

11. Argyris, J.H., "Energy Theorems and Structural Analysis", Aircraft Engineering, Vol.26, Oct.-Nov. 1954, Feb.-May 1955, Energy Theorems and Structural Analysis, Butterworths, London, 1960.

12. Turner, M.J., Clough, R.W., Martin, H.C., and Topp, L.J., "Stiffness and Deflection Analysis of Complex Structures", Journal of the Aeronautical Sciences, Vol.23, No.9, Sept. 1956, pp. 805-823.

13. Islam, S., "A Comparative Study of Virtual Work and Equilibrium Methods Applied to Yield-Line Analysis of Reinforced Concrete Slabs", M.Sc.Tech. Thesis, Manchester College of Science and Technology, Manchester, 1964.

14. Sharpe, R., "The Rational Design of Reinforced Concrete Slabs", M.E. Thesis, University of Melbourne, Melbourne, Australia, 1966.

15. Hedgren (Jr), A.W., "A Numerical and Experimental Study of Translational Shell Roofs", Ph.D. Thesis, Princeton University, New Jersey, 1965.

16. Clough, R.W., "The Finite Element Method in Plane Stress Analysis", Proceedings of the 2nd Conference on Electronic Computation, Pittsburgh, Sept. 1960, pp. 345-378.

17. Pian, T.H.H., "Derivation of Element Stiffness Matrices by Assumed Stress Distributions", American Institute of Aeronautics and Astronautics Journal, Vol.2, No.6, July 1964, pp.1333-1336.

18. Argyris, J.H., Kelsey, S., and Kamel, H., "Matrix Methods of Structural Analysis", Matrix Methods of Structural Analysis, B. Fraeijs de Veubeke, ed., Pergamon Press, Oxford, 1964, pp. 1-164.

19. Felippa, C.A., "Refined Finite Element Analysis of Linear and Non-Linear Two Dimensional Structures", U.C.SEL Report No. 66-22, University of California, Berkeley, 1966.

20. Clough, R.W., "The Finite Element Method in Structural Mechanics", Stress Analysis, O.C., Zienkiewicz and G.S. Holister, eds, J. Wiley & Sons, Inc., London, 1965, pp. 85-119.

21. Fraeijs de Veubeke, B., "Displacement and Equilibrium Models in the Finite Element Method" Stress Analysis, O.C. Zienkiewicz and G.S. Holister, eds., J. Wiley & Sons, Inc., London, 1965, pp. 145-197.

22. Tong, P., and Pian, T.H.H., "The Convergence of the Finite Element Method in Solving Linear Elastic Problems", International Journal of Solids and Structures, Vol.3, No.5, Sept. 1967, pp. 865-879.

23. Pian, T.H.H., and Tong, P., "Basis of Finite Element Methods for Solid Continua", International Journal of Numerical Methods in Engineering, Vol.1, No.1, Jan.-Mar., 1969, pp. 3-28.

24. Oliveira, E.R.A., "Theoretical Foundations of the Finite Element Method", International Journal of Solids and Structures, Vol.4, No.10, Oct. 1968, pp. 929-952.

25. Severn, R.T., and Taylor, P.R., "The Finite Element Method for Flexure of Slabs When Stress Distributions are Assumed", Proceedings of the Institute of Civil Engineers, Vol.34, June 1966, pp.153-170.

26. Bogner, F.K., Fox, R.L., and Schmit, L.A. Jr., "The Generation of Interelement, Compatible Stiffness and Mass Matrices by the Use of Interpolation Formulas", Proceedings of the Conference on Matrix Methods in Structural Mechanics, Air Force Institute of Technology, Dayton, Ohio, Oct. 1965, pp.397-443.

27. Clough, R.W., and Tocher, J.L., "Finite Element Stiffness Matrices for Analysis of Plate Bending", Proceedings of the Conference on Matrix Methods in Structural Mechanics, Air Force Institute of Technology, Dayton, Ohio, Oct. 1965, pp. 515-545.

28. Bazeley, G.P., Cheung, Y.K., Irons, B.M., and Zienkiewicz, O.C., "Triangular Elements in Plate Bending - Conforming and Non-Conforming Solutions", Proceedings of the Conference on Matrix Methods in Structural Mechanics, Air Force Institute of Technology Dayton, Ohio, Oct. 1965, pp. 547-576.

29. Fraeijs de Veubeke, B., "A Conforming Finite Element for Plate Bending", International Journal of Solids and Structures, Vol.4, No.1, Jan. 1968, pp. 95-108.

30. Irons, B.M., "A Conforming Quartic Triangular Element for Plate Bending", International Journal of Numerical Methods in Engineering, Vol.1, No.1, Jan.-Mar. 1969, pp. 29-46.

31. Grafton, P.E., and Strome, D.R., "Analysis of Axisymmetric Shells by the Direct Stiffness Method", American Institute of Aeronautics and Astronautics Journal, Vol.1, No.10, Oct. 1963, pp. 2342-2347.

32. Percy, J.H., Pian, T.H.H., Klein, S. and Navaratna, D.R., "Application of Matrix Displacement Method to Linear Elastic Analysis of Shells of Revolution", American Institute of Aeronautics and Astronautics Journal, Vol.3, No.11, Nov. 1965 pp. 2138-2145.

33. Popov, E.P., Penzien, J., and Lu, Z., "Finite Element Solution for Axisymmetric Shells", Proceedings of the American Society of Civil Engineers, Vol.90, No. EM5, Oct., 1964, pp.119-145.

34. Jones, R.E., and Strome, D.R., "Direct Stiffness Method Analysis of Shells of Revolution Utilizing Curved Elements", American Institute of Aeronautics and Astronautics Journal, Vol.4, No.9, Sept. 1966, pp.1519-1525.

35. Bogner, F.K., Fox, R.L., and Schmit, L.A. "A Cylindrical Shell Discrete Element", American Institute of Aeronautics and Astronautics Journal, Vol. 5, No.4, April 1967, pp.745-750.

36. Cantin, G., and Clough, R.W., "A Curved Cylindrical Shell Finite Element", American Institute of Aeronautics and Astronautics Journal, Vol.6, No.6, June 1968, pp.1057-1062.

37. Connor, J.J., Jr., and Brebbia, C., "Stiffness Matrix for Shallow Rectangular Shell Element", Proceedings of the American Society of Civil Engineers, vol.93, No.EM5, Oct. 1967, pp.43-65.

38. Solkolnikoff, I.S., Mathematical Theory of Elasticity, 2nd. ed., McGraw-Hill Book Co.Inc., New York, 1956.

39. Levy, S., "Structural Analysis and Influence Coefficients for Delta Wings", Journal of the Aeronautical Sciences, Vol.20, No.7, July 1953, pp. 449-454.

40. "Use of Fourier Series in the Finite Element Method", American Institute of Aeronautics and Astronautics Journal, Vol.6, No.4, Apr. 1968, pp. 726-728.

41. Herrmann, L.R., "A Bending Analysis for Plates", Proceedings of the Conference on Matrix Methods in Structural Mechanics, Air Force Institute of Technology, Dayton, Ohio, Oct. 1965, pp. 577-602.

42. Courant, R., "Variational Methods for the Solution of Problems of Equilibrium and Vibrations", Bulletin of the American Mathematical Society, Vol.49, Jan. 1943, pp.1-23.

43. Melosh, R.J., "Structural Analysis of Solids", Proceedings of the American Society of Civil Engineers, Vol.89, No.ST4, Aug.1963, pp.205-223.

44. Zienkiewicz, O.C., and Cheung, Y.K., The Finite Element Method, McGraw-Hill Publishing Co.Ltd., London, 1967.

45. Westlake, J.R., A Handbook of Numerical Matrix Inversion and Solution of Linear Equations, John Wiley & Sons, Inc., New York, 1968.

46. Navaratna, D.R., "Computation of Stress Resultants in Finite Element Analysis", American Institute of Aeronautics and Astronautics Journal, vol.4, No.11, Nov. 1966, pp. 2058-2060.

47. Brebbia, C., and Connor, M., "Geometrically Non-Linear Finite-Element Analysis", Proceedings of the American Society of Civil Engineers, Vol.95, No. EM2, Apr. 1969, pp. 463-481.

48. Hognestad, E., "A Study of Combined Bending and Axial Load in Reinforced Concrete Members", University of Illinois Engineering Experimental Station Bulletin, Series No.399, 1951.

49. Przemieniecki, J.G., "Matrix Structural Analysis of Substructures", American Institute of Aeronautics and Astronautics Journal, Vol.1, No.1, Jan. 1963, pp. 138-147.

50. Tresca, H., Comptes Rendus, Academie des Sciences, Paris, Vol.59, 1864, p. 754.

51. Von Mises, R., "Mechanik der Festen Korper in Plastisch Deformablen Zustand", Nachrichten Math. Phys. Klasse, Gottingen, Germany, 1913, pp. 582-592.

52. Hencky, H., Zeits. ang. Math. Mech., Vol. 4, 1924, p.323.

53. Hodge, P.G., Plastic Analysis of Structures, McGraw Hill Book Co. Inc., New York, 1959, pp. 249-268.

54. Pope, G.G., "A Discrete Element Method for the Analysis of Plane Elasto-Plastic Stress Problems", Aeronautical Quarterly, Vol.17, Part 1, Feb. 1966, pp.83-104.

55. Marcal, P.V., and King, I.P., "Elastic-Plastic Analysis of Two-Dimensional Stress Systems by the Finite Element Method", International Journal of Mechanical Science, Vol.9, No.3, Mar. 1967, pp. 143-155.

56. Marcal, P.V., and Pilgrim, W.R., "A Stiffness Method for Elastic-Plastic Shells of Revolution", The Journal of Strain Analysis, Vol.1, No.4, July 1966, pp. 339-350.

57. Zienkiewicz, O.C., Valliapan, S., and King, I.P., "Elasto-Plastic Solutions of Engineering Problems 'Initial Stress', Finite Element Approach", International Journal for Numerical Methodsin Engineering, Vol.1, No.1, Jan.-Mar. 1969, pp. 75-100.

58. Brotchie, J.F., "Elastic-Plastic Behaviour in Flat Plate Structures", Ph.D. Thesis, University of California, Berkeley, 1961.

59. Brotchie, J.F., "Elastic-Plastic Analysis of Transversely Loaded Plates", Proceedings of the American Society of Civil Engineers, Vol.86, No. EM5, Oct. 1960, pp. 57-90.

60. Wood, R.H., Plastic and Elastic Design of Slabs and Plates, Thames and Hudson, London, 1961, p. 344.

61. Kwiecinski, M.W., "Some Tests on the Yield Criterion for a Reinforced Concrete Slab", Magazine of Concrete Research, Vol.17, No.52, Sept. 1965, pp. 135-138.

62. Moreley, C.T., "Experiments on the Distortion of Steel Bars Across Cracks in Reinforced Concrete Slabs", Magazine of Concrete Research, Vol.18, No.54, Mar. 1966, pp. 25-34.

63. Prince, M.R., and Kemp, K.O., "A New Approach to the Yield Criterion for Isotropically Reinforced Concrete Slabs", Magazine of Concrete Research, Vol.20, No.62, Mar. 1968, pp. 13-20.

64. Kwiecinski, M.W., "Yield Criterion for an Orthotropically Reinforced Slab", International Journal of Solids and Structures, Vol.1, No.4, Nov. 1965, pp. 439-449.

65. Hearman, R.F.S., An Introduction to Applied Anisotropic Elasticity, Oxford University Press, London, 1961.

66. Zienkiewicz, O.C., Cheung, Y.K., and Stagg, K.G., "Stresses in Anisotripic Media with Particular Reference to Problems of Rock Mechanics", Journal of Strain Analysis, Vol.1, No.2, Jan. 1966, pp. 172-182.

67. Pfrang, E.O., Siess, C.P., and Sozen, M.A., "Load-Moment-Curvature Characteristics of Reinforced Concrete Cross-Sections", Proceedings of the American Concrete Institute, Vol.61, No.7, July 1964, pp. 763-778.

68. Ferry-Borges, J., and Oliveira, E.R., "Non-Linear Analysis of Reinforced Concrete Structures", International Association for Bridge and Structural Engineering, Vol.23, 1963, pp. 51-70.

69. Priestley, M.J.N., "Moment Redistribution in Prestressed Concrete Continuous Beams", Ph.D. Thesis, University of Canterbury, Christchurch, New Zealand, 1966.

70. Comité Europeen du Bétan , Bulletin D'Information No.12, Feb. 1959.

71. Neville, A.M., Properties of Concrete, Sir Isaac Pitman and Sons Ltd., London, 1963.

72. Sozen, M.A., Zwoyer, E.M., and Siess, C.P., "Strength in Shear of Beams Without Web Reinforcement", University of Illinois Engineering Experiment Station Bulletin, Series No. 452, April 1959.

73. Walker, S., and Bloem, D.L., "Effects of Aggregate Size on Properties of Concrete", Proceedings of the American Concrete Institute, Vol.57, No.3, Sept. 1960, pp. 283-298.

74. Ramakrishnan, V., Ananthanarayana, Y., and Gopal, K.C., "The Determination of the Tensile Strength of Concrete: A Comparison of Different Methods", Indian Concrete Journal, Vol.41, No.5, May 1967, pp. 202-206.

75. "ACI Standard Building Code Requirements for Reinforced Concrete", ACI 318-63, June 1963.

76. Mains, M.F., "Measurement of the Distribution of Tensile and Bond Stresses Along Reinforcing Bars", Proceedings of the American Concrete Institute, Vol.48, No.3, Nov. 1951, pp. 205-252.

77. Wilson, W.B., "Finite Element Analysis of Two Dimensional Structures", Structures and Materials Research Department of Civil Engineering Report No. 63-2, University of California, Berkeley, 1963.

78. Magura, D.D., "Structural Model Testing-Reinforced and Prestressed Mortar Beams", Journal of the PCA Research and Development Laboratories, Vol.9, No.1, Jan. 1967, pp. 2-24, PCA Development Department Bulletin D113.

79. Martin, H.C., "On the Derivation of Stiffness Matrices for the Analysis of Large Deflection and Stability Problems", Proceedings of the Conference on Matrix Methods in Structural Mechanics, Air Force Institute of Technology, Dayton, Ohio, Oct. 1965, pp. 697-716.

80. Bouma, A.L., van Riel, A.C., van Koten, H., and Beranek, W.J., "Investigations on Models of Eleven Cylindrical Shells Made of Reinforced and Prestressed Concrete", Proceedings of the Symposium on Shell Research, Delft, 1961, pp. 79-101.